Uncertainties in the Quantification of Aerosol-Cloud Interactions

Von der Fakultät für Physik und Geowissenschaften

der Universität Leipzig

genehmigte

DISSERTATION

zur Erlangung des akademischen Grades

Doctor rerum naturalium

(Dr. rer. nat.)

vorgelegt

von M.Sc. Daniel Merk

geboren am 13.05.1987 in Memmingen

1. Gutachter: Prof. Dr. Andreas Macke
2. Gutachter: Prof. Dr. Ralf Bennartz

Tag der Verleihung: 24.04.2017

Bibliographische Beschreibung:
Merk, Daniel
Unsicherheiten bei der Quantifizierung von Aerosol-Wolken-Wechselwirkungen
Universität Leipzig, Dissertation
109 S., 170 Lit., 59 Abb., 14 Tab.

Zusammenfassung:

Aerosole dienen als Kondensationskerne (CCN) und verändern die Wolkentropfenkonzentration (N_d) und weitere Wolkeneigenschaften. N_d ist daher ein Schlüsselparameter von Aerosol-Wolken-Wechselwirkungen (ACI). ACI sind bezüglich ihrer Klimarelevanz nur unzureichend bestimmt. ACI wurden auf verschiedenen Skalen und mit unterschiedlichen Methoden von unterschiedlichen Perspektiven aus untersucht, was zu einer großen Variabilität von ACI Metriken in der Literatur führt. Für eine genauere Quantifizierung von ACI, wurden in dieser Arbeit damit verbundene, entscheidende Unsicherheiten diskutiert, u.a. das Einmischen trockener Luft, Unsicherheiten von Retrieval-Methoden und die Konsistenz von Schlüsselparametern auf verschiedenen Skalen. Um N_d und weitere Wolkeneigenschaften aus passiven Satellitenbeobachtungen für Flüssigwasserwolken abzuleiten, wird oft das adiabatische Modell herangezogen. Es wurde untersucht, inwiefern dieses Modell reale Bedingungen wiedergibt. Es wurde gezeigt, dass Wolken typischerweise subadiabatisch sind, mit stark reduziertem Flüssigwassergehalt nahe der Wolkenoberkante. Der Einmischprozess variiert zeitlich stark und erschwert die Quantifizierung von ACI. Für unterschiedliche Cloudnet-Stationen variieren die Medianwerte des subadiabatischen Faktors von 0.35 ± 0.12 bis 0.48 ± 0.22. Dieser hängt stark von der geometrischen Wolkendicke ab, wobei dickere Wolken subadiabatischer sind. Die Ableitung von N_d aus bodenbasierten Radar-Radiometer-Beobachtungen ist sehr sensitiv gegenüber a-priori Annahmen. Um zusätzliche Beobachtungen und Unsicherheiten berücksichtigen zu können, wurde ein neuartiges Optimal Estimation (OE) Retrieval entwickelt und mittels synthetischer Wolkenprofile evaluiert. Mittels einer Sensitivitätsstudie konnte die Verbesserung der Retrieval-Genauigkeit für die OE Methode gezeigt werden, wenn die Beobachtungen der optischen Dicke mit berücksichtigt werden. Die Annahme einer typischen Breite der Tropfengrößenverteilung ist dabei eine der größten Unsicherheiten von N_d (Unsicherheit für die OE Methode etwa 150%, für die Radar-Radiometer-Methode etwa 200%). Desweiteren wurden aus unterschiedlichen Perspektiven abgeleitete wolkenmikrophysikalische Größen hinsichtlich ihrer Konsistenz untersucht. Beim Vergleich von N_d und des Effektivradius (r_e) vom bodengebundenen Retrieval mit in-situ Beobachtungen für einen Falltag wurde eine gute Übereinstimmung gefunden. Beim Vergleich der von SEVIRI und Bodenstationen abgeleiteten Wolkeneigenschaften haben sich mittlere quadratische Abweichungen des Flüssigwasserpfads und der optischen Dicke von jeweils $65\,\mathrm{g\,m^{-2}}$ und 14 ohne signifikanten Bias gezeigt. Damit zeigt sich SEVIRI für großskalige, statistische ACI-Untersuchungen repräsentativ zur Bodenperspektive. Für individuelle Falltage traten jedoch teils größere Unterschiede auf, welche durch Inhomogenitäten und Auflösungseffekte erklärt werden können. Mit SEVIRI Beobachtungen und aus der MACC Reanalyse abgeleiteten CCN Konzentrationen wurde eine Quantifizierung von ACI für das Jahr 2012 durchgeführt. Dabei wurde für Europa ein deutlicher, mikrophysikalischer Effekt gefunden, d.h. eine Abnahme von r_e und eine Zunnahme von N_d mit zunehmender CCN Konzentration. Im Gegensatz dazu wurde für die Wolkenalbedo kein eindeutiger Anstieg mit der CCN-Konzentration gefunden. Verwendet man die Aerosol-optische Dicke (AOD) anstelle der CCN-Konzentration, sind die Werte der ACI Metrik nur halb so groß. Dieses Ergebnis deutet darauf hin, dass die AOD kein optimaler CCN-Proxy ist.

Bibliographic Description:
Merk, Daniel
Uncertainties in the Quantification of Aerosol-Cloud Interactions
University of Leipzig, Dissertation
109 p., 170 ref., 59 fig., 14 tab.

Abstract:

Aerosols serve as cloud condensation nuclei (CCN) and change the number of cloud droplets (N_d) and further cloud properties. Therefore, N_d is a key parameter for ACI. ACI are still poorly constrained in terms of their climate relevance. ACI have been investigated with different methods from different perspectives and at different scales, leading to a large variability of reported ACI metrics. To obtain a more accurate quantification of ACI, major problems have been addressed within this thesis, such as entrainment, retrieval uncertainties and the consistency of key cloud parameters from different scales. For obtaining properties of liquid cloud layers from passive satellite observations, an adiabatic cloud model is often applied. Its applicability for ACI investigations has been investigated. In this work, it has been shown that liquid clouds are typically subadiabatic and liquid water content is drastically reduced near the cloud top. Entrainment varies strongly with time and complicates the quantification of ACIs. For different stations, median values of the subadiabatic factor range from 0.35 ± 0.12 to 0.48 ± 0.22. It strongly depends on cloud geometrical depth, with thicker clouds being more subadiabatic. The retrieval of N_d from ground-based radar-radiometer observations is very sensitive to a-priori assumptions. In this work, a novel Optimal Estimation (OE) framework has been developed to consider additional observations and uncertainties, and has been evaluated utilizing synthetic cloud profiles. A sensitivity study has shown a general improvement of retrieved N_d utilizing the OE retrieval and including observations of optical depth. The assumption about the width of the drop size distribution remains a large source of uncertainty for retrieved N_d (about 150% uncertainty for the OE method and about 200% for the radar-radiometer approach). Consistency checks of cloud properties observed from different perspectives have been conducted. Contrasting ground-based retrieved N_d and effective radius (r_e) with in-situ observations for a case study has shown a good agreement. Contrasting the cloud properties obtained from SEVIRI with those from ground-based sites, RMSD of liquid water path and optical depth were found to be about $65\,\mathrm{g\,m^{-2}}$ and 14, respectively. With no significant bias, larger-scale statistics from satellite should be representative for the ground perspective. For individual cases larger differences have been found and can be explained by inhomogeneities and resolution effects. Finally, an ACI quantification has been conducted using SEVIRI observations and CCN concentrations from MACC reanalysis data for 2012. A clear microphysical response has been obtained for the European domain, i.e. a decrease of r_e and an increase of N_d with CCN concentration ($ACI_N = 0.28$ over land and $ACI_N = 0.23$ over ocean). In contrast to the cloud microphysical response, the cloud albedo effect is not clearly pronounced. Values of ACI_N are only half as big utilizing aerosol optical depth (AOD) instead of CCN concentrations, indicating that AOD is not an optimal CCN proxy.

Contents

1 Motivation

There is clear evidence that the climate on Earth is changing currently due to anthropogenic emissions, faster than any natural change over the last millenia (Stocker et al., 2013). The global average temperature is currently increasing by about 0.2 K per decade (Hansen et al., 2010) and global mean sea level rises about 3 mm every year[1]. The main reason for the observed changes is the increase in greenhouse gas concentrations driven by anthropogenic emissions. On the other hand, the increase of anthropogenic aerosols is able to partly counteract this warming as it influences atmospheric radiation and cloud-precipitation processes (Haywood and Boucher, 2000; Lohmann and Feichter, 2005). The global influence of aerosols on clouds is currently not well characterized, and attributes to one of the largest sources of uncertainties in current climate projections (Boucher et al., 2013). There is a great need to further investigate the effect of aerosols on clouds to strengthen our understanding of the processes, improve climate models, allowing for more robust projections of the anthropogenic climate change. This could contribute to more effective decision making in policy.

1.1 Clouds, Aerosols and Radiation

The main source of energy for the Earth is the incoming solar radiation. $340\,\mathrm{W\,m^{-2}}$ of solar radiation reach the top of the atmosphere (TOA) on the annual average (Fig. 1.1). It is scattered and absorbed by the constituents of the atmosphere. These are atmospheric gases, aerosols, cloud droplets, ice particles and precipitation particles. Greenhouse gases and clouds are responsible for reemitting the absorbed radiation as thermal energy back to space and back to the Earth's surface (Kiehl and Trenberth, 1997). This leads to the so-called greenhouse effect, as more thermal radiation is emitted towards the Earth's surface than to the space.

Radiative properties of clouds differ in the longwave and shortwave range. On a global average, clouds reflect more radiation in the solar range than they emit longwave radiation to the surface, and therefore cause a net cooling effect of the atmosphere (Boucher et al., 2013). This counteracts the warming effect by greenhouse gases. Locally, the net radiative forcing of clouds depends on their radiative properties.

On a global scale, the change in net radiative effects due to clouds and anthropogenic aerosols is still highly uncertain. Aerosols have a direct radiative effect, a semi-direct effect and indirect effects. The direct effect refers to the scattering and absorption of solar radiation by aerosols (Haywood and Boucher, 2000). The semi-direct effect describes

---

[1] https://sealevel.nasa.gov/, accessed 15. July 2016.

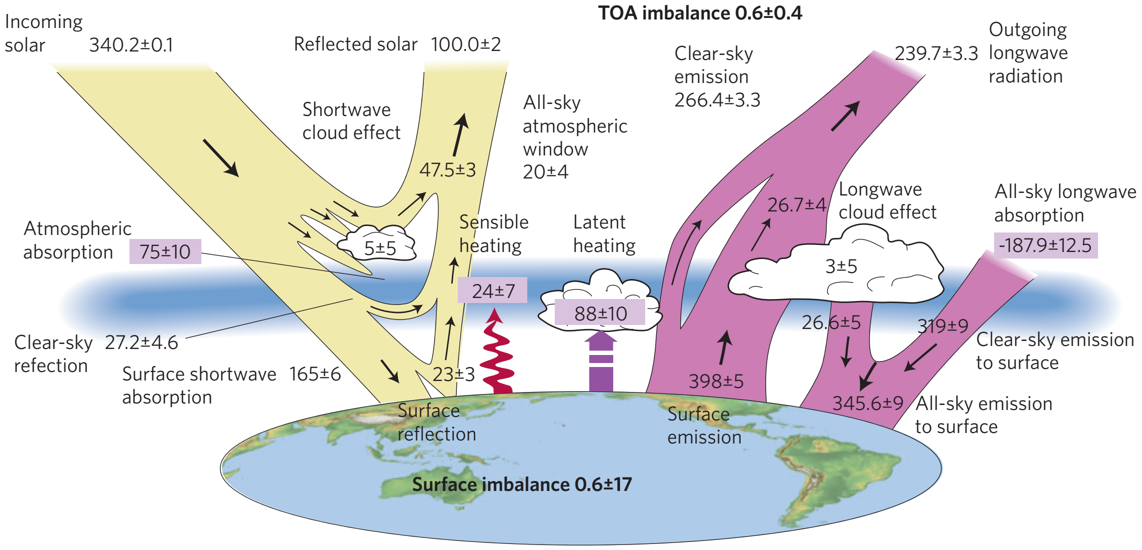

Figure 1.1: Estimate of the Earth's annual and global mean energy balance from 2000–2010. Taken from Stephens et al. (2012).

the influence of absorbing aerosols, e.g., the dissolution of clouds as air is heated due to absorption of solar radiation (Grassl, 1979; Ackerman et al., 2000). Atmospheric aerosols can also cause indirect effects, as they serve as cloud condensation nuclei (CCN) and ice nucleating particles (INP) and hence alter cloud properties. In the latest Intergovernmental Panel on Climate Change (IPCC) report (Boucher et al., 2013), the irradiance changes (effective radiative forcing, ERF) from aerosol cloud interactions (ACI) are seperated into the radiative forcing from the cloud albedo change (Twomey, 1974, RFaci, Twomey effect) and further cloud adjustments. The latter include the increased lifetime of clouds due to suppression of precipitation (formerly referred to as second indirect effects) (Albrecht, 1989; Bellouin et al., 2013).

As ACI are poorly represented in climate models (Boucher et al., 2013), the quantification of the resulting radiative forcing from such models is difficult. The uncertainty of the radiative forcing ranges from $-1.33\,\mathrm{W\,m^{-2}}$ to $-0.06\,\mathrm{W\,m^{-2}}$ with a mean estimate of $-0.55\,\mathrm{W\,m^{-2}}$ (cooling effect). The range estimated from satellite data is -0.2 to $-0.5\,\mathrm{W\,m^{-2}}$ and therefore three to six times smaller than climate model estimates (Yang et al., 2013). Given the total net anthropogenic forcing estimate in 2011 of 2.29 (1.13 to 3.33) $\mathrm{W\,m^{-2}}$, this uncertainty is substantial.

1.2 Twomey Effect

Twomey (1974, 1977), and subsequently many others, reported a change in liquid cloud properties, and hence the radiation budget, due to a change in aerosol concentration. Specific aerosol types act as CCN and form cloud droplets given a supersaturated moist air parcel. The ability of aerosols to act as CCN depends on their size, chemical composition and supersaturation. If the number of CCN is increased, e.g., by anthropogenic pollution,

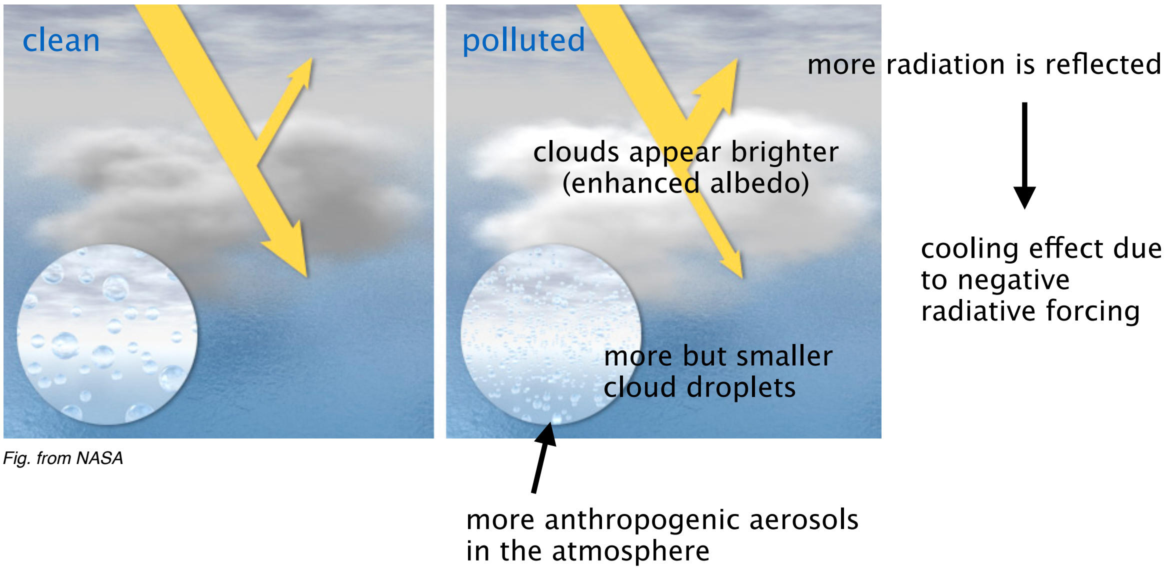

Figure 1.2: Illustration of the Twomey effect. Original illustration from NASA[2].

the number of cloud droplets is likely to increase. If all other parameters are kept constant (particularly the amount of liquid water), the average cloud droplet radius is smaller for increasing droplet number concentration. This increases the clouds volume scattering cross section and enhances the cloud albedo (Fig. 1.2). Another consequence is a possible change in cloud fraction (second indirect effect).

1.3 Quantification of ACI from Observations

To quantify the effect of aerosols on clouds from observations, McComiskey and Feingold (2012) gave an overview of suitable ACI metrics following the method outlined by Feingold et al. (2003). The metrics describe a relative change of cloud microphysical properties as a response to a relative change of the aerosol load. The reported values in previous studies vary beyond the full physical range between 0 and 1 for ACI_N (Fig. 1.3, taken from Schmidt et al. (2015); details on ACI metrics are described in Chapter 2). The major reason is the difference between observation scale and the scale of the actual interaction process (activation of aerosols) (McComiskey and Feingold, 2012). The highest values of these ACI metrics are found for in-situ observations (e.g., Ditas, 2014), where observation and process scales have the same order of magnitude.

Given the high costs and scarcity of in-situ measurements, ground-based remote sensing observations are de facto considered to be more suitable to explore ACI. To obtain cloud properties from ground-based instruments, a large number of retrieval methods have been developed in the past. First attempts were made to retrieve liquid water content from the radar reflectivity (e.g., Liao and Sassen, 1994). Additional liquid water path observations from a microwave radiometer were utilized to better constrain liquid water content (e.g., Frisch et al., 1995, 1998, 2002) or cloud droplet number concentration (Fox and Illingworth, 1997). Solar transmission was also used in this context (Dong et al., 1998;

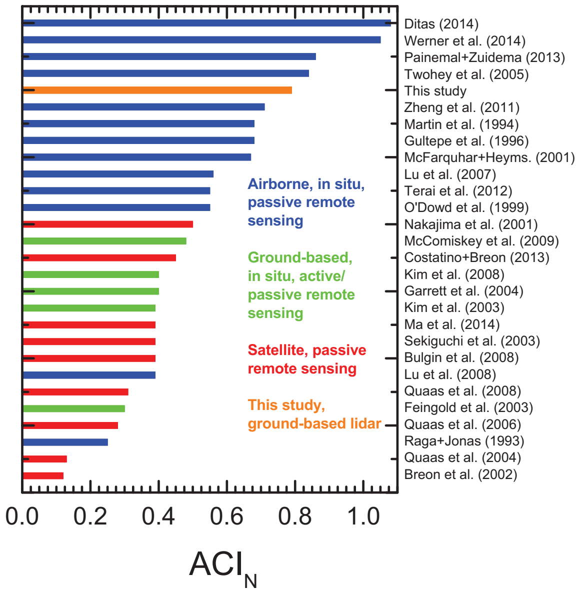

Figure 1.3: Values of the ACI_N metric (will be described in Sect. 2.3) as published in different literature studies. Colors represent different observation platforms (red: satellite, green: ground-based, blue: in-situ). The figure is taken from Schmidt et al. (2015).

Mace and Sassen, 2000; Dong and Mace, 2003). However, most of these methods require implicit assumptions about the width of the droplet size distribution (DSD). Kato et al. (2001) tried to reduce errors due to the unkown DSD employing the Doppler velocity from cloud radars. As those retrieval methods turn out to give quite diverse results (e.g., Turner et al., 2007), the importance of validation has risen over the last years. Independent observation sources are required for validation, e.g., from in-situ observations. In addition, the retrieval methods have been applied to synthetic observations (e.g., Löhnert et al., 2007), and closure studies with shortwave/longwave radiation have been conducted (e.g., McFarlane et al., 2008; Ebell et al., 2011).

While remote sensing from ground provides measurements at specific locations, passive satellite observations from, e.g., MODIS (Moderate Resolution Imaging Spectrometer) cover a large fraction of the globe. Hence, they are the first choice to quantify ACI on a larger scale. Active satellite sensors on the other hand, such as the cloud profiling radar onboard CloudSat (Stephens et al., 2002) or the Cloud-Aerosol Lidar with Orthogonal Polarization (CALIOP) on-board CALIPSO (Cloud-Aerosol Lidar and Infrared Pathfinder Satellite Observation, Winker et al., 2009), are able to provide vertically resolved cloud observations along their tracks and can also be used to investigate aerosol effects on cloud properties (e.g., Christensen and Stephens, 2011). As a drawback, these lack highly-resolved temporal coverage and have a smaller scanning swath than passive sensors onboard polar-orbiting satellites. Christensen et al. (2013) pointed towards the limited capabilities of space-borne radars. Due to their high minimum detectable signal it is difficult to detect low-level liquid clouds reliably. Despite their slightly coarser spatial resolution, geostationary satellite observations, e.g., from Meteosat SEVIRI (Spinning Enhanced Visible and Infrared Imager), benefit from the high temporal coverage of up to

5 min in conjunction with a large spatial coverage. This can be considered as an advantage for the determination of large-scale ACI at a diurnal cycle. In addition, it improves the opportunity for a validation with ground-based observations (e.g., Roebeling et al., 2008b). To our knowledge, the potential of SEVIRI has not yet been fully utilized for quantifying ACI. To obtain key microphysical quantities for ACI from passive satellite observations, usually the adiabatic cloud model is applied (e.g., Schueller et al., 2003; Boers et al., 2006; Bennartz, 2007), but also vertically homogeneous clouds are considered (e.g. Han et al., 1994).

Quantification of ACI from observational studies is complex. Different cloud phases have to be detected and seperated. Concentrating on liquid clouds reduces the complexity only to some extent. Complex feedbacks occur regarding precipitation and cloud lifetime. As the thermodynamic conditions of a cloud cannot be kept constant while only aerosol conditions are changed, usually a larger observation sample of different clouds is considered to quantify ACI from both satellite and ground-based remote sensing studies. This complicates the quantification of ACI for liquid clouds as undesired covariances with e.g., meteorology affect the estimated ACI metrics (Shao and Liu, 2005, 2006). Not only the number of CCN determines the cloud microphysical quantities, but also, e.g., entrainment rates (Kim et al., 2008). Therefore, it is important to have a better understanding and quantification of entrainment effects on cloud microphysics. For all comparisons it is important to keep in mind the different sources of uncertainty for the different observation and retrieval methods.

1.4 Objectives of the Thesis

As outlined, the quantification of ACI from observations for liquid clouds is complicated due to different sources of uncertainties. Several interconnected problems of quantifying ACI are addressed in current studies and need to be investigated in more detail. In this work, we connect the uncertainties regarding the different observation scales relevant for ACI studies.

Cloud microphysical quantities are partly determined by aerosol activation at cloud base given the number of CCN. In addition, entrainment influences cloud microphysics and needs to be considered in the retrievals. Therefore, it is important to better understand the effect of entrainment on the cloud vertical structure and to give an estimate of cloud adiabaticity (Min and Duan, 2005). To better attribute the influence of mixing on ACI we will obtain typical values of cloud adiabaticity for liquid clouds utilizing ground-based remote sensing, explore regional differences, and check for possibilities for its parameterization, relevant for studies on a larger scale.

The cloud droplet number concentration N_d is a key property for the investigation of ACI, and is not easily retrieved from current ground-based retrieval methods (e.g., Brandau et al., 2010; Merk et al., 2016). Hence, we will investigate sensitivities and possibilities applying an Optimal Estimation approach which includes additional constraints from cloud optical depth observations. It is investigated whether such an approach is able to reduce the uncertainty of the retrieved N_d.

Considering the scale dependence of the ACI metrics, the consistency of derived microphysical key properties from passive satellites and ground-based observations will be analyzed. In this work, a new proxy for CCN from the Monitoring Atmospheric Composition and Climate (MACC)-II reanalysis following (Block and Quaas, 2016) is utilized together with SEVIRI observations to quantify ACI for a maritime and continental area in Europe.

Within the scope of this thesis, we formulate the following main research questions:

1. Is the adiabatic cloud model suitable to describe liquid clouds and applicable for ACI investigations?
2. How accurately can N_d be retrieved from ground-based remote sensing?
3. How consistent are cloud key properties relevant for ACIs from observations at different scales?
4. How well can ACIs be quantified for the European region?

This leads to the following structure of this thesis: the theoretical background is given in Chapter 2, including the retrieval theory to obtain cloud microphysical properties. Therein, the applied instruments and datasets covering different scales are described. Afterwards cloud adiabaticity from available observations of the ground-based Cloudnet network is characterized as a proxy for mixing processes (Chapter 3). In Chapter 4 a new Optimal Estimation approach to obtain N_d is motivated from the discussion of sensitivities applying a radar-radiometer approach. Afterwards, microphysical quantities obtained from ground-based sites and from passive satellites are compared to each other (Chapter 5). In Chapter 6, a ground-based case study is conducted to derive ACI metrics and compare microphysical properties to available in-situ data. In Chapter 7, ACI metrics are derived from longer-term passive satellite observations. Finally, conclusions are presented, and an outlook is given (Chapter 8).

2 Theoretical Background

In this chapter, the fundamentals for the thesis are given. We will outline how clouds are characterized microphysically. This serves as a basis to introduce the adiabatic cloud model, which describes the vertical structure of cloud microphysical properties. Afterwards, the interactions of radiation in the atmosphere, especially with clouds, will be presented. This gives the foundation for applying observations with remote sensing instruments. In this work, mainly data from Meteosat SEVIRI and the Cloudnet ground-based network are utilized. Information about aerosols on a larger scale is taken from the MACC-II reanalysis. Instruments, applied retrieval methods and resulting datasets will be delineated in detail. Furthermore, the essentials of ACI are introduced.

2.1 Cloud Microphysics

Liquid clouds consist of liquid and/or frozen water. In this work, only warm clouds are considered, i.e. the ice phase will be neglected. They are initially formed due to condensation of water vapor on CCN particles (activation) in a rising air parcel if conditions of supersaturation are reached (at cloud base) (Pruppacher and Klett, 2010). This is confirmed from in-situ studies. For example, Boers et al. (2006) found a strong correlation between CCN and N_d over the Southern Ocean. The number of activated CCN depends also on updraft velocity and supersaturation (Janssen et al., 2011; McFiggans et al., 2006; Reutter et al., 2009; Schmidt et al., 2015). Droplets are usually lifted within the cloud and grow further due to condensation and collision-coalescence processes. This leads to an ensemble of cloud droplets of different size, which is described by a droplet size distribution (DSD). The bulk microphysical properties are usually expressed by means of different moments of the DSD. Petty and Huang (2011) give similar expressions, e.g., based on cloud droplet mass, which are used in numerical weather prediction (NWP) models (e.g., Seifert and Beheng, 2005). The theory of size distributions and its moments is outlined in the following section.

2.1.1 Moments of the Droplet Size Distribution

The ensemble of cloud droplets of different size is often approximated by either a log-normal or Gamma distribution. This is justified by in-situ observations of droplet size ensembles (e.g., Miles et al., 2000). The definitions of the log-normal and Gamma distribution functions are given in the Appendix. The following theory considers ensembles of droplets in liquid clouds which follow a unimodal size distribution, i.e., do not contain an additional drizzle or rain mode.

Moment	physical parameter	log-normal DSD	Gamma DSD
0	N_d	N_d	N_d
1	r_M	$r_0 \exp(0.5\sigma_x)$	$(1-2\nu)\, r_e$
2	r_a	$\sqrt{r_0^2 \exp(2\sigma_x^2)}$	$\sqrt{(1-\nu)\,(1-2\nu)\, r_e^6}$
3	r_v	$\sqrt[3]{r_0^3 \exp(4.5\sigma_x^2)}$	$\sqrt[3]{(1-\nu)\,(1-2\nu)\, r_e^3}$
	q_L	$\frac{4\,\pi\,\rho_w}{3}\, r_0^3 \exp(4.5\sigma_x^2)$	$\frac{4\,\pi\,\rho_w\,N_d}{3}\,(1-\nu)(1-2\nu)\, r_e^3$
6	Z	$2^6 N_d r_0^6 \exp(18\sigma^2)$	$2^6 N_d\,(\nu-1)\,(\nu+1)\,(2\nu-1)\,(2\nu+1)\,(3\nu+1)\, r_e^6$
-	k_2	$\frac{\exp\left(4.5\sigma^2\right)}{\exp(7.5\sigma^2)}$	$(1-\nu)\,(1-2\nu)$
-	k_6	$\frac{\exp\left(18\sigma^2\right)}{\exp(9\sigma^2)}$	$\frac{(\nu+1)(2\nu+1)(3\nu+1)}{(\nu-1)(2\nu-1)}$

Table 2.1: Moments of the Gamma and log-normal size distribution and associated physical parameters. ν is the effective variance of the Gamma DSD, and σ_x the width of the log-normal DSD.

The n-th moment $M_{f,n}$ of a parameter described by a distribution function $f(r)$ is defined as (Petty and Huang, 2011):

$$M_{f,n} := \int x^k f(r) dr. \tag{2.1}$$

Linking individual moments to each other gives the possibility for retrieving cloud properties from the observation of only a few microphysical quantities. The theory is only valid for unimodal DSDs. In the next section, the physical interpretation of the different moments of a DSD is given.

2.1.2 Physical Interpretation of the Moments of the DSD

The relevant moments of the DSD used in this work are listed in Table 2.1. In the following, we will give a brief overview of their physical interpretation. A detailed derivation of these parameters from the DSD is presented in the Appendix.

The cloud droplet number concentration N_d is determined by the zeroth moment of the DSD. It represents the number of liquid droplets in an air volume. The first moment of the DSD constitutes the mean radius of the distribution (r_M). The area-equivalent radius r_a is obtained from the second moment. It is relevant for applications in remote sensing due to its direct link to the scattering cross section. Therefore, it determines the extinction coefficient. Relevant radiative properties will be described more detailed in Sect. 2.4. The third moment defines the volume radius r_v. It is related to the liquid water content $q_L \propto N_d\, r_v^3$, which describes the mass of condensed water within an air volume. In remote sensing, the effective radius r_e is widely applied and is defined as the third over the second moment of the DSD. In case of Rayleigh scattering (e.g., liquid cloud droplets observed with cloud radars), the radar reflectivity is given by the sixth moment of the

DSD. In addition, factors k_2 and k_6 are introduced to describe the link between individual moments. Both are only a function of the width of the DSD.

2.2 Adiabatic Cloud Model

The adiabatic cloud model is used to describe the vertical structure of cloud microphysical properties. Given adiabatic conditions, cloud droplets initially formed at cloud base and further vertically lifted, will grow due to condensation. For such a moist rising air parcel, the liquid water content $q_\mathrm{L}(z)$ increases linearly with height (Albrecht et al., 1990):

$$q_L(z) = f_\mathrm{ad}(z)\,\Gamma_\mathrm{ad}(T(z), p(z))\,z, \tag{2.2}$$

where Γ_ad is the adiabatic rate of increase of liquid water content. Details of its derivation from the Clausius-Clapeyron equation are given in the Appendix.

f_ad describes the degree of adiabaticity and is called subadiabatic factor. It can be interpreted as a deviation of the actual q_L profile from the theoretical adiabatic q_L profile due to evaporation triggered by the entrainment of drier air masses. This leads to $f_\mathrm{ad} < 1$ (subadiabatic). For f_ad a range of $[0.3, 0.9]$ is commonly observed (Boers et al., 2006).

Integration of Eq. 2.2 over the geometrical cloud depth yields the liquid water path Q_L, representing the liquid water in the whole vertical cloud column (from cloud-base height z_b to cloud-top height z_t):

$$Q_L = \int_{z_b}^{z_t} f_\mathrm{ad}(z)\,\Gamma_\mathrm{ad}(z) z\,\mathrm{d}z. \tag{2.3}$$

In the following, f_ad is assumed to be independent of height. Therefore, it represents an average cloud adiabaticity obtained over the whole cloud geometrical depth H. Similarly, Γ_ad is assumed constant and is calculated from the temperature T and pressure p at the cloud base or top. This results in:

$$f_\mathrm{ad} = \frac{2\,Q_L}{H^2\,\Gamma_\mathrm{ad}}. \tag{2.4}$$

To illustrate the uncertainties that influence the calculation of f_ad, an adiabatic cloud ($f_\mathrm{ad} = 1$) is considered, and a value of $Q_L = 100\,\mathrm{g\,m^{-2}}$ is assumed for a liquid, non-drizzling cloud. Then, for an adiabatic cloud, $H = 324\,\mathrm{m}$ is obtained given $\Gamma_\mathrm{ad} = 1.9 \cdot 10^{-3}\,\mathrm{g\,m^{-4}}$ (calculated from Quaas et al. (2006)). The Q_L retrieval uncertainty (microwave radiometer instrument error and retrieval error) is approximately $25\,\mathrm{gm^{-2}}$ and the vertical resolution of the ceilometer and the cloud radar is 30 m which results in at least 60 m uncertainty of H. Accounting for the maximum possible uncertainty, (Q_L, H) = ($125\,\mathrm{g\,m^{-2}}$, 264 m) or (Q_L, H) = ($75\,\mathrm{g\,m^{-2}}$, 384 m), the resulting f_ad would be 1.89 or 0.54, respectively. This shows that with the current uncertainty limits of the ground-based observations, f_ad is still prone to large uncertainties (especially for geometrically thin clouds).

In Fig. 2.1, the error propagation is expressed considering Gaussian error propagation (see Appendix).

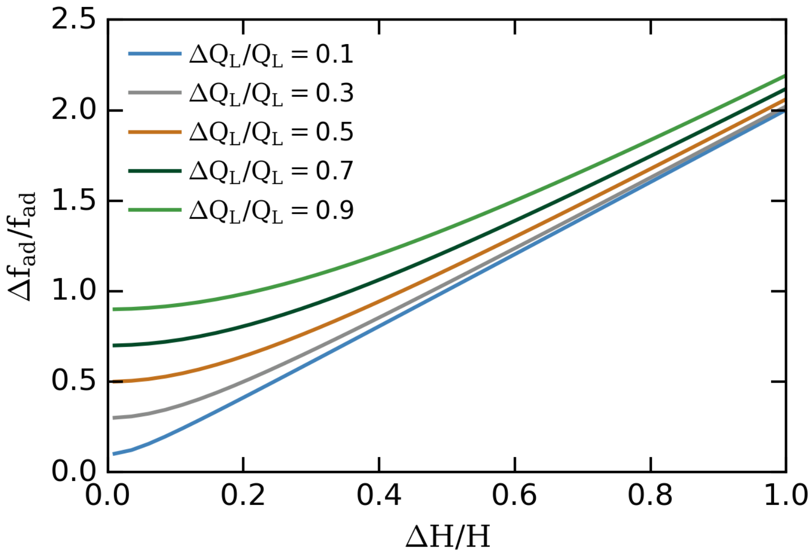

Figure 2.1: Relative error of the subadiabatic factor f_{ad} as a function of the relative error of H. The colors represent different relative errors of Q_L.

The relative uncertainty of f_{ad} shows the strongest dependence on relative uncertainties in Q_L in case of low relative errors of H. With larger relative uncertainties in H, the effect of Q_L uncertainties becomes less important. Relative uncertainties in f_{ad} of 100% and 200% can be reached for about 50% and 100% uncertainty in H, respectively. This emphasizes once more the problem with very thin clouds (low H), which have largest relative uncertainties due to the vertical resolution.

One can calculate the cloud geometrical depth H for an observed liquid water path Q_L and subadiabatic factor f_{ad}, rearranging Eq. 2.4:

$$H(Q_L, f_{\mathrm{ad}}) = \sqrt{\frac{2\,Q_L}{f_{\mathrm{ad}}\,\Gamma_{\mathrm{ad}}}}. \tag{2.5}$$

Since q_L increases linearly with height, the available liquid water will be distributed over all cloud droplets. In other words, the volume-equivalent mean droplet radius r_v is a function of N_d and q_L (Eq. 8.13).

In case of entrainment of dry air masses from the cloud sides or cloud top, cloud droplets will evaporate. Usually two extremes of the mixing process are considered: homogeneous and inhomogeneous mixing. According to Tölle and Krueger (2014), these terms are not uniquely defined in literature. Generally, the mixing time scale defines the mixing process (e.g., Baker et al., 1980; Tölle and Krueger, 2014). When the mixing time scale is way larger than the time scale of evaporation, some droplets are able to completely evaporate in regions of dry air, while others are not affected by the mixing. This is referred to as inhomogeneous mixing. When, on the other hand, the mixing time scale is slow, then all the droplets would be exposed to the same sub-saturated conditions and partially evaporate. As a consequence their radius is reduced, but the total number of droplets is unchanged. This is referred to as homogeneous mixing. The realistic representation of mixing is difficult to assess even on a small scale with airborne instruments (Tölle and Krueger, 2014). Therefore, little is known about a realistic mixing effect on the DSD and N_d.

In the following, homogeneous mixing is assumed, i.e., entrainment leads to a change in the droplet radius only, while the cloud droplet number concentration N_d stays constant with height:

$$\begin{aligned} r_a^2 &= k_2^{\frac{1}{3}} \left(f_{\mathrm{ad}} \, r_{v,\mathrm{ad}}^3 \right)^{\frac{2}{3}}, && (2.6) \\ N_d &= N_{d,\mathrm{ad}}. && (2.7) \end{aligned}$$

At this point, the optical depth (τ) is calculated in case of homogeneous mixing as the vertical integral over the extinction coefficient:

$$\begin{aligned} \tau &= \int_{z_b}^{z_t} 2\,\pi\, N_d\, k_2^{\frac{1}{3}} \left(f_{\mathrm{ad}} \, r_{v,\mathrm{ad}}^3 \right)^{\frac{2}{3}} dz \\ &= \int_{z_b}^{z_t} 2\,\pi\, N_d\, k_2^{\frac{1}{3}} \left(\frac{3 f_{\mathrm{ad}} \, q_{L,\mathrm{ad}}}{4\,\pi\,\rho_w\, N_d} \right)^{\frac{2}{3}} dz. \qquad (2.8) \end{aligned}$$

Inserting the adiabatic q_L profile from Eq. 2.2, and integrating with respect to height, one can express τ in terms of Q_L. This form of the equation is motivated since Q_L is considered constant for ACI investigations:

$$\tau(Q_L, f_{\mathrm{ad}}, N_d) = \frac{9}{5} \left(4\,\pi\, k_2\, N_d\right)^{\frac{1}{3}} \left(18\,\rho_w^4\, f_{\mathrm{ad}}\, \Gamma_{\mathrm{ad}}\right)^{-\frac{1}{6}} Q_L^{\frac{5}{6}}. \qquad (2.9)$$

In a similar way, one can calculate the effective radius, assuming again homogeneous mixing:

$$\begin{aligned} r_e &= k_2^{-\frac{1}{3}} M_3^{\frac{1}{3}} \\ &= \left(\frac{3\, f_{\mathrm{ad}}\, q_{L,\mathrm{ad}}}{4\, k_2\, \pi\, \rho_w\, N_d} \right)^{\frac{1}{3}}. \qquad (2.10) \end{aligned}$$

The effective radius at the cloud top $r_e(z = z_t)$ is then given as:

$$r_e(Q_L, f_{\mathrm{ad}}, N_d) = \left(18\, f_{\mathrm{ad}}\, \Gamma_{\mathrm{ad}}\, Q_L\right)^{\frac{1}{6}} \left(4\,\pi\,\rho_w\, k_2\, N_d\right)^{-\frac{1}{3}}. \qquad (2.11)$$

The relative errors can be estimated with Gaussian error propagation by assuming normally distributed errors that are uncorrelated. Equations are given in the Appendix.

τ and r_e retrieved from passive remote sensing satellites can be used to calculate Q_L, N_d and H by employing the adiabatic cloud model (Wood, 2006):

$$Q_L(\tau, r_e) = \frac{5}{9}\, \rho_w\, \tau\, r_e, \qquad (2.12)$$

study	location	instrument(s)	derived quantities	Γ_{ad} [$\cdot 10^{-3} gm^{-4}$]	f_{ad}	k_2
Szczodrak et al. (2001)	East Pacific Southern Ocean	AVHRR	N_{d}	2.0	n.a.	n.a.
Schüller et al. (2005)	North Atlantic	MODIS	N_{d}, H	n.a.	n.a.	n.a.
Boers et al. (2006)	Southern Ocean	MODIS	N_{d}, H	const.	0.6	0.87
Quaas et al. (2006, 2008)	global	MODIS	N_{d}	1.9	1.0	0.8
Bennartz (2007)	global	MODIS	N_{d}, H	T-dependent	0.8	0.8
Roebeling et al. (2008b)	Europe	SEVIRI	N_{d}, H	Boers et al. (2006)	0.75	0.87
George and Wood (2010)	Southeast Pacific	MODIS	N_{d}	1.95	n.a.	n.a.
Painemal and Zuidema (2010)	Southeast Pacific	MODIS	N_{d}, H	2.0	1.0	0.8
Janssen et al. (2011)	Finnland	MODIS	N_{d}, H	1.44	0.6	0.87
Painemal and Zuidema (2011)	Southeast Pacific	MODIS	N_{d}	2.0	1.0	0.8
Min et al. (2012)	Southeast Pacific	MODIS	N_{d}, H	T-dependent	calc.	0.5-1.0
Ahmad et al. (2013)	Puijo	MODIS	N_{d}	n.a.	1.0	0.67
Painemal and Zuidema (2013)	Southeast Pacific	MODIS, aircraft	N_{d}	$T_{\text{cbh}}, p_{\text{cbh}}$	0.9	0.88
Zeng et al. (2014)	global	A-Train	N_{d}, H	$T_{\text{cth}}, p_{\text{cth}}$	1.0	0.6438
Merk et al. (2016)	Germany	SEVIRI	N_{d}, H	T_{cbh}, p_{cbh}	calc.	0.72

Table 2.2: Overview of assumptions made in the adiabatic cloud model to derive N_d and H in literature studies. The table lists the values chosen for Γ_{ad}, f_{ad} (calc. refers to explicitely calculated values from additional data) and k_2 as defined in Table 2.1. The table is sorted by publication year starting with the oldest one.

$$N_d(\tau, r_e) = (4\pi k_2)^{-1}(10 f_{\text{ad}}\Gamma_{\text{ad}}\tau)^{\frac{1}{2}}(\rho_w r_e^5)^{-\frac{1}{2}}. \tag{2.13}$$

$$H(\tau, r_e) = \left(\frac{10\,\rho_w\,\tau\,r_e}{9\,f_{\text{ad}}\,\Gamma_{\text{ad}}}\right)^{\frac{1}{2}}. \tag{2.14}$$

The errors of Q_L and N_d are again estimated from Gaussian error propagation (see Appendix).

In previous studies very different assumptions regarding the parameters of the adiabatic cloud model for retrievals from passive satellite observations have been made (Table 2.2). Often a constant value for Γ_{ad} is considered, while it is actually mainly a function of temperature. Similarly, the subadiabatic factor and the width of the DSD are often kept at constant values for the full sample of clouds. Differences for the assumed width parameter are mainly motivated from the different cloud regimes considered in the studies (maritime vs. continental).

2.3 Aerosol-Cloud Interaction Metrics

As introduced in Chapter 1 aerosols impact cloud properties. In the past, many studies linked aerosol and cloud microphysical properties from different scales and methods. Typically, this relationship is described by ACI metrics, introduced by Feingold et al. (2001) (therein referred to as Indirect Effect, IE). The ACI metrics link the natural logarithms of cloud microphysical properties and an aerosol proxy.

Using τ, r_e and N_d as cloud microphysical properties and an aerosol proxy α the ACI metrics are defined as (McComiskey et al., 2009):

$$ACI_\tau = \left.\frac{d\ln\tau}{d\ln\alpha}\right|_{Q_L},\ 0 < ACI_\tau < 0.33, \tag{2.15}$$

$$ACI_r = -\left.\frac{d\ln r_e}{d\ln\alpha}\right|_{Q_L},\ 0 < ACI_r < 0.33, \tag{2.16}$$

$$ACI_N = \frac{d\ln N_d}{d\ln\alpha},\ 0 < ACI_N < 1. \tag{2.17}$$

They are connected to each other via:

$$ACI_\tau = -ACI_r = \frac{1}{3}ACI_N. \tag{2.18}$$

McComiskey and Feingold (2012) and Schmidt et al. (2014) gave an overview of ACI metric values. A dependence of the ACI metric values on the relation of observation scale to the process scale (i.e. activation of CCN) is found. Values for ACI_N range in the order of 0.1 for global satellite studies (Bréon et al., 2002) to the maximum theoretically value of 1 in combined in-situ and model experiments (Ditas, 2014). A value of 0 would mean that the increased aerosol load does not influence N_d, while a value of 1 would mean that the increased aerosol load is fully activated to cloud droplets. Considering r_e as the microphysical proxy, a negative slope with an aerosol proxy has often been found in previous studies (e.g., Wetzel and Stowe, 1999; Schwartz et al., 2002; Nakajima et al., 2001; Bréon et al., 2002; Quaas et al., 2004). For example, Quaas et al. (2004) reported that this slope may change also with the magnitude of the aerosol proxy. In recent studies, several different proxies are used increasing the deviations of the reported absolute values for the ACI metrics.

2.4 Radiative Transfer in the Cloudy Atmosphere

The propagation of electromagnetic radiation in the atmosphere, and its interaction with the atmospheric components is described by the radiative transfer equation (Mayer, B., 2009). Its plane-parallel, horizontally-homogeneous, one-dimensional approximation is given as:

$$\mu\frac{\mathrm{d}L}{\mathrm{d}\tau} = -L + \frac{\omega_0}{4\pi}\int_{4\pi} P(\Omega,\Omega')L(\Omega')d\Omega' + (1-\omega_0)\,B(T). \tag{2.19}$$

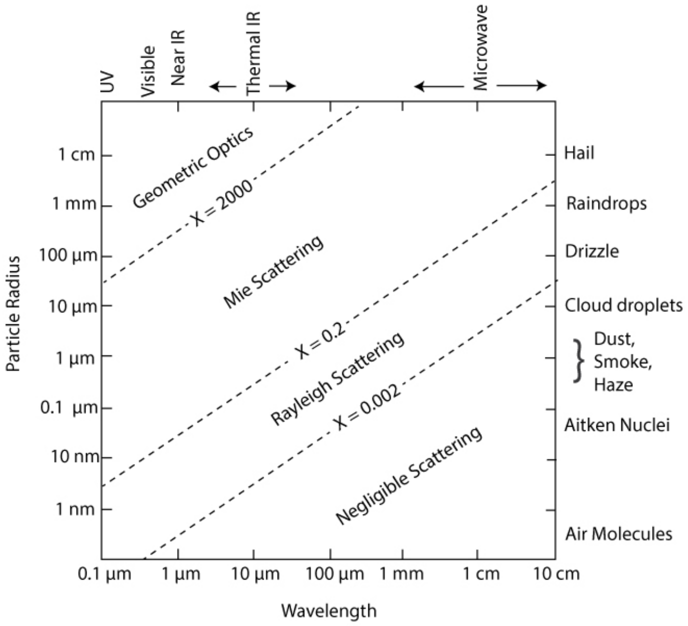

Figure 2.2: Scattering regimes as defined by the wavelength and particle radius. Taken from: W. Brune (after Grant Petty)[1].

It describes the change of the radiance L in an atmosphere of optical depth τ. Radiance is defined as the energy flux per time-unit trough a perpendicular surface projection area.

τ is defined as:

$$\tau = \int \alpha_{ext}(z)\, dz, \tag{2.20}$$

with the extinction coefficient α_{ext}. The extinction coefficient can be described, given an ensemble of particles with a size distribution $n(r)$ for particle radii r (Hansen and Travis, 1974):

$$\alpha_{ext} = \int Q_{ext}\, n(r)\, \pi\, r^2\, dr, \tag{2.21}$$

where Q_{ext} is the extinction efficiency. The extinction coefficient describes how effective the radiation is absorbed and scattered by the particle, and is the sum of the absorption and scattering coefficient.

$P(\Omega', \Omega)$ in Eq. 2.19 is the scattering phase function with the incident and scattering directions Ω', Ω, respectively. The single scattering albedo ω_0 describes the fraction of attenuated incident radiation due to scattering over extinction. μ is defined as the cosine of the angle of the incident radiation.

Depending on the relation of wavelength to particle size, which is usually described with the size parameter $x = 2\,\pi\, r/\lambda$ (r being the particle radius and λ the wavelength, Bohren and Clothiaux (2006)), the scattering regime is defined (Fig. 2.2).

For particles smaller than the wavelength ($x << \lambda$), the Rayleigh approximation can be used. If $r \approx \lambda$ the Mie theory has to be applied. For water clouds, and typical DSD, the single scattering properties are determined by the effective radius (Hansen and Travis, 1974; Mayer et al., 2004), which is the third over second moment of the DSD:

$$r_e = \frac{\int n(r) r^3 dr}{\int n(r) r^2 dr}. \tag{2.22}$$

For particles larger than the wavelength, the scattering processes are usually described via geometrical optics. In this thesis, only the Rayleigh regime and Mie regime are relevant. For example, cloud droplets in the visible range are characterized by Mie scattering, cloud droplets observed with usual cloud radars satisfy the Rayleigh approximation.

$B(T)$ in Eq. 2.19 is the Planck function for a given temperature T. It describes how much radiation is emitted by a blackbody with temperature T, whereby a blackbody is an idealized body which absorbs all incident radiation. For remote sensing applications in the infrared spectrum, it is often assumed that atmospheric components behave like blackbodies, and scattering can be neglected. For blackbodies the absorptivity is equal to one. A body with absorptivity smaller than one is called gray body.

Remote sensing instruments can use active or passive radiation sources that interact with the constituents of the atmosphere by scattering and/or absorption. Depending on the scientific focus of each instrument, a specific spectrum of wavelengths is applied (e.g., visible and infrared wavelengths for SEVIRI, wavelengths in the microwave spectrum for microwave radiometer and radar) in order to obtain information of the atmospheric properties using inversion mechanisms (Rodgers, 2000). The instruments used for remote sensing will be described in Sect. 2.5.

2.5 Instruments and Datasets

The combination of cloud microphysical properties obtained from either ground- or satellite-based remote sensing together with information on aerosol load give the chance to explore ACI. In this section, the relevant instruments for this work, retrieval methods and resulting datasets are described. From the satellite perspective mainly the Meteosat SEVIRI instrument is used. At times also data from MODIS is considered. Ground-based observations are taken from sites of the Cloudnet network. Additional information on aerosol distributions over a larger domain are taken from the MACC-II reanalysis product.

2.5.1 Passive Satellite Sensors

Meteosat SEVIRI Instrument

SEVIRI is a passive imager on a geostationary orbit (Schmetz et al., 2002) on-board Meteosat Second Generation (MSG). It provides 12 spectral channels covering the visible, the near infrared, and the infrared spectrum (see Table 2.3). The channels used in the framework of this work have a nadir resolution of 3 km x 3 km. The spatial resolution

nr	channel	λ_{min} (μm)	λ_{cen} (μm)	λ_{max} (μm)	application
01	VIS0.6	0.56	0.635	0.71	window
02	VIS0.8	0.74	0.81	0.88	window
03	NIR1.6	1.50	1.64	1.78	window
04	IR3.9	3.48	3.90	4.36	window
05	WV6.2	5.35	6.25	7.15	water vapour
06	WV7.3	6.85	7.35	7.85	water vapour
07	IR8.7	8.30	8.70	9.10	water vapour
08	IR9.7	9.38	9.66	9.94	ozone
09	IR10.8	9.80	10.80	11.80	window
10	IR12.0	11.00	12.00	13.00	window
11	IR13.4	12.40	13.40	14.40	CO_2
12	HRV	broadband (about 0.4–1.1)			window / water vapour

Table 2.3: Spectral characteristic of observation channels from the SEVIRI instrument, given the minimum (λ_{min}), central (λ_{cen}) and maximum (λ_{max}) wavelength.

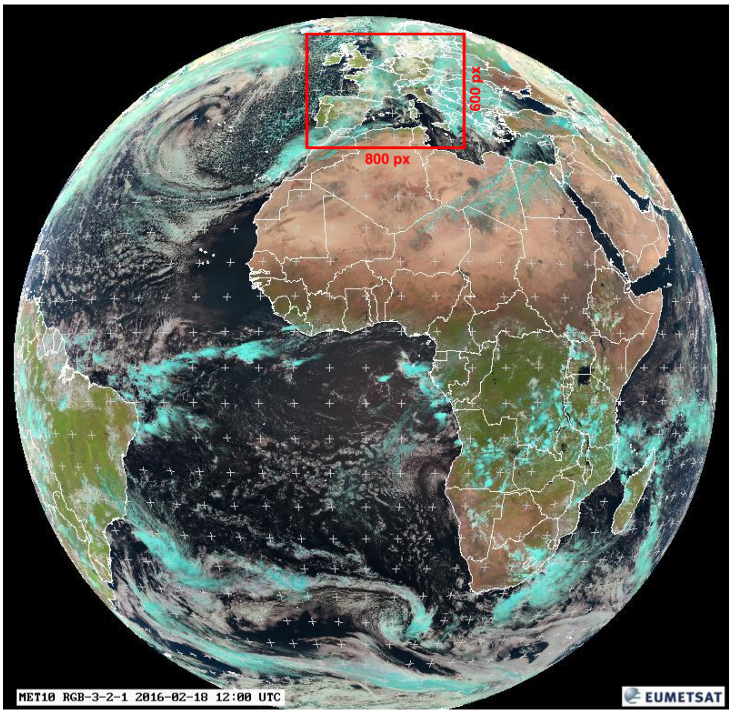

Figure 2.3: SEVIRI full disk RGB natural color image and Central European region (red rectangle).

decreases towards the poles and is about 4 km x 6 km over our region of interest (Europe). SEVIRI also provides a high-resolution visible (HRV) channel of 1 km x 1 km nadir resolution (1.5 km x 1.5 km over Europe). For Europe, a temporal resolution of 5 min is available from the Rapid Scan Service (RSS). The whole Earth disk is sampled every 15 min. In this study, the RSS data for a European cutout is used (see Fig. 2.3), which is processed in the satellite remote sensing group at the Leibniz Institute for Tropospheric Research (TROPOS).

Retrieval theory

Passive satellite sensors detect radiation from natural sources. For observations in the visible channels, the backscattered solar radiance is typically converted to reflectance. Reflectance is defined as the amount of backscattered solar radiation to the amount of incoming solar radiation. The Bidirectional Reflectance Factor for SEVIRI channels is defined as (EUMETSAT, 2012):

$$r_{BDRF} = \frac{\pi\, L\, d_{SE}(t)^2}{F\, \cos{(\theta_s)}}, \tag{2.23}$$

where $d_{SE}(t)$ is the sun-earth (SE) distance as a function of time t, L is the measured radiance, F the incoming solar irradiance for a given channel, and θ_s the solar zenith angle.

τ and r_e can be retrieved using the reflectance observations of passive satellites at two different wavelengths $\Delta\lambda$ (in the following called channel). This method was introduced by Nakajima and King (1990). The reflection in the non-absorbing visible range is primarily a function of optical depth τ, while in the absorbing, near infrared, it also depends strongly on the effective particle size. Therefore, from the combined observations in these two channels, τ and r_e can be retrieved simultaneously (Fig. 2.4). For a number of viewing conditions (satellite zenith angle, relative azimuth angle and solar zenith angle), lookup-tables are created by applying radiative transfer calculations for idealized atmospheric conditions (usually vertically homogeneous clouds are assumed).

As can be seen from Fig. 2.4, for low values of τ and r_e the retrieval might give ambiguous results.

Passive satellites use the emitted radiation in the infrared spectrum to derive the equivalent blackbody temperature of clouds or the surface. This temperature is used to define the temperature that a blackbody emitting the same radiance would have. In the inversion process, from radiance to blackbody temperature, also the response function of a satellite channel must be taken into account (Tjemkes, 2005).

The blackbody temperature is derived from the radiance $L_{\Delta k}$ (mW m^{-2} sr^{-2} cm) for a given channel:

$$L_{\Delta k} = \frac{\int_{\Delta k} f_k B_k(T_B) d\nu}{\int_{\Delta k} f_k dk}, \tag{2.24}$$

with $B_k(T_B)$ being the Planck function, T_B the equivalent blackbody temperature (in K), k the wavenumber (in cm^{-1}), and f_k the spectral response function.

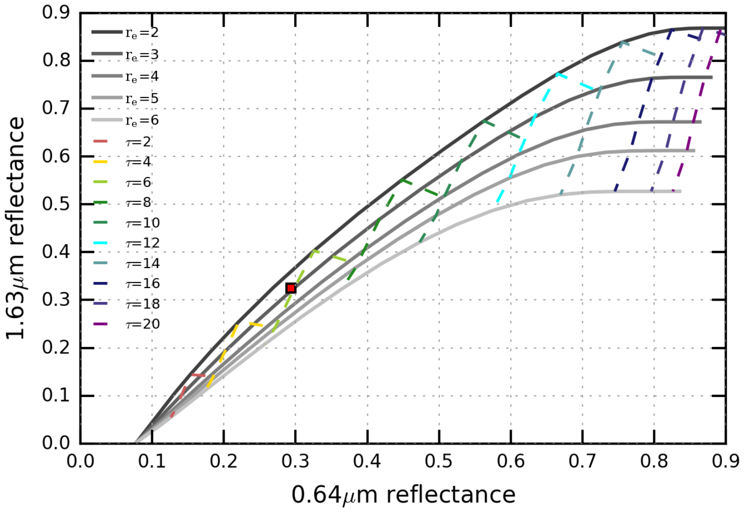

Figure 2.4: Illustration of the Nakajima and King (1990) retrieval approach. Lookup-table for optical depth τ and r_e from the KNMI CPP DAK radiative transfer simulations. The viewing geometry of SEVIRI for Leipzig at the end of October is taken (solar zenith angle 65°, satellite viewing zenith angle 58.8 °, relative azimuth angle 169 °). As an example, the observed reflectances from 27 October 2011 at 11:45 UTC are depicted by a red square. Resulting τ and r_e can be seen from the crossing of the τ and r_e isolines.

Clouds are behaving as gray bodies with an emissivity smaller than one. Emissivity is mainly a function of liquid water content within the cloud (e.g., Chylek and Ramaswamy, 1982). Consequently, the main emitted signal may not originate from the cloud top. Therefore, derived products have to be interpreted as radiatively relevant quantities. In addition, atmospheric trace gases and aerosols absorb and re-emit radiation, and the emission of clouds cannot be directly observed. This has to be corrected in the inversion process. For large viewing angles, the obtained information may also originate from cloud sides rather than cloud tops, leading to errors in retrievals (Zinner and Mayer, 2006). Furthermore, for lower spatial resolution there is increased likelihood that not the full pixel is filled with clouds.

NWC SAF Products

The Satellite Application Facility for Nowcasting and Very Short Range Forecasting (NWC SAF) provides a number of cloud products that are relevant for nowcasting applications. In this thesis, mainly the products related to cloud masking and cloud-top pressure (CTP), cloud-top temperature (CTT), and cloud-top height (CTH) are relevant. Given the observations of equivalent brightness temperatures in different SEVIRI channels, the CTH that is related to the equivalent blackbody temperature (in the following called: radiative CTH) can be retrieved using NWP temperature and humidity fields. In the dataset used for this work the European Centre for Medium-range Weather Forecast (ECMWF) model is applied. The NWP data is used as input for a radiative transfer model (here: RTTOV Saunders et al. (1999)) to simulate the observed radiances at SEVIRI channels (WV6.2, WV7.3, IR13.4, IR10.8, IR12.0), putting clouds successively on

band	λ_{min} (μm)	λ_{max} (μm)	ground resolution	purpose
01	0.620	0.670	250 m	τ land
02	0.841	0.876	250 m	τ ocean
05	1.230	1.250	500 m	τ snow/ice
06	1.628	1.625	500 m	r_e, thermodynamic phase
07	2.105	2.155	500 m	r_e
20	3.660	3.840	1000 m	r_e
31	10.780	11.280	1000 m	thermal correction

Table 2.4: Spectral characteristics, resolution and atmospheric purpose for MODIS channels used for the retrieval of cloud properties (King et al., 1997). Wavelengths (λ) are given in μm.

each pressure level, for cloud-free and overcast conditions (Derrien, 2012). The algorithm separates the processing of different cloud types.

For low, optically thick clouds the best fit between the simulated and observed T_B at IR10.8 is used. The algorithm threats thermal inversions. If these are present in NWP fields, only in case of lower brightness temperatures compared to those below the inversion, the CTH is set above the inversion layer. From the retrieved CTP, the CTH can be calculated using interpolation between the two nearest pressure levels in the vertical NWP profile.

Since for sub-pixel clouds the retrieved T_B depends on the effective cloudiness (emissivity and cloud-fraction within one pixel), the retrieved CTH under such conditions is highly uncertain.

KNMI-CPP Products

In this thesis, products of τ and r_e from the Koninklijk Nederlands Meteorologisch Instituut Cloud Physical Properties (KNMI-CPP) algorithm calculated at the satellite remote sensing group at TROPOS for SEVIRI are used. The lookup-table was built from 1D radiative transfer calculations with the Doubling Adding KNMI (DAK) radiative transfer model (Stammes, 2001), assuming plane-parallel clouds. The spatial resolution of the products is 3 km x 3 km. These are available at a 5 min temporal resolution for a Central European area cutout as presented in Fig. 2.3.

In case of $\tau < 8$, the effective radius for water clouds is weighted towards a mean climatological value of $r_e = 8\,\mu$m as its retrieval less unreliable (Roebeling et al., 2006). Retrievals are only applied for satellite pixels which are marked as cloudy from the NWC SAF cloud mask.

MODIS Collection 6 Products

In some parts of this work, data from the MODIS instrument is utilized. MODIS on-board the satellites Terra (descending node) and Aqua (ascending node) probes the Earth's atmosphere from a polar orbit. This results in one daytime overpass per satellite over the

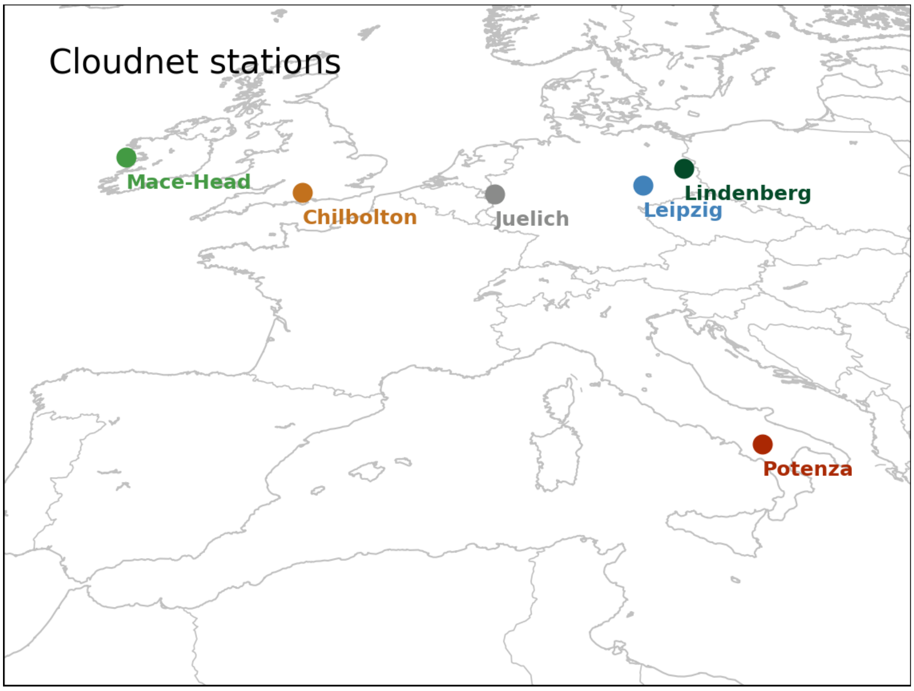

Figure 2.5: Locations and names of the ground-based observation sites in the Cloudnet project, whose data is investigated in this thesis.

region of interest. The equatorial crossing times are 10:30 UTC (Terra) and 13:30 UTC (Aqua). MODIS measures in 36 bands in the visible, near-infrared, and infrared spectrum, with some bands having a spatial resolution of up to 250 m (King et al., 1992). It has a 2300 km wide swath aiming to obtain land, ocean and atmospheric products (Platnick et al., 2003). The channels used for the retrieval of cloud products are listed in Table 2.4.

The details of MODIS retrieval algorithms are described in Platnick et al. (2003). It is based on the principles of the Nakajima and King (1990) retrieval method, which have been outlined before. The spatial resolution of MODIS cloud products is given at 1 km. In this work, data from Collection 6 is used. This is the latest processed dataset available with some refinements as described by Baum et al. (2012). While the cloud products of SEVIRI are based on one absorbing channel, MODIS calculates the products for three different absorbing channels. The closest of the MODIS channels to the SEVIRI NIR1.6 channel in terms of its central wavelength is band 6. The bands 7 and 20 are strongly affected by absorption and therefore the vertical sampling from cloud top is more shallow.

2.5.2 Cloudnet

Cloudnet Network Stations

Data from different Cloudnet (Illingworth et al., 2007) stations is used in this study. The location of these stations is depicted in Fig. 2.5. In the framework of the Cloudnet project (Illingworth et al., 2007) the following instruments are required:

site	lat	lon	cloud radar	ceilometer	microwave radiometer	model
Leipzig	12.37	51.33	MIRA-35	CHM15kx	HATPRO	COSMO-EU
Juelich	6.41	50.90	MIRA-35	Vaisala 905-nm CT25K	HATPRO-TOPHAT	COSMO-EU
Potenza	15.72	40.60	MIRA-35	Vaisala CT25K	MWP3000	COSMO-EU
Mace-Head	-9.90	50.33	MIRA-35	CHM070045	HATPRO	UK4 Unified Model
Chilbolton	-1.44	51.14	COPERNICUS-35	Vaisala 905-nm CT75K	Radiometrics MP1516A	Meteo-France ARPEGE
Lindenberg	14.12	52.21	MIRA-35	CHM100110	MWP3000	DWD LM

Table 2.5: Instrumental configuration used at different Cloudnet stations.

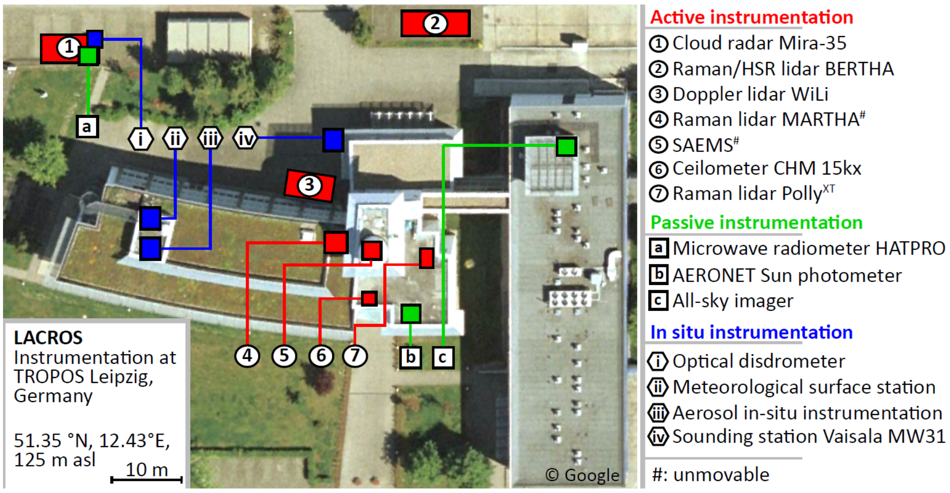

Figure 2.6: Configuration of LACROS at TROPOS in Leipzig. Current setup of active (red), passive (green) remote sensing, and supplementing instruments (blue). Part of the setup is deployable for field campaigns. From Bühl et al. (2013).

- cloud Doppler radar,
- ceilometer,
- microwave and infrared radiometer,
- rain gauge.

An overview of the available instruments at these sites is given in Table 2.5. Although the same processing chain of the Cloudnet algorithm is applied, the diversity in instruments and model data may result in differences between the stations Cloudnet products.

In Fig. 2.6 the Leipzig Aerosol and Cloud Remote Observations System (LACROS) station is depicted in more detail as a surrogate.

In the next sections, the measurement principles of the cloud radar, the ceilometer and the microwave radiometer (shown in Fig. 2.7) will be described.

Cloud Radar The millimeter wavelength Doppler cloud radar is an excellent instrument to detect non-precipitating stratiform clouds. It is suited to obtain the Doppler spectra of

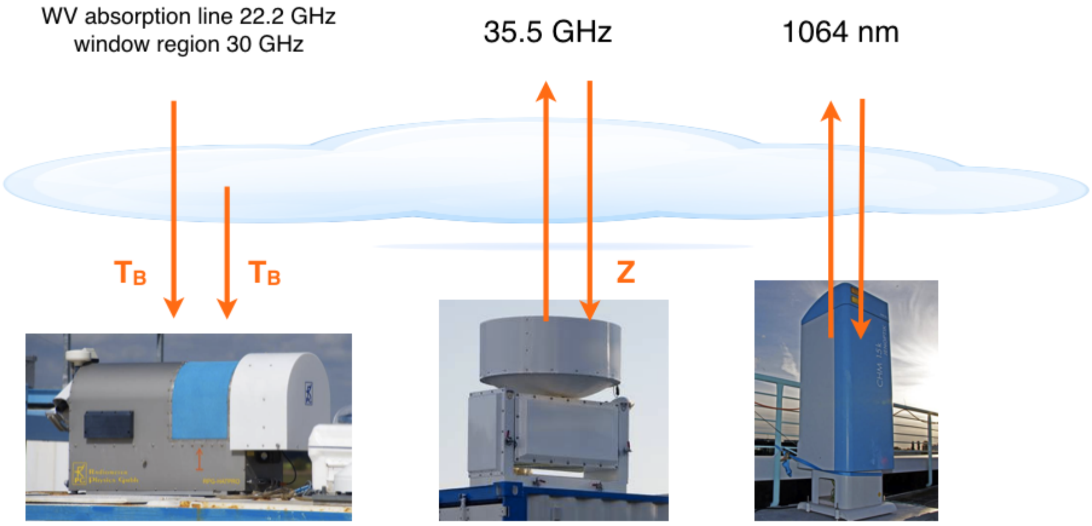

Figure 2.7: Illustration of the main instruments and their wavelength range used for Cloudnet. From left to right: microwave radiometer, cloud radar, and ceilometer.

water droplets or ice crystals (Kollias et al., 2007, 2011; Görsdorf et al., 2015). The radar reflectivity Z in dBZ (decibels of Z) describes the amount of backscattered power to the radar as the zeroth moment of the Doppler spectrum (sixth moment of the DSD). The mean Doppler velocity v_D is obtained from the first moment of the Doppler spectrum. The spectral width σ_D of the Doppler spectrum is also provided within Cloudnet.

The Doppler radar at LACROS operates at 35 GHz (8 mm). From the data of the year 2012, an average Z sensitivity of −66 dBZ at 800 m, −62 dBZ at 1200 m, −59 dBZ at 1600 m, and −57 dBZ at 2000 m can be deduced. The average sensitivity of Z at 2000 m for the other Cloudnet stations as evaluated for the available observations in 2012 are: −52 dBZ for Juelich (quite variable over the year), −41 dBZ for Chilbolton, −61 dBZ for Lindenberg, −60 dBZ for Potenza, and −56 dBZ for Mace-Head.

Ceilometer A ceilometer emits pulsed radiation with a laser (1064 nm wavelength for JENOPTIK instruments, 905 nm for Vaisala instruments) and obtains the backscattered signal under nearly 180°. The lidar attenuated backscatter coefficient β^* is approximately proportional to r_v^2, meaning it is sensitive mainly to higher concentrations of small particles (cloud droplets and aerosols). Therefore, the base height of liquid water clouds can be identified as a sharp increase of the backscatter coefficient embedded within the weaker precipitation signal or aerosol signal. On the other hand, the signal from the lidar is rapidly extinguished in liquid water clouds, so it is not suitable to detect the cloud-top height.

Microwave Radiometer The microwave radiometer detects emitted microwave radiation in the range from 20 GHz to 60 GHz. The Humidity And Temperature PROfiler

(HATPRO) instrument measures at 14 frequencies: 7 at the H_2O line (22.2 GHz to 31.4 GHz) and 7 at the O_2 absorption complex (51.2 GHz to 58 GHz).

For microwave radiation, the Rayleigh-Jeans approximation for Plancks law can be applied and the brightness temperature (T_B) can be obtained. With an observation of T_B in the water vapor absorption window and another one outside of this window, a retrieval of Q_L and the integrated water vapor Q_V is possible (Gaussiat et al., 2007).

The main uncertainties in the retrieval arise from assumptions about the water vapor, liquid water, and dry air absorption coefficients of the atmospheric columns. Another source of uncertainty is the radiometric calibration (Gaussiat et al., 2007). Typical uncertainties for Q_L retrieved from microwave radiometer are reported as 15–25 $\mathrm{g\,m^{-2}}$ (Zuidema et al., 2005; Gaussiat et al., 2007) for an accuracy of 0.3 K in the obtained brightness temperatures.

Cloudnet Products

The aim of the Cloudnet project is to provide a systematic evaluation of clouds in forecast models (Illingworth et al., 2007). Therefore, it is important to provide vertical profiles of cloud variables with a uniform set of instruments and algorithms for a number of different observational sites. All observations are unified at a temporal resolution of 30 s and a vertical resolution of the radar (30 m for LACROS). The data is calibrated and the radar reflectivity is corrected for gaseous and liquid attenuation. For that the algorithm further uses NWP data to provide additional meteorological fields (temperature, pressure and humidity). For calculating the liquid attenuation, the adiabatically scaled liquid water content profile is used. The key products of the Cloudnet package used in this work are: Q_L, Z, v_D, CBH, CTH, as well as model fields of pressure p and temperature T. The two latter ones are required to obtain Γ_{ad}.

Liquid Cloud Mask

Cloudnet provides a target classification for each vertical profile by applying a number of tests to define categorization bits (see Table 2.6). This target classification is used for sampling suitable cases, and defining the CTH of the liquid cloud layer. For each profile, cloud geometrical limits are only obtained in case of no rain or drizzle. Only the first liquid cloud layer between 300 m and 4000 m above ground is considered. It should be noted, that the CTH used in this work (in the following called liquid CTH) may differ from the CTH that is reported from the Cloudnet algorithm. A cloud mask is defined for this work to mark the one-layer liquid clouds using the following conditions:

- No occurrence of drizzle/rain in Cloudnets target classification (and no drizzle/rain in the 2 nearest neighbor profiles).
- The liquid cloud layer must be elevated between 300 m and 4000 m above ground.
- Ice cloud layers are excluded from the calculation of cloud geometrical depth. The microwave radiometer is not sensitive to ice, so that Q_L is not affected.

target classification	category bits	color
clear sky	none	white
cloud liquid droplets	0	light blue
drizzle or rain	1	red
drizzle coexisting with liquid droplets	0+1	dark blue
ice particles	1+2	yellow
ice coexisting with supercooled liquid	0+1+2	green
melting ice	3	orange
melting ice with liquid	0+3	navy green
aerosol, no cloud / precipitation	4	light gray
insects, no cloud / precipitation	5	dark gray
aerosol + insects, no cloud / precipitation	4+5	dark gray

Table 2.6: Cloudnet target classification as obtained from the Cloudnet category bits: 0 small liquid droplets, 1 falling hydrometeors, 2 wet-bulb temperature $< 0°C$, 3 melting ice present, 4 aerosol present and visible to lidar, 5 insects present and visible to radar.

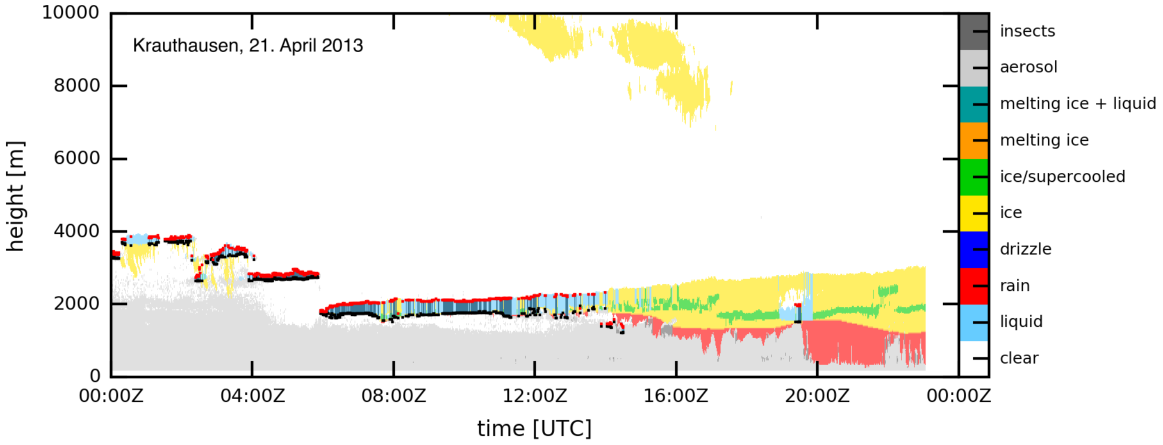

Figure 2.8: Example of the cloud mask and the according detected CBH and CTH for the case of 21 April 2013 in Krauthausen (using LACROS instruments). Colors represent the Cloudnet target classification and highlighted areas in dark the cloud mask. Black dots mark the CBH, red dots the CTH.

- No vertical gaps in the cloud profile are present.

The liquid CTH is then determined by the uppermost pixel where the cloud mask is set. An example for the resulting cloud mask and the according CBH and liquid CTH is shown in Fig. 2.8 (case study of 21. April 2013, Krauthausen).

Retrieval Theory

In the following, the retrieval theory of different cloud properties for the given set of ground-based instruments used within the Cloudnet framework is described. These properties make use of the standard Cloudnet products as introduced before.

Cloud Geometrical Depth While the radar is suitable to obtain the CTH, it is difficult to retrieve the cloud base in case of drizzle, since the radar is highly sensitive to few large droplets ($Z \propto r_v^6$). In addition, the radar detection limit in case of very small cloud droplets and presence of insects complicates the determination of cloud base. To obtain the CBH, a ceilometer is utilized.

The CBH is retrieved using the attenuated lidar backscatter. In case of multilayer clouds, it is possible to retrieve several cloud-base heights when the attenuation (β^*) of the lowermost cloud layers is not too strong. In this study, only single layer clouds and therefore only the lowermost cloud layer is considered. It is located at the lowest pixel in the profile where $\beta^* > 2 \cdot 10^{-5}\,\mathrm{m}^{-1}\,\mathrm{sr}^{-1}$ and where the value 250 m higher up is lower by a factor of 10 (called pivot value). The increase of β^* a hundred meters below the pivot point is calculated. The liquid cloud base is defined as the lowest pixel where the difference between the latter and the above pixel exceeds $\Delta\beta^*/4$ (Hogan and O'Connor, 2004).

Combining the CBH with the liquid CTH, one can easily calculate the cloud geometrical depth H (e.g., Boers et al., 2000) for liquid clouds.

Due to the vertical resolution of the Cloudnet algorithm, the resolution uncertainty of H is 60 m. Further uncertainties arise from the radar sensitivity of the cloud top (if there are too few, small droplets in the volume), so that the 60 m uncertainty is a rather conservative estimate.

Radar-Radiometer Retrieval The radar reflectivity Z can be expressed as a function of the cloud droplet number concentration N_d, the width of the DSD (k_6), and the liquid water content q_L (Fox and Illingworth, 1997), assuming Rayleigh scattering:

$$Z = \frac{36}{\pi^2\,\rho_w^2} k_6 \frac{q_L^2}{N_d}. \tag{2.25}$$

Integrating over the cloud geometrical depth H, one can solve the equation for the liquid water path Q_L:

$$Q_L = \left(\frac{\pi^2\,\rho_w^2}{36\,k_6}\right)^{\frac{1}{2}} \int_{z_b}^{z_t} \sqrt{N_d(z) Z(z)}\,dz. \tag{2.26}$$

In the homogeneous mixing model, $N_d(z)$ is assumed to be constant with height. Rémillard et al. (2013) consider a column-averaged N_d by weighting with the square-root of radar-reflectivity Z:

$$\int \sqrt{N_d(z)}dz = \frac{\int \sqrt{N_d(z)}\sqrt{Z(z)}dz}{\int \sqrt{Z(z)}dz} = \sqrt{\overline{N_d}}. \tag{2.27}$$

As a consequence, the following retrieval method is derived for $\overline{N_d}$:

$$\overline{N_d}(Q_L, Z, k_6) = \left(\frac{36}{\pi^2\,\rho_w^2}\right) k_6 \frac{Q_L^2}{\left(\int \sqrt{Z}dz\right)^2}. \tag{2.28}$$

The relative error is calculated with Gaussian error propagation (see Appendix).

If N_d is substituted into Eq. 2.9 and Eq. 2.11 from the adiabatic cloud model, these equations can be solved given the observed quantities. While this method allows the retrieval of N_d, we will show in Sect. 4.1 that N_d is very sensitive to the required assumptions about the width of the DSD.

Following Brandau et al. (2010), the profile of q_L can also be obtained from observations of Q_L and Z:

$$q_L(Q_L, Z) = \left(\frac{1}{36}\,\rho_w^2\,\pi^2\,k_6\,\overline{N_d}\,Z\right)^{\frac{1}{2}}. \tag{2.29}$$

2.5.3 MACC-II Aerosol Reanalysis

Information about the aerosol distribution is taken from the ECMWF MACC model (Morcrette et al., 2009). The MACC-II reanalysis can be seen as a state-of-art aerosol reanalysis since it makes use of the ECMWF integrated forecast system (IFS) extended with an aerosol model, and employing the full data-assimilation scheme operational at ECMWF. Furthermore, MODIS AOD is assimilated into the MACC aerosol products. The MACC-II reanalysis provides the mass mixing ratio for the following species: dust, sea salt, sulphate aerosols, black carbon (BC), and organic matter (OM). These species are further split up into hydrophobic and hydrophilic (for BC and OM) aerosols and different size bins (for dust and sea salt). Furthermore the Aerosol Optical Depth (AOD) is provided for several wavelengths (469 nm, 550 nm, 670 nm, 865 nm, 1240 nm). The AOD for dust and BC at 550 nm is also available. Reanalysis products are available from 2003 to 2012.

A new version of the MACC aerosol reanalysis product is currently under development with a number of refinements within the European Copernicus program (CAMS).

3 Cloud Adiabaticity - Investigation Using Ground-Based Observations

In Sect. 2.2 the adiabatic cloud model was introduced, for which a linear increase of q_L with height is obtained. From observations it is found that clouds often contain less water than the adiabatic model would suggest. Entrainment of dry air into clouds, but also radiative heating/cooling lead to evaporation of cloud water, and therefore, a reduction of the adiabatic q_L. As a proxy for the entrainment process the subadiabatic factor f_{ad} (e.g., Kim et al., 2008) can be used. Its knowledge is required to calculate key quantities for investigating ACI from larger scale passive satellite observations.

In this section, cloud adiabaticity is investigated utilizing ground-based remote sensing. First, the sampling method to obtain one-layer liquid clouds is described. Second, the typical cloud vertical structure is discussed. Third, differences between ground stations within the Cloudnet network are explored with the objective to obtain a regime or environmental dependence of f_{ad}. Finally, we check for possibilities to parameterize f_{ad} for large-scale studies.

Results of this section were partly presented in Merk et al. (2016), but the statistical analysis here is extended.

3.1 Sampling Method

Observations available for Cloudnet stations in Europe were used to calculate f_{ad} with Eq. 2.4. Required inputs were Q_L from the microwave radiometer, H calculated as the difference of cloud radar CTH and ceilometer CBH, and $\Gamma_{\mathrm{ad}}(T_{\mathrm{cbh}}, p_{\mathrm{cbh}})$ estimated from NWP data.

The investigation requires a sampling of clouds to a suitable subset. The focus is on single-layer cloud systems which consist entirely of liquid cloud droplets and are non-drizzling. Cloud profiles as observed from the ground are filtered according to the cloud mask used to obtain the geometrical borders of the liquid cloud layer (described in Sect. 2.5.2). The following conditions are additionally applied:

- The values of Q_L are between $25\,\mathrm{g\,m^{-2}}$ and $400\,\mathrm{g\,m^{-2}}$. The lower limit is selected according to the uncertainty of the microwave radiometer and the upper limit in accordance with a typical threshold for drizzle (Löhnert et al., 2001).
- The cloud geometrical depth lies between 300 m and 2000 m. Too thin clouds are affected by large relative errors. More information is given later in this section.

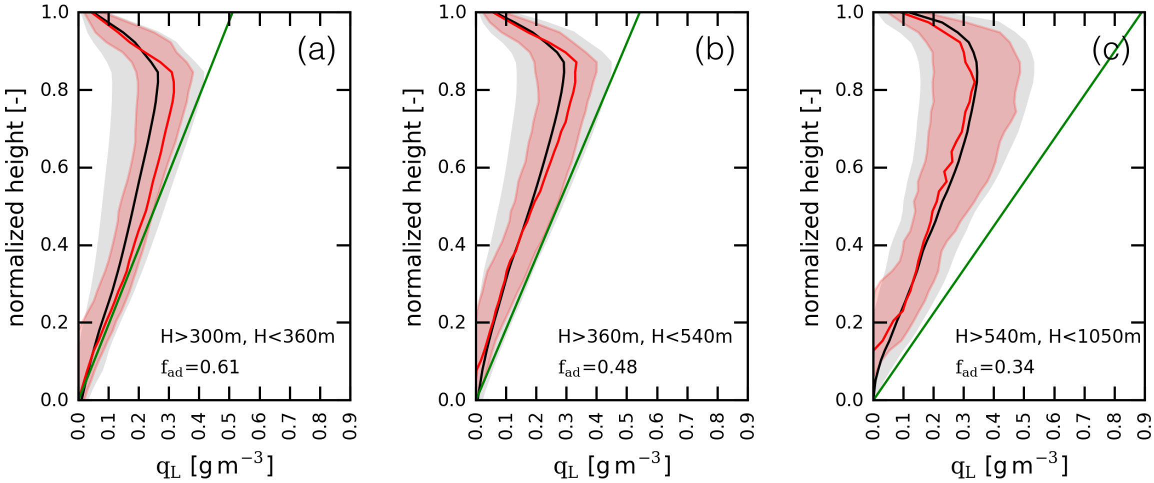

Figure 3.1: Average profiles of q_L normalized with respect to the height above cloud base for cases observed with LACROS instruments. The mean q_L for each level is depicted by the black solid line while the standard deviation of each level is shown in gray. The median q_L is depicted by the red line and the interquartile range is shaded red. The average q_L profiles are shown for three classes of H: (a) 300 m to 360 m, (b) 360 m to 540 m, and (c) 540 m to 1050 m. The green line represents the adiabatic q_L profile.

- Z_{max} is below -20 dBZ within the cloud profile to avoid occurence of drizzle (Rémillard et al., 2013; Mace and Sassen, 2000).

This automatic sampling was applied to pre-selected cases with indicated suitable cloud conditions. Furthermore, a number of such cases with longer time-periods of a liquid cloud layer have been selected as examples that will be comprehensively investigated. They are presented in Fig. 3.3. It should be noted that the occurrence of ideal conditions over a longer time-period for the given Cloudnet stations is rare (2% to 4% of profiles for the stations considered in this work).

3.2 Vertical Cloud Structure

Adiabatic clouds possess a linearly increasing q_L. Depending on the entrainment rate, there is a deviation of this adiabatic profile from the one observed in clouds. To explore which parts of the cloud profile are typically most influenced by entrainment, cases from the LACROS observations are taken to obtain the mean q_L profiles for different classes of H. The classification limits are set in a way that there is a sufficient amount of samples in each class.

The q_L profile is retrieved following the method of Fox and Illingworth (1997) (Eq. 2.29) using the radar and microwave radiometer observations. The adiabatic scaled q_L available from Cloudnet assumes a linearly increasing profile and is therefore not suitable for the investigation of the q_L profile structure. The Fox and Illingworth (1997) retrieval method has uncertainties regarding the absolute values of q_L. Nevertheless, mainly the typical vertical structure of q_L is of interest, so that the method is applicable for the intercomparison of mean profile structures. However, care has to be taken when comparing with the theoretical adiabatic q_L values. Due to the radar detection limits it is possible that there is no reliable retrieval of q_L near the cloud base. As a result, mean values of q_L can be 0. For each profile, f_{ad} is calculated using Eq. 2.4 and averaged over each class of H. Profiles are normalized between CBH and CTH, so that 0 refers to the CBH and 1 to the CTH. The average q_L profiles for different classes of H are presented in Fig. 3.1.

The average f_{ad} is clearly decreasing with thicker cloud classes, which is consistent with the increasing spread of the mean q_L profile and the adiabatic q_L profile. The profiles for all H classes show a nearly linear increase up to about 85–90% of H, while entrainment seems to influence strongly the 10–15% uppermost cloud parts. The lower values of f_{ad} can be explained from two effects visible in Fig. 3.1: (a) a deeper layer of entrainment at the cloud top and (b) a less steep increase of q_L for the geometrically thicker clouds compared to the adiabatic q_L. Interestingly, Korolev et al. (2007) also reported thin cloud layers with a nearly adiabatic q_L profile, but a slightly different behavior for clouds with $H > 500\,\mathrm{m}$. For the latter, q_L in the central part of the cloud was found to be rather constant with height. This is not the case for the sample in our study. In agreement with our study, they observed a sharp decrease of q_L at the uppermost 10–15% cloud part near the cloud top. Such a feature is also obtained from other in-situ observations (e.g., Noble and Hudson, 2015). The LACROS observations for the liquid cloud sample suggest that the adiabatic model is more valid when accounting for f_{ad} than, e.g., a vertically homogeneous description of the cloud vertical structure. The observed strong entrainment at cloud top recommends to further adjust the adiabatic model for a more accurate description of typical vertical profiles of liquid clouds.

So far, only the validity of the assumption of a linearly increasing q_L profile as expected from the adiabatic model has been checked. It is difficult to explore if the reduction of q_L is a result of reduced droplet size or depletion of whole droplets or both, i.e. which mixing model describes the conditions best. This would require in-situ observations and is hence not addressed in this study.

3.3 Statistics at Different Locations

Statistics of f_{ad} might depend on typical environmental conditions for the different Cloudnet stations. In the following, the statistics of f_{ad} are compared between these stations, starting with a more detailed discussion of the data from the LACROS station.

An exemplary time series (21 April 2013, Krauthausen) observed with the instruments of LACROS during the High Definition Clouds and Precipitation for advancing Climate Prediction Observational Prototype Experiment (HOPE)-Juelich campaign is presented in Fig. 3.2. It illustrates that even for a cloud layer, that appears temporally quite homogeneous on the first glance, f_{ad} can vary significantly. For this case, values of f_{ad} between 0.2 and 0.6 are seen before 09:00 UTC. Measurements of Z (Fig. 3.3d) reveal that the cloud base is more inhomogeneous during this time period than later on. After 09:00 UTC, f_{ad} varies between 0.5 and 1.0 with values below 0.5 at the end of the sample.

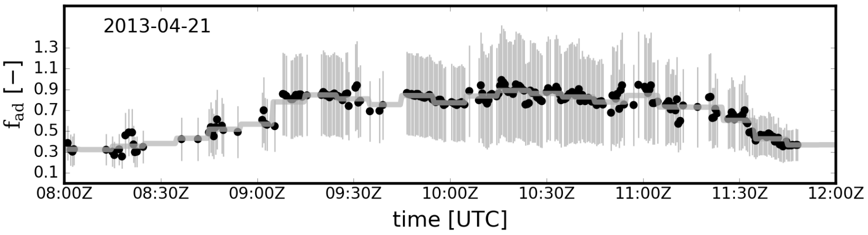

Figure 3.2: Time series of f_{ad} for 21 April 2013, observed in Krauthausen, neglecting superadiabatic values. Black dots represent f_{ad} derived using ground-based H and Q_L, with gray error bars depicting uncertainties following Gaussian error propagation. The gray solid line represents the 10-min averaged and interpolated f_{ad}.

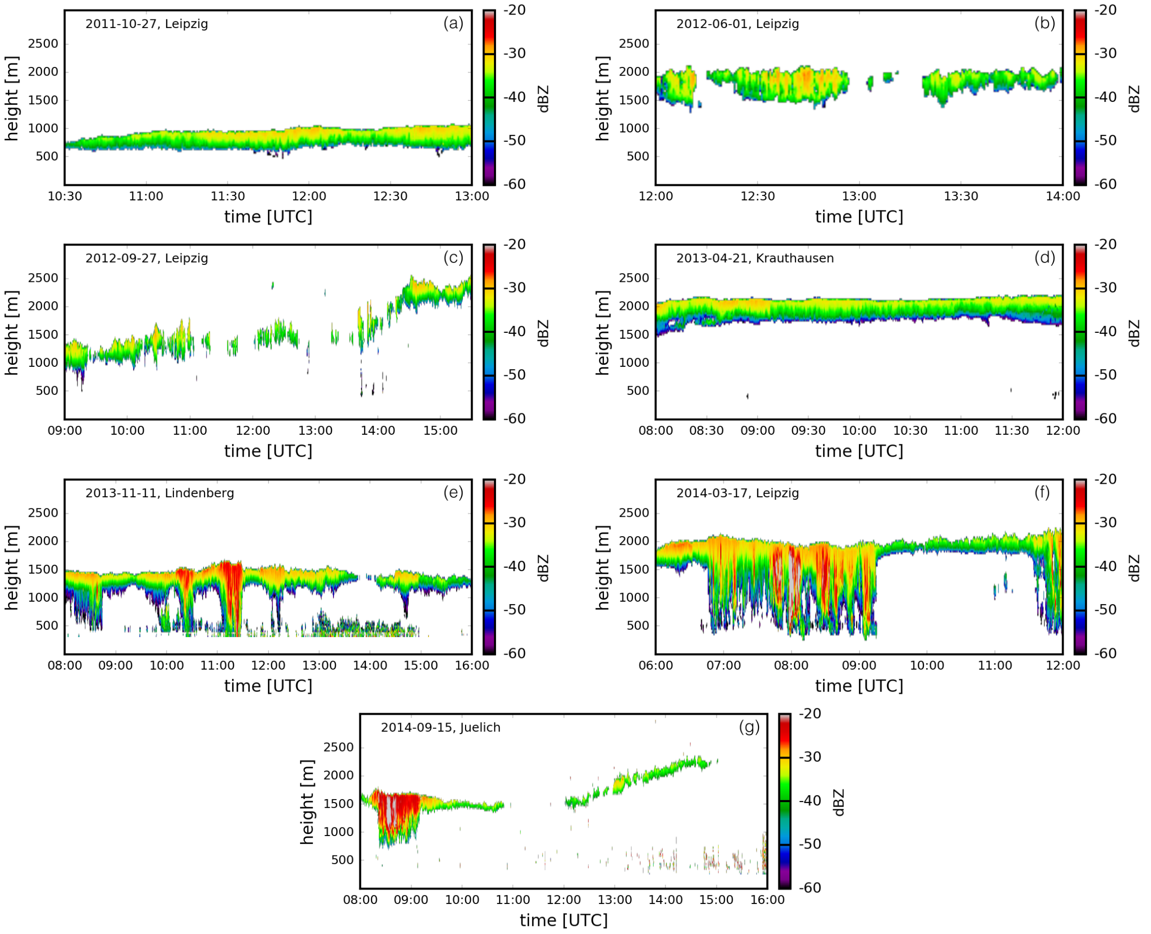

Figure 3.3: Time series of radar reflectivity for case studies: (a) 27 October 2011, Leipzig; (b) 1 June 2012, Leipzig; (c) 27 September 2012, Leipzig; (d) 21 April 2013, Krauthausen; (e) 11 November 2013, Lindenberg; (f) 17 March 2014, Leipzig; (g) 15 September 2014, Juelich.

case	$\overline{f_{\mathrm{ad}}}$	$\widetilde{f_{\mathrm{ad}}}$	σf_{ad}	$\widetilde{f_{\mathrm{ad}}}[v \geq 0]$	$\sigma f_{\mathrm{ad}}[v \geq 0]$	$\widetilde{f_{\mathrm{ad}}}[v < 0]$	$\sigma f_{\mathrm{ad}}[v < 0]$
27 Oct 2011	0.62	0.61	0.09	0.71	0.07	0.60	0.09
01 Jun 2012	0.43	0.44	0.22	0.50	0.16	0.35	0.22
27 Sep 2012	0.59	0.62	0.18	0.54	0.17	0.63	0.18
21 Apr 2013	0.74	0.80	0.17	0.80	0.18	0.79	0.17
11 Nov 2013	0.68	0.68	0.20	0.85	0.16	0.67	0.20
17 Mar 2014	0.70	0.68	0.14	0.91	0.00	0.68	0.13
15 Sep 2014	0.55	0.54	0.04	0.52	0.00	0.55	0.04
all cases	0.69	0.76	0.19	0.79	0.19	0.75	0.19

Table 3.1: Mean, median and standard deviation of f_{ad} (calculated from Eq. 2.4) for the case studies as shown in Fig. 3.3. Furthermore, the median and standard deviation of f_{ad} is listed, classified into updraft ($v \geq 0$) and downdraft ($v < 0$) regimes at cloud base.

The cases shown in Fig. 3.3 for which a longer time-period of suitable liquid clouds were observed have been selected to check the variability of f_{ad} with time and among individual cases. The mean values of f_{ad} for these cases are listed in Table 3.1. f_{ad} not only changes from case to case, but also varies with time for individual days, reflecting the natural variability of entrainment processes. Therefore, considering a constant f_{ad} as often assumed in previous studies (Table 2.2) could affect retrievals of cloud properties. Anyhow, the majority of clouds seems to be subadiabatic, independent from temporal cloud homogeneity.

The statistics of f_{ad} for Leipzig in the years 2012–2015 (19,394 liquid cloud profiles, Fig. 3.4) show a mean of $f_{\mathrm{ad}} = 0.45$ and the interquartile range (IQR) as [0.29,0.61]. Overall, there is a large spread of values covering the full physical range from 0 to 1. The obtained statistics are in agreement with typical values of $[0.3, 0.9]$ suggested in Boers et al. (2006) and $[0.1, 0.9]$ in Lonitz et al. (2015). From modelling studies (Zhang et al., 2011) it is expected that f_{ad} becomes smaller as clouds are decaying.

Values of $f_{\mathrm{ad}} > 1.0$ are most likely caused by the measurement uncertainties, since the occurrence of "superadiabatic" cloud profiles in nature is physically implausible. Such artifacts especially arise due to uncertainties in Q_L and H for thin clouds. Within Cloudnet, "superadiabatic" profiles are avoided by increasing the CTH if the integrated adiabatic q_{L} is smaller than Q_L (measured by the microwave radiometer). In contrast to the original Cloudnet code, our calculation of f_{ad} does modify the observed geometrical cloud depth.

The statistical analysis of the sampling method outlined in Sect. 3.1 is extended also to other Cloudnet stations (see Fig. 2.5). During the data inspection problems in Q_L retrieved from the MWR for the Potenza station (not shown here) were detected and therefore this data is omitted for the analysis. A comparison of the histograms of the different stations for H, Q_L and f_{ad} is presented in Fig. 3.5. The statistics are summarized in Table 3.2.

For the sample in this study the highest probability is to find values of about $50\,\mathrm{g\,m^{-2}}$. It decreases exponentially with Q_L, similar to the study of Ebell et al. (2011). Sena et al. (2016) created a sample of one-layer liquid clouds from 14 years of ground-based observational data at the ARM Southern Great Planes site. They showed a very similar

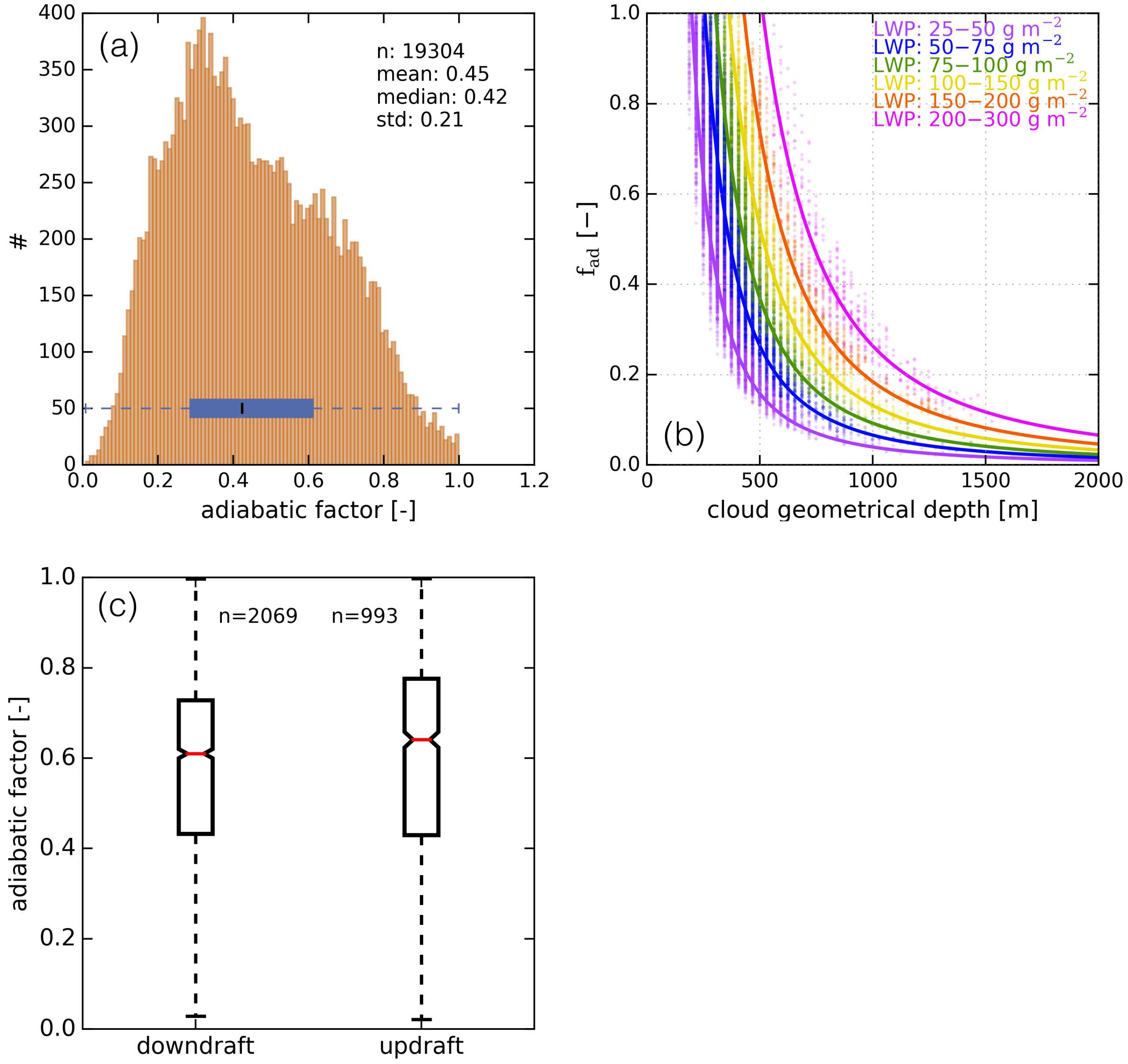

Figure 3.4: Observations from the 2012–2015 sample at Leipzig: (a) Histogram of f_{ad}. (b) f_{ad} as a function of the observed H. The colors indicate different Q_L bins. The solid lines represent the relationship described in Eq. 2.4 for the mean Q_L of each bin and $\Gamma_{\text{ad}} = 1.9 \cdot 10^{-3}\,\text{g}\,\text{m}^{-4}$. (c) Box-Whisker plot of f_{ad}, separated into occurrence of up- and downdrafts at the cloud base.

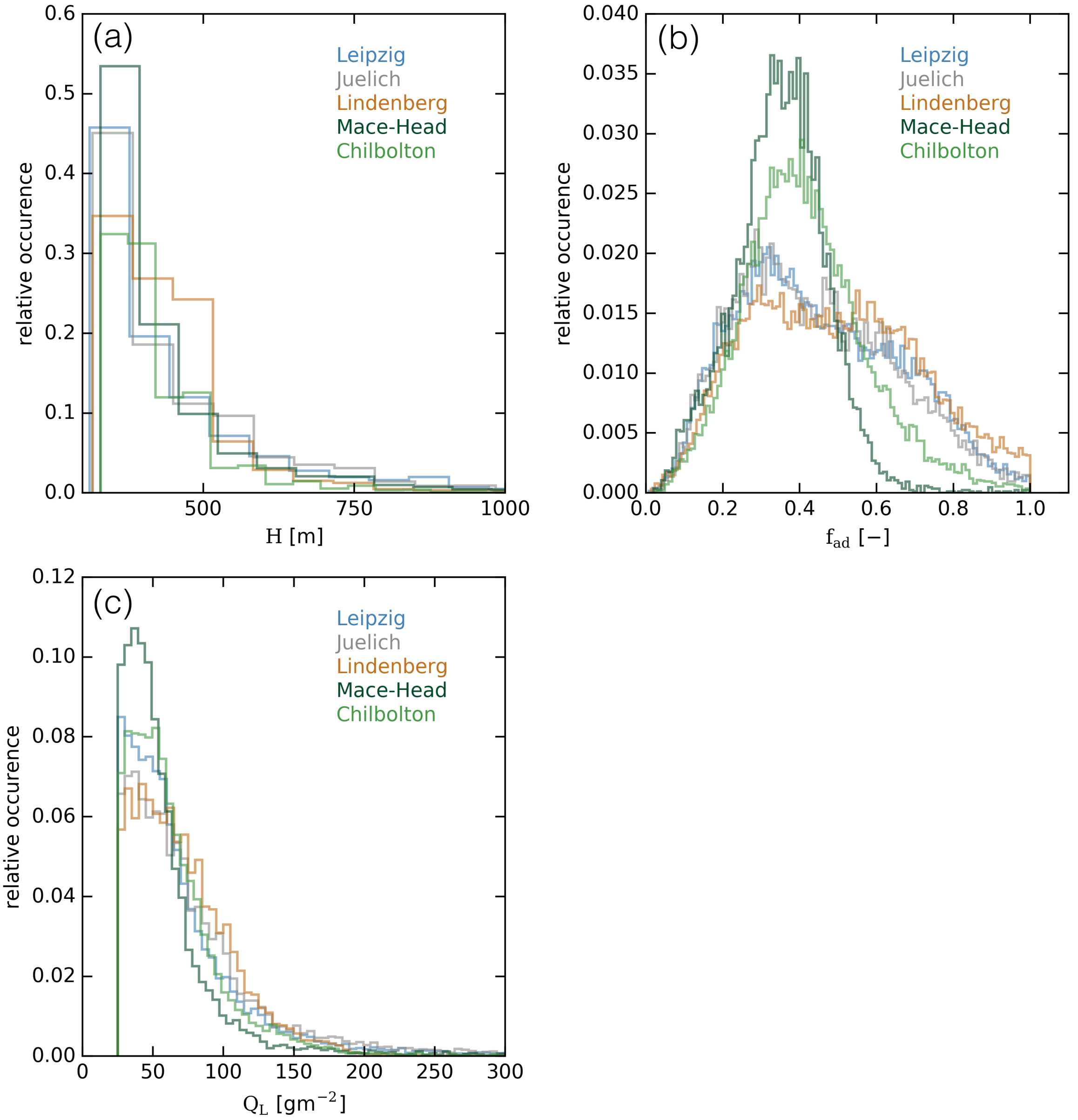

Figure 3.5: Relative occurrence of (a) H, (b) Q_L, and (c) f_{ad} for different Cloudnet stations and the liquid cloud sample filtered using the method described in Sect. 3.1.

station	n	period	$\overline{Q_L}$ [g m^{-2}]	$\tilde{Q_L}$ [g m^{-2}]	$\sigma(Q_L)$ [g m^{-2}]	$\overline{H}$ [m]	$\tilde{H}$ [m]	$\sigma(H)$ [m]	$\overline{f_{\mathrm{ad}}}$	$\tilde{f_{\mathrm{ad}}}$	$\sigma(f_{\mathrm{ad}})$
Leipzig	19304	2012-2015	72	57	49	453	405	168	0.45	0.42	0.21
Juelich	9417	2010-2015	80	64	56	454	403	158	0.44	0.42	0.20
Lindenberg	33159	2004-2013	72	65	37	437	420	126	0.49	0.48	0.22
Mace-Head	8566	2008-2013	58	49	37	440	390	142	0.35	0.35	0.12
Chilbolton	16796	2010-2012	64	56	35	430	420	103	0.41	0.4	0.16

Table 3.2: Statistics of Q_L, H and f_{ad} for different Cloudnet stations and the liquid cloud sample filtered using the method described in Sect. 3.1. The mean (overline), median (tilde), and standard deviation (σ) is given for each property.

distribution of Q_L, which they regard as representative for their site and selection criteria. According to the adiabatic cloud model, higher values of Q_L are associated with thicker clouds, which is reflected by a high correlation of H and Q_L. The distribution of H follows a similar pattern for most stations. Only for Lindenberg there is a more frequent occurrence of clouds with H between 400 m and 500 m.

For the stations at Mace-Head and at Chilbolton, there is a stronger peak at lower Q_L values and a smaller standard deviation of the Q_L distribution. Mace-Head is located directly at the coastline of the Atlantic, and therefore influenced by maritime conditions. Chilbolton is also embedded in an environment for which a more maritime influence is prevalent. This is in agreement with the satellite study of Kniffka et al. (2014), who report higher Q_L over land than over sea. The difference in the Q_L distribution is reflected in the distribution of f_{ad}. The lowest median value of f_{ad} is found for the Mace-Head station ($\tilde{f}_{\mathrm{ad}}$=0.35). At Chilbolton, the median f_{ad} value is closer to the continental stations at Juelich and Leipzig, but a smaller standard deviation of f_{ad} as compared to the continental stations is obtained. The highest median value and largest standard deviation of f_{ad} occur at Lindenberg. To confirm the hypothesis that the distribution of f_{ad} is more narrow and has its maximum at lower values under maritime conditions, a more dense network of ground-based sites with homogenized set of instruments is desirable.

The influence of differences in each stations sample size cannot be ruled out, although the results seem to be stable. For example, the station in Juelich shows similar statistics to stations in Leipzig and Lindenberg, even though the Juelich sample size is smaller. Note that both cumuli-like and stratocumulus clouds have been considered, since their separation is not straight forward. Therefore, a different likelihood of occurrence of cumulus and stratocumulus for maritime and continental stations might be responsible for the observed difference in the distributions of cloud properties.

A dependence of f_{ad} on cloud regimes and/or environmental conditions is able to affect estimates of ACI as pointed out by Shao and Liu (2006), since for ACI investigations it is often assumed that clouds have the same f_{ad}. Differences in statistics of f_{ad} as indicated might be useful to address such a regime dependence.

3.4 Parameterization of the Subadiabatic Factor

Cloud adiabaticity can be obtained given the measurements of ground-based observations utilizing a cloud radar, ceilometer and microwave radiometer. These observations are only available for few ground-based sites. Finding descriptors of cloud adiabaticity to parameterize f_{ad} over a larger domain is important as it is known to influence estimates of ACI.

From previous studies it has been reported that cloud adiabaticity shows a connection to geometrical depth and vertical velocity. In the following, the relationship between adiabaticity and possible descriptors is investigated.

3.4.1 Cloud Geometrical Depth

When looking for proxies of f_{ad}, there is a clear trend that geometrically thicker clouds are less adiabatic (Figure 3.4b). This is independent of the location of the Cloudnet observation site. Already Warner (1955) reports a decrease in f_{ad} with increasing cloud geometrical depth. It also supports the results of Min et al. (2012), who observed the tendency that thicker clouds are less adiabatic in the Southeast Pacific. Mainly thin clouds ($H < 300\,\mathrm{m}$) will result in $f_{\mathrm{ad}} > 1$, in agreement with Miller et al. (1998). This can be seen as an artifact due to measurement uncertainties as already discussed earlier in this chapter. Therefore, the investigation of such thin clouds remains challenging (Turner et al., 2007). The statistics of very thin clouds are unreliable and are not considered due to the impact of measurement uncertainties. Omitting thin clouds $H < 300\,\mathrm{m}$ could shift mean values of f_{ad} towards lower values. In agreement with the previous studies, one can conclude that f_{ad} is strongly dependent on H. In contrast, there is no clear dependency of f_{ad} on CBH or CTH only.

3.4.2 Inversion Strength

As the maximum vertical extent can be influenced by the presence of temperature inversion, and the temperature inversion is also known to suppress vertical mixing (Katzwinkel et al., 2012), there might also be a relationship between the inversion strength and f_{ad}.

To investigate if such a relationship exists, an inversion strength parameter T_{inv} is defined as the difference of the NWP model temperature at 150 m above CTH and the model temperature 30 m above CTH. An inversion is present in case of $T_{inv} > 0$. It gets stronger for larger positive values. The use of such a simplified parameter from NWP data is motivated from its ease to be applied over a large domain.

For geometrically thick clouds the likelihood to find negative values of T_{inv} is higher (Fig. 3.6). However, for such values a large number of geometrically thin clouds can be found. The reason for this is multifold. The inversion strength does not tell about the actual height of the inversion layer. Also, clouds can be in an early stage of development and may not have reached their theoretical vertical limit. On the other hand, for $T_{inv} > 0$ the likelihood to find clouds with $H > 600\,\mathrm{m}$ is very low. From the results it is clear, that thicker clouds can only develop if no inversions are present.

As mentioned above, f_{ad} is strongly dependent on H. The inversion strength is a factor that determines the vertical limit of cloud development, and therefore, the statistics of f_{ad}. Another parameter that determines H is the CBH. In case of unknown H and considering only the measure of inversion strength as a proxy for f_{ad}, there is some spread in f_{ad} for a given inversion strength. For stronger inversions the likelihood to find higher values of f_{ad} is increased.

For calculating T_{inv}, thicker layers up to 270 m above the CTH have also been investigated. However, the results were similar.

In case H is unknown, taking instead into account CTH and having reliable NWP data of vertical temperature profiles, might give a chance to estimate a typical distribution of f_{ad}.

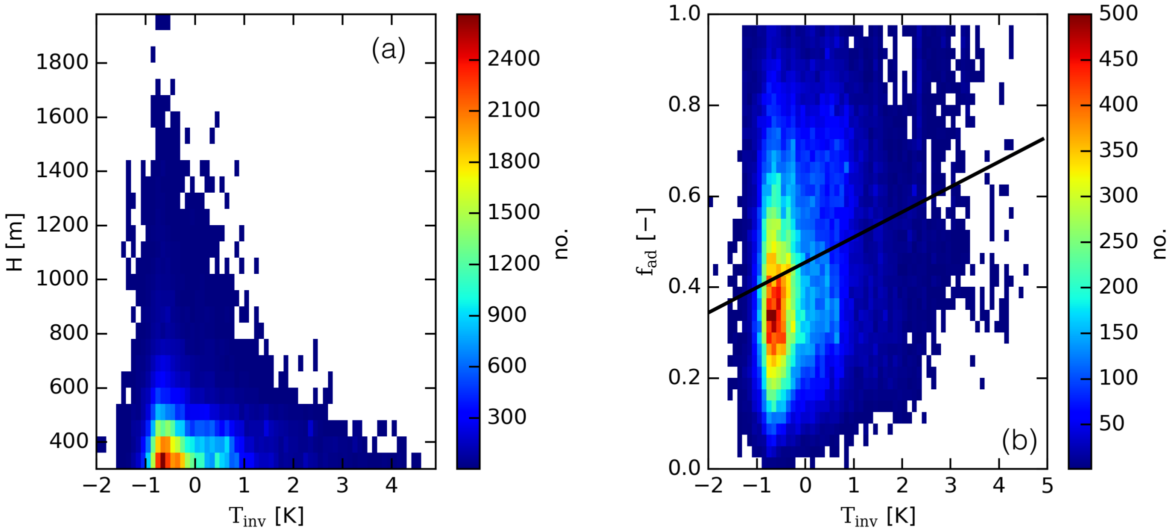

Figure 3.6: (a) Inversion strength T_{inv} versus H, and (b) T_{inv} versus f_{ad}, using data from all Cloudnet stations as a two-dimensional histogram. The colors represent the number of occurrence of (T_{inv}, H) and (T_{inv}, f_{ad}) in each bin interval. The solid line represents a linear least-square fit.

While radiosonde might give more reliable temperature profiles, their horizontal coverage is too sparse. This method is applicable mainly for statistical investigations rather than for individual case studies as the spread of f_{ad} for a given inversion strength is large.

3.4.3 Vertical Wind Speed

Vertical motions essentially control processes in clouds and probably also cloud adiabaticity. Schmidt et al. (2014) employed observations with temporally homogeneous stratocumulus clouds over Leipzig, Germany. They found that in case of updrafts in clouds, the q_{L} profile tends to be more adiabatic. To investigate if such a behavior also occurs for the cases in this study the cloud radar Doppler velocity at the cloud base is applied. Negative values refer to downdrafts, while positive values correspond to updrafts. The average vertical velocity at cloud base for all samples from 2012 to 2015 is found to be $-0.26\,\mathrm{m\,s^{-1}}$ with the majority of points (91%) in the range of $[-1{,}1]\,\mathrm{m\,s^{-1}}$. The change of updraft and downdraft periods on a short timescale might be considered as a typical pattern as seen from Fig. 11 in Schmidt et al. (2014). Considering f_{ad} as a function of the vertical velocity, a large spread is found, which complicates the detection of a clear influence of updraft speed on the cloud adiabaticity. For the cases as presented in Fig. 3.3, the mean and median f_{ad} are calculated for updraft and downdraft regimes. On average, clouds are slightly more adiabatic in the updraft regime for most cases (see Table 3.1). Since the sample size for individual cases is quite small, we considered a larger sample of the period from 2012 to 2015 in Leipzig. For this sample the notch around the median in the box-whisker-plot (Fig. 3.4c) is found not to overlap for updraft and downdraft regimes. According to Krzywinski and Altman (2014), the median differs significantly on the 95%

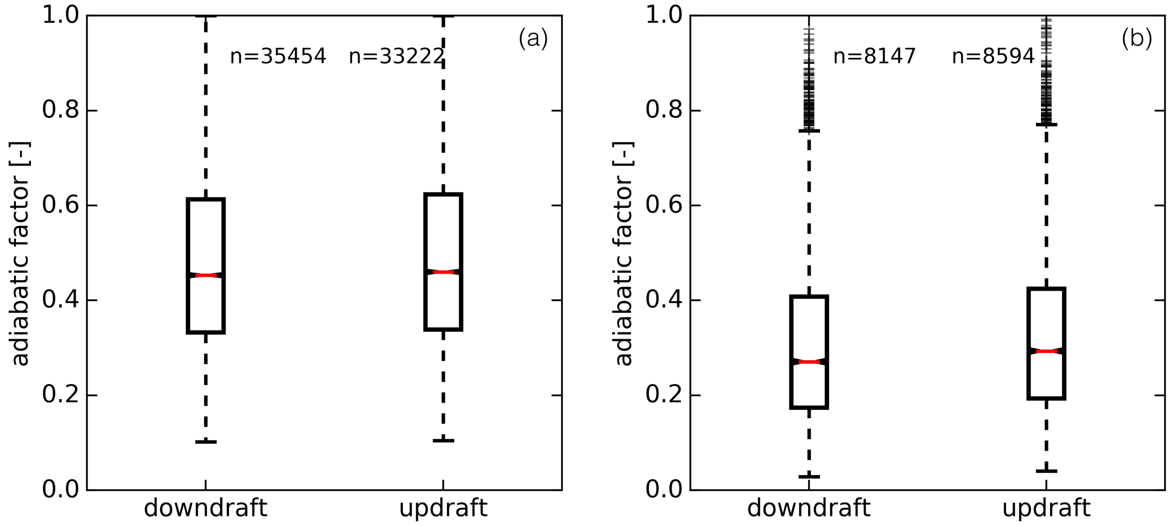

Figure 3.7: Box-Whisker plot for f_{ad}, split into up- and downdraft regimes. The mean vertical Doppler velocity for the cloud column between CBH and CTH is considered. From left to right: (a) H=300 m–500 m, (b) H=500 m–1000 m.

v	300 m–500 m		500 m–1000 m	
mean over	$\overline{f_{\mathrm{ad}}}\ [v > 0]$	$\overline{f_{\mathrm{ad}}}\ [v < 0]$	$\overline{f_{\mathrm{ad}}}\ [v > 0]$	$\overline{f_{\mathrm{ad}}}\ [v < 0]$
z_b to z_t	0.489	0.481	0.322	0.305
z_b to $0.5\,H$	0.504	0.490	0.326	0.318
CBH to 0.33 H	0.523	0.502	0.323	0.329
at z_b	0.556	0.516	0.317	0.348

Table 3.3: Mean f_{ad} for up- and downdraft regimes in the cloud column (CBH to CTH), separated into different classes of H. Results are presented for different vertical averages of v.

confidence interval if there is no overlay in the notches. This is in agreement with the findings of Schmidt et al. (2014). In other words, in case of updrafts there is a tendency towards more adiabatic clouds for the sample at Leipzig. In case of updrafts at the CBH, no clear signal for more adiabatic clouds can be detected for most other Cloudnet stations. As f_{ad} depends on H, the behavior of v in two different classes of H is investigated. The following classes are defined: 300 m–500 m and 500 m–1000 m. The range is more narrow for the first class because more thin clouds occur and f_{ad} is quadratically dependent on H.

If the vertical velocity averaged from CBH to CTH is considered, the lowest values of f_{ad} are found for very thick clouds. The separation into higher and lower f_{ad} for mean up- and downdrafts, respectively, in the cloud column is strongest for the thickest clouds (Fig. 3.7). It cannot be excluded that this is due to the lower number of thick-cloud samples, and therefore, poorer statistics. The uncertainty of f_{ad} has also to be taken into account.

Schmidt et al. (2014) report that for updrafts the effect of a higher subadiabatic factor is found to be strongest at the cloud base. Additionally, it blurs when the data points are averaged over the whole cloud profile. Taking the mean v in the lowermost half or third of the cloud column, and at the CBH, the results were only slightly different (Table 3.3). The reason why the dependence of f_{ad} on v cannot be clearly reproduced from this work might be explained by the lower temporal resolution as well as the less accurate vertical velocities obtained from the Cloudnet dataset. This can be understood as the cloud radar is biased towards negative velocities as the cloud radar is more sensitive to larger particles compared to the Doppler lidar.

Given the current data, no conclusive results can be drawn with respect to the influence of the up- and downdrafts on f_{ad}. More detailed data (e.g. Doppler lidar, Schmidt et al. (2014)) might be suitable to investigate the connection between the vertical velocity and f_{ad}. Additionally, one must take into account that f_{ad} represents the average adiabaticity over the whole liquid cloud column, i.e., entrainment at the cloud top might be of greatest importance. It could lead to strong subadiabaticity in the uppermost cloud part, while updrafts might prevail in the lowermost cloud part. This would lead to nearly-adiabatic conditions in this lower part, but the cloud appears subadiabatic over the whole column (compare Fig. 3.1).

3.5 Discussions and Conclusions

For retrieving cloud properties from remote sensing observations, often adiabatic clouds or even vertically homogeneous clouds are assumed in many studies. However, it was shown in this work that clouds are typically subadiabatic, consistent with previous reports from in-situ and remote sensing observations. Median values of the subadiabatic factor f_{ad} range from 0.35 to 0.48 with respective standard deviations of 0.12 and 0.22. q_L typically exhibits a nearly linearly increase up to about 90% of H, and a drastic reduction near the cloud top. It is anticipated that this is due to entrainment processes (Chin et al., 2000), although it cannot be proven from ground-based remote sensing instruments alone.

Cloud geometrical depth H strongly influences f_{ad}. The maximum H for the cloud regimes considered here (stratocumulus and cumulus clouds) is determined by the thermodynamic conditions (especially by inversions). Stronger inversions correspond to a higher likelihood for lower H and higher f_{ad}, respectively. Although Schmidt et al. (2014) report a connection between the updraft velocity at cloud base and cloud adiabaticity, no clear signal could be produced from the datasets used in this work. Overall, while typical distributions of f_{ad} for known thermodynamic conditions and typical cloud regimes might be obtained, an accurate parameterization of f_{ad} for individual cases is difficult to acquire with the given observations.

f_{ad} can vary from case to case, even for the same location, and is usually not constant over time. The explanation is likely the statistical nature of the entrainment processes. However, indications for different statistics of f_{ad} for the cloud regimes at particular regions (maritime vs. continental) were found. The median value of f_{ad} is lower with smaller standard deviation at coastal sites. To obtain ACI key quantities from, e.g., passive satellite observations, f_{ad} is required for a larger domain. Even though satellites provide a good spatial coverage, the retrieval uncertainties complicate the estimate of f_{ad}. This is discussed more detailed in Sect. 5.

Although a deviation at the uppermost 10-15% of the cloud from the adiabatic q_L profile is observed from our data, also consistent with previous reports, the adiabatic model is suggested to be a sufficient description for typical liquid clouds when taking into account f_{ad}, which accounts for the clouds' overall deviation from adiabaticity. It will therefore be used in the remainder of this work for the retrieval of cloud properties.

4 Optimal Estimation of Cloud Properties From Ground-Based Remote Sensing

An accurate retrieval of cloud properties is very important for studies of cloud processes and ACI. Several efforts to quantify ACI utilizing cloud properties retrieved from ground-based remote sensing have been made (e.g., Feingold et al., 2003; Sarna and Russchenberg, 2016; Schmidt et al., 2015). Cloud properties such as r_e and N_d have been used for that. N_d is directly influenced by the CCN concentration, and does not require a constraint on Q_L for ACI investigations, allowing for more robust statistics. It is hence a desirable candidate for ACI investigations. However, the retrieval of N_d from a radar-radiometer approach is highly uncertain. This demonstrates the need of more advanced retrieval methods that can further improve the retrieval using additional observations (Zhao et al., 2012). In this work an Optimal Estimation (OE) framework to retrieve N_d and q_L is developed focusing on observations from ground-based remote sensing. The OE framework combines different observations together with a-priori information, and provides uncertainty estimates of the retrieval results (e.g., Rodgers, 2000; King and Vaughan, 2012; Ebell et al., 2013).

In the following, we will first explore the uncertainty of the radar-radiometer approach following Brandau et al. (2010) (referred to as B2010 in the following) on the example of cloud profiles obtained from ground-based instruments at Cloudnet sites. Afterwards, the OE framework is described. The OE framework allows to easily add more observations. Here, it is discussed if the 2nd moment of the DSD in terms of τ is able to better constrain the retrieval. τ can be observed from ground with remote sensing instruments utilizing the solar spectrum, such as the Multifilter Rotating Shadowband Radiometer (MFRSR) (Min and Duan, 2005) or the two-channel narrow field-of-view radiometer (2NFOV) (McComiskey et al., 2009). Alternatively, it can also be obtained from passive satellite observations.

In the following, the performance of the OE retrieval with additional τ observations is explored utilizing synthetic cloud profiles. The sensitivity of the OE results is investigated for the assumption about the width of the DSD, homogeneous mixing, the a-priori and observation errors, and the choice of the a-priori state.

	ΔN_d (case 1)	ΔN_d (case 2)	$\Delta\tau$ (case 1)	$\Delta\tau$ (case 2)	Δr_e (case 1)	Δr_e (case 2)
$\Delta Z = -2\,\mathrm{dBZ}$	266 (58%)	126 (58%)	3.0 (17%)	2.3 (17%)	1.1 (17%)	1.3 (17%)
$\Delta Z = +2\,\mathrm{dBZ}$	168 (37%)	80 (37%)	2.6 (14%)	1.9 (14%)	1.0 (14%)	1.1 (14%)
$\Delta Q_L = -25\,g\,m^{-2}$	267 (59%)	140 (64%)	4.7 (26%)	6.8 (49%)	0.7 (10%)	0.9 (11%)
$\Delta Q_L = +25\,g\,m^{-2}$	384 (84%)	209 (96%)	4.1 (22%)	7.8 (57%)	1.1 (16%)	1.5 (18%)
$\nu = 0.200$	614 (135%)	292 (135%)	2.9 (16%)	2.2 (16%)	1.0 (14%)	1.1 (14%)
$\nu = 0.043$	174 (38%)	83 (38%)	1.7 (9%)	1.3 (9%)	0.7 (10%)	0.8 (10%)

Table 4.1: Uncertainty estimation for N_d and τ by varying Z, Q_L and the effective variance of the Gamma distribution (ν). Relative uncertainties are given in brackets. Case 1: 21 April 2013, 11:00 UTC; $Q_L = 69\,\mathrm{g\,m^{-2}}$, $H = 311\,\mathrm{m}$, $f_{\mathrm{ad}} = 0.76$; retrieved values: $N_d = 456\,\mathrm{cm^{-3}}$, $\tau = 18$, $r_e = 6.88\,\mu\mathrm{m}$, applying ν=0.1. Case 2: 1 June 2012, 13:30 UTC; $Q_L = 62\,\mathrm{g\,m^{-2}}$, $H = 342\,\mathrm{m}$, $f_{\mathrm{ad}} = 0.55$; retrieved values: $N_d = 216\,\mathrm{cm^{-3}}$, $\tau = 13.6$, $r_e = 7.97\,\mu\mathrm{m}$.

4.1 Uncertainties of Ground-Based Radar-Radiometer Retrievals

The sensitivity of the retrieved N_d to the uncertainties of the input parameters of the radar-radiometer method is evaluated following B2010. Two liquid cloud profiles from ground-based observations with the mobile LACROS instruments are considered. Results are presented in Table 4.1.

The radar-radiometer retrieval approach (Sect. 2.5.2) depends on the observations of Q_L, H and $Z(z)$, as well as on the choice of the mixing model. The latter determines whether N_d is vertically constant. Boers et al. (2006) has shown that the effect of the choice of the mixing model on the retrieval results is small. N_d depends further on k_6 (Eq. 2.28), which is a function of the width of the DSD ν only.

Table 4.1 lists the sensitivities of retrieved N_d, τ and r_e to each input parameter, considering the upper and lower uncertainty limits as described in the following, and keeping the other input parameters constant. Gaussian error propagation is applied as expressed in Eq. 8.29, Eq. 8.27, Eq. 8.28.

The uncertainty of $Z(z)$ is assumed as $\pm\,2\,\mathrm{dBZ}$ following B2010. This corresponds to a calibration bias constant with height. Z is very sensitive to even a few large droplets (e.g., Battan, 1973; Löhnert et al., 2003). Therefore, drizzle-containing profiles are filtered out by a maximum threshold of $-20\,\mathrm{dBZ}$ for $Z(z)$ in each profile (Rémillard et al., 2013; Mace and Sassen, 2000). The uncertainty of H is anticipated to be $\pm\,60\,\mathrm{m}$, and for Q_L observations to be $\pm\,25\,\mathrm{g\,m^{-2}}$ (compare Sect. 2.2). A wide range of values is reported for the width of the DSD (ν) for continental clouds (Miles et al., 2000). Considering the range of reported values, the effective variance ν of the Gamma size distribution lies between 0.043 and 0.2, corresponding to $k_2 = 0.87$ and $k_2 = 0.48$, respectively. For the standard retrieval $\nu = 0.1$ ($k_2 = 0.72$) is assumed.

N_d is most sensitive to the assumed width of the DSD, especially to changes of ν if its values are high. This can be understood as $N_d \propto k_6$ and k_6 is a monotonically increasing function of ν. For lower ν values other uncertainty contributions become equally or more important. Since the DSD shows a large natural variability and is usually unknown, it is difficult to estimate the actual uncertainty when assuming $\nu = 0.1$. From the sample cases it is found that the Q_L uncertainty might be more important than the uncertainty in radar reflectivity. Both can result in more than 50% relative uncertainty of the retrieved N_d.

As can be seen from the sub-adiabatic model (Eq. 2.9), the retrieval of τ depends on the same observed quantities as the retrieval of N_d, but also on f_{ad}. In f_{ad} a combined uncertainty of Q_L and H is reflected. τ is most sensitive to uncertainties in Q_L (Table 4.1), especially if Q_L is low. In contrast to N_d, τ is relatively insensitive to the assumption of the width of the DSD. While for N_d, the uncertainty for low values of ν is above 100%, it is below 20% for τ. Since the natural variability of DSDs is large and difficult to constrain without in-situ observations, τ appears to be a more robust quantity for contrasting to other observations, as already suggested by B2010 and Knist (2014). A bias in Z of $\pm 2\,\mathrm{dB}$ would result in 14–17% errors in τ retrievals.

For comparison, errors of 30–60 % have to be anticipated for q_{L} profile retrievals using Z observations, based on the same principles as the radar-radiometer method (Löhnert et al., 2001).

In a next step, the retrieval of the full time series of the case of 21 April 2013 in Krauthausen (as presented in Fig. 3.3) is investigated. In Fig. 4.1 the uncertainty of τ as a function of Q_L is presented. Representative averages of N_d and f_{ad} over the whole time-period are used (blue solid line) to demonstrate the effect of its temporal variability on the retrieved τ. The red and green solid lines represent the uncertainty range considering the IQR of f_{ad} and N_d observations. The dotted lines represent the uncertainty range for assuming a 50% uncertainty for f_{ad} and N_d. For both uncertainty estimates, there is an increasing uncertainty of τ with Q_L, with the uncertainty due to ΔN_d being slightly larger than due to Δf_{ad}.

Recognizing the difficulty in retrieving N_d from the 3rd and 6th moments, Frisch et al. (2002) used a climatological mean value for N_d in order to retrieve r_e. This would be similarly possible for the retrieval of τ. They reported an average N_d of $212 \pm 107\,\mathrm{cm}^{-3}$ at the Southern Great Plains site for continental clouds, which is similar to the median value found for the example cases in Fig. 4.1.

4.2 Application of the Optimal Estimation Framework for the Ground-Based Retrieval of Cloud Properties

Due to the large sensitivity of radar-radiometer retrieved N_d to the assumption about the width of the DSD, the question remains if it is possible to better constrain the retrieval of N_d and reduce its uncertainties.

In the following, the hypothesis is tested that the inclusion of an additional observation of τ is able to improve the retrieval of N_d. It is assumed that the retrieval of the 0th

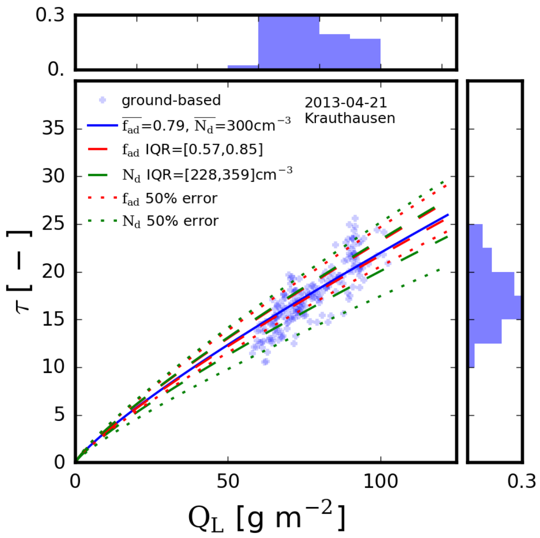

Figure 4.1: Relationship between Q_L and τ for the case of 21 April 2013 in Krauthausen (compare Fig. 3.3). Blue crosses represent the Cloudnet observations for the case day. The solid blue line represents the relationship between τ and Q_L for the median f_{ad} and N_d of the ground-based observations. Uncertainty estimates of τ as a function of Q_L are given in terms of temporal variability using the IQR of the time series (dashed), and as 50% relative uncertainty in N_d and f_{ad} (dotted). Furthermore the histogram of ground-based observations is shown on each axis.

(N_d) moment using the 2nd (τ), 3rd (Q_L) and 6th (Z) moment is better constrained than taking only the 3rd and 6th moment. This is done by a OE framework which utilizes the different moments of the DSD in the observation vector. The connection of the different moments allows the use of forward models that are easy to handle and numerically cheap.

The performance of the OE method is investigated in comparison to the radar-radiometer approach as described in B2010 assuming cloud profiles, ranging from simple to more realistic cases. Results from the investigation of q_L profiles (Sect. 3.2) will be used for that. For all cloud profiles, the DSD is given at each cloud level, so that all moments, i.e. microphysical quantities, can be explicitly calculated and be used for validation. To simulate typical uncertainties of remote sensing instruments, white noise can be added to the microphysical quantities.

4.2.1 Optimal Estimation Retrieval of N_d and q_L

Remote sensing applications have to deal with the problem of inversion to obtain microphysical properties from observations. As the number of observations is typically limited, a set of different atmospheric states might result in the same observations. If no additional observations are available to constrain the results, the combination of the observations and their covariances with a-priori information helps to limit the possible set of solutions (Rodgers, 2000). The OE approach is build upon these considerations. The OE method will search for the solution which is most likely, i.e. the solution that maximizes a Probability Density Function (PDF) P:

$$P = P_p \cdot P_o = \exp(\log P_p + \log P_o), \tag{4.1}$$

where P_p is the a-priori PDF and P_o is the PDF of the observations. The PDFs are described given

- an a-priori state vector $\vec{x_p}$ and its uncertainty $\vec{x_\epsilon}$,
- and an observation vector $\vec{y}$ and its uncertainty $\vec{y_\epsilon}$.

The uncertainties of the a-priori state and the observations need to be independent and Gaussian-distributed. Finding the most likely state from the combined PDFs (Eq. 4.1) can be achieved by minimizing their cost function $J(x)$:

$$J(x) = (\vec{x} - \vec{x_p})^T \, \mathbf{B}^{-1} \, (\vec{x} - \vec{x_p}) + (\vec{y} - \mathbf{K}\vec{x})^T \, \mathbf{R}^{-1} \, (\vec{y} - \mathbf{K}x), \tag{4.2}$$

with

- $\mathbf{B}$ being the a-priori error covariance matrix, with $\mathbf{B}_{ij,i=j} = x^2_{\epsilon,i}$,
- $\mathbf{R}$ being the observation error covariance matrix, with $\mathbf{R}_{ij,i=j} = y^2_{\epsilon,i}$,
- K being the forward model, that transforms the state vector ($\vec{x}$) into the observation space ($\vec{y}$): $\vec{y} = K\vec{x}$,
- and $\mathbf{K}$ being the Jacobian of the forward model.

The probability is maximized in terms of minimizing the cost function, so that an optimal state is retrieved, combining observations, a-priori and their error characteristics (Rodgers, 2000; Hewison, 2007):

$$0 = \nabla J = \mathbf{B}^{-1}\delta\vec{x_a} + \mathbf{K}^T\mathbf{R}^{-1}\mathbf{K}\delta\vec{x_a} - \mathbf{K}^T\mathbf{R}^{-1}\delta\vec{y}, \tag{4.3}$$

with the innovation $\delta\vec{y} = \vec{y} - K(\vec{x_p})$, and $\delta\vec{x_a} = \vec{x} - \vec{x_p}$.

Rewriting for the optimal state vector $\vec{x_a}$, results in:

$$\vec{x_a} = (\mathbf{B}^{-1} + \mathbf{K}^T\mathbf{R}^{-1}\mathbf{K})^{-1}\mathbf{K}^T\mathbf{R}^{-1}\delta\vec{y} + \vec{x_p}. \tag{4.4}$$

This equation is solved applying the Levenberg-Marquardt minimization method. It is described by the following iteration scheme:

$$\vec{x}_{i+1} = \vec{x_i} + \Big((1+\gamma)\mathbf{B}^{-1} + \mathbf{K}^T\mathbf{R}^{-1}\mathbf{K})\,(\mathbf{K}^T\mathbf{R}^{-1}(\vec{y} - K(\vec{x_i}) - \mathbf{B}^{-1}(\vec{x_i} - \vec{x_p})\Big)^{-1}. \tag{4.5}$$

The iteration starts with the a-priori state $\vec{x_i} = \vec{x_p}$ and is continued until $\vec{x_{i+1}} - \vec{x_i} < \epsilon$ with a defined threshold ϵ=0.01. If no convergence is reached, the iteration process is stopped after 30 cycles, no result is obtained and an invalid retrieval is reported.

The a-posterior error covariance matrix can be calculated after the successful iteration, and gives the resulting uncertainties of the retrieval:

$$\mathbf{S} = \left(\mathbf{K}^T\mathbf{R}^{-1}\mathbf{K} + \mathbf{B}^{-1}\right)^{-1}. \tag{4.6}$$

The degrees of freedom (DGF) of the signal express the pieces of independent information which are obtained from the observations:

$$DGF = \mathrm{tr}(\mathbf{X}), \tag{4.7}$$

with the averaging kernel X,

$$\mathbf{X} = \mathbf{S}\,(\mathbf{K}^T\,\mathbf{B}\,\mathbf{K}). \tag{4.8}$$

In this work, the OE method aims to retrieve N_d and q_L. For this work, the algorithm has been implemented utilizing the Python programming language.

The observation vector $\vec{y}$ contains the attenuation-corrected $Z(z)$ from the cloud radar, Q_L from the microwave radiometer, and τ, e.g., from a MFRSR:

$$\vec{y} = \left(Z(z), Q_L, \tau\right)^{\mathrm{T}}. \tag{4.9}$$

The state vector $\vec{x}$ contains the vertically constant N_d, and the natural logarithm of $q_L(z)$:

$$\vec{x} = \left(N_d, \ln\left(q_L(z)\right)\right)^{\mathrm{T}}. \tag{4.10}$$

The logarithm is applied to avoid the occurrence of unphysical negative liquid water content values in the minimization process, and because $\ln(q_L)$ is more closely following the assumption of a Gaussian distribution (Ebell et al., 2010).

The forward model K consists of three parts:

- the model for $Z(z)$ (Eq. 2.25),
- the model for Q_L: $Q_L = \int_{z_b}^{z_t}\, q_L(z)\; dz$, and
- the model for τ (Eq. 2.9).

The model for $Z(z)$ requires an assumption about the DSD. A Gamma-shaped DSD with ν=0.1 is assumed in the following.

The Jacobians are calculated numerically using finite forward differences:

$$\mathbf{K}(x) = \frac{\delta y_i}{\delta x_j} = \frac{F(x_i + dx_i) - F(x_i)}{dx_i}. \tag{4.11}$$

The a-priori state is defined as follows: $q_L(z)$ is set to the adiabatic profile scaled by the observed Q_L. N_d is set to the value retrieved with the B2010 radar-radiometer retrieval. This means that the OE method can be also interpreted as a post-processor on existing retrieval methods using additional observations as constraints.

It is assumed that no cross-correlations occur in the a-priori covariance matrix, implying both, no correlations of q_L uncertainties at different height levels, and no correlation between $q_L(z)$ and N_d. This yields a matrix with only diagonal elements. Cross-correlations in the observation error covariance matrix are also neglected. This assumption is rather simplistic, but until better knowledge it is a typical first guess for such OE methods (Ebell

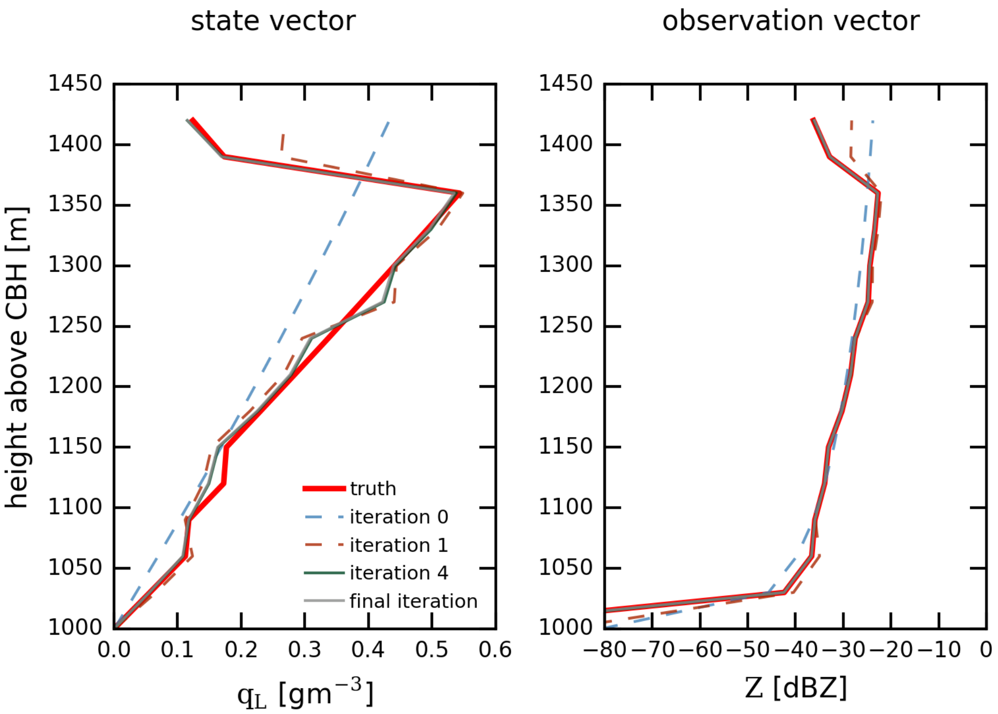

Figure 4.2: Profiles of state (q_L) and observation vector (Z) elements during different iteration steps of the OE retrieval as well as the truth value (red).

et al., 2010). The background variance for N_d is set according to the sensitivity study in Sect. 4.1, for which the largest relative uncertainty of 135% is found for the uncertainty in the width of the DSD. As in-situ observations typically show a deviation of q_L from the adiabatic profile in the uppermost cloud parts due to entrainment processes (e.g. Brenguier et al. (2000), compare our Fig. 3.1), an increasing background variance with height is assumed. For the lowest third of the cloud a q_L standard deviation of 30% is set, for the middle third 50% and for the uppermost third 70%. The observation error covariance matrix can be split into individual contributing parts such as forward model error, radiometric noise error, and representativeness error. Here, only the radiometric errors are considered. Radiometric errors are set to $\Delta Q_L = 25\,\mathrm{g\,m^{-2}}$, $\Delta Z = 15\%$, and $\Delta\tau = 5\%$ for MFRSR measurements (e.g., Madhavan et al., 2012).

The main aim of the OE approach is to obtain N_d with better accuracy and get an estimate of its uncertainty given background and observation uncertainties. In addition, the method also retrieves a q_L profile. The advantage over other methods (e.g., Frisch et al., 1998), is the inclusion of more observations and the combination with an a-priori state.

In Figs. 4.2 and 4.3, the iteration procedure is illustrated for an example profile. The initial iteration step equals the a-priori adiabatic condition. In the beginning of the iteration procedure, the cost function strongly decreases, in conjunction with a decrease of the differences between profile truth and the values in the state and observation vectors.

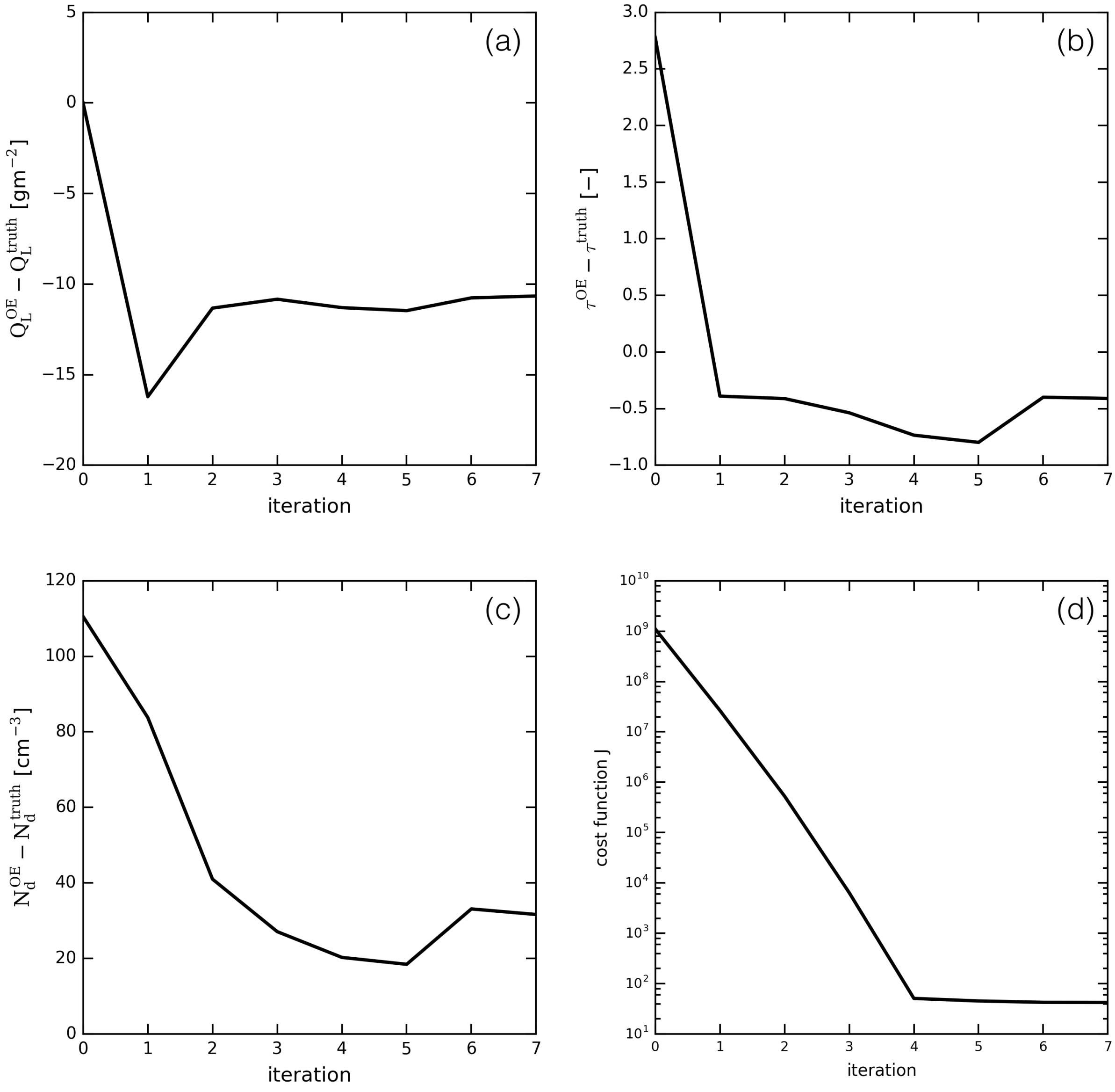

Figure 4.3: Integral values of the observation and state vectors as a function of iteration steps: (a) Q_L, (b) τ, (c) N_d; and (d) cost function J.

Towards the end of the iteration process, convergence of the cost function is reached and the iteration process is stopped. The reason that $Q_L^{truth} - Q_L^{OE}$ is close to zero at the beginning of the iteration process, is explained by taking the adiabatic scaled q_L profile as an a-priori. During the iteration some fluctuations can be seen for the individual quantities, as the procedure tries to find the optimal state for all quantities together. In the end, the difference of Q_L is slightly larger than for the a-priori. This is because the OE method accounts for uncertainties of the different quantities, and allows for an optimal state that must not exactly equal the observations.

4.2.2 Idealized and Synthetic Cloud Profiles

Idealized and synthetic cloud profiles are used to investigate the sensitivities and shortcomings of the OE retrieval and the more simple radar-radiometer approach. The advantage of using synthetic profiles is the full knowledge of the DSD at all cloud levels. A Gamma-shaped DSD is used as defined in Eq. 8.2. All microphysical quantities can then be calculated from the moments of the DSD. The retrieved values can thereby always be checked against the truth value. Three simplified cloud profiles are defined, as well as profiles are derived from the ICON Large Eddy Simulation (LES) model (Dipankar et al., 2015).

Idealized Cloud Profiles

The following simplified cloud profiles are defined:

- Profile (A): Vertically homogeneous cloud. This most simple case assumes a vertically homogeneous DSD, i.e., vertically constant microphysical properties. Such cloud profiles are for example assumed in retrieval algorithms for passive satellites.
- Profile (B): Adiabatically stratified cloud, as described by the adiabatic cloud model (Sect. 2.2). With q_L increasing with height, N_d and the width of the DSD are assumed constant with height, so that the average droplet radius is increasing with height.
- Profile (C): Subadiabatic homogeneous mixed cloud. This represents the most realistic of the three ideal profiles. Starting from profile B, mixing processes are assumed to reduce $q_L(z)$ especially in the upper cloud part, consistent with the observations of typical cloud profiles. For homogeneous mixing N_d is assumed constant with height. Thus, r_e is changed according to the reduced $q_L(z)$.

Cloud profiles (A), (B) and (C) (compare Fig. 4.4) have a cloud base at 1000 m and a geometrical depth of 450 m. The vertical resolution is set to 30 m, consistent with the Cloudnet resolution at the LACROS site. For profiles (B) and (C), r_e needs to be calculated for each cloud layer explicitly, given $q_L(z)$.

To simulate observations with remote sensing instruments, the observed quantities are first calculated from the given DSD. Afterwards random errors are added. The random errors are assumed of being normally distributed with an instrument specific standard

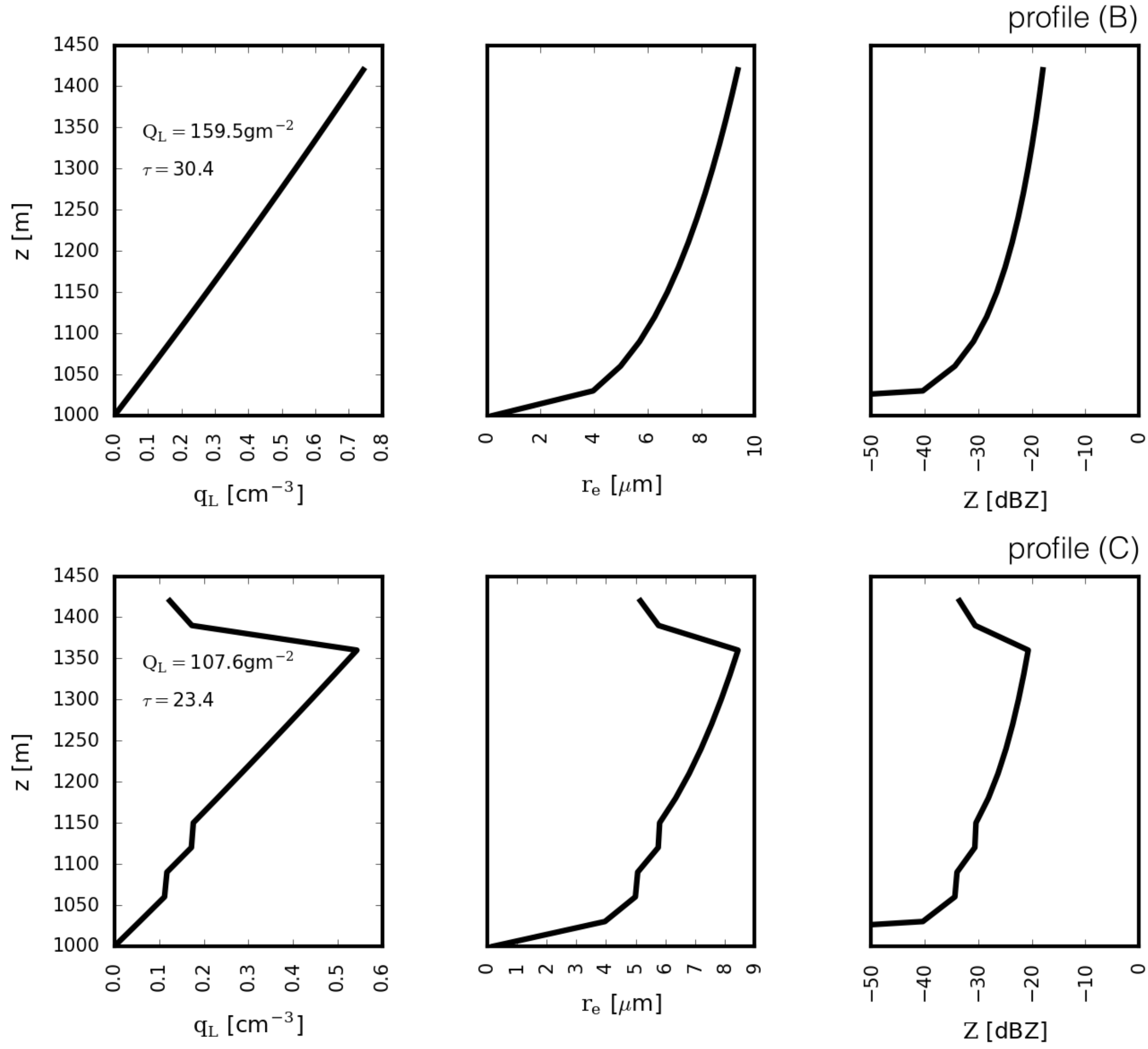

Figure 4.4: Synthetic cloud profiles (B) and (C) for a given Gamma DSD as described in the text. From left to right: q_L profile from cloud base to top, profile of effective radius r_e, and profile of radar reflectivity Z. The profiles are utilized in the OE sensitivity study. Profile (A) is not explicitly shown as all parameters are constant with height.

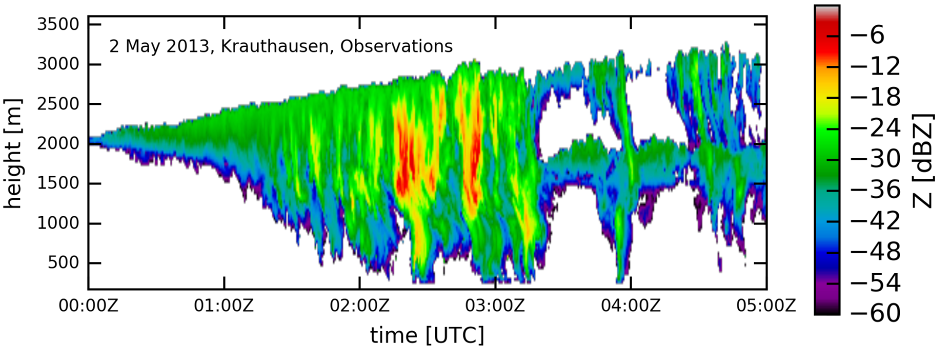

Figure 4.5: Time-height cross section of observed radar reflectivity Z for the 2 May 2013 at Krauthausen, between 01:00 UTC and 05:00 UTC.

deviation. For Q_L the standard deviation is $25\,\mathrm{g\,m^{-2}}$, for τ it is 5% and for $Z(z)$ it is 0.5 dB.

Synthetic Profiles From ICON Large Eddy Simulations

To use realistic cloud profiles, model simulations are applied from the high-resolved ICON LES model, which was developed during the HD(CP)^2 project. The ICON LES model uses a double-moment parameterization scheme to simulate cloud microphysics (Seifert and Beheng, 2005). The model outputs the zeroth moment (N_d) and the first moment (q_L) of the mass distribution of cloud droplets. For consistency and since the retrieval theory was described in terms of the DSD, the mass distribution is transformed into a DSD (see Appendix). Its moments can then be calculated consistently to the model simulations. Note that N_d can vary vertically in the model simulations (compare Fig. 4.6), but the width of the DSD is assumed constant.

In the following, a liquid cloud layer is considered that occurred at 2 May 2013 over Krauthausen from around 00:00 UTC to 05:00 UTC. The cloud was also observed with the LACROS instruments (Fig. 4.5). In contrast to the ICON simulations the LACROS observations showed a strongly drizzling cloud. The ICON model simulated only short periods of drizzle that occurred after periods of strong updrafts leading to q_L maxima near the cloud tops with values greater than $1\,\mathrm{g\,m^{-3}}$. In Fig. 4.6 the time-height cross-sections of the original ICON moments (N_d and q_L) is shown. Profiles of r_e and Z reconstructed from the DSD moments are presented in Fig. 4.7.

At a vertical depth of 20–80% within the clouds the average N_d profile is roughly constant with mean values around $350\,\mathrm{cm^{-3}}$ (Fig. 4.8), while the vertical distribution of N_d within individual profiles can be quite variable (Fig. 4.6). Many remote sensing retrievals assume homogeneous mixing. Therefore, the ICON simulations are a suitable testbed to study the retrieval accuracy for such a simplified assumption. The q_L profiles show on average a nearly linear increase within the cloud and a sharp decrease at cloud top (Fig. 4.8), consistent with observations from remote sensing and in-situ. The mean normalized ICON profile is considered as sample profile (D).

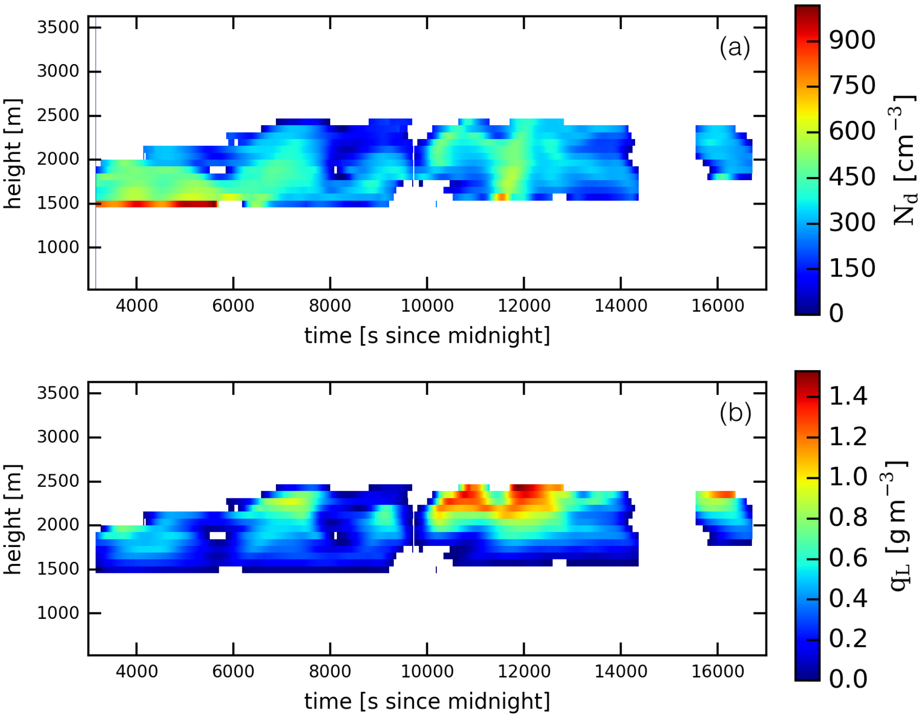

Figure 4.6: Time-height cross section of ICON-simulated moments: (a) N_d and (b) q_L for 2 May 2013 from around 01:00 UTC to 05:00 UTC.

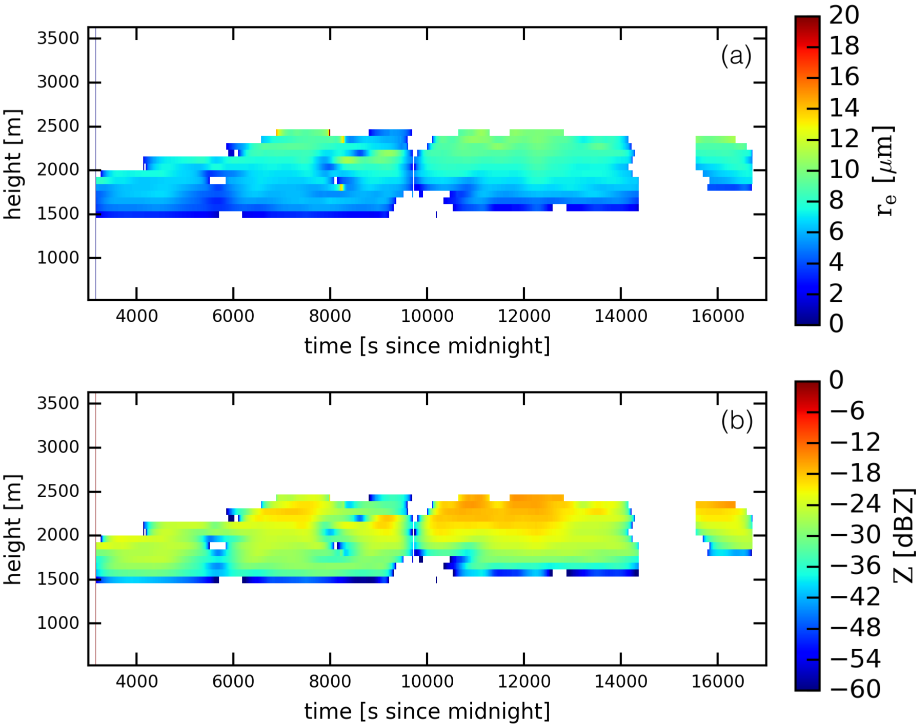

Figure 4.7: Time-height cross section of derived microphysical properties from ICON: (a) effective radius r_e, and (b) radar reflectivity Z.

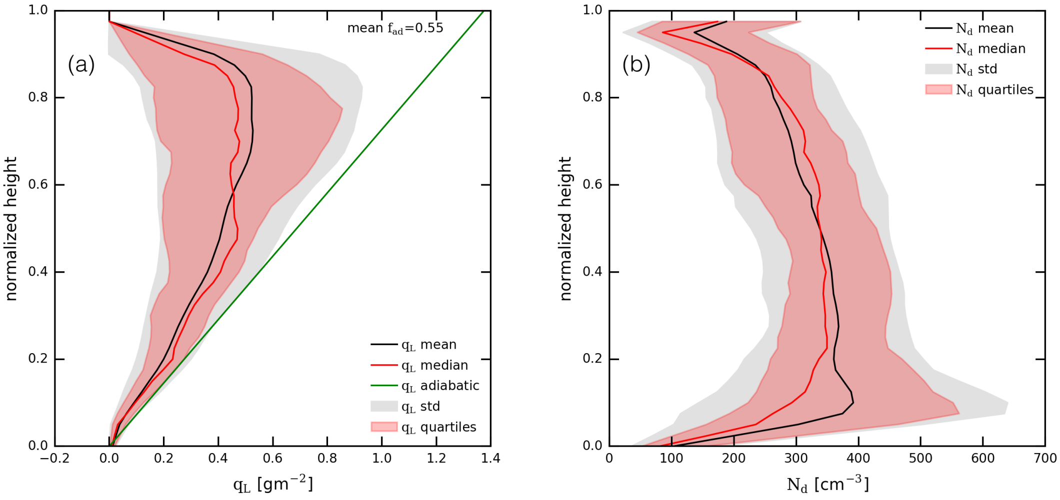

Figure 4.8: ICON-simulated mean q_L and N_d profiles averaged over the time period as shown in Fig. 4.6. The height coordinate was normalized from the CBH to the CTH. The black solid line represents the mean, the gray shaded area the standard deviation, the red solid line the median and the red shaded area the interquartile range. The green solid line in (a) depicts the mean adiabatic q_L profile.

4.2.3 Sensitivity of the OE Retrieval Method

The idealized and synthetic profiles (A)–(D) are used to study the sensitivities of the OE retrieval method to the influence of the assumption about the DSD and its width in particular, the mixing assumption, the given observation and a-priori errors. In addition, the information content of τ on the retrieval result as well as its dependence on the a-priori state will be investigated.

Influence of the DSD Assumption

The available observations used in this work provide no direct information about the DSD. A Gamma DSD and a typical value of the effective variance ν is hence chosen for the retrieval process. In this section, it will be investigated how this assumption influences the retrieval results.

The DSD of the idealized and synthetic cloud profiles are also described by a Gamma distribution. For the synthetic profiles, the retrieval error of N_d is shown in Figs. 4.9 and 4.10 as a function of ν which is assumed in the retrieval. The range of ν is motivated from typical values for continental stratocumulus clouds as listed in Table 2 in Miles et al. (2000) (note the different symbols used to define the DSD). Adding random instrumental observation errors, 20 repetitions of the retrieval process are conducted to obtain the mean and standard deviation for each ν. Three different values for N_d are set in the synthetic cloud profiles, covering a representative range for continental stratocumulus clouds ($50\,\mathrm{cm}^{-3}$, $300\,\mathrm{cm}^{-3}$, $1500\,\mathrm{cm}^{-3}$).

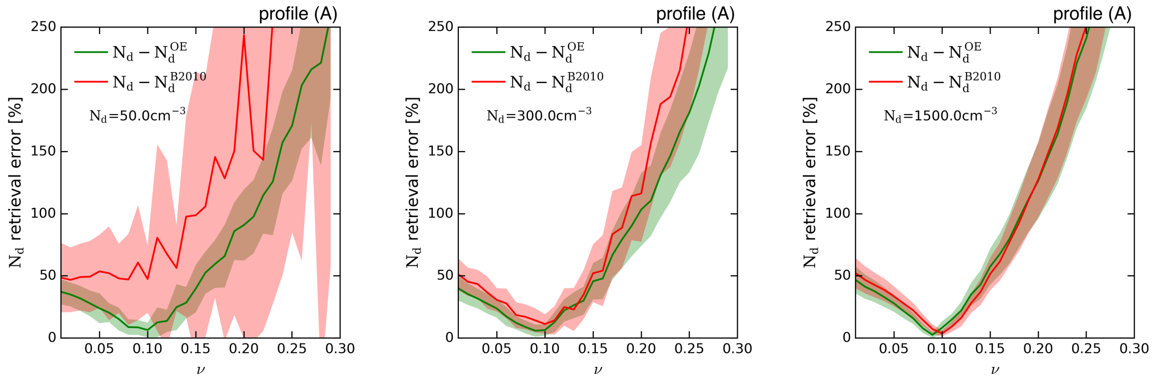

Figure 4.9: Relative deviation [%] of the retrieved from the synthetic N_d as a function of ν chosen in the retrieval. The deviation of N_d of the OE method from the truth value is shown in green, the deviation of the a-priori B2010 radar-radiometer N_d from the truth is shown in red. 20 runs with randomly added instrument observation uncertainties were performed. The solid line refers to the mean, while the shaded area represents one standard deviation about this mean. The first column shows the results for N_d=50 cm^{-3}, the middle column for N_d=300 cm^{-3} and the right column for N_d=1500 cm^{-3}. Results are for profile (A).

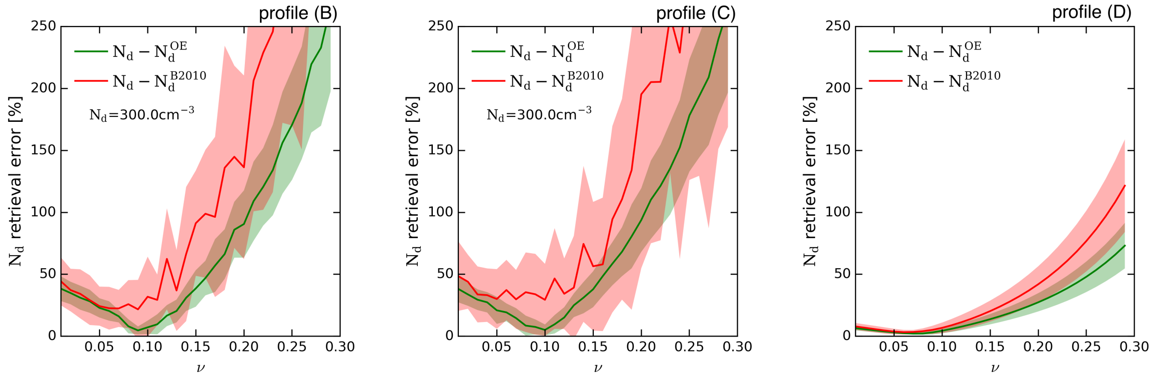

Figure 4.10: Same illustration as in Fig. 4.9 for N_d=300 cm^{-3}, but for profile (B), (C) and (D). The N_d retrieval error for profile (D) represents the mean error over the full vertical profile.

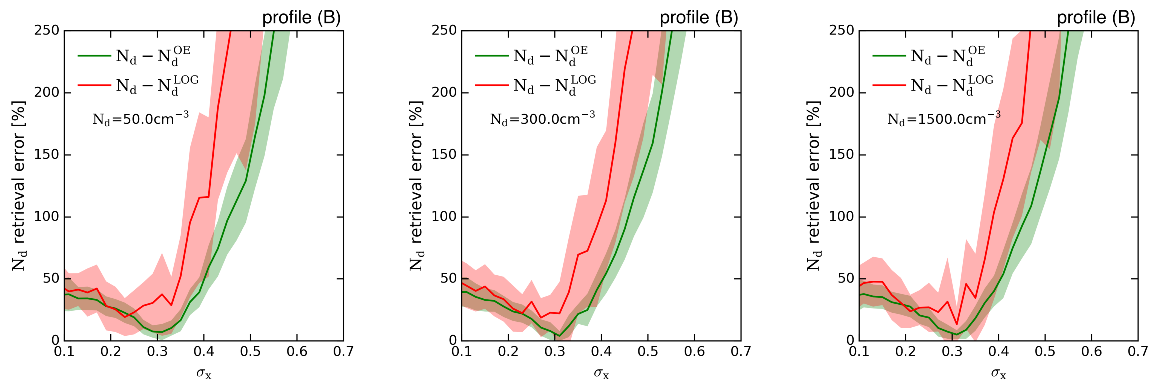

Figure 4.11: Same illustration as in Fig. 4.9, but the synthetic DSD is assumed to follow a log-normal shape with varying parameter σ_x. The retrieval is performed for profile (B) assuming a Gamma distribution with ν=0.1.

For profiles (A)–(C), the accuracy of the retrieval is explored by varying ν in the retrieval and keeping $\nu = 0.1$ in the synthetic cloud profiles. For both retrieval methods (OE and B2010) and all profiles, the smallest deviation of N_d is found close to the value assumed in the retrieval algorithm. Independent of the assumed cloud profile, the relative deviation of N_d increases with larger difference between ν set in the profile and the one assumed in the retrieval. For all these profiles, the OE method gives overall smaller N_d retrieval errors compared to the B2010 method for the full range of ν. For profile (A) and larger N_d the N_d retrieval errors of both methods are close, likely explained by the a-priori within the OE method, which does not represent homogeneous conditions for q_L as given by profile (A). For the cloud profiles (B) and (C) the relative deviation of the B2010 retrieval is about 25% for $\nu = 0.05$ and about 250% for $\nu = 0.25$. For the OE method, the relative deviations are about 25% and 150%, respectively. Therefore, the larger differences between both retrieval methods are found for large ν values. The mean behavior for profiles (B) and (C) is rather independent of N_d and therefore only the situation for N_d =300 cm^{-3} is shown in Fig. 4.10. The smaller standard deviation of the OE method suggests the retrieval to being more stable in case of observation errors compared to the B2010 radar-radiometer approach.

Both retrievals yield vertically constant N_d. For profile (D), N_d is variable with height. Therefore, the N_d retrieval error of each vertical level is calculated and the mean over the errors of all levels of each profile is considered.

One can also investigate the effect of assuming a log-normal DSD in the retrieval while a Gamma DSD is set for the cloud profiles. This scenario might yield as an illustration for problems in real case conditions when the DSD does not follow the conditions assumed by the retrieval. The range of values for σ_x is based on Table 2 in Miles et al. (2000) (continental stratocumulus clouds). Again a vertically constant value of $\nu = 0.1$ for the Gamma DSD of the synthetic cloud profiles is assumed. In Fig. 4.11 the results for the adiabatic profile (B) are presented. The relative deviation of N_d between both retrieval approaches is rather independent of the magnitude of the synthetic N_d. The minimum deviation of N_d is found for σ_x around 0.3. The difference between both retrieval methods is largest for large values of σ_x and becomes small for small values of σ_x. For large σ_x values the OE retrieval is clearly superior to the B2010 retrieval method assuming the

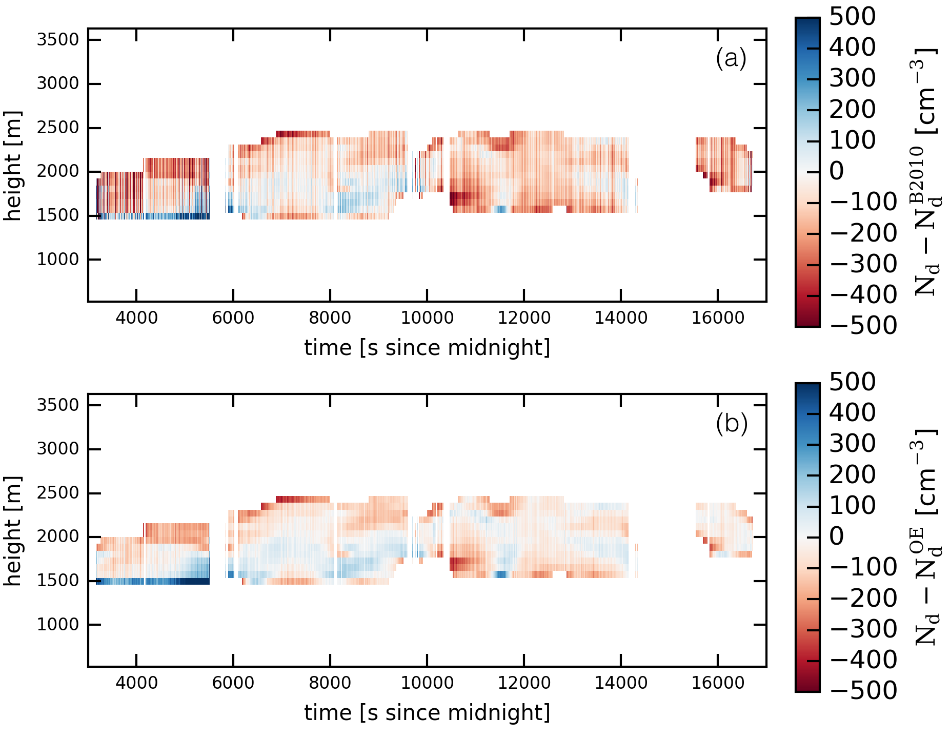

Figure 4.12: Difference of the reference ICON N_d and (a) the B2010 retrieved N_d, (b) the OE N_d.

log-normal DSD. As the OE method is as good as the radar-radiometer approach also for $\sigma_x < 0.35$, the OE method seems to give overall more accurate results.

Influence of Vertically Varying Cloud Droplet Number Concentration

The effect of mixing processes on the vertical structure of N_d is not yet well understood. For this work, the aim is to adopt a realistic mixing scenario using ICON LES profiles. In these simulations the width of the DSD is assumed to be unchanged, but N_d varies with height. This refers to the extreme inhomogeneous mixing assumption (Baker et al., 1980), as outlined also in Sect. 2.2. In this way, the ICON LES profiles enable the investigation of the effect of the simplified assumption of homogeneous mixing on the retrieval results.

We conducted sensitivity tests to find the optimal ν for the retrieval process (Fig. 4.10). The smallest difference of the ICON N_d and the retrieved N_d is obtained for ν of 0.07. This value is used in both retrieval schemes (OE and radar-radiometer). In Fig. 4.12, the resulting difference between the retrieved N_d and ICON LES N_d is shown for the full time-height cross-section. Overall, differences are smaller utilizing the OE method with the mean difference over all profiles of $-33\,\mathrm{cm}^{-3}$ compared to $-96\,\mathrm{cm}^{-3}$ utilizing the B2010 method. This can be seen also from Fig. 4.13, where the histogram of the vertical average of all profiles is depicted. The OE method peaks at smaller N_d differences and shows a more narrow distribution. To conclude, in case of inhomogeneous mixing the OE approach is more accurate than the B2010 retrieval.

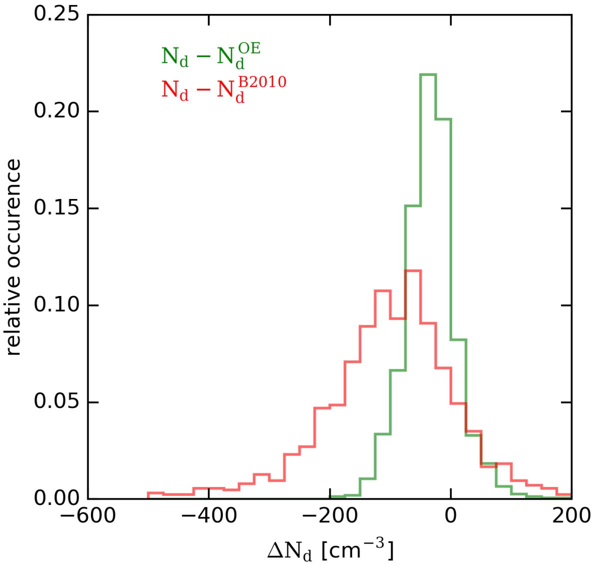

Figure 4.13: Histogram of the difference of the reference ICON N_d and the B2010 retrieved N_d (red), and the OE N_d (green). The mean differences of each profile are considered.

Sensitivity to A-Priori Errors

The OE technique is known to strongly rely on an accurate choice of uncertainty estimates. To investigate the sensitivity of the retrieval to the a-priori error, two benchmarks are used, similar to the study of Ebell et al. (2010): the DGF and the relative a-posteriori N_d error. The latter is defined as the standard deviation of N_d after the successful iteration of the OE method, normalized with the retrieved N_d. The standard deviation is obtained from the a-posterior error covariance matrix $\mathbf{S}$. The DGF are normalized with respect to the length of the state vector for better comparability between different profiles.

The sensitivity study is done for profile (B) with $N_d = 300\,\text{cm}^{-3}$ and for profile (D). $\nu = 0.1$ is assumed in the retrieval process, i.e., the retrieval describes the width of the DSD correctly for profile (B), but not for profile (D). No additional noise is added to the observations. This makes the interpretation of sensitivities easier since disturbance factors can be ignored.

In Fig. 4.14 the DGF and the relative N_d a-posteriori error are presented for increasing a-priori errors (diagonal elements of $\mathbf{B}$). The a-priori error of q_L is changed while the a-priori error of N_d is kept constant, and vice versa. As the a-priori errors of q_L and N_d increase, both, the relative N_d a-posteriori error and the DGF increase. The N_d a-posteriori error depends more strongly on the given a-priori N_d error. If the a-priori error for N_d is close to zero the a-posteriori error is close to zero as well, since in this case the a-priori state would already be an optimal solution and the retrieval procedure would not be required. At around 100% N_d a-priori error the a-posteriori error converges to a maximum value. This is close to the a-priori error which is set due to the unknown width of the DSD (135%). The increase of DGF is strongest in the range of 2% to 100% a-priori errors, similarly for N_d and q_L a-priori errors. The larger number of DGF as the

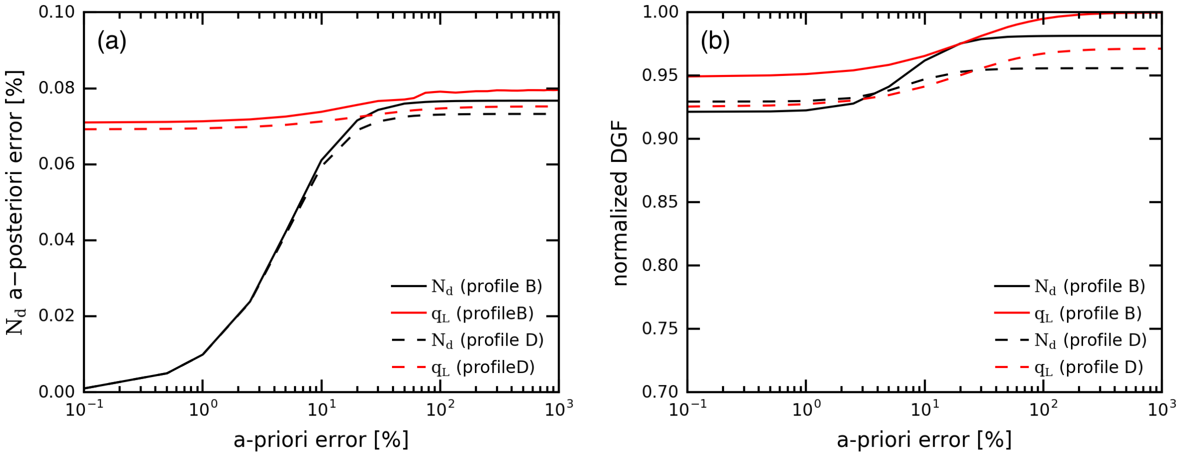

Figure 4.14: (a) Relative a-posteriori error of N_d in percent, (b) DGF normalized by the length of the observation vector as a function of a-priori error. Results are presented for profile B (solid line) with N_d=300 cm^{-3} and profile D (dashed line). In the retrieval a Gamma DSD with $\nu = 0.1$ is assumed.

a-priori error is increased implies that the observations gain more weight, and therefore, have a stronger influence on the retrieval result.

To summarize, the less accurately the a-priori can be described (the higher its uncertainties) in comparison to the observations, the more weight is put to the observations in the OE retrieval process.

Sensitivity to Observation Errors

The sensitivity of the DGF and the relative N_d a-posteriori uncertainty to the observation uncertainties is also investigated.

The experiments are applied as before, i.e., the observation error is changed for each quantity individually, while the other errors are kept constant (values as described in Sect. 4.2.1). By increasing the observation error, the N_d a-posteriori uncertainty increases and the DGF are reduced (Fig. 4.15). The reduction of the DGF can be understood as less information is gained from the observations due to their larger errors. The largest change in the DGF occurs for varying the error in Z. The normalized DGF drastically decrease from 1 to 0 if the observation error in Z (in mm^6 m^{-3}) is increased from 10% to 200%. This shows the importance of a correct calibration and attenuation correction of the cloud radar for this retrieval approach. In contrast, only a small sensitivity of the DGF is obtained to the integral quantities τ and Q_L.

Increasing τ observation error in the range of 1% to 10% has a strong effect on the relative N_d a-posteriori error. Given the errors of the other observation quantities, the retrieval error of N_d saturates for errors in τ larger than 20%. In this case, the N_d error is still reduced from an a-priori error of 135 % to around 20%. In case no observation of τ from ground-based observations is available, one can consider taking τ from passive satellites. For the latter, a 10% uncertainty can be assumed for homogeneous conditions under

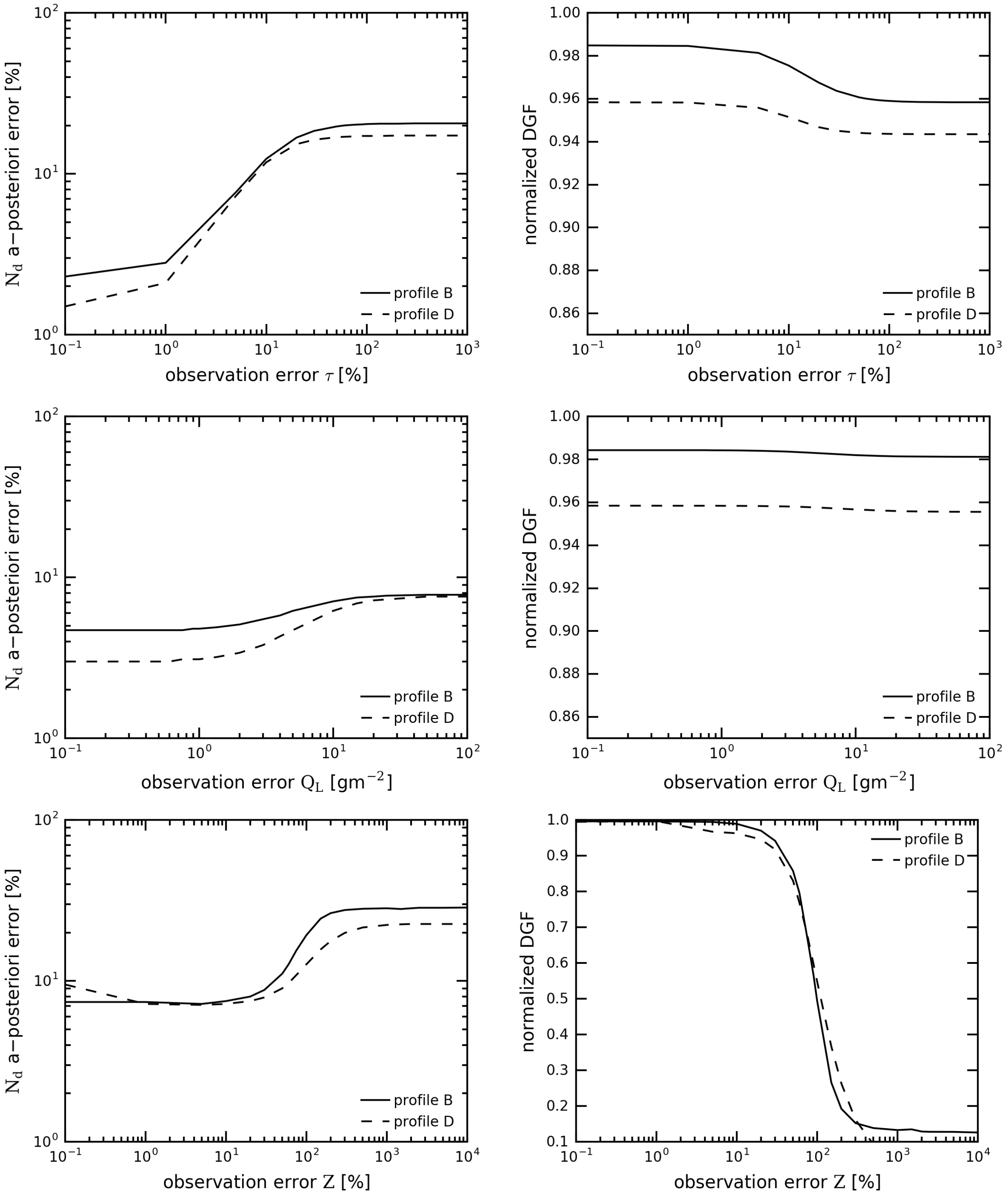

Figure 4.15: Left column: relative N_d a-posteriori error (in %), right column: normalized DGF as a function of observation errors. Note that the axes can be different between individual plots. τ and Z (processed in $\mathrm{mm^6\,m^{-3}}$) errors are given in percent, Q_L errors in $\mathrm{g\,m^{-2}}$.

favorable viewing conditions (Roebeling et al., 2008a). Due to collocation issues and a lower spatial resolution the uncertainty would usually be larger. Given the results of the sensitivity study, τ from SEVIRI might still be able to add constraints to the retrieval if no ground-based observations of τ are available. If the accuracy of Q_L observations could be improved from $20\,\mathrm{g\,m^{-2}}$ to $1\,\mathrm{g\,m^{-2}}$, and keeping the errors of the other observations constant, the relative N_d a-posteriori error is reduced from 8% to 5% for profile (B). While these error values are low, they reflect only the given errors of the a-priori and observations within the OE approach. It does not take into account uncertainties due to the assumption of the width of the DSD, which is able to result in larger deviations of N_d as shown in Sect. 4.2.3.

To summarize, the information gain from the different observations for the retrieved N_d depends on the observation errors. For the retrieval of N_d the accuracy of τ turns out to be quite important (Fig. 4.15), and the vertically resolved measurements of Z add the most information for the retrieval of the q_L profile (Fig. 4.15). The latter is reflected in the strong sensitivity of the DGF to the observation error in Z.

Information Content of Optical Depth Observations

In the following, the OE method is applied with and without τ as an element in the observation vector. Comparing the retrieval results for both options, gives information on the importance of τ observations. For the experiment, cloud profiles (B) and (D) are considered, assuming a Gamma DSD with ν=0.1. The observation uncertainty of τ is assumed to be 5%.

For profile (B), the DGF increases from 15.34 to 15.71 adding observations of τ, and the relative N_d a-posteriori error decreases from 28% to 6%. For profile (D) the results are similar, with an increase of DGF from 33.02 to 33.45 and a decrease of the relative N_d a-posteriori error from 15% to 7%. This shows that adding τ observations improves the retrieval of N_d. If the uncertainty of τ is considered to be 25%, there is only a very small information gain. In this case the N_d a-posteriori error would be 14% for profile (B) and 17.5% for profile (D).

Adding τ observations also reduces the relative a-posteriori error of the q_L profile. The mean a-posteriori error over the full profile decreases from 14% to 10% for profile (B), and from 17% to 15% for profile (D). The a-posteriori error of q_L is generally smaller than for N_d. The decrease in the a-posteriori error by adding τ is smaller compared to N_d. This can be explained as τ provides an integral value over the full cloud column, and a good constraint on q_L is already available from the column liquid water path Q_L. The vertically resolved information required for the q_L profile comes from Z, and τ does not add constraints on the profile shape. For an observation error of τ of 25%, the information gain is quite small with resulting a-posteriori errors of 13% and 16.5% for profile (B) and (D), respectively. This shows the importance of providing observations with good accuracy to be able to reduce the uncertainty of retrieved quantities.

Dependence on the A-Priori State

The a-priori in the OE approach is described with an adiabatic q_L profile, scaled by the observed Q_L. As can be seen from the observations in Fig. 3.1, realistic cloud profiles possess a sharp decrease of q_L near the cloud top due to entrainment. The effect of taking such a profile shape as an a-priori is explored. This is done applying profile (D), since the ICON LES profiles are considered to represent realistic clouds.

The clouds in the ICON LES simulation have a geometrical depth between 500 and 1000 m. The mean profile for the comparable height class from Fig. 3.1c is considered as an a-priori. The according a-priori error is obtained from the standard deviation of the profile.

The effect of the different a-priori state is seen mainly in the lower q_L a-posteriori error. Using the observed mean q_L profile as an a-priori, the relative q_L a-posteriori error is reduced from 15% to 9%.

In conclusion, a more accurate description of the a-priori from available observations in the OE approach is desirable and expected to be useful for realistic cloud profiles. The a-priori can be set according to different classes of geometrical depth, since the cloud adiabaticity depends mostly on this parameter (see Chapter 3). Assuming that the ICON LES model realistically represents the statistics of cloud profiles, the model results can also be considered as a source for the a-priori state. Validation against observations within the HD(CP)^2 project (Heinze et al., 2016) is a crucial step for this.

4.3 Discussions and Conclusions

Given the uncertainty of the radar-radiometer approach to retrieve N_d, an Optimal Estimation technique was developed, including additional constraints from τ observations. These could be obtained, e.g., from 2NFOV or MFRSR measurements, but also from passive satellite observations. A sensitivity study was conducted to investigate the influence of the assumption about the width of the DSD, homogeneous mixing, a-priori errors and observations errors on the retrieval results. Synthetic profiles have been constructed, which have the advantage that the DSD is given with accurate knowledge and the microphysical properties are available for validation. Idealized cloud profiles (homogeneous, adiabatic, homogeneous mixing) as well as more complex synthetic profiles from ICON LES have been applied in the sensitivity study.

One of the major advantages of the OE framework is that it can easily be extended for additional observations. Our approach can be applied as a post-processing utilizing additional observations such as τ to existing radar-radiometer retrievals such as the one of B2010.

The assumption about the width of the DSD remains a large uncertainty source in the OE approach. Uncertainties of about 150% can occur for N_d retrieved with OE if $\nu = 0.25$ instead of $\nu = 0.1$ is assumed in the retrieval process. Uncertainties are even larger for the B2010 approach with up to 200% in this case. It is therefore important to better constrain the width of the DSD by additional observations in a next step. A possible observation could be the Doppler velocity (e.g., Kato et al., 2001; Rémillard et al., 2013). Not assuming a fixed width but instead add relationships between the different DSD moments as a-priori taken from LES or in-situ observations following the method of McFarlane et al. (2002) could be promising, too.

By adding τ observations with sufficiently small uncertainties, the resulting relative N_d error can be reduced by about 10 to 20 percentage points. For the retrieval of the q_L profile the observations of Z are very important since the radar is the only instrument providing vertically resolved information. As N_d is assumed vertically constant, also column integrated quantities are of great interest for better constraints.

Overall, we conclude that the OE approach yields promising results towards a more accurate retrieval of N_d as shown for synthetic cloud profiles. For realistic profiles simulated with ICON LES, the OE retrieval is advantageous over the B2010 approach. Currently, the adiabatic assumption is used as an a-priori in the OE scheme. It can be easily exchanged with more realistic, subadiabatic cloud profiles, e.g., from ICON LES statistics or observational climatologies. For further validation, real-case scenarios with ground-based remote sensing observations and in-situ data are required. While the OE method has been tested for suitable conditions, in real clouds, e.g., drizzle can lead to a multi-modal or more skewed DSD, which leads to further uncertainties as the retrieval assumptions are violated.

Generally, also the direct use of the radiative quantities observed from remote sensing instruments instead of retrieved microphysical quantities can be considered, although this approach adds a lot of implementation complexity and has to deal with enhanced computation costs for the application of more complex forward models (as those have to be called multiple times for each iteration step). Considering cloud products from tested algorithms which can also provide reliable uncertainties such as from Cloudnet, is more convenient and more easily implemented in current retrieval schemes.

5 Contrasting Cloud Properties From Satellite and Ground Perspectives

ACI studies are available for a wide range of spatio-temporal scales, leading to large differences in the obtained ACI metrics (compare Fig. 1.3 in Chapter 1). Therefore, it is important to check for consistency of the cloud key properties from different perspectives. In this section a statistical comparison of satellite and ground-perspective is conducted, and uncertainties of the satellite-retrieved products are discussed. For that data from SEVIRI and Cloudnet are used. In Chapter 6, in-situ data are compared with ground-based retrieval data for a case study.

Several cloud properties are important for ACI investigations from passive satellite observations. Aerosols alter cloud properties such as N_d, and consequently τ and cloud albedo, while τ is influenced also by dynamical processes. Twomey considered Q_L to be kept constant to account for the same dynamical conditions, but also H might differ for subadiabatic clouds. Therefore, N_d, Q_L, τ and H turn out be key parameters for ACI studies.

Janssen et al. (2011) emphasize the need of validating satellite-retrieved N_d using in-situ observations. N_d is also retrieved from ground-based radar-radiometer approaches, but as shown in Chapter 4 the retrieval of N_d remains highly uncertain due to the required assumptions about the DSD. Hence, Brandau et al. (2010) aimed to retrieve τ instead of N_d, as τ is less sensitive to the required assumption about the width of the DSD. τ is also used for ACI studies, but implicitly depends on Q_L, while N_d is usually considered to be more directly influenced by CCNs. In this thesis, τ is used as an alternative for comparisons between the satellite and ground perspective, given the high uncertainty of ground-retrieved N_d. A longer-term retrieval of N_d with the OE method is not yet applied due to missing observations of τ within the Cloudnet dataset.

H can be estimated from passive satellites with the sub-adiabatic cloud model, but f_{ad} is usually unknown. The combination of CBH from a ceilometer network and the CTH from passive satellites may give an alternative opportunity to obtain H. With additionally obtained Q_L from passive satellites, f_{ad} can be calculated. The question whether Q_L and CTH from passive satellites are accurate enough to estimate f_{ad} is still unclear and is addressed in this Chapter.

5.1 Sampling Method

Liquid clouds for the time period 2012–2014 are investigated, for which products from SEVIRI and Cloudnet are available. Data sampling is mainly done using filters for the satellite data. An area of 5x5 pixels (total of 25 pixels) is considered for each available SEVIRI observation. The latter area is centered on the location of the ground site. For this field the average and standard deviation of CTH, and the liquid cloud fraction are calculated. The liquid fraction is determined from the cloud type classification using the KNMI-CPP data. About 90% (23 out of 25) pixels need to be classified as liquid clouds. In addition, the standard deviation of CTH for the 25 pixels is required to be smaller than 400 m. Cloudnet observations are averaged over 10 min around the SEVIRI observation time. In case 10% of the ground-based profiles (10 min averaging window) are contaminated by ice clouds, the data points are also excluded. This procedure should remove most remaining cases of thin ice clouds not detected by SEVIRI. Data from the Cloudnet stations in Leipzig, Juelich, Lindenberg and Mace-Head are used. The data from Chilbolton is omitted since an insufficient number of collocated observations with SEVIRI were obtained.

5.2 Cloud Top Height

The CTH can be compared between passive satellite and ground-based observations at day- and nighttime. The actual geometrical CTH is inferred from the cloud radar (see Sect. 2.5.2), while from passive satellites a radiative CTH is obtained. The SEVIRI CTH is found positively biased for all the Cloudnet stations (Fig. 5.1). The bias is obtained over the full range of CTHs, but deviations are largest for CTH $>$ 4000 m (Fig. 5.1f). This cannot be explained by the physical difference between geometrical and radiative CTH. The bias for all Cloudnet stations is 492 m (in the range of 476 m to 499 m for individual stations) with a standard deviation of 562 m (480 m to 603 m) and a RMSD of 747 m. Derrien et al. (2005) report a slightly lower overestimation (320 m) but an even larger standard deviation of 1030 m for low, opaque clouds. Hamann et al. (2014) report an overestimation in the order of 500 m with an RMSD of about 1100 m for some CTH retrieval algorithms. Considering the field's central pixel instead of the field average, results are not significantly altered, showing that the cloud fields are rather homogeneous and should therefore be suitable for such comparisons. The observed bias is not explained by the limited vertical step size (200 m) in the NWC SAF CTH product. It might be attributed to the representation of inversions by NWP model data. In this study, the NWC SAF products utilize ECMWF global forecast model data interpolated on specific pressure levels. This results in a reduced vertical resolution of the data. It is also possible that the model has problems to correctly represent inversions and a regional model may be better suited. An overestimation of CTH due to low-level inversions has been also reported for MODIS Collection 5 products (Holz et al., 2008). It is known that the conversion from cloud top temperature to CTH causes problems especially in case of such inversions (Holz et al., 2008; Hamann et al., 2014).

In comparison, the RMSD of the CTT is 3 K. If considering the dry adiabatic lapse rate as rough estimate this would represent a CTH difference of around 300 m, only half of the CTH RMSD. The RMSD of the CTP is 90 hPa and is therefore equivalent to the found CTH deviation.

In Fig. 5.2 three cases with positively biased NWC SAF CTH compared to Cloudnet

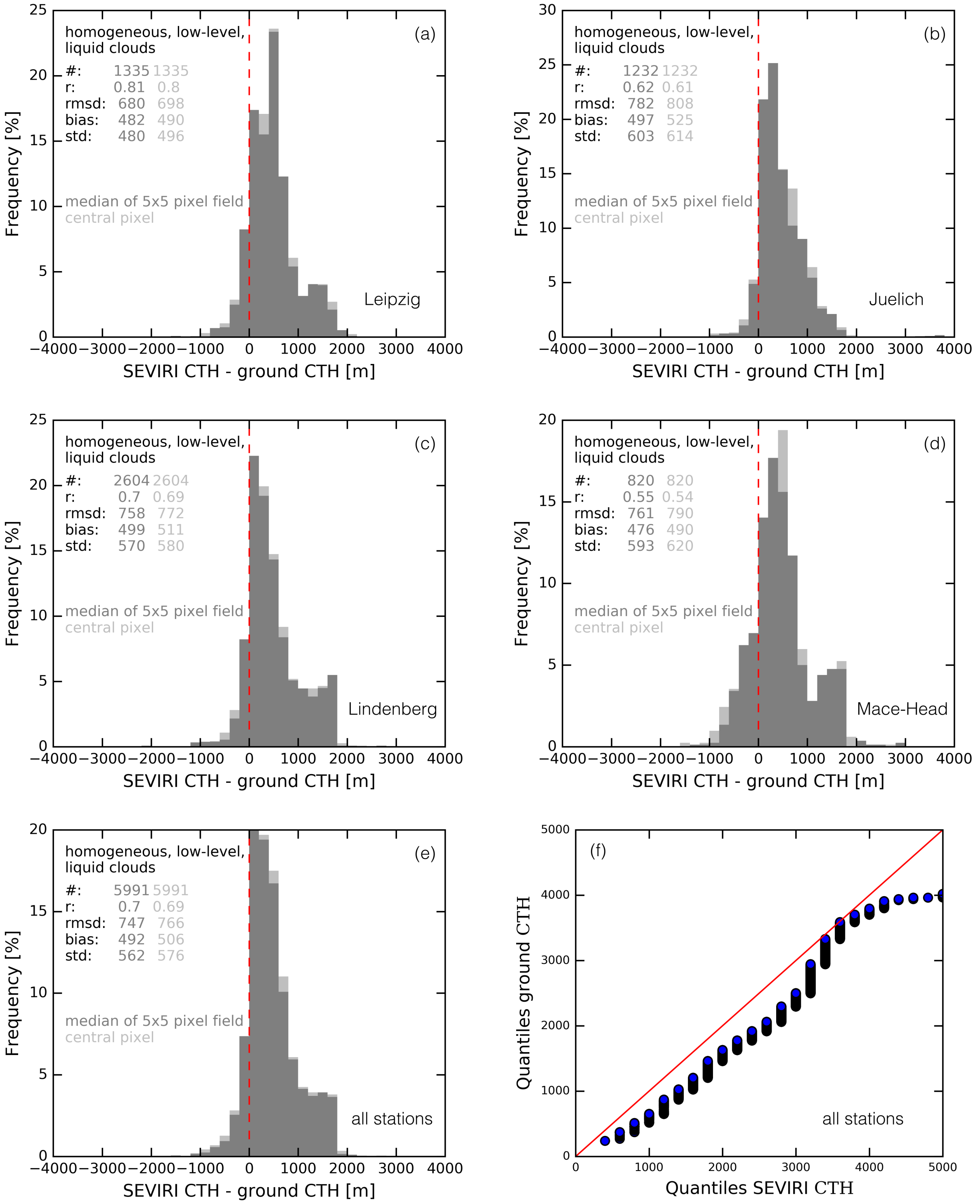

Figure 5.1: Histogram of CTH differences derived from SEVIRI and ground-based (2012–2014) for different Cloudnet stations: (a) Leipzig, (b) Juelich, (c) Lindenberg, (d) Mace Head, (e) stations a–d combined. Median of 5 x 5 SEVIRI pixels centered at the ground site (dark gray), and the closest pixel to the ground site (light gray). Zero difference is marked by a dashed red line. (f) QQ-Plot showing the quantiles of SEVIRI and ground-based CTH.

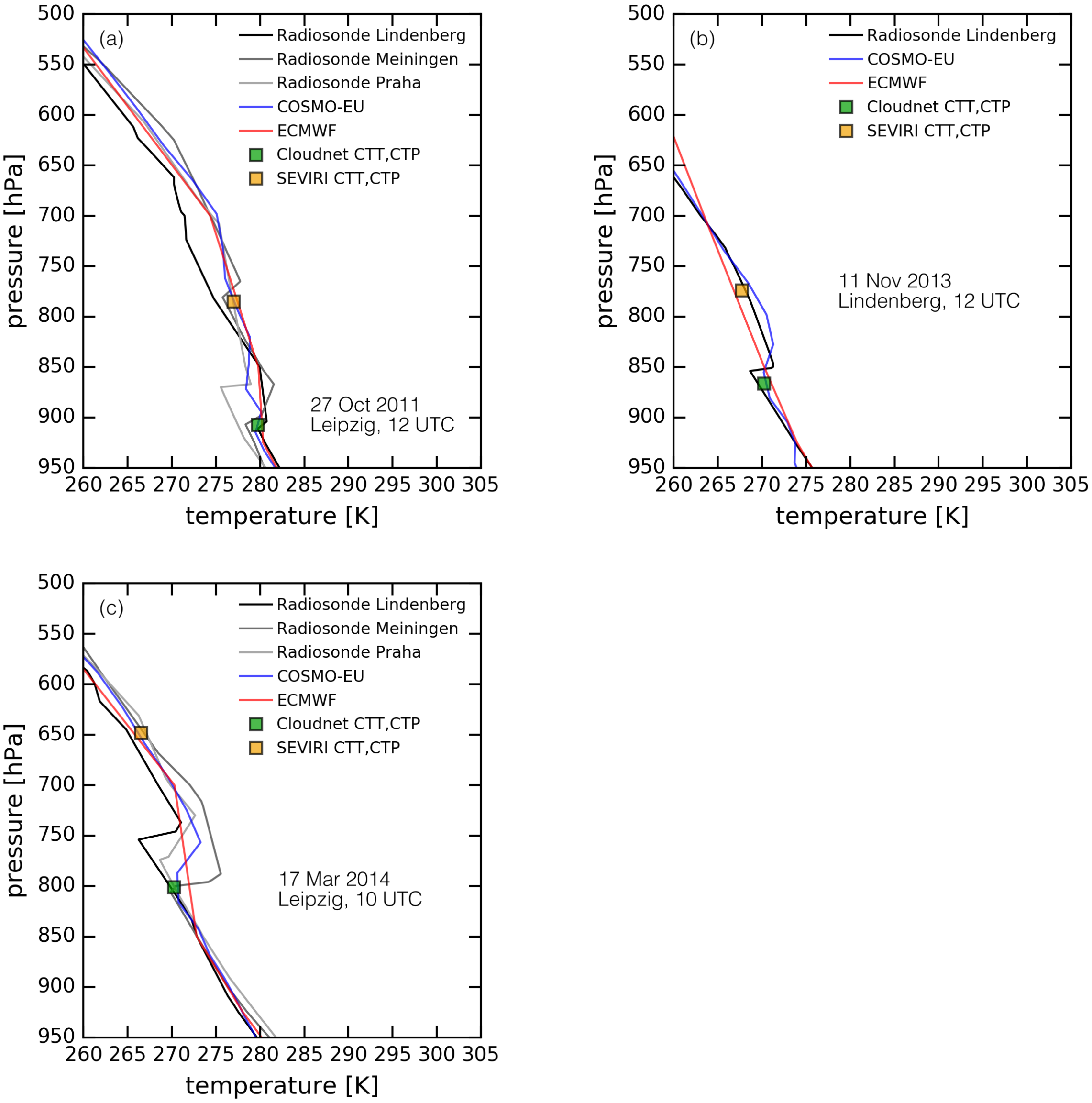

Figure 5.2: Illustration of the problematic representation of inversions, leading to a bias in the CTH, comparing NWC SAF and Cloudnet. For 3 cases, the temperature profile is shown as a function of pressure for ECMWF NWP data (used for NWC SAF, red line), for COSMO-EU (used for Cloudnet, blue line) and the closest radiosonde profiles from 12 UTC (gray lines). The CTP and CTT from NWC SAF (orange square) and Cloudnet (green square) are also shown.

CTH are shown. It can be seen that the occurrence of inversions is better represented by COSMO-EU as compared to interpolated ECMWF data used in the current products. Substantial differences to the Lindenberg radiosonde profile can be found. For the cases in Leipzig, this may be partially explained by the spatial distance of the stations (around 200 km).

Meerkötter and Zinner (2007) applied CTH and Q_L from AVHRR (Advanced Very High Resolution Radiometer) to compare the spatially and temporally averaged satellite CBH with ceilometer CBH. They reported a standard deviation of about 369 m, assuming adiabatic clouds. They also compared SEVIRI and radiosonde observations and resulted in a standard deviation of 290 m (Meerkötter and Bugliaro, 2009). They suggest that this method can be applied for convective clouds in their early growth stage. Their sample is focused on relatively thin water clouds (H in the order of 250 m). These clouds are more close to adiabaticity (Fig. 3.4b). The better agreement in retrieved cloud geometrical properties can be explained by the use of radiosonde data to obtain CTH. This should avoid bias effects, but such an approach is not feasible for a large domain, given the sparse radiosonde network.

Differences in CTH may in general also result from semitransparent clouds, cirrus cloud layers (e.g., case 21 April 2013), or broken cloud conditions (e.g., case 1 June 2012 and 27 September 2012, compare Fig. 3.3) (Hünerbein et al., 2014). In both cases, a mixed signal from two different layers is sensed due to the spatial resolution of SEVIRI. In the first case, the signal stems from the cirrus and the underlying liquid cloud layer and in the second case, comes from the ground and the liquid clouds. These effects might be mitigated by increasing the satellite spatial resolution. An approach for improving retrievals under multilayer cloud conditions using Optimal Estimation was suggested by Watts et al. (2011).

5.3 Cloud Liquid Water Path

The comparison of Q_L from the satellite and ground perspective can only be applied during daytime hours, since the satellite retrieval relies on observations at solar wavelengths. Q_L is further restricted to values between $20\,\mathrm{g\,m^{-2}}$ and $400\,\mathrm{g\,m^{-2}}$. The lower limit is set because of the typical uncertainty of the microwave radiometer observations and the upper limit due to increased likelihood of drizzle for high Q_L. This strongly reduces the number of Q_L samples compared to the CTH samples.

The distribution of the Q_L difference shows a distinct peak close to zero for all Cloudnet stations (Fig. 5.3). There is a small negative bias of $-15\,\mathrm{g\,m^{-2}}$ ($-8\,\mathrm{g\,m^{-2}}$ to $-21\,\mathrm{g\,m^{-2}}$ for individual stations), i.e., larger values obtained from the ground compared to the satellite. This is within the uncertainty range of the ground-based measurements, without considering the uncertainty of the satellite-based estimate. More than 50% of the sample has differences lower than $30\,\mathrm{g\,m^{-2}}$, more than 75% lower than $60\,\mathrm{g\,m^{-2}}$. The standard deviation of the Q_L difference is larger when taking the fields central pixel instead of the field average, but the shape of the distribution remains similar for both approaches. As can be seen in Fig. 5.3f, up to $75\,\mathrm{g\,m^{-2}}$ there is a close agreement of the distributions, with increasing deviation for larger Q_L up to a maximum at $250\,\mathrm{g\,m^{-2}}$.

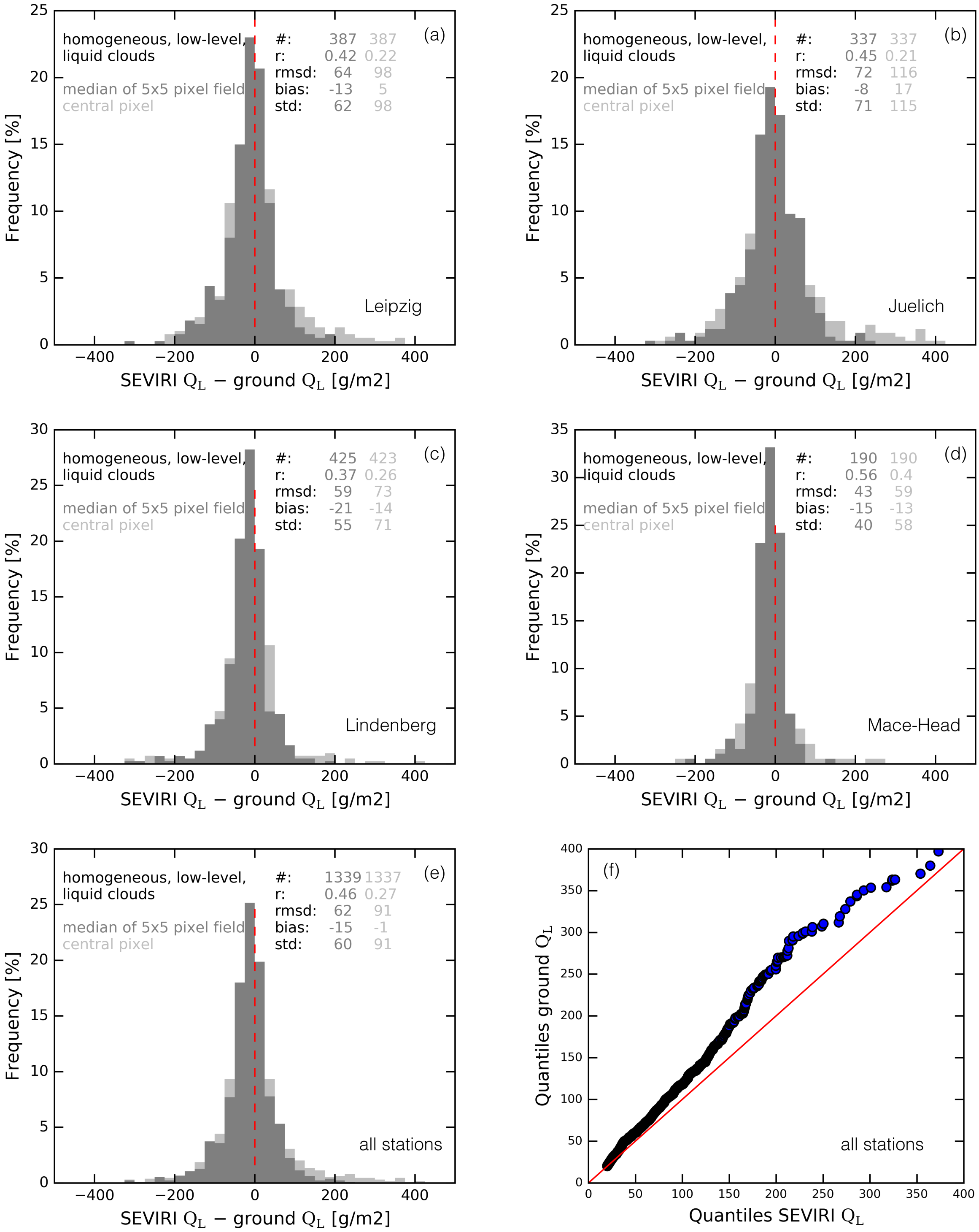

Figure 5.3: As in Fig. 5.1, but for the difference of Q_L between SEVIRI and ground-based observations.

date	location	Q_L RMSD in $\mathrm{g\,m^{-2}}$	Q_L BIAS in $\mathrm{g\,m^{-2}}$	abs. Q_L diff. in $\mathrm{g\,m^{-2}}$	rel. Q_L diff. in %
01 Jun 2012	Leipzig	52	9	36	48%
27 Sep 2012	Leipzig	51	−29	36	62%
21 Apr 2013	Krauthausen	9	3	8	11%
17 Mar 2014	Leipzig	59	34	50	58%
15 Sep 2014	Juelich	19	−10	17	42%
27 Oct 2011	Leipzig	21	−12	18	26%
11 Nov 2013	Lindenberg	21	−10	16	30%

Table 5.1: Difference of Q_L from satellite and ground for case studies as shown in Fig. 3.3.

The distribution and the standard deviation are consistent with the observations in the validation study of Roebeling et al. (2008b) for the Cloudnet stations of Chilbolton and Palaiseau. In comparison to their study more outliers are found in this work. This may be explained by their temporal averaging of the ground-based Q_L, smoothing extreme values. In agreement with their study a slight negative skewness is seen. This stems from larger Q_L values, measured by the ground-based microwave radiometer. Roebeling et al. (2008b) reported that the accuracy of Q_L, derived from passive satellites, is reduced for higher values. Further explanations for such differences in Q_L are the cloud inhomogeneities and sampling differences. Generally, unfavorable viewing conditions with a low solar zenith angle can lead to large uncertainties in the satellite retrieval. This occurs especially in winter time or in morning/evening hours. Nevertheless, omitting solar zenith angles greater than 50° does not change the distribution significantly.

Q_L is in reasonable agreement for specific case studies between satellite and ground-based observations given the uncertainties from both perspectives (Table 5.1). For low Q_L values, the relative uncertainties are high. A clear explanation for such differences are the inhomogeneities in the cloud field (e.g., 1 June 2012, 27 September 2012). The difference is lowest for the case with the most stable Q_L over time (21 April 2013).

5.4 Cloud Geometrical Depth

H obtained with two independent physical retrieval techniques can be investigated when contrasting the SEVIRI observations (Eq. 2.5, using f_{ad} from ground-based observations), with the ground-based ones. The correlation coefficient is 0.84 considering all cases. With a RMSD of 363 m between the SEVIRI and ground-based H, the vertical resolution of the ground-based observations (30 m) already accounts for about 10% uncertainty. Further uncertainties arise from the satellite retrievals of τ and r_e.

The correlation of our sample is in the range of the values reported by Roebeling et al. (2008b), Min et al. (2012), and Painemal and Zuidema (2010). For a homogeneous stratocumulus cloud layer Roebeling et al. (2008b) found correlations of 0.71 between SEVIRI and Cloudnet. Min et al. (2012) obtained correlations of 0.62 between in-situ and MODIS retrieved H, and showed a better agreement in H when f_{ad} is explicitly calculated and

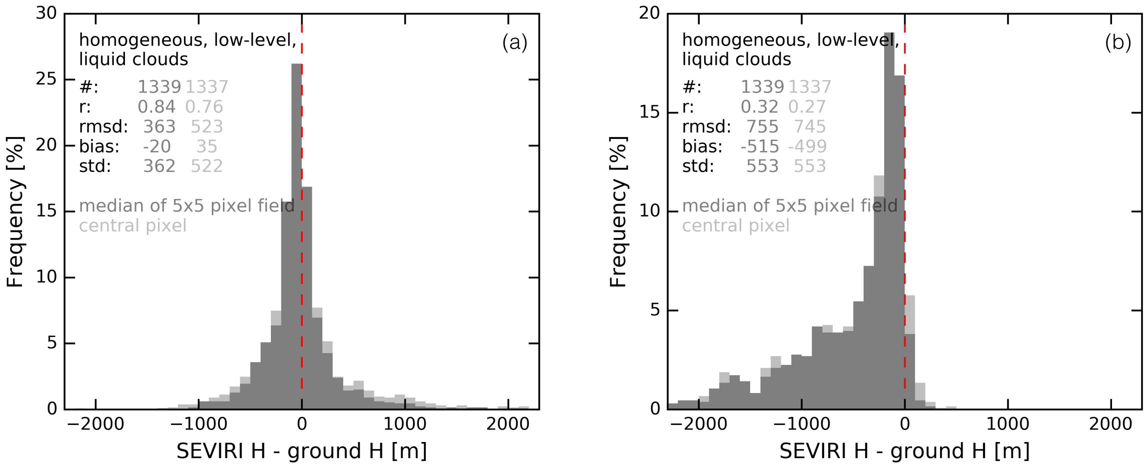

Figure 5.4: Histogram of differences between SEVIRI and ground-based H as in Fig. 5.1. The left figure corresponds to the conditions if f_{ad} from ground-based observations is taken into account, the right figure if $f_{\text{ad}} = 1$.

considered. This is also the case for our sample as can be seen in Fig. 5.4. By considering adiabatic clouds ($f_{\text{ad}} = 1$), the correlation is reduced to 0.32 and a clear bias is introduced ($-515\,\text{m}$ compared to $-20\,\text{m}$). Painemal and Zuidema (2010) reported correlations of 0.54 (0.7 for $H < 400\,\text{m}$ with cloud fraction $> 90\,\%$) comparing radiosonde-derived H to MODIS observations. Painemal and Zuidema (2010) stated that satellite values were higher compared to the ground-based ones. This can potentially be explained by a bias of MODIS-retrieved r_e or by the choice of f_{ad} in the retrieval of H.

5.5 Cloud Optical Depth

In Fig. 5.5, the distribution of differences between SEVIRI and ground-retrieved τ is presented. There is a distinct peak around zero with negligible bias similar to Q_L, but a considerable standard deviation of 14. For the distributions of τ there is a good agreement between ground and satellite perspective up to values of 40. This means that satellite and ground-based τ agree reasonably well, considering the number of uncertainties in the retrieval as well as uncertainties due to parallax shifts, collocation issues and low spatial resolution. Applying different values for the DSD width parameter ν does not lead to significant differences. This is expected from the sensitivity of the ground-based retrieval (Sect. 4.1). When varying ν, the RMSD of τ for the LACROS station is changed from 17 (for $\nu = 0.2$) to 16 (for $\nu = 0.08$) and the distribution remains nearly identical (not shown).

For individual case studies as presented in Fig. 3.3, the median conditions agree within the uncertainty range (Figs. 5.6 and 5.7). For some cases, the satellite values show a peak at low values of τ and Q_L, which is not observed from ground-based observations. This could be explained by broken cloud layers (e.g., 27 September 2012) when SEVIRI received a combined signal from the clouds and the surface for broken clouds within a pixel. From the satellite perspective, moving broken cloud fields result in a smoother

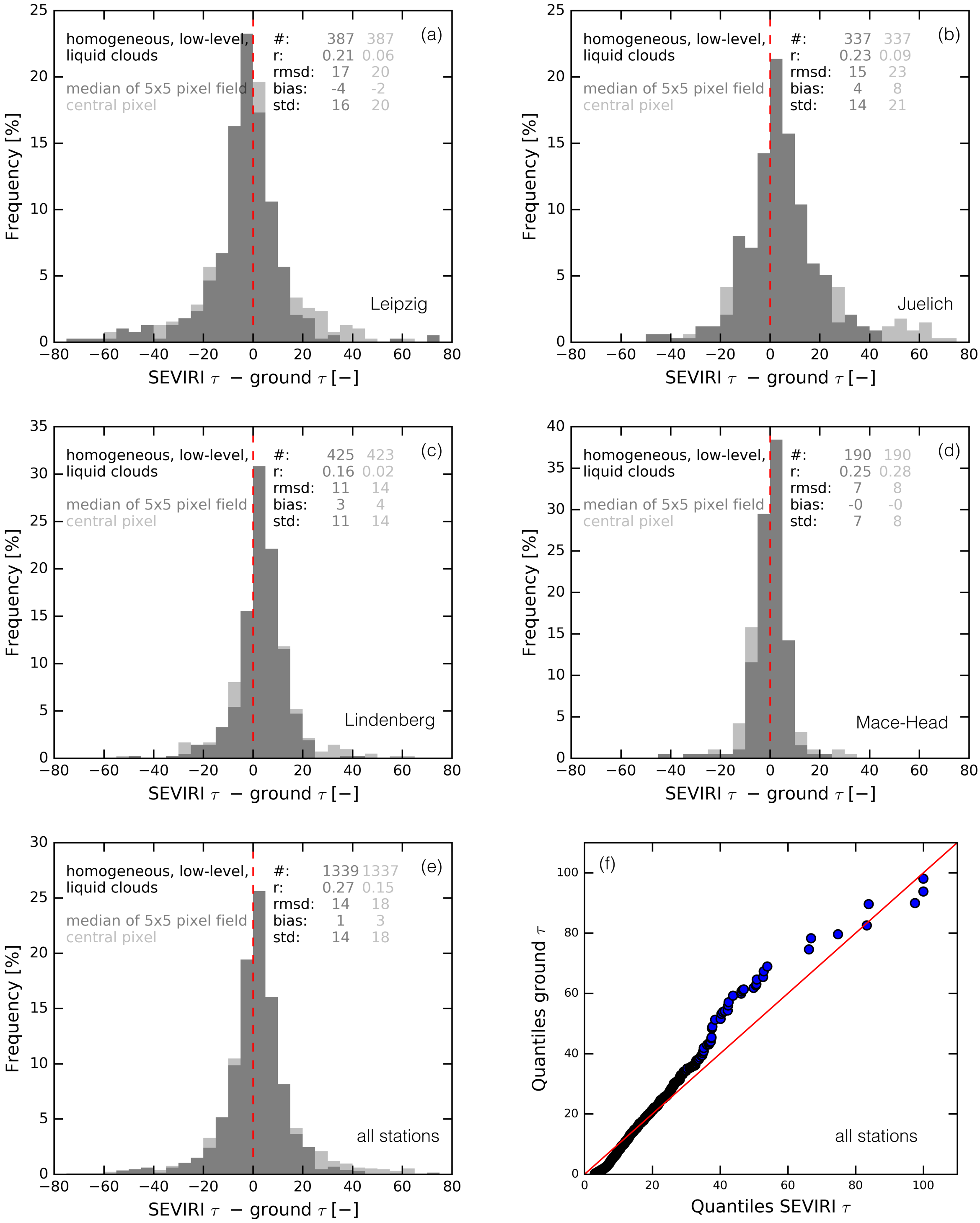

Figure 5.5: As in Fig. 5.5, but for the difference of τ between SEVIRI and ground-based observations.

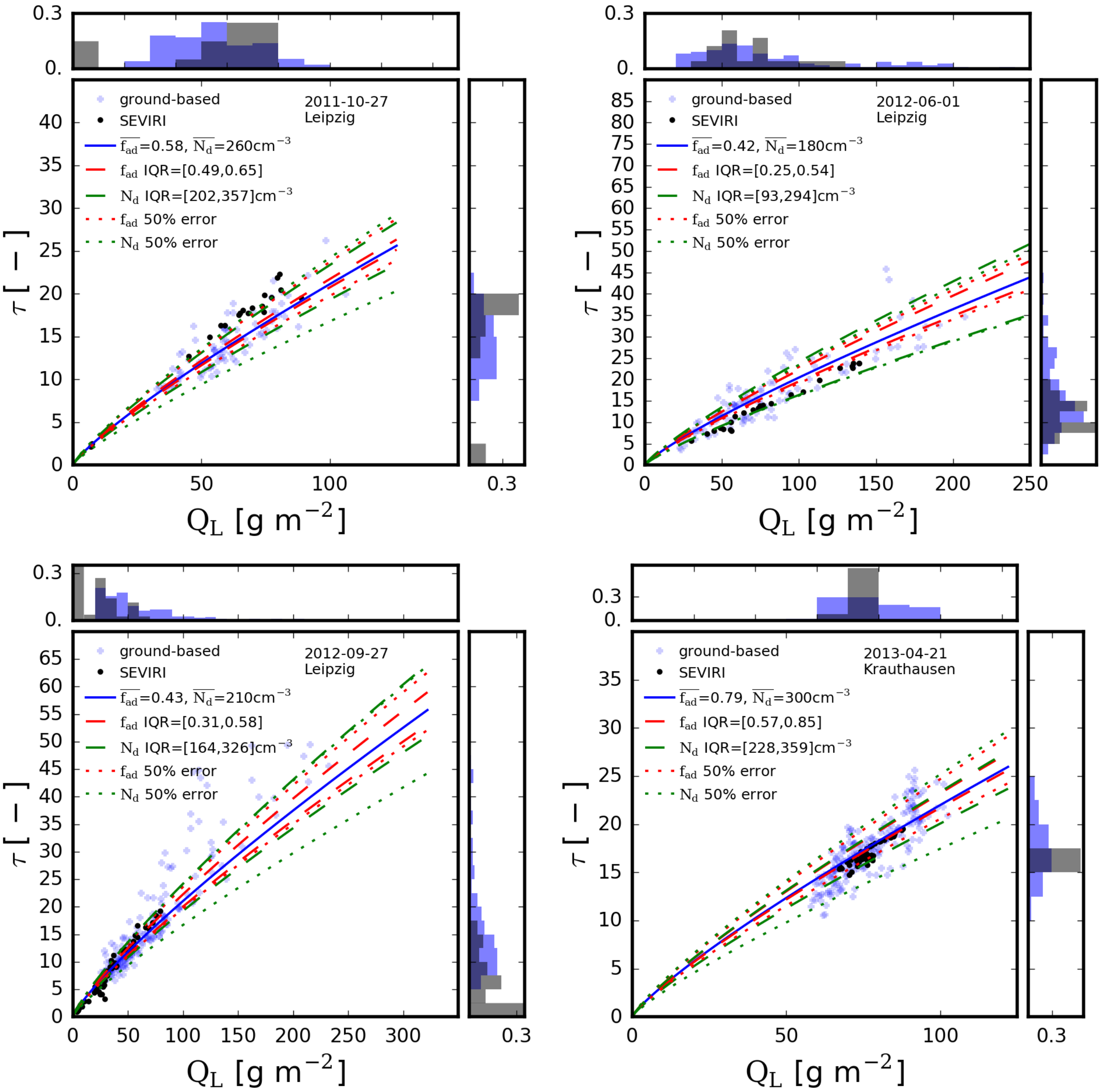

Figure 5.6: Relationship between Q_L and τ for case studies as shown in Fig. 3.3. Blue crosses represent the Cloudnet observations, black dots the SEVIRI observations. The solid blue line represents the relationship between τ and Q_L for the median f_{ad} and N_d of the ground-based observations. Uncertainty estimates of τ as a function of Q_L are given in terms of temporal variability using the IQR of the time series (dashed), and as 50% relative uncertainty in N_d and f_{ad} (dotted). Furthermore the histograms of ground-based and SEVIRI observations are shown on each axis in the same colors as stated before.

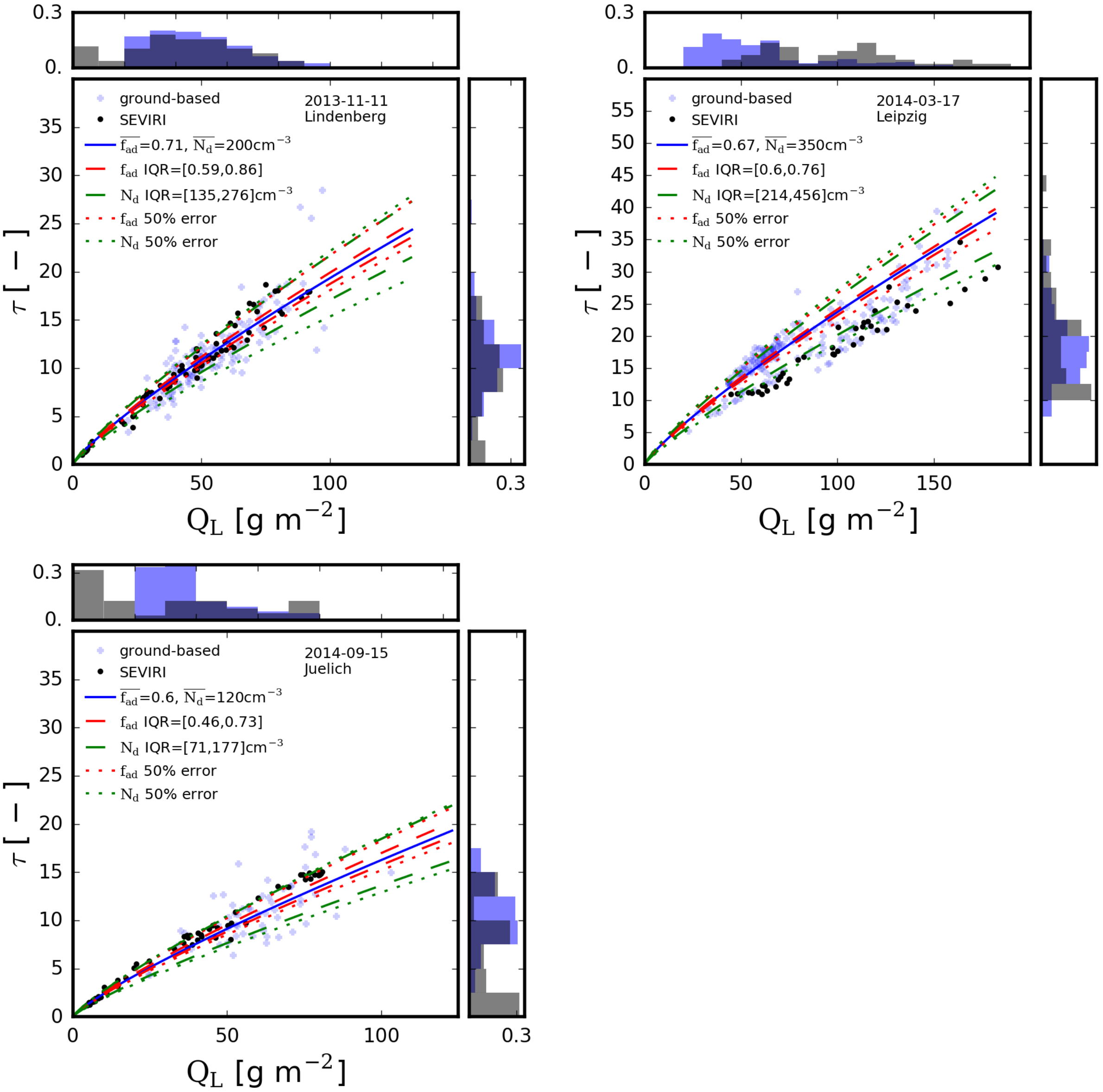

Figure 5.7: Continued figure 5.6.

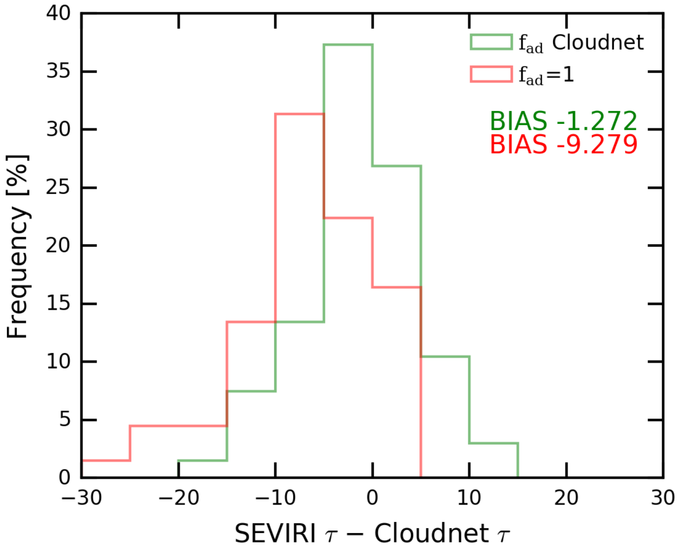

Figure 5.8: Histogram of differences in τ from SEVIRI and Cloudnet for the cases as presented in Fig 3.3. The green line represents the situation accounting for f_{ad} obtained from the Cloudnet observations, the red line if $f_{\mathrm{ad}} = 1$ is assumed.

temporal pattern due to nonlinear averaging of unresolved, subpixel clouds. From the time-height cross-section of Z on 27 September 2012 between 11:00 UTC and 15:00 UTC, a larger number of cloud gaps can be detected (Fig. 3.3), which result in a subpixel surface contamination, and therefore lower values from the satellite perspective. At the same time, Cloudnet observations reveal rapid changes of Q_L with peaks around 400 g m^{-2} as well as cloud-free periods.

Considering the actual f_{ad} for the retrieval process is important. This is highlighted by calculating ground-based τ (Eq. 2.9) with the radar-radiometer approach setting f_{ad} to 1 and to the ground-obtained value, respectively, and comparing it to the satellite-retrieved τ. Applying $f_{\mathrm{ad}} = 1$ for all case studies, the bias between satellite and ground-based optical depth increases from -1.3 to -9.3 (Fig. 5.8).

5.6 Uncertainties of Retrieved Cloud Properties From Satellite Retrievals

In the following, the uncertainty of retrieved N_d from satellite retrievals is discussed. N_d is obtained from the sub-adiabatic model as a function of τ and r_e using Eq. 2.13. Its uncertainty depends on the uncertainties of τ and r_e, as well as on f_{ad}, k_2, and Γ_{ad}.

Roebeling et al. (2008a) reported an uncertainty of about 150 cm^{-3} for optically thick clouds (τ >20) resulting from a 10% error in τ. The absolute error of N_d increases with increasing τ, assuming a constant error in r_e. N_d is very uncertain for values of $r_e < 8\,\mu$m. For liquid clouds, Han et al. (1994) found that cases with $r_e < 5\,\mu$m are rare compared to a typical value of $10\,\mu$m. Roebeling et al. (2008a) argue that those low values of r_e should not be considered due to their large uncertainties.

Uncertainties in the satellite-based retrieval of τ and r_e stem from the plane-parallel assumption, vertical-uniform cloud layers, partially covered cloud pixels (Zinner and Mayer, 2006), 3D effects (Loeb and Coakley, 1998), and large solar zenith angles (Roebeling et al., 2008a). Uncertainties in r_e further arise from its vertical profile. The use of different channels can also result in differences in r_e. MODIS uses a channel centered at 2.1-μm, while SEVIRI utilizes the 1.6-μm channel for the standard retrieval. From MODIS, additional r_e retrievals from channels at 1.6-μm and 3.7-μm are available. Theoretically, the 3.7-μm channel should represent r_e closer to the cloud top for adiabatic clouds, while the 2.1-μm and 1.6-μm channels receive the main signal from deeper layers within the cloud. Cloud observations do not always reflect an increase of r_e from channel 1.6-μm to 2.1-μm, and to 3.7-μm as is expected for plane-parallel, adiabatic clouds (Platnick, 2000; King et al., 2013). Here, the uncertainties in passive satellite retrievals of τ and r_e are estimated as 10%, following Roebeling et al. (2008a) (SEVIRI) and Platnick and Valero (1995) (MODIS). These uncertainties are probably significantly larger under unfavorable conditions (large solar zenith angles, broken clouds).

For Δf_{ad}, a relative uncertainty of 35% (maritime) and 45% (continental) is assumed as has been obtained in this work from Cloudnet observations (Table 3.2, Chapter 3). For comparison, Janssen et al. (2011) assumed an uncertainty in f_{ad} of about 30%. This results in a relative error of about 26% considering typical values of r_e and τ.

Janssen et al. (2011) estimated the uncertainty of k_2 to be negligible (around 3%) for $N_d < 100\,\mathrm{cm}^{-3}$, following Boers et al. (2006). In a global study, Bennartz (2007) used a variability of $k_2 = 0.8 \pm 0.1$, which results in a relative uncertainty of 12.5%. Brenguier et al. (2011) reported a similar mean value for 33 cases of stratocumulus and cumulus clouds with a smaller variability, slightly lower than the variability in Martin et al. (1994). Here, 12.5% is considered as a typical uncertainty for k_2.

In this study, Γ_{ad} is explicitly determined from model data instead of considering a constant value of Γ_{ad} as in e.g., Quaas et al. (2006). Γ_{ad} is calculated from satellite cloud top and from LACROS cloud top temperature and pressure for the cases shown in Fig. 3.3 in Chapter 3. Comparing both, an uncertainty of 16% is obtained, likely due to the obtained difference in CTH. In comparison, Janssen et al. (2011) obtained an uncertainty of 24% for $\Gamma_{\mathrm{ad}}(T,p)$ by considering the whole seasonal variability of cloud base temperature.

For satellite retrievals of N_d (and also H), Janssen et al. (2011) conclude that f_{ad} and Γ_{ad} are the most important uncertainty factors. Considering our uncertainty estimates, in contrast to Janssen et al. (2011) the largest contribution to the uncertainty of N_d is given by the relative uncertainty of r_e (25%), followed by f_{ad} (23% for continental and 18% for maritime conditions), k_2 as a parameter of the width of the DSD (12.5%), Γ_{ad} (8%), and τ (5%). Considering the error propagation for the calculation of H and assuming the same errors as for N_d, the largest uncertainty is found for f_{ad} with 23% and 18%, for continental and maritime conditions, respectively. Followed by relative uncertainties of Γ_{ad} (8%), τ (5%), and r_e (5%).

The importance of r_e for the retrieval of N_d from passive satellite imagers has already been pointed out in previous studies. They are mainly based on observations from MODIS

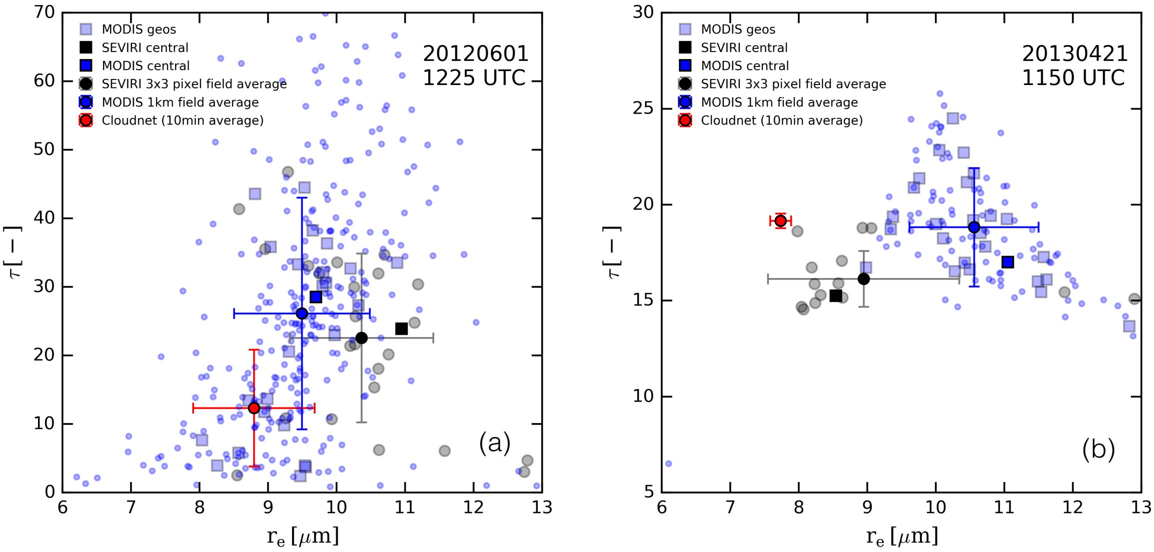

Figure 5.9: Effect of spatial resolution by comparing MODIS and SEVIRI observations for two timesteps: (a) inhomogeneous case, 1 June 2012 at 12:25 UTC, (b) homogeneous case, 21 April 2013 at 11:50 UTC. SEVIRI values are shown in black, MODIS values in blue, and ground-based ones in red. The closest pixel (central) to LACROS is shown as a dark square. Field averages from the sensors original resolution are given as dots. For MODIS, the average to SEVIRI resolution is presented (MODIS geos, light blue square). Error bars represent the standard deviation.

(Painemal and Zuidema, 2010, 2011; Ahmad et al., 2013; Zeng et al., 2014) and report a high bias of MODIS r_e, especially for broken clouds (Marshak et al., 2006). Painemal and Zuidema (2010) also state that the choice of the other parameters in the retrieval (namely k_2, Γ_{ad}) is able to compensate for this effect, so that still a good agreement between MODIS-retrieved and in-situ values could be achieved. This uncertainty estimate further demonstrates the importance of having an accurate estimate of the subadiabatic factor when retrieving key properties for ACI. In the following the effect of the satellite spatial resolution is addressed.

5.6.1 Uncertainties Due to Resolution and Collocation

To investigate the effect of spatial resolution, collocated MODIS and SEVIRI observations are considered. MODIS products are available at 1 km spatial resolution. First, all MODIS pixels are reprojected to the 3 x 3 SEVIRI pixels so that both instruments cover the same area. Second, the MODIS 1-km-resolution data is averaged to receive SEVIRIs spatial resolution (4 km x 6 km). Third, the fields from SEVIRI and the MODIS pixels are averaged, and their standard deviation is calculated. In this way, MODIS is used to account for SEVIRIs' subpixel variability, while neglecting deviations due to the differences in both instruments and retrievals.

In Fig. 5.9, the results for (a) an inhomogeneous case on 1 June 2012 and (b) a homogeneous case on 21 April 2013 are shown. For the inhomogeneous case, one can clearly see the large temporal diversity in τ obtained from MODIS. Averaging MODIS τ to SEVIRI resolution results in a similar spread of τ from both instruments. The spread of τ is larger than the spread of r_e. For the homogeneous case the spread is overall smaller for both quantities. Differences between MODIS and SEVIRI after averaging are in a similar range for both cases. However, the differences between both satellites, especially in terms of r_e, can be of the same magnitude as the differences between satellite and ground-based values. There is a considerable difference when taking either the closest pixel to the ground-based location or the spatially averaged value. The closest pixel does not necessarily result in a better agreement with the ground-based value (Fig. 5.9). Therefore, one can conclude that especially for inhomogeneous cases, the sub-pixel variability introduces an important additional uncertainty factor.

5.6.2 Implications on the Estimate of f_{ad}

In order to quantify whether the combined view from satellite and ground can give reasonable information about cloud properties the ceilometer network data of the DWD can be used to obtain the CBH. For some stratocumulus regions it is suggested that calculating the Lifted Condensation Level (LCL) from NWP reanalysis data would be also suitable to obtain the CBH (e.g., Shao and Liu, 2009). Combining the CBH with the SEVIRI obtained CTH would enable an estimate of f_{ad}. From the comparison of Q_L and CTH between ground-based and SEVIRI observations, it is obvious that an instantaneous estimate of f_{ad} is not feasible due to a number of uncertainties. Therefore, the aim would be to get a climatological estimate of f_{ad}. However, the bias in CTH turns out to be problematic. This can be exemplified for an adiabatic cloud of $Q_L = 100\,\mathrm{g\,m^{-2}}$ and $H = 324\,\mathrm{m}$, considering the root-mean-square differences (RMSD) from the comparison of ground and satellite-based values with ΔQ_L=67 $\mathrm{g\,m^{-2}}$ and ΔCTH=1174 m. This results in a relative uncertainty for the subadiabatic factor of 727%. This estimate even neglects uncertainties of the CBH. Considering a thicker cloud $(2 \cdot H)$, the relative uncertainty is still 362%. With the observed bias in the current NWC SAF CTH product, it is impossible to determine the adiabaticity of clouds with reasonable accuracy. As one likely reason for the obtained bias is the reduced vertical resolution of the applied NWP data, the approach might be reattempted after a recalculation of the CTH dataset with better input data.

5.7 Discussions and Conclusions

Understanding the difference between satellite and ground-based retrievals is an important step to validate observations from passive satellites, and to quantify uncertainties in ACI studies.

When comparing satellite- and ground-based retrievals of Q_L and τ from liquid clouds, RMSD of about $65\,\mathrm{g\,m^{-2}}$ and 14 are found, respectively. However, the comparability can be quite difficult for individual cases. The latter is due to a number of effects, such as retrieval uncertainties, and especially the spatial resolution. For inhomogeneous conditions, a comparison with higher resolved MODIS observations demonstrates the effect of sub-pixel variability on the retrieved τ and r_e. This leads to a limited number of observations with large differences between satellite and ground-based values. Overall, no significant bias for Q_L and τ was observed.

A bias of about 478 m is seen for the NWC SAF CTH product. A likely explanation is the used NWP model data, which is unable to adequately represent vertical temperature inversions. It remains an open question if this is due to the reduced vertical resolution of the interpolated data used here or a general issue of the ECMWF model. With this bias, a determination of f_{ad} from the currently available CTH product is unrealistic. Active satellite sensors may be better suited for such an approach, but f_{ad} is generally quite sensitive to the input parameters, especially H. The sounder capabilities of the upcoming MTG should give new opportunities to overcome problems of cloud geometrical depth retrievals from passive satellites by using additional information from the oxygen A-band (e.g., Yang et al., 2013; Fischer et al., 1991), and therefore might give the possibility to obtain f_{ad} over a larger domain.

ACI parameters from passive-satellite studies are reported at the lower physical range of possible values (Schmidt et al., 2015). Studies using ground-based or even in-situ observations usually give higher values. The ACI parameter is obtained from a fit on a log-log scale of the aerosol and microphysical proxies. A uniform offset of the microphysical parameters from both perspectives over the full observation range would not affect the slope of the fit, in contrast to a random-difference distribution. Here, typically a Gaussian shape of the difference distribution is obtained. McComiskey and Feingold (2012) suggest using observations preserving cloud heterogeneity, which could be achieved from a spatial resolution better than 1 km. Cloud products at this resolution are available from MODIS on a polar orbit, and will be available from the upcoming Meteosat Third Generation (MTG, Stuhlmann et al., 2005) from a geostationary perspective.

6 Aerosol-Cloud Interactions: Ground-Based Case Study

ACI metrics as introduced in Chapter 2 are known to be quite sensitive to the observation scale (McComiskey and Feingold, 2012). In this chapter, a method for quantifying ACI is tested utilizing ground-based remote sensing observations. Furthermore, cloud microphyiscal properties are compared to in-situ data. Unfortunately in-situ measurements together with Cloudnet observations are currently available only for one case, which we focus on in this section.

First, the meteorological conditions and observations of the case will be described. Subsequently, the retrieved microphysical cloud properties are cross-checked with the in-situ observations. Afterwards, an assessment of the ACI metric will be performed utilizing ground-based observations, following the method described by Sarna and Russchenberg (2016). Furthermore, the sensitivity of the ACI metric on the choice of the aerosol proxy is discussed.

6.1 Meteorological Conditions

In September and October 2013, the HOPE-Melpitz experiment took place, aiming to investigate clouds, aerosols and their interactions. The LACROS instruments were set up at Melpitz, Germany (12.94 °E, 51.53 °N). For this study, the backscatter coefficients from the ceilometer are replaced with the one from the Polly$^{\mathrm{XT}}$-OCEANET system defined in Engelmann et al. (2016). Additional airborne in-situ measurements with the ACTOS platform (Siebert et al., 2006) were realized for some time periods on 22 September 2013.

A low-level stratocumulus cloud layer was present on 22 September 2013 with an average CTH at about 1700 m. Some breaks in the cloud layer occurred as well as periods with drizzle (e.g., after 17 UTC), as can be seen from the Cloudnet target classification (Fig. 6.1). Until 16 UTC, multiple ice cloud layers above 4 km were present. These unfortunately make a comparison of the microphysical properties of the stratocumulus cloud with passive satellites impossible since these obtain only the path-integrated signal from the liquid and ice cloud layers. However, with the vertically resolved ground-based observations, a retrieval of the liquid cloud microphysics is possible. Like the satellite observations, passive radiation measurements from the ground cannot be used, since they may also be influenced by the ice clouds. This means an application of the OE retrieval as described in Chapter 4 is not feasible. During daytime, e.g., from 10 to 15 UTC, also shallow cumulus clouds formed below the stratocumulus layer. A radiosonde profile from

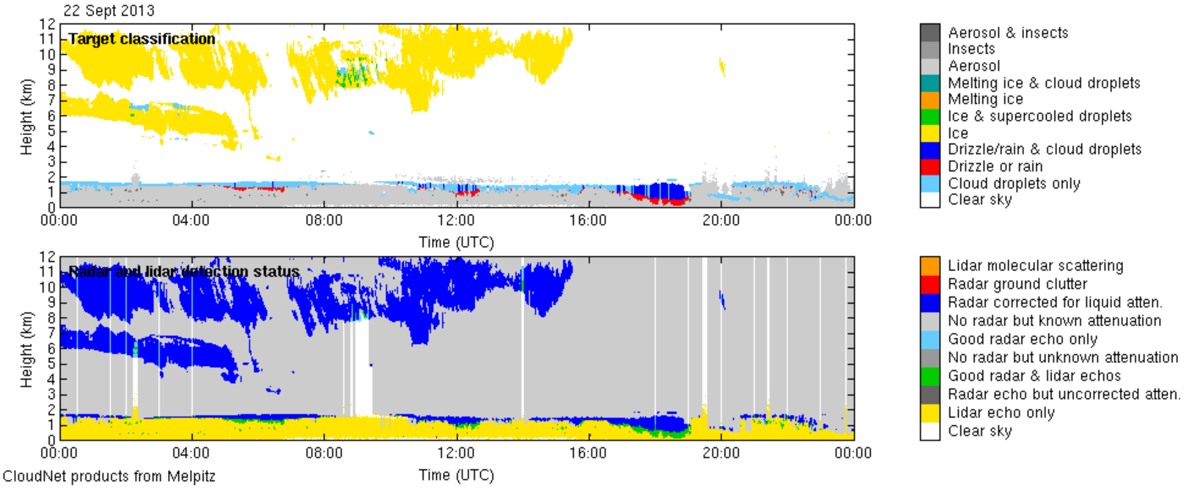

Figure 6.1: Cloudnet target classification and detection status for the case study of 22 September 2013 in Melpitz.

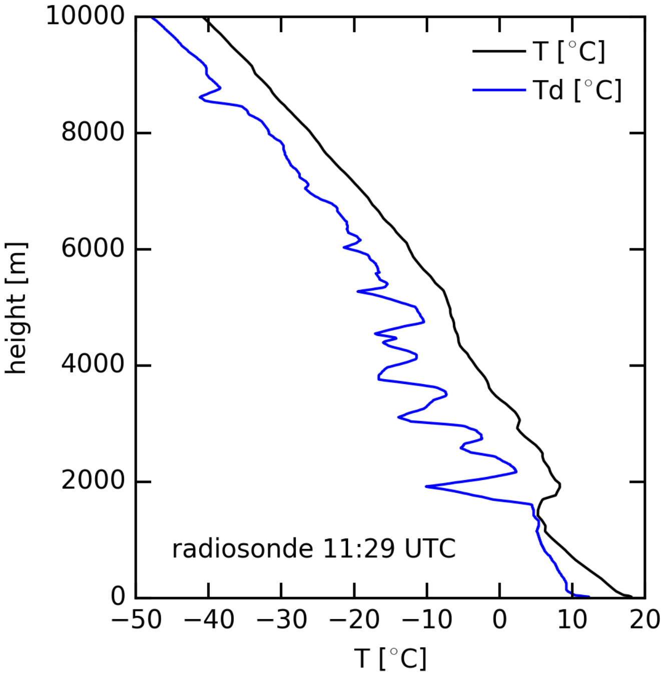

Figure 6.2: Radiosonde profile from 11:29 UTC on 22 September 2013 in Melpitz. The black line depicts the temperature, the blue line the dew point temperature.

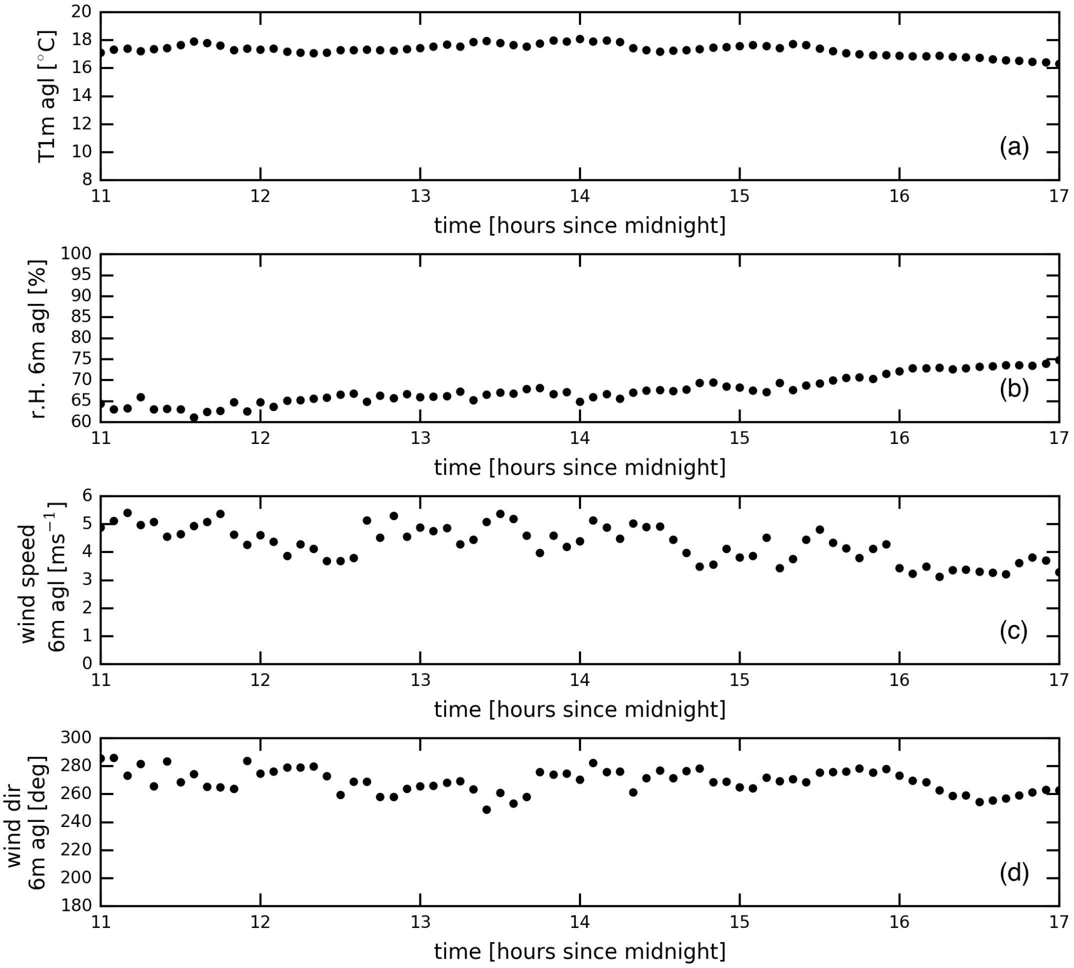

Figure 6.3: Meteorological surface observations on 22 September 2013 in Melpitz. From top to bottom: (a) temperature at 1 m above ground level (agl), (b) relative humidity 6 m agl, (c) wind speed 6 m agl, (d) wind direction 6 m agl.

11:29 UTC in Melpitz (Fig. 6.2) shows a well-mixed boundary layer and a strong inversion layer at about 1700 m, consistent with the observed average CTH.

Although the meteorological conditions with multiple cloud layers do not seem to be ideal for the retrieval of microphysical properties, the occurrence of a layer with an increased attenuated backscatter coefficient (β^*) in the developing boundary layer during the morning hours makes this case a very interesting candidate for studying ACI. As can be seen in Fig. 6.3, the temperature, relative humidity, wind speed, wind direction at the ground vary only slightly. At 16 UTC the values of β^* within the boundary layer decrease rapidly. This is likely due to the occurrence of drizzle in the surrounding which may have caused a wash-out of aerosols in the boundary layer and the advection of this airmass to the observation site. The meteorological surface observations show that no abrupt change in wind speed or direction occurred. Past 16 UTC the stratocumulus layer produces drizzle also over the measurement site, and dissipates after the precipitation event.

Microphysical cloud properties are retrieved with the method described in Sect. 2.5.2 (Fig. 6.4). The decrease in β^* is related to an increase in r_e to values above 14 μm. This value is usually considered as a drizzle threshold for satellite-derived cloud top values (Rosenfeld et al., 2012). Note that retrievals are performed under the condition that $Z < -20\,\text{dBZ}$ to avoid drizzle profiles within the retrieval. The retrieved values of r_e during the transition from non-drizzling to drizzling should therefore be plausible, but the uncertainties during this period might be larger.

6.2 Consistency-Check of Retrieved Microphysical Properties Against In-Situ Observations

A short period of in-situ observations from 9:58:30 to 10:05:07 UTC is available for this case. A consistency check of the ground-based retrieval products can therefore be conducted, and especially the assumptions made for the DSD in the retrieval process can be checked. A Phase-Doppler-Interferometer (PDI) measures the size of droplets during the flight with ACTOS. Additionally, from a Particle-Volume-Monitor (PVM) bulk microphysical properties such as q_L, r_e and N_d are available.

The comparison of ground-based values with in-situ observations shows a good agreement on average (Fig. 6.5) considering the given uncertainties and possible sampling of different cloud portions. Given the DSD created from the observations over the whole period, a fit with a theoretical log-normal distribution setting σ_x to 0.33 seems to describe the average observed DSD over the observation period well (Fig. 6.6). The mean deviation between in-situ and retrieved values (using lognormal distribution with σ_x=0.33) is 8% for r_e and 18% for N_d. The vertical position of the ACTOS observation in the cloud is unknown, but the cloud layer is very thin and updraft vertical Doppler velocities prevail at CBH, so that the horizontal displacement of both observations is likely the most relevant uncertainty source next to the assumption about the DSD. A few time steps exist where the retrieval yields too high values of N_d, independent of the assumption about the width of the DSD. It is difficult to judge which width parameter is most valid, since the sample size of retrieved values is small compared to the in-situ observations.

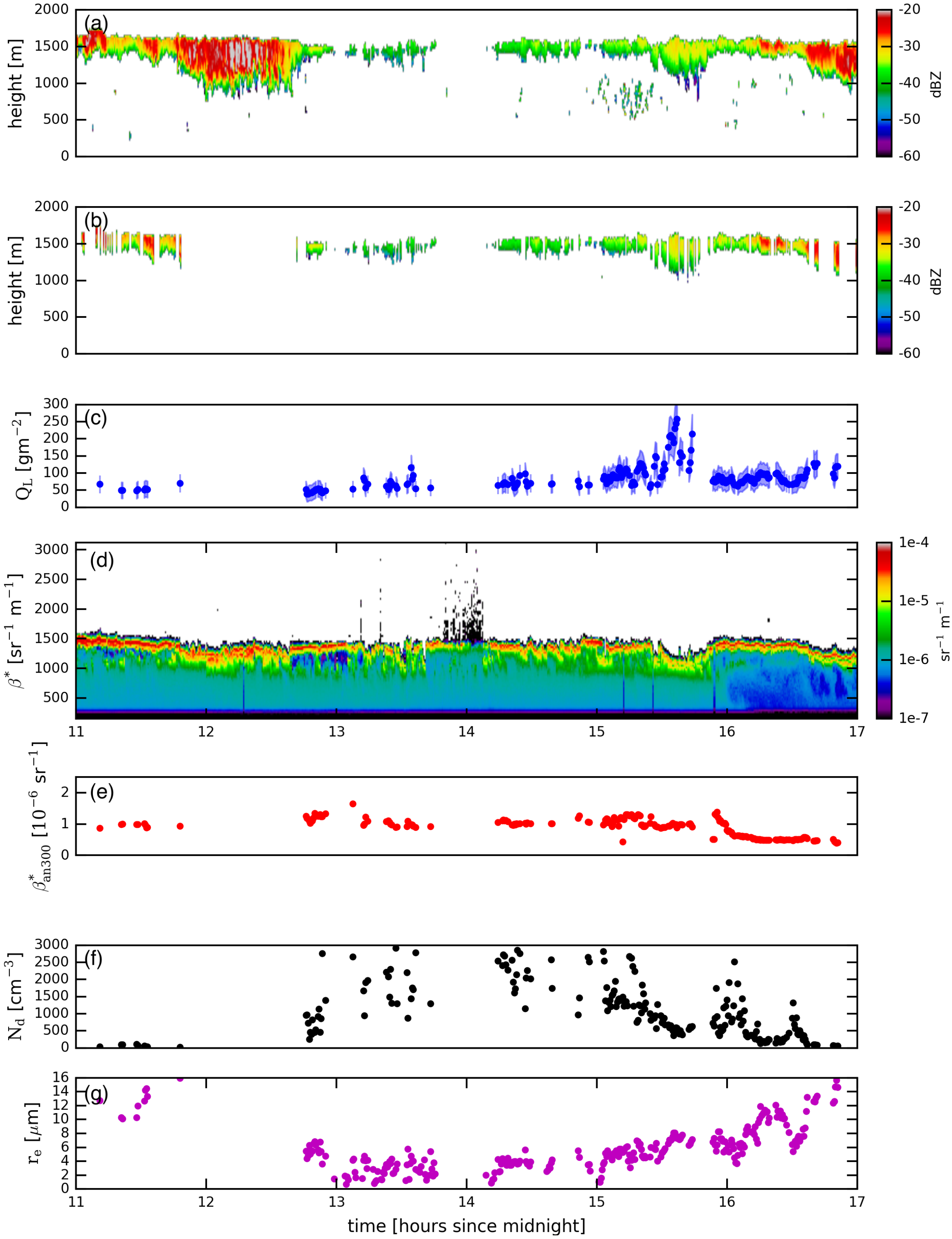

Figure 6.4: Observations on 22 September 2013 in Melpitz processed with the Cloudnet algorithm between 11:00 UTC and 17:00 UTC. From top to bottom: (a) complete observations of Z, (b) sample of suitable Z profiles (c) Q_L, (d) attenuated backscatter β^* and (e) its integral normalized by the integration height (β^*_{an300}, Eq. 6.1), (f) retrieved N_d (using B2010 method, Eq. 2.28, as described in Chapter 2) and (g) r_e (Eq. 2.11, Chapter 2) are shown.

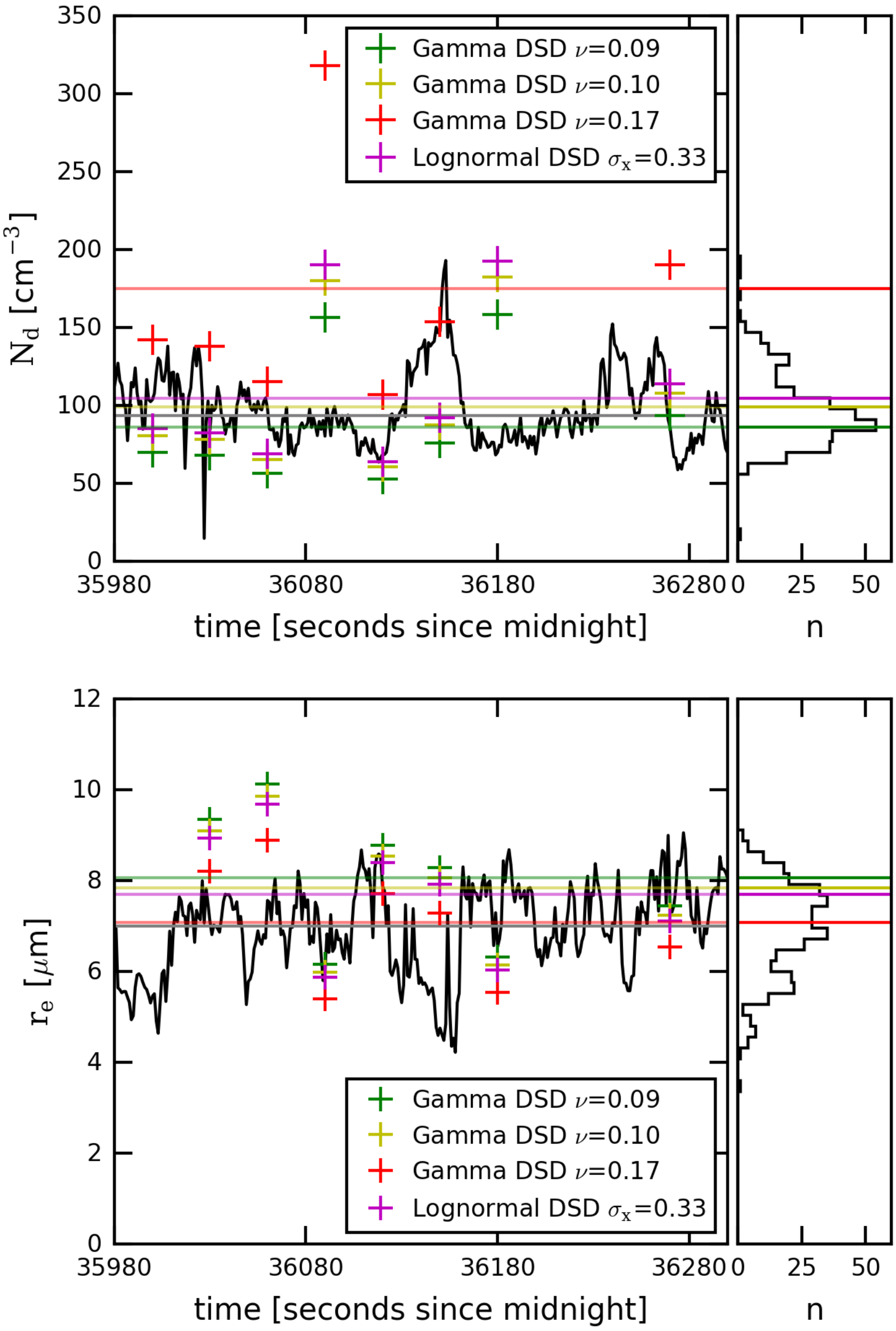

Figure 6.5: Comparison of in-situ observed cloud properties and retrieved cloud properties for different assumptions about the width of the DSD: (a) N_d, (b) r_e. The horizontal solid line represent the average values over the time period. The different colors refer to the assumption made for the width parameter of the DSD (Gamma and log-normal) within the retrieval. The black line refers to the in-situ values.

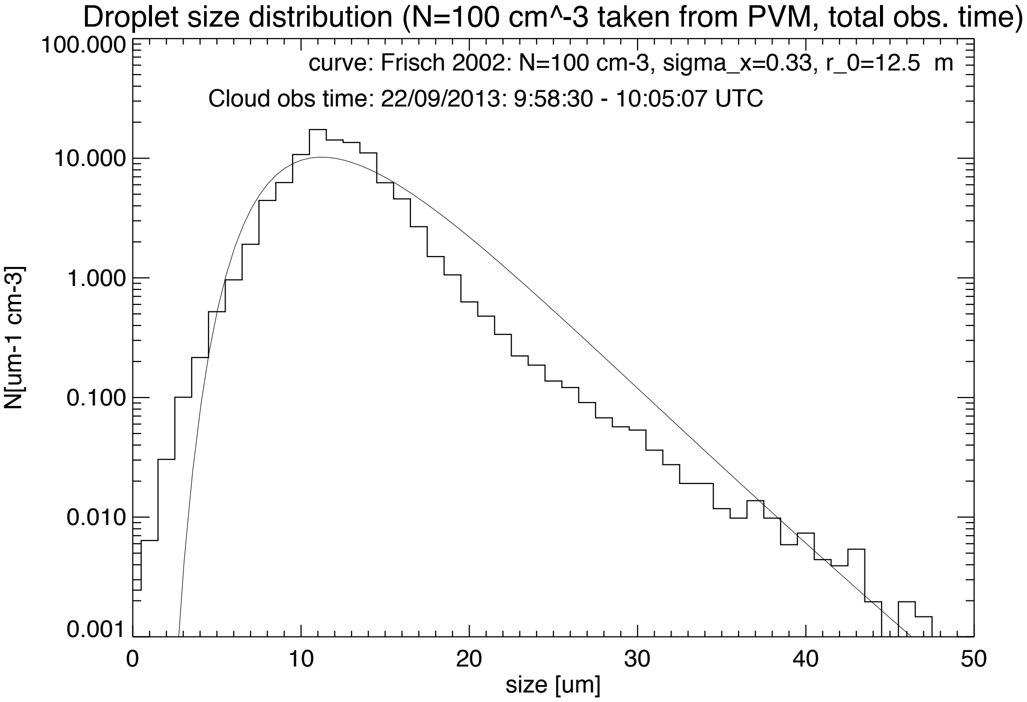

Figure 6.6: Distribution of droplet size from ACTOS in-situ observations, and theoretical fit line following Frisch et al. (2002). Courtesy of Patric Seifert (TROPOS).

Considering the reasonable agreement of retrieved values, it is suggested that the assumption of homogeneous mixing is valid for this case.

6.3 ACI Parameter

For the investigation of ACI the observation period between 11:00 UTC and 17:00 UTC is used. The sampling approach as outlined in Sect. 3.1 is used to avoid for too large retrieval errors. The remaining Z cloud profiles after sampling are presented in Fig. 6.4b.

The aerosol load in the boundary layer increases after the early morning hours with the evolution of the well-mixed planetary boundary layer. At the same time, low-level liquid clouds are present, which enable us to study ACI.

Following the paper from Sarna and Russchenberg (2016), the integrated attenuated backscatter coefficient (β_a^*) is used as a proxy for CCN. The integration is done from 300 m above ground (to avoid problems with the overlap height of the Polly$^{\mathrm{XT}}$ lidar), to 300 m below the CBH (to avoid haze that might give higher values of the attenuated backscatter coefficient). In addition to Sarna and Russchenberg (2016), the integrated attenuated backscatter coefficient is normalized with respect to the vertical layer depth, i.e.:

$$\beta_{an}^* = \frac{\int \beta_a^* dz}{\int dz}, \tag{6.1}$$

where dz refers to the depth of the aerosol layer as defined above. The proxy of the

parameter	ACI_N	ACI_r (50-100)	ACI_r (100-150)
n	215	72	23
β^*_{a0}	1.1 ± 0.13	0.18 ± 0.12	0.45 ± 0.08
β^*_{a60}	1.25 ± 0.14	0.21 ± 0.12	0.49 ± 0.08
β^*_{a150}	1.38 ± 0.15	0.18 ± 0.14	0.51 ± 0.09
β^*_{a300}	1.32 ± 0.16	0.14 ± 0.15	0.49 ± 0.11
β^*_{an0}	1.20 ± 0.14	0.30 ± 0.12	0.56 ± 0.08
β^*_{an30}	1.31 ± 0.14	0.34 ± 0.12	0.62 ± 0.08
β^*_{an150}	1.55 ± 0.16	0.37 ± 0.14	0.72 ± 0.09
β^*_{an300}	1.66 ± 0.18	0.42 ± 0.15	0.86 ± 0.11

Table 6.1: ACI metric for different Q_L bins (given in brackets in $\mathrm{g\,m^{-2}}$) and for different aerosol proxies: β^*_a refers to the integrated attenuated backscatter coefficient from 240 m above surface to a height below CBH in meters, which is given by the suffix number. β^*_{an} is the integrated attenuated backscatter coefficient, but normalized by the integration height. The uncertainty is obtained from the standard deviation of the linear least square regression.

available aerosol in the boundary layer should subsequently be independent of the actual boundary layer depth. We would expect this aerosol proxy to be more stable in case of a variable CBH than without normalization. In contrast to Sarna and Russchenberg (2016), larger Q_L bins of $50\,\mathrm{g\,m^{-2}}$ (instead of $10\,\mathrm{g\,m^{-2}}$) are taken. This is motivated by the following reasons: (a) the typical uncertainty of the microwave radiometer is estimated at about $25\,\mathrm{g\,m^{-2}}$, (b) to get larger sample sizes for a given Q_L bin for more robust statistics. Kim et al. (2008) also use a bin size of $50\,\mathrm{g\,m^{-2}}$. The ACI metric is only calculated if at least 20 data points are available.

The sensitivity of the ACI metric to the integration height of the attenuated backscatter below the cloud base is investigated in Table 6.1. The ACI turns out to be quite sensitive to the integration height for both, the normalized and non-normalized attenuated backscatter. Therefore, the received ACI metric has to be interpreted with care, especially since the sample number is small. For integration heights closer to the cloud base the ACI metric tend to give lower values.

ACI values are sometimes above the theoretical limits (1.0 for ACI_N and 0.33 for ACI_r) for both ACI metrics (Table 6.1, and Figs. 6.7 and 6.8). The explanation might be multifold: as only one case study is considered, the number of data points is small and therefore a large spread of values in the attenuated backscatter or the microphysical cloud properties can have a large impact. As already noted in previous chapters, the microphysical retrievals of r_e and N_d can have large uncertainties when drizzle droplets start to form, with the retrieval uncertainties being larger for N_d than for r_e. Both microphysical parameters are derived from the same observed quantities and are therefore not independent from each other. In Fig. 6.8 the retrieved r_e values are plotted as a function of the maximum in the vertical profile of Z (Z_{max}). It is expected that the likelihood for retrieval errors is higher for larger Z_{max}, especially with values close to $-20\,\mathrm{dBZ}$, as it is more likely to find few drizzle-sized droplets that dominate the reflectivity signal. In comparison, r_e obtained from the real DSD might be lower under such conditions. An overestimation of r_e for higher Z_{max} can result in an overestimation of the slope, as can be seen in the Q_L

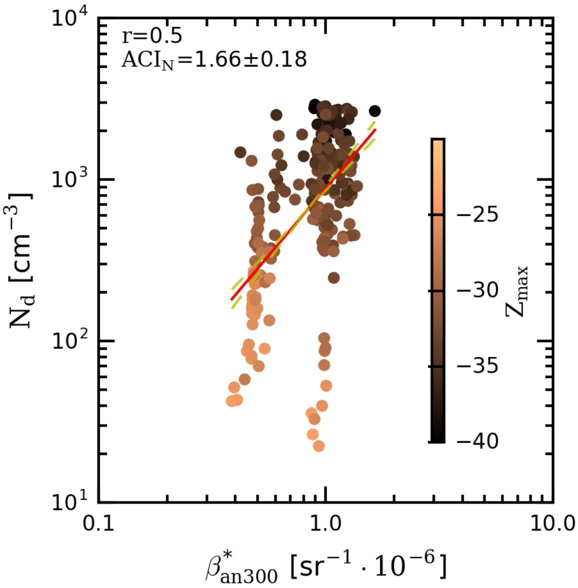

Figure 6.7: Integrated attenuated backscatter coefficient normalized by height (β^*_{an300}) versus retrieved N_d on double-logarithmic scale. The red line represents the least square fit made for $\ln(N_d)$ and $\ln(\beta^*_{an})$. The yellow dashed lines give the uncertainty range of the fit. The Pearson correlation coefficient r and the ACI_N metric value are listed. The fill-color of the circles refer to the maximum radar reflectivity (Z_{max}) within the cloud profile.

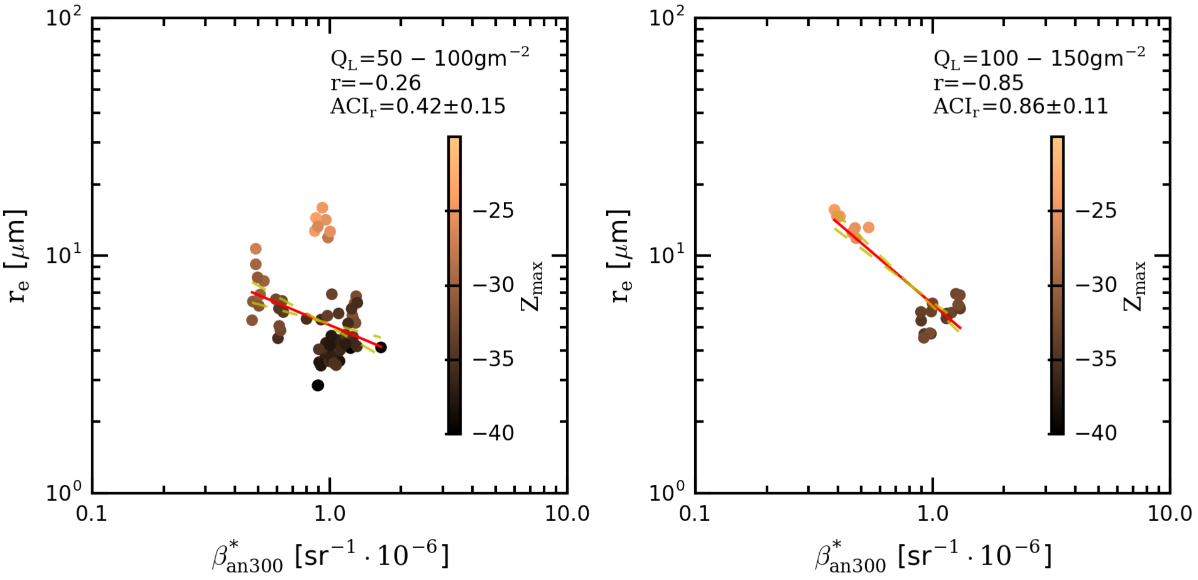

Figure 6.8: Similar to Fig. 6.7, but for ACI_r, using r_e and two different Q_L bins from 50–100 g m^{-2} and 100–150 g m^{-2}.

bin of 100–150 $\mathrm{g\,m^{-2}}$ where the sample number is quite low. In similar fashion N_d would be underestimated for high Z_{max} and ACI_N be overestimated.

In the following, the discussion is focused on ACI_r as it enables easier comparison to literature values. The values of ACI_r reported by McComiskey and Feingold (2012) are in the range of 0.04 to 0.15, up to 0.09 in Sarna and Russchenberg (2016), and between 0.04 and 0.17 in Kim et al. (2008). The values of $ACI_r(\beta_a^*)$ for the case study in this work are generally higher. Using β_{an}^*, ACI_r is shifted towards even higher values. Additionally to the uncertainties of the cloud microphysics that influence ACI_r, the choice of the aerosol proxy might bias the ACI values. Attenuated backscatter as an aerosol proxy includes not only the CCNs, but also other aerosols. The characteristics of the actual aerosol plume differ among literature studies, and can be seen as a further explanation for differences in ACI_r. Furthermore, the small sample size results in an uncertainty of the least square fit, which is found to be above 100% for some Q_L bins.

Interestingly, Sarna and Russchenberg (2016) found indications that ACI is more significant in the lower Q_L range, while for the case study in this work the larger values of ACI occur for the larger Q_L bin. This might be explained by the overall small sample size, which is similarly a problem in the study of Sarna and Russchenberg (2016). In contrast to the study of Sarna and Russchenberg (2016) a continental case is considered here. For continental clouds, the occurence of larger N_d values is expected and therefore drizzle might not occur as frequently at low Q_L as for maritime clouds.

6.4 Discussions and Conclusions

In this chapter, a case study has been explored utilizing ground-based remote sensing observations with the aim to test the possibilities of quantifying ACI and compare the microphyiscal properties to in-situ observation. Although the sample case is not suitable for application of the more advanced OE retrieval method due to the overlying cirrus cloud layer, the rapid change in aerosol load at 16:00 UTC makes this case an interesting candidate to study ACI metrics. Given a short observation period of in-situ observations a good agreement of the retrieved values of N_d (18% mean deviation) and r_e (8% mean deviation) was found. The derived ACI metrics turn out to be quite sensitive to the definition of the integration height of the backscatter coefficient. Retrieval results are expected to be less reliable for larger values of Z close to the drizzle threshold and can partly explain the overestimation of the regression slopes. This effect is amplified by the small sample size. Overall, our investigations emphasize once again the need for accurate retrievals of key properties such as N_d and r_e from ground-based remote sensing.

To investigate the effect of Q_L on ACI more closely, a larger number of case studies would be required, ideally accounting for similar meteorological conditions. According to McComiskey et al. (2009) the question remains if the variability of ACI values found in different studies is due to real physical processes, measurement and retrieval uncertainties or a combination of those. Considering only one case study, we conclude that the uncertainties are too large due to the small sample size to reliably quantify ACI and larger statistics are required.

In the next chapter, a larger scale is considered, and a statistical analysis is conducted to quantify ACI with observations from Meteosat SEVIRI.

7 Aerosol-Cloud Interaction: Statistical Analysis from SEVIRI and MACC

To quantify the climatological relevance of ACI, investigations over large domains are required. While single supersites offer the opportunity to improve the process understanding of ACI, they are too sparsely distributed to obtain reliable information on the resulting large-scale radiative effect. Although ACI quantification from passive satellites comes with a number of limitations (McComiskey and Feingold, 2012; Merk et al., 2016), only those provide the required spatial coverage to acquire longer-term results over different regions. According to the 5th IPCC report (Boucher et al., 2013), satellite-based remote sensing continues to be the primary source for global investigations of ACI.

In the past a variety of aerosol proxies has been applied for satellite-based ACI studies (e.g., AOD in Wetzel and Stowe (1999); Shao and Liu (2005); Gryspeerdt and Stier (2012); Ma et al. (2014), the aerosol index (AI) in Quaas et al. (2004); Bréon et al. (2002), or the column CCN in Nakajima et al. (2001); Sekiguchi et al. (2003)). This diversity, and the different observation scales, result in ACI values covering a wide range as reported in Schmidt et al. (2015). While CCN is the quantity that is physically most directly connected to cloud microphysics via aerosol activation, it is difficult to be observed over a larger domain. Recently, global daily-mean CCN values have been derived from MACC-II reanalysis (Morcrette et al., 2009; Benedetti et al., 2009) data by Block and Quaas (2016). The reason for the choice of this particular dataset is the demonstrated improvement of correlations to in situ observations in comparison to observed AOD (Block and Quaas, 2016), which is due to the refinement in CCN distribution and coverage, while the link of the bulk aerosol distribution to AOD is retained.

The CCN concentration from this dataset is used as a surrogate for the aerosol activation process together with SEVIRI data to quantify cloud microphysical response and cloud albedo effects for the European domain. Results are compared utilizing AOD instead of CCN as an aerosol proxy. In this context, the feedback mechanisms between thermodynamics and cloud microphysics, as well as uncertainties that complicate the interpretation of ACI, will be discussed.

7.1 CCN from the MACC-II Reanalysis

The CCN derived from MACC-II reanalysis has been provided by Block and Quaas (2016). This dataset will be publicly available soon.

The advantage of taking MACC-II reanalysis data comes from the assimilation with MODIS AOD observations, the validation against other observation sources, and the possibility to use collocated information about aerosols and clouds, which is difficult from a pure satellite-based study. The advantage of considering CCN instead of the mass mixing ratio of different aerosol species for ACI studies (Merk et al., 2015), is that CCN accounts only for the aerosol particles that are activated to cloud droplets.

To obtain the CCN concentration, the aerosol mass mixing ratios of the different species available in MACC were transformed into aerosol number concentrations using assumptions on the aerosol size distribution that are used within MACC to convert between aerosol mass and AOD of each species. In that way, on the one side the relationship between the bulk aerosol concentration and assimilated AOD is still valid, while on the other side estimated CCN concentrations are given as vertical profiles.

Fine-mode aerosols are considered to act more likely as CCN compared to the coarse mode (Bulgin et al., 2008; Bréon et al., 2002; Quaas et al., 2004). Furthermore, aerosols must be hygroscopic or at least contain a hygroscopic coating (Bulgin et al., 2008) to act as CCN. The latter is especially important for dust, which is otherwise not considered (Nakajima et al., 2001). In the dataset from Block and Quaas (2016), dust is not accounted for as a CCN. The CCN concentration of their dataset is the sum of the aerosol concentrations of hydrophilic BC, OM, sea salt and sulphate.

7.2 Sampling Method

For the satellite-based ACI investigation, the dataset is sampled to account for suitable conditions. SEVIRI observations are taken for the European domain (see Fig. 7.1) for the year 2012 at 5 min temporally resolution between 9 and 15 UTC. MACC daily mean products of AOD (which is constrained by MODIS-observed AOD) and vertically resolved total CCN are available from Block and Quaas (2016). It is assumed that the daily mean values of the aerosols quantities are representative for the applied higher-resolved SEVIRI observations, i.e., they are temporally homogeneous. Such an assumption is also made in comparable studies when only sparse aerosol information are available (e.g., Shao and Liu, 2005). The MACC products are available on a coarser grid than the SEVIRI observations, but the aerosol distribution can be assumed to be spatially more homogeneous than clouds. In a first step, the MACC data is interpolated on the SEVIRI grid.

To ensure that the investigation only treats warm, low-level liquid clouds, the following criteria are used to subsample our dataset:

- τ is between 4 and 23. The lower limit is set as a large uncertainty is expected in the KNMI-CPP retrieval for low values of τ. The upper limit is set according to the International Satellite Cloud Climatology Project (ISCCP) cloud scheme, selecting low clouds.
- r_e lies between $4\,\mu$m and $14\,\mu$m. The lower limit is set for the same reason as for τ. The upper limit can be seen as a typical threshold for an increased likelihood of drizzle as seen from the satellite perspective.
- τ and r_e values with a retrieval uncertainty larger than 25% as obtained from the KNMI-CPP algorithm are omitted.

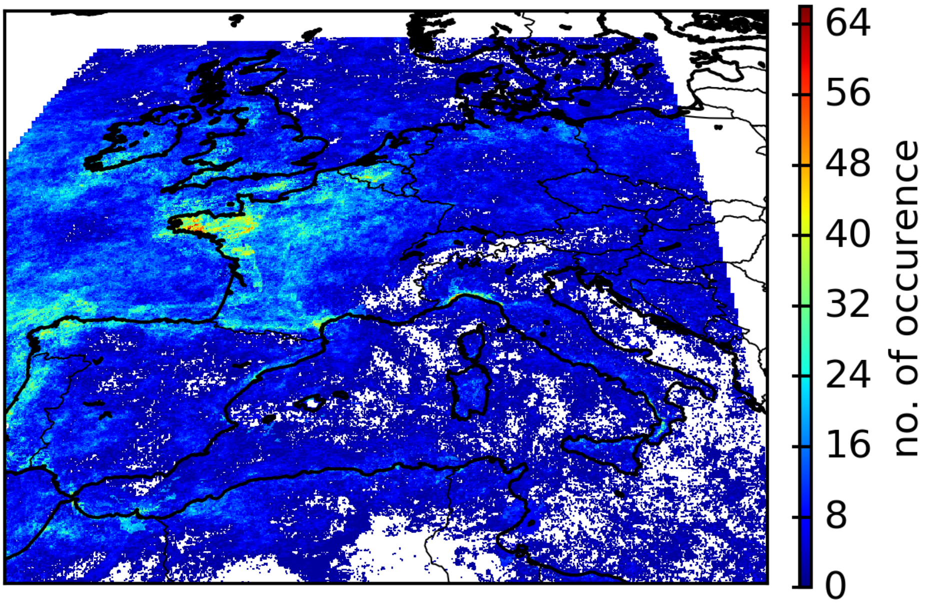

Figure 7.1: Occurence of liquid clouds per pixel applying the described sampling method in the text.

- Only liquid clouds according to the cloud phase obtained from the KNMI-CPP cloud mask are considered.
- CTP is higher than 680 hPa, according to the ISCCP cloud scheme to sample for low clouds.
- CTT is warmer than 273 K to select for warm clouds.

The number of filtered sample points is presented in Fig. 7.1. Most of the cloud samples are found over the Atlantic and at the coastal regions of Great Britain, France and Spain. These areas seem to be preferable for occurrence of low-level liquid clouds. This is probably due to the advection of cold air masses from the Northwest over the warmer water surface - a quite typical synoptic pattern for the Central European domain. Secondary maxima can be seen along the North-Western coast of Italy.

To study regional differences, the investigation domain is split into different regions (Fig. 7.2): the European land domain, the North African land region (Sahara), the Mediterranean, and the North-West ocean area including Atlantic, North Sea and Baltic Sea. The European land region is further separated into a western and eastern part dividing the land mass at the domain center.

7.3 Cloud Microphysical Proxies

Cloud microphysical quantities are obtained from the SEVIRI KNMI-CPP product. With τ and r_e, one can calculate Q_L (Eq. 2.12) and N_d (Eq. 2.13), using $f_{\mathrm{ad}} = 0.4$, and

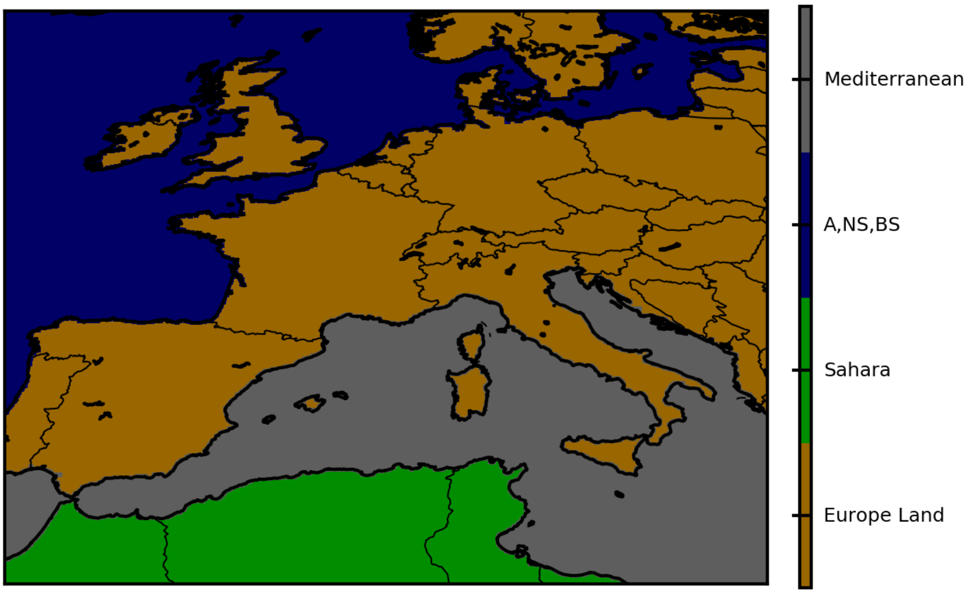

Figure 7.2: Definition of regions for the European cutout: the European land domain (brown), the North African land region (green), the Mediterranean (gray), and the ocean area in the North-West including Atlantic, North Sea and Baltic Sea (blue).

$\Gamma_{\mathrm{ad}} = 1.4 \cdot 10^{-3}\,\mathrm{g\,m^{-4}}$. The latter is estimated from the minimum allowed CTT of 273 K at a CTP of 680 hPa. As it is currently not feasible to get an estimate of f_{ad} for each cloud, it is assumed that clouds are subadiabatic on average. The value is motivated from the median value obtained in Sect. 3 for different Cloudnet stations.

7.4 Aerosol Proxies

To quantify ACI, the ACI metrics as described in Sect. 2.3 are used. They are calculated from an aerosol and a cloud microphysical proxy using Eq. 2.17, Eq. 2.16 and Eq. 2.15.

Three different aerosol proxies are derived from the MACC-II products: 1) the CCN at the CTP level (CCN_{CTP}), 2) the mean CCN between the surface and the CTP level (CCN_m), and 3) the AOD. The required CTP level is obtained from SEVIRI NWCSAF and is matched to the closest MACC pressure level. CCN concentrations are available at three different supersaturations (0.1%, 0.4%, 1.0%). In this study, CCN concentrations at a supersaturation of 0.4% are considered. This is motivated from the findings of Andreae (2009) that CCN concentrations at this supersaturation show a good correlation with the AOD at 500 nm.

For calculating ACI_r and ACI_τ, a constant Q_L is required. Discrete bins of $25\,\mathrm{g\,m^{-2}}$ are used, smaller than for the ground-based case study presented in the previous chapter due to the larger sample size for the satellite observations. For comparison, Kim et al. (2008)

use bin widths of $50\,\mathrm{g\,m^{-2}}$. In satellite studies the Q_L constraint is often neglected due to missing independent observations of Q_L. McComiskey and Feingold (2012) discuss the effect of the Q_L constraint and use a bin width of $10\,\mathrm{g\,m^{-2}}$. Such a small bin size might be too small for our approach regarding the retrieval uncertainties. For the linear regression of the natural logarithms of the aerosol and cloud microphysical proxy, a minimum threshold of at least 25,000 available sampling points is set.

7.5 Results

An impression of the typical aerosol distribution over the investigation domain, the temporal mean CCN concentration between the surface and the 680-hPa level (maximum allowed CTP) for the year 2012 is given in Fig. 7.3. The distribution shows lowest values of CCN concentrations over the Atlantic, the North and Baltic Sea (referred to as North-West ocean region). A gradient exists at the coastal region of West-Europe towards the South-East. Over the Mediterranean, higher CCN concentrations prevail compared to the ocean region in the North-West. The largest ones are found over Eastern Europe. CCN concentrations are expected to be larger over the continental area, where more aerosols are emitted. The dominance of westerly winds over Europe explains the gradient at the coastal region in Western Europe, as clean air is advected from the ocean towards the land.

The annual mean CCN distribution does not reflect variations in the daily distributions of aerosols. The standard deviation of CCN concentrations in Fig. 7.3b shows that the largest variations occur over the land region, likely close to emission sources. But such polluted airmasses are also advected to otherwise more clean areas. From the Twomey hypothesis it is expected that the advection of larger CCN concentrations leads to a change in cloud microphysics and cloud albedo. This effect will be investigated in the following, combining the daily mean aerosol proxies with the temporally higher resolved SEVIRI microphysical properties.

An overview of the mean and standard deviation of cloud and aerosol properties, as well as their correlations for the defined regions is given in Table 7.1. For the whole domain a statistically significant large number of sample points ($>$ 35 million) is available. Lowest sample sizes for individual regions still exceed 1 million.

Similarly to the study of Sekiguchi et al. (2003), the values of CCN_m are plotted against the microphysical properties (N_d, r_e, τ, Q_L) using the median and interquartile range for small CCN_m bins (Fig. 7.4, 7.7). A striking feature is the large IQR of the microphysical properties. While it is expected that aerosol properties are more or less spatially homogeneous, clouds are to first order controlled by dynamical and thermodynamical processes. The large variability of the microphysical properties is typical for ACI studies and can be seen similarly also in Sekiguchi et al. (2003).

It is expected to find an increase of N_d with CCN_m due to the activation of more aerosols. As a consequence, the mean droplet radius is anticipated to decrease. Both effects are herein referred to as the microphysical response. Furthermore, cloud albedo should increase, which is referred to as cloud albedo response. τ is closely related to cloud albedo,

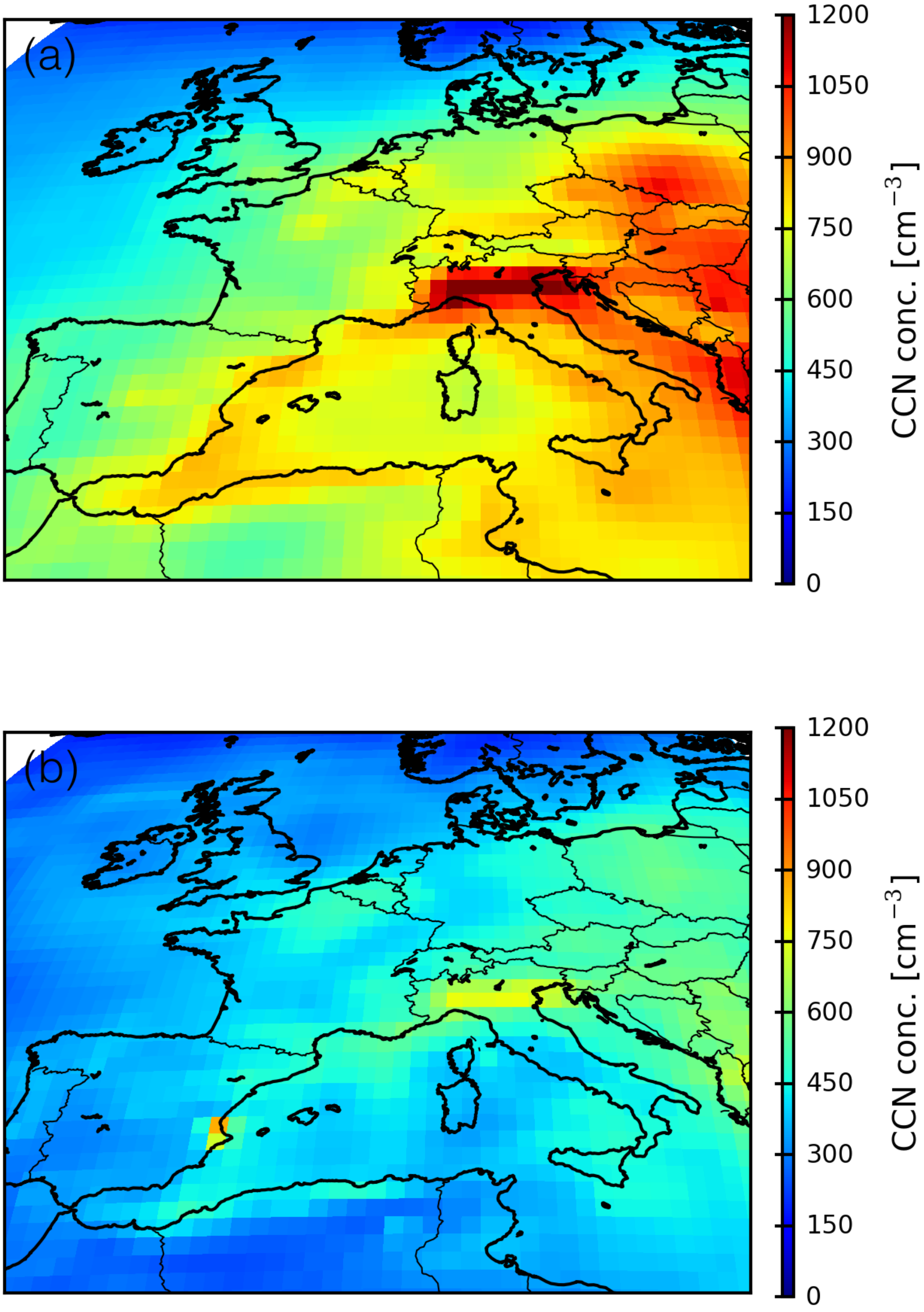

Figure 7.3: Spatial distribution of the (a) mean and (b) standard deviation of the average CCN concentration between surface and the 680-hPa level for the year 2012.

	Full domain	Land	Ocean	Europe Land	Europe West	Europe East	Sahara	Atlantic	Mediterranean
Nr.	35,409,100	17,219,320	18,189,780	15,427,750	11,517,345	3,910,405	1,791,570	14,387,150	3,802,630
τ	15.25 ± 4.79	15.21 ± 4.86	15.29 ± 4.73	15.45 ± 4.79	15.13 ± 4.8	16.37 ± 4.64	13.12 ± 4.91	15.58 ± 4.58	14.22 ± 5.08
r_e	10.03 ± 1.93	9.95 ± 1.92	10.11 ± 1.93	9.95 ± 1.92	10.0 ± 1.93	9.81 ± 1.86	9.95 ± 1.91	10.29 ± 1.92	9.43 ± 1.83
N_d	143.49 ± 74.41	146.93 ± 77.27	140.24 ± 71.44	148.2 ± 77.63	145.37 ± 77.96	156.51 ± 76.06	136.0 ± 73.23	135.79 ± 70.31	157.1 ± 73.16
Q_L	85.06 ± 31.6	83.75 ± 30.93	86.31 ± 32.16	85.06 ± 30.63	83.72 ± 30.63	88.99 ± 30.28	72.44 ± 31.19	89.21 ± 31.4	75.32 ± 32.62
CCN_m	658.64 ± 499.25	711.2 ± 489.29	608.87 ± 503.46	719.17 ± 507.4	637.78 ± 459.97	958.89 ± 561.78	642.59 ± 280.64	520.41 ± 464.81	943.56 ± 503.46
CCN_{CTP}	604.97 ± 435.69	549.43 ± 373.28	657.55 ± 481.6	553.59 ± 384.61	525.79 ± 358.01	635.45 ± 444.0	513.61 ± 252.81	644.68 ± 493.72	706.25 ± 429.17
AOD	0.21 ± 0.1	0.2 ± 0.1	0.23 ± 0.1	0.19 ± 0.08	0.18 ± 0.08	0.21 ± 0.07	0.29 ± 0.18	0.21 ± 0.08	0.28 ± 0.14
$ACI_N(CCN_m)$	0.26	0.23	0.28	0.23	0.27	0.11	0.20	0.31	0.19
$ACI_N(CCN_{CTP})$	0.21	0.21	0.22	0.21	0.23	0.13	0.18	0.22	0.18
ACI_N(AOD)	0.13	0.12	0.17	0.16	0.18	0.02	0.07	0.17	0.05
r(CCN_m,r_e)	−0.32	−0.28	−0.36	−0.28	−0.32	−0.20	−0.22	−0.35	−0.22
r(CCN_m,N_d)	0.35	0.31	0.38	0.32	0.37	0.17	0.22	0.41	0.19
r(AOD,r_e)	−0.1	−0.08	−0.14	−0.11	−0.13	−0.02	−0.02	−0.1	−0.08
r(AOD, N_d)	0.11	0.11	0.13	0.17	0.20	0.02	0.03	0.16	0.00

Table 7.1: Region statistics. For the aerosol and microphysical properties the regional mean ± standard deviation is given. r is the Pearson correlation coefficient between several aerosol and microphysical proxies.

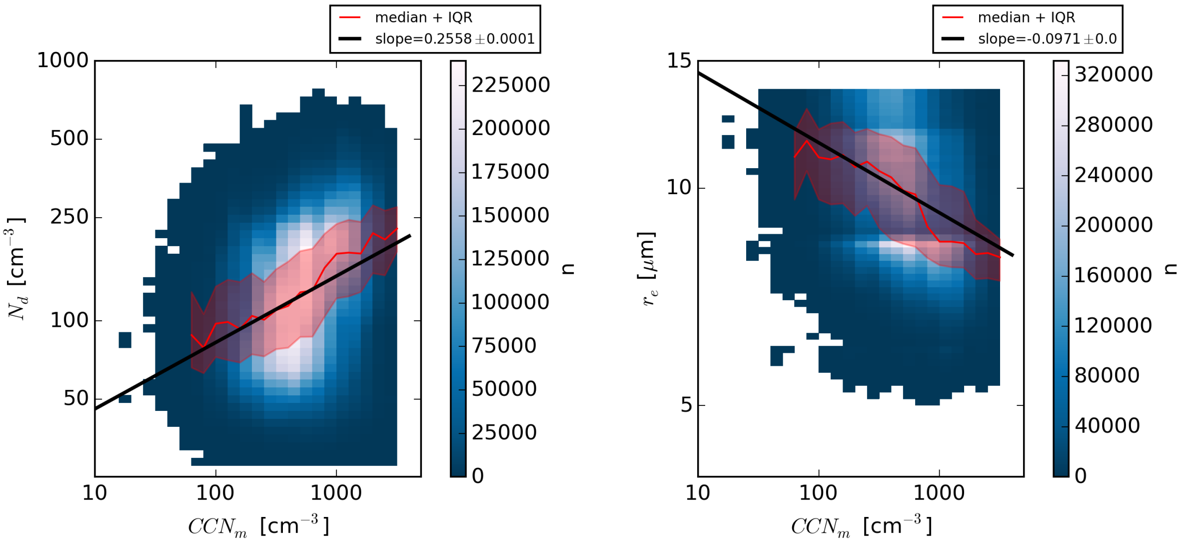

Figure 7.4: 2D histogram in blueish color, showing the number of occurrence of CCN_m and (a) N_d and (b) r_e for the full domain. The linear least square fit is shown as a black line. The red line represents the median values of each CCN_m bin, and the red shaded area the according interquartile range.

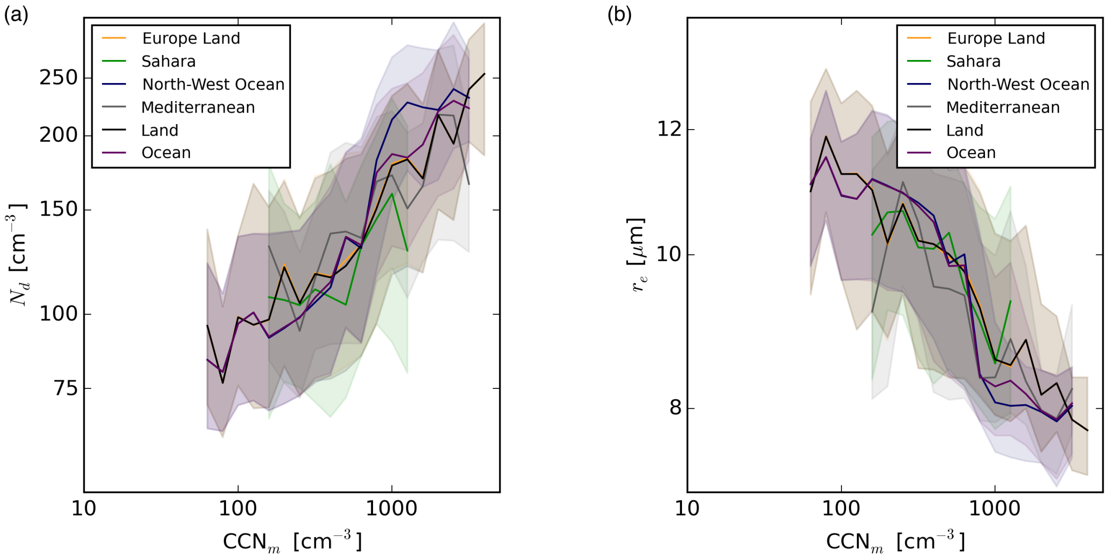

Figure 7.5: Median and interquartile range for the different regions depicted by different colors. (a) CCN$_m$ versus N_d, (b) CCN$_m$ versus r_e.

and is to first order determined by Q_L. Hence, a change of τ due to a change of CCN concentration would be only seen if the amount of liquid water in the cloud is constant.

The median lines for N_d and r_e show a nearly linear dependency on CCN_m (Fig. 7.4). Previous studies report a stronger sensitivity of N_d and r_e to lower CCN_m concentrations and a saturation effect for higher CCN_m (Verheggen et al., 2007). This is not the case here.

ACI_N, utilizing CCN_m, are slightly lower over the whole land area with 0.23, compared to the whole ocean area with 0.28. Using CCN_{CTP} as an aerosol proxy to calculate ACI_N does slightly change the results. In this case, ACI_N are 0.21 and 0.22 for land and ocean region, respectively. Considering AOD for ACI_N results in the lowest values with 0.12 and 0.17. This suggests that AOD is not always a good proxy for ACI studies, corroborating reports from Stier (2016), as it does not always reflect the CCN correctly, especially since it does not give information about the vertical distribution of aerosols, and might result in too low values of the ACI metric.

In agreement with previous studies (e.g., Bréon et al., 2002; Quaas et al., 2004), positive values of ACI_N are obtained. Ma et al. (2014) found that slopes of ACI_N calculated from AOD are overall higher over ocean than over land, implying a stronger response of N_d to the change of aerosol load over the ocean. Although, the linear regression slope in this work gives slightly different results for land and ocean, the average microphysical response looks similar over land and ocean, considering the median values for each CCN_m bin (Fig. 7.5). The microphysical response is quite similar for individual regions. A close look reveals that the ocean region in the North-West is slightly more sensitive to CCN_m concentration changes around $100\,\mathrm{cm}^{-3}$.

To calculate ACI_r, we account for the requirement of constant Q_L. In Fig. 7.6 the ACI_r is shown for different Q_L bins. Considering r_e as the microphysical proxy, a negative slope with an aerosol proxy was found in many previous studies (e.g., Wetzel and Stowe, 1999; Schwartz et al., 2002; Nakajima et al., 2001; Bréon et al., 2002; Quaas et al., 2004), i.e., positive values of ACI_r, consistent with our results. ACI_r is positive for all bins and regions. ACI_r shows some variability over the Q_L bins, which is stronger pronounced over the ocean areas. This variability might be partly attributed to the different sample size for each Q_L bin. Especially the peak for the last Q_L bin is likely explained by missing higher CCN_m concentrations. Missing higher CCN_m concentrations over the southern part of the domain (especially Mediterranean) might be attributed to the negligence of dust as CCN in the dataset of Block and Quaas (2016). We believe that missing higher CCN_m concentrations affect the stability of the slope, leading to an overestimation for the last Q_L bin. Taking the mean ACI_r over all Q_L bins, its value is slightly larger over ocean (0.12) compared to land (0.10), consistent with the result for ACI_N.

In contrast to the clear microphysical response, the detection of a cloud albedo response is a greater challenge. Fig. 7.7 shows the median τ as a function of Q_L bins for the different regions. For the whole land area no clear increase of τ with CCN_m can be obtained. For the ocean area there is a slight trend of increase of τ, which mainly stems from the North-West ocean region. For the latter, an increase in τ for low CCN_m is seen, and a saturation effect for high CCN_m. This region is also the one with the lowest mean CCN_m

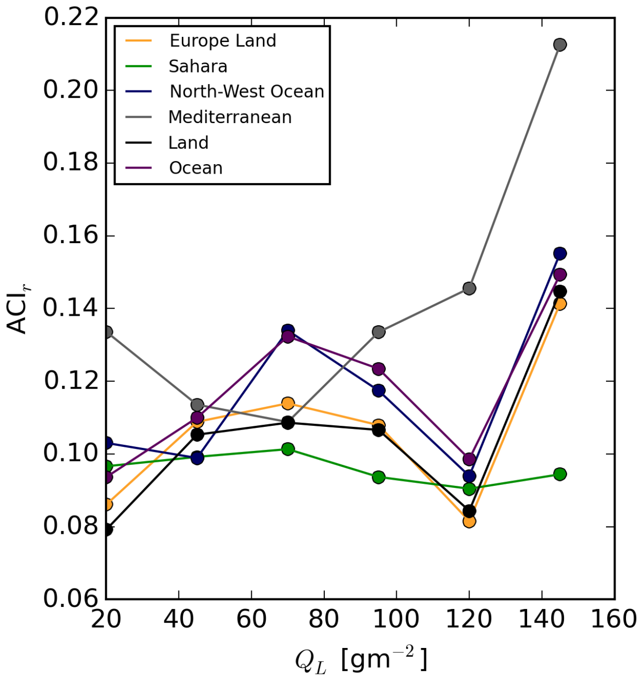

Figure 7.6: ACI_r as a function of Q_L bins, utilizing CCN_m as a microphysical proxy. The differently colored lines depict different regions.

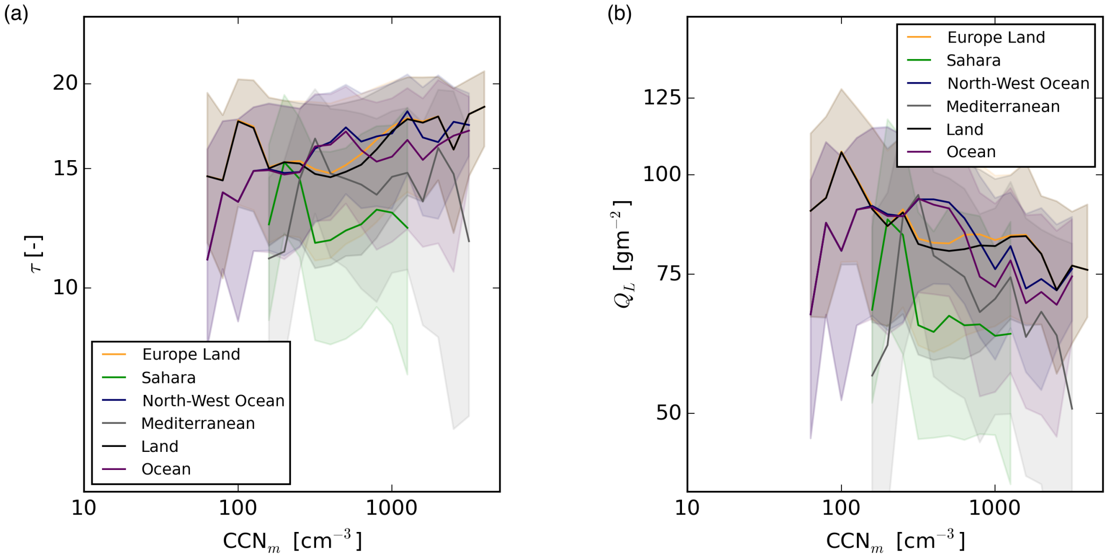

Figure 7.7: Median and interquartile range for the different regions depicted by different colors. (a) CCN$_m$ versus τ, (b) CCN$_m$ versus Q_L.

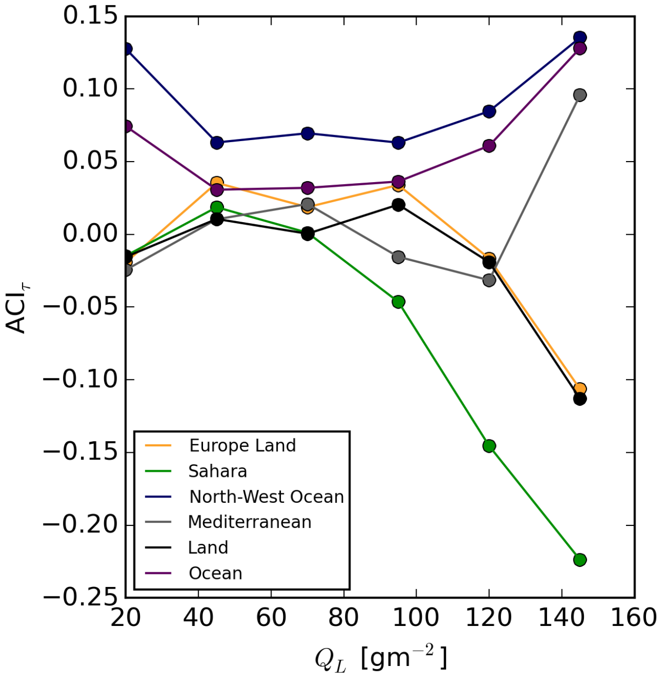

Figure 7.8: ACI_τ as a function of Q_L bins, utilizing CCN_m as an aerosol proxy. The differently colored lines depict different regions.

concentrations, which could mean that the cloud albedo effect is stronger pronounced in regions where usually lower mean CCN concentrations dominate.

On the other hand, Q_L is not constant over the range of CCN_m. Costantino and Bréon (2013) point towards correlations of CCN with Q_L due to various reasons, e.g., due to covariances with local meteorology (Menon et al., 2008). This can be explained as aerosols are determined by the history of the airmass. While larger CCN concentrations lead to the expected microphysical response, the change in cloud albedo, or τ, might not be seen due to changes in Q_L. This means, less Q_L would counteract the increase of τ due to more CCN_m, mitigating the signal of the cloud albedo effect due to aerosol activation. This would also mean that while cloud microphysics are clearly affected, the cloud radiative forcing due to aerosols over the investigation domain is counterbalanced by dynamical effects.

Accounting for constant Q_L by considering discrete bins, for most regions the ACI_τ varies between values of -0.05 to 0.05 (Fig. 7.8), neglecting the extreme values at the edges, which are most likely due to the low sample number in these Q_L bins and therefore less reliable slopes. Quaas et al. (2004) expects only a slight change if the analysis is done at fixed Q_L bins instead of considering all Q_L. As the slope is more reliable for a large sample number over the full range of CCN_m, it might be more useful to consider ACI_N for such studies, which do not require a constraint with Q_L. Furthermore, Q_L is calculated from τ and r_e in this study. It would be desired to have independent Q_L observations. Possible correlations of Q_L with CCN concentrations need to be further investigated, which can be linked to thermodynamic cloud processes as reported from Shao and Liu (2005). Han et al. (1998) report that neglecting the Q_L constraint, there is a difference in the albedo response for optically thick and thin clouds. For optically thick clouds (τ >15) cloud albedo increases with decreasing droplet radius, and vice versa for optically thin clouds.

7.6 Sources of Uncertainty

In the following, different sources of uncertainties will be discussed. First, the representativeness of the aerosol proxies used for the study are discussed. Second, resolution effects will be addressed. And finally, the problem of covariances with thermodynamics will be reviewed.

7.6.1 Representativeness of the Aerosol Proxies

Besides the accuracy of the retrieved microphysical properties, the calculated ACI depends further on the estimate of the aerosol proxies. The accuracy of the CCN concentration depends primarily on the correct representation of mass mixing ratios in the MACC-II reanalysis product (which is evaluated in Block and Quaas (2016)) and an appropriate assumption on aerosol size distributions. A validation of MACC-derived near-surface CCN with in-situ observations from the Atmospheric Radiation Measurement (ARM) network (DMT CCN counter, Roberts and Nenes (2005)) give a correlation of 0.64 and an overestimation of MACC CCN of about 50% (Block and Quaas, 2016). In comparison, the correlation of MODIS-observed AOD to the same surface in-situ observations of CCN results only in a correlation of 0.35. One major difficulty in the derivation process of CCN is the assumption of a globally uniform aerosol size distribution, which might be mitigated in a next version of the MACC reanalysis product (Mann et al., 2010).

Regarding the activation theory of CCN to cloud droplets, it would be desirable to obtain the CCN concentration at CBH. However, the CBH is difficult to be reliably obtained from passive satellite observations. Therefore, in this study CCN concentrations (CCN_m and CCN_{CTP}) were derived utilizing the CTP instead. It was shown in Sect. 5 that there is a bias of the NWCSAF CTP product when validating against Cloudnet stations. On the other hand, comparing the results of ACI_N using CCN_m and CCN_{CTP}, respectively, shows similar results, although there is a slight change in the absolute numbers. It is believed that due to the bias of the CTP product the column average product is more robust. Although the CBH might be estimated using the adiabatic geometrical cloud depth, the comparison utilizing CCN_m and CCN_{CTP} suggests that the expected changes are small, and is predominated by other uncertainties, and was not carried out. Other studies apply the lifted condensation level as a proxy for CBH (e.g., Shao and Liu, 2005), or subsample with CALIPSO observations (Costantino and Bréon, 2013).

Using the mean CCN concentration between surface and the cloud top instead of AOD as an aerosol proxy results in larger values for the ACI metric. As CCN are physically closer connected to the activation process, this suggests that the CCN concentration is better suited as an aerosol proxy for ACI studies, despite its uncertainties. The overall correlation between AOD and CCN_m is 0.42 (Fig. 7.9). From Table 7.2 it can be seen

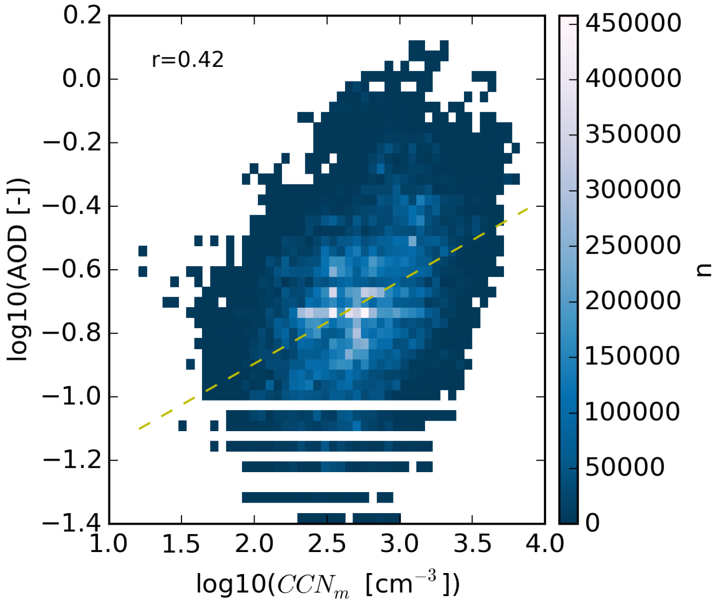

Figure 7.9: 2D histogram of $\log_{10}(CCN_m)$ and $\log_{10}(\text{AOD})$. The yellow dashed line represents a linear least square fit.

Region	r(CCN_m,AOD)
Full domain	0.42
Land	0.39
Ocean	0.46
Europe Land	0.51
Europe West	0.49
Europe East	0.53
Sahara	0.35
North-West ocean	0.4
Mediterranean	0.43

Table 7.2: Correlation between CCN_m and AOD for different regions.

that the AOD is not necessarily a good proxy for the mean CCN concentrations in the boundary layer in all regions. In the Sahara region the highest mean AOD is found, while the mean CCN_m concentration is as low as at oceanic regions. This can be explained as over the Sahara region more dust is present, which is not accounted for as a CCN in the model, but attributes to the total AOD. It is currently under debate how dust attributes to CCN concentrations (Dusek et al., 2006; Karydis et al., 2011).

7.6.2 Resolution Effects

Using N_d as a cloud microphysical proxy, McComiskey and Feingold (2012) and Schmidt et al. (2014) report a dependence of the ACI values on the relation of observation scale to the process scale. Values for ACI_N range from 0.1 (Bréon et al., 2002) for global satellite studies to the maximum theoretically value of 1 in combined in-situ and model experiments (Ditas, 2014). This can be partly also attributed to the results from Schmidt et al. (2015), that ACI is stronger seen at cloud base than over the whole cloud column.

As a long time period and a larger domain with variable synoptic conditions and seasonal effects is investigated in a statistical sense, the ACI will not only represent the cloud droplet activation process from aerosols alone, but the full response due to microphysical interaction processes. According to McComiskey and Feingold (2012) those problems are enhanced if no constraint with respect to Q_L is made for calculating ACI_r and ACI_τ. In this context, utilizing daily mean CCN concentrations and assuming them to be temporally constant, might lead to further uncertainties in the resulting ACI.

Connected to resolution effects is also the sensitivity of ACI to cloud fraction (Gryspeerdt and Stier, 2012). Su et al. (2010) state that biases due to incorrectly considered cloud fraction within a given grid box will cause an overestimation of the ACI metric. With the resolution of SEVIRI in the observation domain of 4 km x 6 km, this is potentially an issue, which should be mitigated with the next generation satellite MTG that provides a higher spatial resolution.

Several studies discuss aerosol effects on clouds by looking at spatial distributions of aerosols and microphysical properties that are averaged over even longer time periods. For example, Bréon et al. (2002) relate global mean values of AI and r_e over a period of 3 months to obtain the microphysical response and report an ACI_r of 0.085. Bulgin et al. (2008) argue that such seasonal averages are suitable to study ACI. In this context, the correlations of aerosol and microphysical properties for larger regional and longer temporal averages are investigated from our dataset similar to their study. The question is if the cloud microphysical response is also detectable on this larger scale, given the rather small domain size compared to global studies. The mean CCN_m values differ for the individual regions (Table 7.1). Over the ocean the mean CCN_m concentration is around $100\,\mathrm{cm}^{-3}$ lower compared to the land region. The lowest concentration is found over the North-West ocean region, while over the Mediterranean CCN_m concentrations are quite large. This is consistent with the CCN distribution shown in Fig. 7.3, where the CCN concentration generally increases towards the South-East. If the European land region is further split up into a Eastern and Western region by separating the land masses in the middle of the domain, the highest mean values are found in Eastern Europe.

The differences in mean CCN_m concentration are clearly connected to differences in r_e and N_d and result in good correlations of area mean properties. For example, over Eastern Europe the mean CCN_m concentration is larger with smaller mean r_e and larger mean N_d compared to the Atlantic. The cloud albedo response is not clearly manifested also at the larger scale. While a good correlation/anti-correlation between the region-mean CCN_m and mean N_d or mean r_e is obtained (0.94, –0.87), the correlation of the different region-mean CCN_m with τ is low (0.18). This is likely due to the high correlation of region-mean τ with mean Q_L (0.95). This points to the main influence of τ being cloud dynamical processes. If we calculate ACI_N from this aggregated sample, we end up with a value of 0.25, which is quite similar to the one obtained from the original scale. According to McComiskey and Feingold (2012), aggregation increases the correlation. This is also seen here for the correlation when taking the regionally averaged dataset.

Uncertainties might also arise due to the different sample numbers for the individual regions. Given the overall similar shape of distributions in the different regions, despite the difference in sample number, we believe this has only a minor impact.

Overall, by looking at a larger scale from a longer temporal and regional average, the microphysical response is still observed, although the mean differences of microphysical properties are small. From the standard deviations of aerosol and microphysical properties, it is expected that the temporal variability is more significant than the spatial difference.

7.6.3 Covariances with Thermodynamics

As already pointed out in this thesis, the effect of mixing can exacerbate the quantification of ACI. In the study of Kim et al. (2008) thicker clouds with higher Q_L tend to be more subadiabatic. This is also in agreement with our results showing a strong dependence of f_{ad} on H.

Given the spatio-temporal variability of the mixing process, estimates of adiabaticity for liquid clouds are useful. While statistics have been derived for individual stations within this work, it is currently difficult to obtain typical adiabaticity for a large domain with high accuracy as required to correct ACI for entrainment.

Shao and Liu (2006) tried to account for mixing effects using other observations. They assume inhomogeneous mixing for stratocumulus clouds, but at the same time N_d being constant with height. As it is shown in our study, mixing is typically strongest pronounced near the cloud top. The assumption of Shao and Liu (2006) is valid for homogeneous mixing, but not for inhomogeneous mixing. They state that the entrainment effect may have a similar impact on the calculation of the ACI metric as the effect of aerosol activation.

Currently it is difficult to disentangle cloud dynamics, local meteorology and aerosol effects on clouds, as further covariance effects can occur. Also the cloud geometrical depth comes into play for subadiabatic clouds (Shao and Liu, 2005). Furthermore, a dependence of ACI on cloud regimes is reported in several studies, connected to cloud-fraction and possible cloud-retrieval biases.

7.7 Discussions and Conclusions

The ACI metrics following Feingold et al. (2001) and McComiskey and Feingold (2012) were quantified from SEVIRI observations and CCN concentrations from the MACC-II reanalysis (Block and Quaas, 2016). Different aerosol proxies were compared and uncertainties were discussed.

Consistent with previous studies, our results suggest that aerosols affect cloud microphysical properties. From the statistical method, the microphysical response is clearly obtained for the European area. Given the synergistic MACC-SEVIRI dataset, this effect is slightly stronger over ocean than over land. ACI_N utilizing the average CCN concentration between surface and CTP (CCN_m) is 0.28 and 0.23 over ocean and land areas, respectively. Anyhow, the median relationship between CCN_m and N_d or r_e is similar for all regions. Utilizing CCN_m or CCN_{CTP} as an aerosol proxy instead of CCN_{AOD} leads to twice as large ACI_N values. It might be worth to also consider the aerosol index (AI), which is reported to be a better proxy for CCN than AOD. Results for ACI_r are consistent with ACI_N, with slightly larger values over ocean (mean of 0.12 over all Q_L bins) than over land (0.10). These values are overall in agreement with previous satellite-based studies.

In contrast to the cloud microphysical response, the cloud albedo effect is not clearly pronounced. Positive values of ACI_τ are mainly found over the North-West ocean area, while the signal over the other regions is more difficult to interpret. The results give indications that the cloud albedo effect is stronger pronounced in regions where usually lower CCN concentrations dominate, consistent with reports from Ma et al. (2014). As a drawback of the applied method, especially for longer-term satellite observations, ACI cannot easily be interpreted as pure interaction between aerosols and clouds due to covariances of aerosols and local meteorology, cloud fraction, and mixing effects. It is, however, directly connected to the ERFaci (effective radiative forcing due to ACI and rapid adjustments) as introduced in the latest IPCC report (Boucher et al., 2013). Cloud optical depth is to first order determined by Q_L, which is able to obscure aerosol effects on clouds. The amount of reflected energy is approximately two-and-a-half times more sensitive to changes in Q_L than to changes in N_d (Boers and Mitchell, 1994). Therefore, cloud dynamical processes, such as entrainment, are very important. The better quantification of these covariances is a major difficulty for current ACI studies (Costantino and Bréon, 2013). Earlier in this work, the spatio-temporal variability of the mixing process has been already pointed out, complicating interpretation and possible corrections of the ACI metric for optical depth. Modeling studies trying to obtain ACI have to deal with the problem of accounting for realistic mixing processes, which can have a significant impact on cloud albedo as shown by Chosson et al. (2007).

Currently only one year of data was investigated for the European domain. An extension of the presented study, utilizing the derived CCN from MACC for other regions and longer time periods might be promising to investigate, e.g., larger-scale regional differences and/or seasonal trends.

8 Summary, Conclusions and Outlook

This closing chapter provides a summary of the central results of this thesis, and lessons learned from the processed datasets in terms of uncertainties relevant for quantifying aerosol-cloud interactions. It also addresses open questions that should be investigated in future studies.

Aerosols directly influence the radiation budget, and also indirectly due to their interaction with clouds. Aerosols serve as CCN and change the number of cloud droplets, subsequently altering further cloud properties, such as the cloud albedo (Twomey effect). These aerosol-cloud interactions (ACI) are still poorly constrained in terms of their general relevance for climate. They are not easily quantified due to the complex interaction of aerosol composition and distribution, cloud microphysics, and meteorology. They have been investigated from different perspectives and scales such as in-situ, ground-based remote sensing and satellites, leading to a large variability of reported ACI metrics (as introduced by Feingold et al. (2001)). This demonstrates the need to closer investigate uncertainties that influence the quantification of ACI on the different scales. Within this thesis, we have addressed several major topics connected to the problem of quantifying ACI, such as entrainment (Chapter 3), retrieval uncertainties (Sect. 4.1) and the consistency of cloud key parameters over different scales (satellite vs. ground in Chapter 5, and ground vs. in-situ in Sect. 6.2). In this context, a novel OE framework has been developed to improve the retrieval of N_d as a key microphysical property from ground-based remote sensing (Chapter 4). This work also has provided one of the first studies quantifying ACI over Europe utilizing data from Meteosat SEVIRI in combination with reanalysis data from MACC-II CCN concentrations and AOD (Chapter 7).

The given uncertainties when quantifying ACI from different scales have motivated four research questions, which have been formulated in the motivation (Chapter 1). Their discussion is summarized in the following, also given possibilities for further extension of this work.

8.1 Is the Adiabatic Cloud Model Suitable to Describe Liquid Clouds and Applicable for ACI Investigations?

An adiabatic cloud model is typically applied for obtaining cloud microphysical properties from passive satellite observations for single-layer, non-drizzling liquid clouds (e.g., Bennartz, 2007; Merk et al., 2016). It assumes a moist adiabatic rising parcel, leading to a linear increase of the liquid water content (q_L) with height above cloud base. Observations from previous in-situ studies have shown, however, that clouds are in most cases subadiabatic, which is mainly caused by entrainment processes. This complicates the quantification of ACIs. Therefore, it is important to better understand and quantify mixing processes in liquid clouds.

In this work, it has been confirmed that liquid clouds observed at ground-based Cloudnet stations in Europe are typically subadiabatic, consistent with results of previous studies (e.g., Boers et al., 2006; Kim et al., 2008). For the quantification of mixing processes usually a subadiabatic factor f_{ad} is applied (Kim et al., 2008), relating the observed liquid water path Q_L to the maximum possible value for adiabatic clouds of the same geometrical depth. f_{ad} can be obtained for ground-based supersites. Given the measurement uncertainties of about $25\,\mathrm{g\,m^{-2}}$ in Q_L and 60 m in geometrical depth, the resulting f_{ad} remains uncertain for thin clouds (about $< 300\,\mathrm{m}$). It has been found that entrainment varies strongly with time, but with indications of average statistics showing slightly lower mean f_{ad} values with smaller standard deviation for coastal sites compared to continental sites. Median values of f_{ad} range from 0.35 to 0.48 for different stations in the Cloudnet network with respective standard deviations of 0.12 to 0.22. The investigated q_L profiles typically exhibit a drastic reduction near the cloud top due to entrainment. A model that can describe the q_L reduction at cloud top might be considered in future applications, although by accounting for f_{ad} the adiabatic cloud model seems to be a sufficiently simple description for the liquid clouds seen in our samples.

To obtain an estimate of f_{ad} over larger domains, it has been attempted to find characterizations and parameterizations by other quantities. f_{ad} is clearly dependent on cloud geometrical depth, with thicker clouds being less adiabatic, consistent with previous reports (e.g., Warner, 1955; Min et al., 2012). Currently it remains challenging to infer geometrical depth from passive satellite sensors. The vertical cloud growth is hampered by inversion layers. An increased likelihood for higher f_{ad} with stronger inversion strength (using temperature increase as a proxy) has been seen. Temperature profiles over larger domains are available from NWP models. Previous reports of a correlation of updraft strength with f_{ad} (Schmidt et al., 2014) could not have been fully reproduced.

It is concluded that with the highly variable nature of entrainment, it is currently difficult to assess instantaneous cloud adiabaticity over a large domain as required for ACI quantification. This leads to the typical assumption of a fixed subadiabatic factor in current ACI studies, which remains a major source of uncertainty. Retrieving cloud geometrical depth from active satellite sensors or oxygen A-band observations (e.g., Yang et al., 2013; Fischer et al., 1991), in combination with Q_L, might give opportunities to obtain f_{ad} also from a satellite perspective. Alternatively, from the investigated dependence of f_{ad} on other properties a typical statistical range of f_{ad} might be inferred. It should be further explored if there is a cloud-regime dependence. A larger network of ground-based observation sites, as planned within the ACTRIS (Aerosols, Clouds, and Trace gases Research InfraStructure Network) project[1], will give the possibility to validate the difference that has been seen for sites located at the coastal region and sites on the continent.

While the investigation of cloud adiabaticity of liquid clouds is only one aspect for a better quantification of ACI, the importance of the role of entrainment has been stressed several

---

[1] www.actris.eu

times in previous studies (e.g., Shao and Liu, 2006; Kim et al., 2008; Min et al., 2012) and is therefore a relevant piece in the puzzle.

8.2 How Accurately can Cloud Droplet Number Concentration be Retrieved from Ground-Based Remote Sensing?

Cloud droplet number concentration (N_d) is directly connected to the activation process of aerosols to cloud droplets via CCNs, and it is therefore desired to retrieve this quantity from ground-based remote sensing with high accuracy. It has been shown that retrieving N_d from combined radar-radiometer observations is very sensitive to a-priori assumptions, especially to the width of the DSD. This demonstrates the need to reduce the uncertainties of this quantity to be useful for ACI studies. It also suggests that retrieval methods need to be thoroughly reviewed and enhanced to include more observational constraints.

In this work, a novel Optimal Estimation framework has been developed to account for additional observations, and has been tested utilizing synthetic cloud profiles. The gain in information content by adding observations of optical depth τ has been explored. τ can be obtained from passive spectral measurements of solar radiation, for example from ground-based MFRSR or 2NFOV instruments, but also from satellite observations. The assumption about the width of the DSD remains a large source of uncertainty in the OE retrieval approach with up to 150% relative uncertainty of N_d, while for the radar-radiometer approach the uncertainty in the retrieved N_d even reaches up to 200%. A sensitivity study has shown a general reduction of uncertainties by 10–20% including observations of optical depth. The OE framework with additional τ observations has turned out to be superior also for realistic cloud profiles obtained from ICON LES compared to the more simple radar-radiometer approach described in Brandau et al. (2010). It should be noted that τ obtained from the instruments mentioned above is only available during daytime hours.

Additional observations that are able to better constrain the width of the DSD (such as Doppler velocity (Rémillard et al., 2013)) should be considered in the future. The OE retrieval algorithm can be further enhanced by, e.g., improving the assumed a-priori state taking into account typical cloud profiles from LES or typical observations. In a next step, the OE method should be tested for suitable real-case conditions given additional in-situ measurements of N_d and q_L profiles for validation of retrieval results. For that, it is helpful to receive more data from field campaigns such as the HOPE-Melpitz experiment that combines remote sensing with in-situ observations. Equipping more ground sites with instruments to measure solar radiation and including those into the retrieval in combination with cloud radar, ceilometer and microwave radiometer should be striven for.

8.3 How Consistent are Cloud Key Properties Relevant for ACIs from Observations at Different Scales?

Investigating the difference of cloud properties observed at different scales and from different perspectives is an important step to check the consistency of cloud microphysical properties from those perspectives and to quantify resulting uncertainties in ACI studies.

Contrasting ground-based retrievals of N_d and r_e with in-situ observations for one case study during HOPE-Melpitz has shown a good agreement (18% and 8% mean deviation, respectively), given the retrieval uncertainties and possible sampling of different cloud portions. Unfortunately, only one case study of collocated observations from ground-based remote sensing instruments and in-situ measurements has been available for this study, stressing the need for more such field experiments.

Contrasting the cloud quantities obtained from SEVIRI with those from ground-based sites within the Cloudnet network, RMSD of Q_L and τ retrieved from satellite and ground have been found to be about $65\,\mathrm{g\,m^{-2}}$ and 14, respectively. On average, no significant bias has been seen for both quantities, indicating that larger scale statistics are comparable from both perspectives. Given a strict sampling approach, this suggests that cloud properties from both perspectives should be consistent for ACI studies in a statistical sense. In contrast, for individual cases larger differences have been found and can be explained by inhomogeneities and resolution effects. A larger bias (478 m) has been obtained for the CTH product from the NWCSAF algorithm. It is likely explained from the NWP model data utilized in this work, that does not adequately represent temperature inversions. With a more accurate CTH product, an estimate of H utilizing CBH from the DWD ceilometer network, and an estimate of f_{ad} using Q_L and H might be possible. MTG might also give new possibilities to overcome problems of cloud geometrical depth retrievals (e.g. using the oxygen A-band (Yang et al., 2013; Fischer et al., 1991)).

8.4 How well can ACIs be Quantified for the European Region?

To address the scale dependence of the ACI metric (McComiskey and Feingold, 2012), the focus in this study has been set on the ground and satellite perspective.

The possibilities to quantify ACI from the ground perspective following the method of Sarna and Russchenberg (2016) have been explored by means of a case study. The ACI metric has turned out to be quite sensitive to the integration height of the attenuated backscatter coefficient. The small sample size of a single case together with possible retrieval uncertainties has resulted in very large values of the ACI metric ($ACI_N = 1.66 \pm 0.18$). Similar studies usually report smaller values between 0.3 and 0.8 (Schmidt et al., 2015). For more reliable values larger statistics need to be applied in a further step.

A large scale ACI quantification approach has been conducted for SEVIRI observations and CCN concentrations available from MACC reanalysis data (Block and Quaas, 2016) for the year 2012. Using the average CCN concentration between the surface and the CTP, a clear microphysical response has been obtained for the European region. The effect is slightly stronger over ocean than over land with ACI_N of 0.28 and 0.23, respectively, supporting results of Ma et al. (2014). The range of the obtained values is in agreement with previous satellite-based ACI studies (Schmidt et al., 2015). Values of ACI_N are only half as big utilizing AOD as an aerosol proxy, indicating that AOD is not an ideal proxy for CCN concentrations. While large scale observations of CCN are not available, the use of assimilated model predictions of CCN might be worthwhile to consider for future ACI investigations on these scales. In contrast to the cloud microphysical response, the cloud albedo effect is not as clearly pronounced. Positive values of ACI_τ have been mainly found over the ocean area in the North-West of the domain, while the signal over the other regions is more difficult to interpret. The results give indications that the cloud albedo effect is more clearly seen in regions where lower mean CCN concentrations dominate. Especially for longer-term satellite observations, the ACI metrics cannot easily be interpreted as the pure interaction between aerosols and clouds due to the covariances of aerosols, local meteorology, cloud fraction, and mixing. It is, however, directly connected to the ERFaci (effective radiative forcing due to ACI and rapid adjustments) as introduced in the latest IPCC report. The better quantification of covariances is a major difficulty for current ACI studies (Costantino and Bréon, 2013), and requires further work. It is an important step towards determining the radiative forcing from the anthropogenic CCN fraction. The available SEVIRI observations collocated with MACC-II CCN concentrations over a larger domain and for more than 10 years, enable to extend the study for other regions and longer time series in order to explore also seasonal trends. Especially the difference of microphysical and albedo response over land and ocean area should be examined in more detail, given data from a larger domain. New possibilities might arise with upcoming measurement sensors. The spatial resolution of microphysical products from MTG with 1 km is in closer agreement with the suggestions given from McComiskey and Feingold (2012) and might be able to mitigate issues related to the scale dependence. Comparing the values obtained from satellite- and ground-based studies, the previously reported uncertainties have to be taken into account.

In summary, this work has enhanced our understanding of major uncertainties relevant for the quantification of aerosol-cloud interactions, and has provided possibilities for improvements in future studies. The focus of this work has been on processed observational datasets of liquid clouds on different scales. The presented results are a step forward towards a better constraint of the radiative effect of aerosols and clouds in the changing climate.

Appendix

A1. Gamma Size Distribution

The three-parameter Gamma distribution $\eta(r)$ is often used to approximate the distribution of cloud droplets with radius r:

$$\eta(r) = A r^{\beta} \exp\left(-\Lambda r\right). \tag{8.1}$$

An alternative form is given by Hansen and Travis (1974). It employs the effective radius r_e, its effective variance ν, and the total number density of droplets N_d and is therefore easier to physically interpret:

$$\eta(r) = \frac{N_d}{\Gamma(\frac{1-2\nu}{\nu})\, r_e\, \nu^{\frac{1-2\nu}{\nu}}} \left(\frac{r}{r_e}\right)^{\frac{(1-3\nu)}{\nu}} \exp\left(-\frac{1}{\nu}\frac{r}{r_e}\right), \tag{8.2}$$

with

$$\begin{aligned} \beta &= \frac{1-3\nu}{\nu}, \\ \Lambda &= \frac{1}{r_e \nu}, \\ A &= \eta_0 \frac{\Lambda^{\beta+1}}{\Gamma(\beta+1)}, \end{aligned} \tag{8.3}$$

and Γ being the Gamma function.

The n-th moments of the Gamma size distribution can be derived following Eq. 2.1 (Petty and Huang, 2011):

$$\begin{aligned} M_{\eta,n} &= A \int r^{n+\beta} \exp\left(-\Lambda r\right) dr \\ &= A \frac{\Gamma(\beta+n+1)}{\Lambda^{(\beta+n+1)}}. \end{aligned} \tag{8.4}$$

A2. Log-Normal Size Distribution

A log-normal distribution can also be assumed. The log-normal distribution is given in the following form (e.g. Rémillard et al., 2013):

$$\zeta(r) = \frac{N_d}{\sqrt{2\pi}\sigma_x r} \exp \frac{-\left(\ln r - \ln r_0\right)}{2\sigma_x^2}, \tag{8.5}$$

where r_0 is the median radius, and σ_x the log-normal width.

The n-th moment of the log-normal distribution is given by:

$$M_n = \int_0^\infty r^n \zeta(r) dr = N_d \, r_0^n \, \exp\left(\frac{n^2}{2}\sigma_x^2\right). \tag{8.6}$$

A3. Derivation of Moments of the DSD

The zeroth moment of a size distribution M_0 is the total droplet number concentration N_d, obtained by integrating over all radii:

$$N_d = \int_0^\infty f(r)\, dr. \tag{8.7}$$

If a probability distribution for the droplet size is sought, N_d has to be set to one so the integral is normalized to unity.

The first moment (normalized by the zeroth moment) M_1 yields the mean radius r_M of the DSD. In other words, M_1 acts as a weighting function for calculating the mean:

$$r_M = \int_0^\infty r\, \eta(r)\, dr, \tag{8.8}$$

Setting the total cross-sectional area of a monodisperse DSD with a droplet density N_d in a volume V equal to that of a size distribution in the same volume, we obtain:

$$N_d\, V\, \pi\, r_a^2 \;=\; V\, \pi \int_0^\infty r^2 f(r)\, dr. \tag{8.9}$$

In addition, the area-equivalent radius r_a can be derived from the second moment of the DSD:

$$r_a = \sqrt{\frac{1}{N_d}\, M_2}. \tag{8.10}$$

For radiative transfer, the physical relevance of r_a results from the link of the extinction cross section $\alpha_{ext}(r)$ for a droplet to its radius r. For solar wavelengths and typical cloud droplet sizes, the scattering efficiency Q_e is nearly constant and close to 2. Hence, the extinction of the cloud droplet distribution becomes:

$$\alpha_{ext} = \int_0^\infty Q_e(r) \pi r^2 \eta(r) dr = 2\pi\, N_d\, r_a^2 = 2\pi\, M_2. \tag{8.11}$$

Similar to the area-equivalent radius, a volume-equivalent radius r_v can be defined from the third moment of the droplet size distribution:

$$r_v = \sqrt[3]{\frac{1}{N_d} M_3}. \tag{8.12}$$

It is related to the liquid water content q_L through:

$$q_L = \frac{4\,\pi}{3}\, N_d\, \rho_w\, r_v^3 = \frac{4\,\pi\,\rho_w}{3}\, M_3, \tag{8.13}$$

with ρ_w being the density of liquid water.

Combining Eq. 8.11 and Eq. 8.13, the extinction α_{ext} is obtained:

$$\alpha_{ext} = \frac{3}{2\,\rho_w}\,\frac{q_L}{r_e}, \tag{8.14}$$

which no longer depends directly on the effective variance ν of the DSD. The latter motivates the wide use of the effective radius in remote sensing. The standard definition of the effective radius r_e is consistent with (Hansen and Travis, 1974):

$$r_e = \frac{r_v^3}{r_a^2} = \frac{M_3}{M_2}. \tag{8.15}$$

Given the extinction profile, the optical depth is obtained by integration over the cloud geometrical depth, i.e., from cloud base height (z_b) to cloud top height (z_t):

$$\begin{aligned} \tau &= \int_{z_b}^{z_t} \alpha_{ext}(z)\, dz && (8.16)\\ &= \int_{z_b}^{z_t} 2\,\pi\, N_d\, r_a^2(z)\, dz. && (8.17) \end{aligned}$$

The effective radius can be linked to the mean volume radius (r_v) with the following relationship:

$$r_e^3 = k_2^{-1}\, r_v^3. \tag{8.18}$$

Therefore the factor k_2 is given by:

$$k_2 = \frac{r_v^3}{r_e^3} = r_v^3 \left(\frac{r_a^2}{r_v^3}\right)^3. \tag{8.19}$$

The factor k_2 is only a function of the width of the DSD. $\beta = 7$ ($\nu = 0.1$) considering the Gamma size distribution[2] is a typical value for water clouds and results in $k_2 = 0.72$. If we consider $\sigma = 0.35$ as a typical value using the log-normal distribution (e.g. Frisch et al., 1995), then k_2 is 0.69.

In case of the Rayleigh approximation, the radar reflectivity is given by the 6th moment:

$$Z = 2^6 M_6. \tag{8.20}$$

This is valid for cloud droplets in the microwave spectrum.

---

[2] http://nit.colorado.edu/shdom/shdomdoc/cloudprp.html

The radar reflectivity can be expressed as a function of N_d, k_6, and q_L (Brandau et al., 2010):

$$Z = \frac{36}{\pi^2\,\rho_w^2} k_6 \frac{q_L^2}{N_d}, \tag{8.21}$$

where k_6 is defined by

$$k_6 = \frac{M_6}{M_3^2}. \tag{8.22}$$

A4. Adiabatic Increase of Liquid Water Content

The adiabatic increase of the liquid water content mixing ratio A_{ad} is obtained from the first law of thermodynamics and the Clausius-Clapeyron equation:

$$A_{\text{ad}} = \frac{dq_L}{dz} = -\left(1 - \frac{c_p T}{L_v \epsilon}\right)\left(\frac{c_p T}{L_v \epsilon} + \frac{L_v q_s \rho_a}{(p - e_s)}\right)^{-1}\left(\frac{\rho_a g \epsilon}{(p - e_s)^2}\right), \tag{8.23}$$

with air pressure p, air temperature T, saturation vapour pressure e_s, heat capacity c_p (here: heat capacity of water), latent heat $L_v = 2.5 \cdot 10^6\,\mathrm{J\,kg^{-1}}$, the constant $\epsilon = 0.622$, and saturation mixing ratio q_s. The latter is defined by:

$$q_s = \frac{\epsilon e_s}{(p - e_s)}. \tag{8.24}$$

Γ_{ad} is given as:

$$\Gamma_{\text{ad}}(T, p) = A_{\text{ad}}(T, p)\rho_a(T, p), \tag{8.25}$$

with ρ_{a} being the air density.

A5. Gaussian Error Propagation

Relative errors are calculated for a number of properties applying Gaussian error propagation. It is assumed that errors are normally distributed and uncorrelated.

The relative error for the subadiabatic factor obtained from H and Q_L (Eq. 2.4, Sect. 2.2) is calculated with Gaussian error propagation:

$$\left(\frac{\Delta f_{\text{ad}}}{f_{\text{ad}}}\right)^2 = \left(\frac{\Delta Q_L}{Q_L}\right)^2 + \left(2\,\frac{\Delta H}{H}\right)^2. \tag{8.26}$$

The relative error for optical depth τ obtained from the adiabatic cloud model (Eq. 2.9, Sect. 2.2) is given as:

$$\left(\frac{\Delta \tau}{\tau}\right)^2 = \left(\frac{\Delta k_2}{3k_2}\right)^2 + \left(\frac{\Delta N_d}{3N_d}\right)^2 + \left(\frac{\Delta f_{\text{ad}}}{6f_{\text{ad}}}\right)^2 + \left(\frac{\Delta \Gamma_{\text{ad}}}{6\Gamma_{\text{ad}}}\right)^2 + \left(\frac{5\Delta Q_L}{6Q_L}\right)^2. \tag{8.27}$$

Similarly for the effective radius, calculated from the adiabatic cloud model (Eq. 2.11, Sect. 2.2), we find:

$$\left(\frac{\Delta r_e}{r_e}\right)^2 = \left(\frac{\Delta f_{\text{ad}}}{6f_{\text{ad}}}\right)^2 + \left(\frac{\Delta \Gamma_{\text{ad}}}{6\Gamma_{\text{ad}}}\right)^2 + \left(\frac{\Delta Q_L}{6Q_L}\right)^2 + \left(\frac{\Delta k_2}{3k_2}\right)^2 + \left(\frac{\Delta N_d}{N_d}\right)^2. \tag{8.28}$$

The relative error for N_d, calculated from the radar-radiometer approach following (Brandau et al., 2010) (Eq. 2.28, Sect. 2.5.2) is given as:

$$\left(\frac{\Delta N_d}{N_d}\right)^2 = \left(2\frac{\Delta Q_L}{Q_L}\right)^2 + \left(\frac{\Delta k_6}{k_6}\right)^2 + \left(\frac{\Delta iZ}{iZ}\right)^2, \tag{8.29}$$

and defining $iZ = \int \sqrt{Z(z)}\,dz$.

The relative errors of Q_L, N_d, and H derived from passive satellite observations and assuming the adiabatic cloud model (Eqs. 2.13, 2.14 and 2.12, Sect. 2.2), are given by:

$$\left(\frac{\Delta Q_L}{Q_L}\right)^2 = \left(\frac{\Delta \tau}{\tau}\right)^2 + \left(\frac{\Delta r_e}{r_e}\right)^2, \tag{8.30}$$

and

$$\left(\frac{\Delta N_d}{N_d}\right)^2 = \left(\frac{\Delta k_2}{k_2}\right)^2 + \left(\frac{\Delta \Gamma_{\text{ad}}}{2\Gamma_{\text{ad}}}\right)^2 + \left(\frac{\Delta f_{\text{ad}}}{2f_{\text{ad}}}\right)^2 + \left(\frac{\Delta \tau}{2\tau}\right)^2 + \left(\frac{5\Delta r_e}{2r_e}\right)^2, \tag{8.31}$$

and

$$\left(\frac{\Delta H}{H}\right)^2 = \left(\frac{\Delta\Gamma_{\rm ad}}{2\Gamma_{\rm ad}}\right)^2 + \left(\frac{\Delta f_{\rm ad}}{2f_{\rm ad}}\right)^2 + \left(\frac{\Delta\tau}{2\tau}\right)^2 + \left(\frac{\Delta r_e}{2r_e}\right)^2 . \tag{8.32}$$

A6. Reconstruction of the DSD from ICON LES

Starting with the simulated moments (N_d, q_L) in each model layer, we follow the underlying assumption of the mass distribution in Seifert and Beheng (2005), which is a generalized gamma distribution:

$$\int f(x_m)dx_m = \int A\, x_m^{\beta_m} \exp{(-\Lambda_m x_m^{\mu})}, \tag{8.33}$$

where x_m denotes the mass of a cloud droplet and $f(x_m)$ the mass distribution function. Its n-th moment is given by:

$$M_n^m = \int_0^\infty x_m^n f(x_m) dx = \frac{A_m}{\mu_m \Lambda_m^{(\beta_m+n+1)/\mu_m}} \Gamma\left(\frac{\beta_m+n+1}{\mu_m}\right), \tag{8.34}$$

with $M_0^m = N_d$ [m^{-3}] and $M_1^m = q_L$ [gm^{-3}].

Writing explicitely the definition for the zeroth and first moment:

$$M_0^m = N_d = \frac{A_m}{\beta_m\, \Lambda_m^{\alpha_0^m}}\, \Gamma(\alpha_0^m), \tag{8.35}$$

and

$$M_1^m = q_L = \frac{A}{\mu\, \Lambda^{\alpha_1^m}}\, \Gamma(\alpha_1^m). \tag{8.36}$$

Hereby we defined $\alpha_n^m = \frac{\beta_m+n+1}{\mu_m}$.

To reconstruct the mass size distribution we need to find the two unknown parameters A_m and Λ_m from the two given moment equations. The parameters $\beta_m = 1$ and $\mu_m = 1$ are taken from Table 1 in Seifert and Beheng (2005) (in their manuscript our β is denoted as ν), which is valid only for cloud droplets in the model parameterization.

Dividing Eq. 8.36 and Eq. 8.35, and setting $\mu_m = 1$ and $\beta_m = 1$ for cloud droplets, we yield:

$$\Lambda_m = \left(\frac{\Gamma(2)}{\Gamma(3)}\, \frac{q_L}{N_d}\right)^{-1} = \left(0.5\, \frac{q_L}{N_d}\right)^{-1}, \tag{8.37}$$

and

$$A_m = \frac{N_d}{\Gamma(2)} \Lambda_m^2. \tag{8.38}$$

For probability density functions the following relationship is valid:

$$F(D)\, dD = f(x_m(D))\, dx_m, \tag{8.39}$$

where D is a droplet diameter (e.g., the geometrical diameter D_g or the effective diameter D_e).

Following Seifert and Beheng (2005) and Petty and Huang (2011) a power law is applied to connect mass and droplet diamater:

$$x_m = aD^b \; dx = abD^{(b-1)}dD, \tag{8.40}$$

with $a = \frac{\pi\rho_w}{6}$ and b = 3 (Petty and Huang, 2011) for the geometrical diameter D_g for spherical particles.

Petty and Huang (2011) give the transformation factors between the droplet mass and droplet diameter in their Table 2. Using those relations one can calculate the moments for the diameter given the parameters of the mass distribution. The suffix m denotes the parameters of the mass distribution and g for the geometrical diameter. The transformation factors are as follows:

$$A_g = bA_m a^{(\beta_m+1)}, \tag{8.41}$$

$$\beta_g = b(\beta_m + 1) - 1, \tag{8.42}$$

$$\lambda_g = \Lambda_m a^{\beta_m}, \tag{8.43}$$

$$\mu_g = b\beta_m. \tag{8.44}$$

Then the moments of the DSD for the geometrical diameter M_n^g are given by:

$$M_n^g = \frac{A_g \Gamma\left(\frac{1+\beta_g+n}{\mu_g}\right)}{\mu_g \Lambda_g^{(1+\beta_g+n)/\mu_g}}. \tag{8.45}$$

N_d would be the zeroth moment of the droplet size distribution, and q_L would be related to the third moment of the DSD (multiplied by a), and all further moments are defined as outlined in Sect. 2.1.1.

Putting the parameters for the cloud droplets ($\mu_m = 1$, $\beta_m = 1$, $b = 1/3$) into Eq. 8.45:

$$M_n^g = \frac{A_m \, a^2 \, \Gamma(\alpha_n^g)}{a^{\alpha_n^g} \, \Lambda^{\alpha_n^g}}, \tag{8.46}$$

with $\alpha_n^g = \frac{1-1/3+n}{1/3}$.

For the moments M_n^e of the size distribution of the effective diameter D_e we yield the same a, b parameters in case of spherical particles (Petty and Huang, 2011).

Bibliography

Ackerman, A. S., Toon, O. B., Stevens, D. E., Heymsfield, A. J., Ramanathan, V., and Welton, E. J.: Reduction of tropical cloudiness by soot, Science, 288, 1042–1047, `http://science.sciencemag.org/content/288/5468/1042`, 2000.

Ahmad, I., Mielonen, T., Grosvenor, D., Portin, H., Arola, A., Mikkonen, S., Kühn, T., Leskinen, A., Juotsensaari, J., Komppula, M., Lehtinen, K., Laaksonen, A., and Romakkaniemi, S.: Long-term measurements of cloud droplet concentrations and aerosol-cloud interactions in continental boundary layer clouds, Tellus B, 65, `http://www.tellusb.net/index.php/tellusb/article/view/20138`, 2013.

Albrecht, B. A.: Aerosols, cloud microphysics, and fractional cloudiness, Science, 245, 1227–1230, `http://science.sciencemag.org/content/245/4923/1227`, 1989.

Albrecht, B. A., Fairall, C. W., Thomson, D. W., White, A. B., Snider, J. B., and Schubert, W. H.: Surface-based remote sensing of the observed and the adiabatic liquid water content of stratocumulus clouds, Geophys. Res. Lett., 17, 89–92, `http://dx.doi.org/10.1029/GL017i001p00089`, 1990.

Andreae, M. O.: Correlation between cloud condensation nuclei concentration and aerosol optical thickness in remote and polluted regions, Atmospheric Chemistry and Physics, 9, 543–556, `http://www.atmos-chem-phys.net/9/543/2009/`, 2009.

Baker, M. B., Corbin, R. G., and Latham, J.: The influence of entrainment on the evolution of cloud droplet spectra: I. A model of inhomogeneous mixing, Quarterly Journal of the Royal Meteorological Society, 106, 581–598, `http://dx.doi.org/10.1002/qj.49710644914`, 1980.

Battan, L. J.: Radar observation of the atmosphere, University of Chicago Press, 1973.

Baum, B. A., Menzel, W. P., Frey, R. A., Tobin, D. C., Holz, R. E., Ackerman, S. A., Heidinger, A. K., and Yang, P.: MODIS cloud-top property refinements for collection 6, Journal of Applied Meteorology and Climatology, 51, 1145–1163, `http://dx.doi.org/10.1175/JAMC-D-11-0203.1`, 2012.

Bellouin, N., Quaas, J., Morcrette, J.-J., and Boucher, O.: Estimates of aerosol radiative forcing from the MACC re-analysis, Atmospheric Chemistry and Physics, 13, 2045–2062, `http://www.atmos-chem-phys.net/13/2045/2013/`, 2013.

Benedetti, A., Morcrette, J.-J., Boucher, O., Dethof, A., Engelen, R. J., Fisher, M., Flentje, H., Huneeus, N., Jones, L., Kaiser, J. W., Kinne, S., Mangold, A., Razinger, M., Simmons, A. J., and Suttie, M.: Aerosol analysis and forecast in the European Centre for Medium-Range Weather Forecasts Integrated Forecast System: 2. Data assimilation, Journal of Geophysical Research: Atmospheres, 114, D13 205, `http://dx.doi.org/10.1029/2008JD011115`, 2009.

Bennartz, R.: Global assessment of marine boundary layer cloud droplet number concentration from satellite, Journal of Geophysical Research: Atmospheres, 112, L05 807, `http://dx.doi.org/10.1029/2006JD007547`, 2007.

Block, K. and Quaas, J.: A CCN climatology from the MACC-II aerosol re-analysis, in prep., 2016.

Boers, R. and Mitchell, R. M.: Absorption feedback in stratocumulus clouds influence on cloud top albedo, Tellus A, 46, 229–241, 1994.

Boers, R., Russchenberg, H., Erkelens, J., Venema, V., van Lammeren, A., Apituley, A., and Jongen, S.: Ground-based remote sensing of stratocumulus properties during CLARA, 1996, Journal of Applied Meteorology, 39, 169–181, `http://dx.doi.org/10.1175/1520-0450(2000)039<0169:GBRSOS>2.0.CO;2`, 2000.

Boers, R., Acarreta, J. R., and Gras, J. L.: Satellite monitoring of the first indirect aerosol effect: Retrieval of the droplet concentration of water clouds, Journal of Geophysical Research: Atmospheres, 111, D22 208, `http://dx.doi.org/10.1029/2005JD006838`, 2006.

Bohren, C. F. and Clothiaux, E. E.: Fundamentals of atmospheric radiation: an introduction with 400 problems, John Wiley & Sons, 2006.

Boucher, O., Randall, D., Artaxo, P., Bretherton, C., Feingold, G., Forster, P., Kerminen, V., Kondo, Y., Liao, H., Lohmann, U., et al.: Clouds and aerosols, Climate Change, pp. 571–657, 2013.

Brandau, C., Russchenberg, H., and Knap, W.: Evaluation of ground-based remotely sensed liquid water cloud properties using shortwave radiation measurements, Atmospheric Research, 96, 366 – 377, `http://www.sciencedirect.com/science/article/pii/S0169809510000207`, 15th International Conference on Clouds and Precipitation {ICCP} 2008, 2010.

Brenguier, J.-L., Pawlowska, H., Schüller, L., Preusker, R., Fischer, J., and Fouquart, Y.: Radiative properties of boundary layer clouds: droplet effective radius versus number concentration, Journal of the Atmospheric Sciences, 57, 803–821, `http://dx.doi.org/10.1175/1520-0469(2000)057<0803:RPOBLC>2.0.CO;2`, 2000.

Brenguier, J.-L., Burnet, F., and Geoffroy, O.: Cloud optical thickness and liquid water path – does the k coefficient vary with droplet concentration?, Atmospheric Chemistry and Physics, 11, 9771–9786, `http://www.atmos-chem-phys.net/11/9771/2011/`, 2011.

Bréon, F.-M., Tanré, D., and Generoso, S.: Aerosol effect on cloud droplet size monitored from satellite, Science, 295, 834–838, `http://www.sciencemag.org/content/295/5556/834.abstract`, 2002.

Bühl, J., Seifert, P., Wandinger, U., Baars, H., Kanitz, T., Schmidt, J., Myagkov, A., Engelmann, R., Skupin, A., Heese, B., Klepel, A., Althausen, D., and Ansmann, A.: LACROS: the Leipzig Aerosol and Cloud Remote Observations System, Proc. SPIE, Remote sensing of clouds and the atmosphere XVIII and optics in atmospheric propagation and adaptive systems XVI, 8890, 889 002, `http://dx.doi.org/10.1117/12.2030911`, 2013.

Bulgin, C. E., Palmer, P. I., Thomas, G. E., Arnold, C. P. G., Campmany, E., Carboni, E., Grainger, R. G., Poulsen, C., Siddans, R., and Lawrence, B. N.: Regional and seasonal variations of the Twomey indirect effect as observed by the ATSR-2 satellite instrument, Geophysical Research Letters, 35, L02 811, `http://dx.doi.org/10.1029/2007GL031394`, 2008.

Chin, H.-N. S., Rodriguez, D. J., Cederwall, R. T., Chuang, C. C., Grossman, A. S., Yio, J. J., Fu, Q., and Miller, M. A.: A microphysical retrieval scheme for continental low-level stratiform clouds: Impacts of the subadiabatic character on microphysical properties and radiation budgets, Monthly Weather Review, 128, 2511–2527, `http://dx.doi.org/10.1175/1520-0493(2000)128<2511:AMRSFC>2.0.CO;2`, 2000.

Chosson, F., Brenguier, J.-L., and Schüller, L.: Entrainment-mixing and radiative transfer simulation in boundary layer clouds, Journal of the Atmospheric Sciences, 64, 2670–2682, `http://dx.doi.org/10.1175/JAS3975.1`, 2007.

Christensen, M. W. and Stephens, G. L.: Microphysical and macrophysical responses of marine stratocumulus polluted by underlying ships: Evidence of cloud deepening, Journal of Geophysical Research: Atmospheres, 116, D03 201, `http://dx.doi.org/10.1029/2010JD014638`, 2011.

Christensen, M. W., Stephens, G. L., and Lebsock, M. D.: Exposing biases in retrieved low cloud properties from CloudSat: A guide for evaluating observations and climate data, Journal of Geophysical Research: Atmospheres, 118, 12 120–12 131, `http://dx.doi.org/10.1002/2013JD020224`, 2013.

Chylek, P. and Ramaswamy, V.: Simple approximation for infrared emissivity of water clouds, Journal of the Atmospheric Sciences, 39, 171–177, `http://dx.doi.org/10.1175/1520-0469(1982)039<0171:SAFIEO>2.0.CO;2`, 1982.

Costantino, L. and Bréon, F.-M.: Aerosol indirect effect on warm clouds over South-East Atlantic, from co-located MODIS and CALIPSO observations, Atmospheric Chemistry and Physics, 13, 69–88, `http://www.atmos-chem-phys.net/13/69/2013/`, 2013.

Derrien, M.: Algorithm theoretical basis document for cloud products (cma-pge01 v3.2, ct-pge02 v2.2, ctth-pge03 v2.2), Tech. rep., SAFNWC, `http://www.nwcsaf.org/HTMLContributions/SUM/SAF-NWC-CDOP2-MFL-SCI-ATBD-01_v3.2.1.pdf`, 2012.

Derrien, M., Gléau, H., Daloze, J.-F., and Haeffelin, M.: Validation of SAFNWC/MSG cloud products with one year of SEVIRI data, in 2005 EUMETSAT Meteorological Satellite Conference, pp. 95–103, 2005.

Dipankar, A., Stevens, B., Heinze, R., Moseley, C., Zängl, G., Giorgetta, M., and Brdar, S.: Large eddy simulation using the general circulation model ICON, Journal of Advances in Modeling Earth Systems, 7, 963–986, `http://dx.doi.org/10.1002/2015MS000431`, 2015.

Ditas, F.: Microphysical properties of aerosol particles in the trade wind regime and their influence on the number concentration of activated particles in trade wind cumulus clouds, Ph.D. thesis, University of Leipzig, 2014.

Dong, X. and Mace, G. G.: Profiles of low-level stratus cloud microphysics deduced from ground-based measurements, Journal of Atmospheric and Oceanic Technology, 20, 42–53, `http://dx.doi.org/10.1175/1520-0426(2003)020<0042:POLLSC>2.0.CO;2`, 2003.

Dong, X., Ackerman, T. P., and Clothiaux, E. E.: Parameterizations of the microphysical and shortwave radiative properties of boundary layer stratus from ground-based measurements, Journal of Geophysical Research: Atmospheres, 103, 31 681–31 693, `http://dx.doi.org/10.1029/1998JD200047`, 1998.

Dusek, U., Frank, G. P., Hildebrandt, L., Curtius, J., Schneider, J., Walter, S., Chand, D., Drewnick, F., Hings, S., Jung, D., Borrmann, S., and Andreae, M. O.: Size matters more than chemistry for cloud-nucleating ability of aerosol particles, Science, 312, 1375–1378, `http://science.sciencemag.org/content/312/5778/1375`, 2006.

Ebell, K., Löhnert, U., Crewell, S., and Turner, D. D.: On characterizing the error in a remotely sensed liquid water content profile, Atmospheric Research, 98, 57–68, `http://www.sciencedirect.com/science/article/pii/S0169809510001420`, clouds, Aerosols and RadiationEGU09, 2010.

Ebell, K., Crewell, S., Löhnert, U., Turner, D. D., and O'Connor, E. J.: Cloud statistics and cloud radiative effect for a low-mountain site, Quarterly Journal of the Royal Meteorological Society, 137, 306–324, `http://dx.doi.org/10.1002/qj.748`, 2011.

Ebell, K., Orlandi, E., Hünerbein, A., Löhnert, U., and Crewell, S.: Combining ground-based with satellite-based measurements in the atmospheric state retrieval: Assessment of the information content, Journal of Geophysical Research: Atmospheres, 118, 6940–6956, `http://dx.doi.org/10.1002/jgrd.50548`, 2013.

Engelmann, R., Kanitz, T., Baars, H., Heese, B., Althausen, D., Skupin, A., Wandinger, U., Komppula, M., Stachlewska, I. S., Amiridis, V., Marinou, E., Mattis, I., Linné, H., and Ansmann, A.: The automated multiwavelength Raman polarization and water-vapor lidar Polly^{XT}: the neXT generation, Atmospheric Measurement Techniques, 9, 1767–1784, `http://www.atmos-meas-tech.net/9/1767/2016/`, 2016.

EUMETSAT: Conversion from radiances to reflectances for SEVIRI warm channels, Tech. Rep. EUM/MET/TEN/12/0332, EUMETSAT, 2012.

Feingold, G., Remer, L. A., Ramaprasad, J., and Kaufman, Y. J.: Analysis of smoke impact on clouds in Brazilian biomass burning regions: An extension of Twomey's approach, Journal of Geophysical Research: Atmospheres, 106, 22 907–22 922, `http://dx.doi.org/10.1029/2001JD000732`, 2001.

Feingold, G., Eberhard, W. L., Veron, D. E., and Previdi, M.: First measurements of the Twomey indirect effect using ground-based remote sensors, Geophysical Research Letters, 30, 1287, `http://dx.doi.org/10.1029/2002GL016633`, 2003.

Fischer, J., Cordes, W., Schmitz-Peiffer, A., Renger, W., and Mörl, P.: Detection of cloud-top height from backscattered radiances within the Oxygen A Band. Part 2: Measurements, Journal of Applied Meteorology, 30, 1260–1267, `http://dx.doi.org/10.1175/1520-0450(1991)030<1260:DOCTHF>2.0.CO;2`, 1991.

Fox, N. I. and Illingworth, A. J.: The retrieval of stratocumulus cloud properties by ground-based cloud radar, Journal of Applied Meteorology, 36, 485–492, `http://dx.doi.org/10.1175/1520-0450(1997)036<0485:TROSCP>2.0.CO;2`, 1997.

Frisch, A. S., Fairall, C. W., and Snider, J. B.: Measurement of stratus cloud and drizzle parameters in ASTEX with a Ka-Band Doppler radar and a microwave radiometer, Journal of the Atmospheric Sciences, 52, 2788–2799, `http://dx.doi.org/10.1175/1520-0469(1995)052<2788:MOSCAD>2.0.CO;2`, 1995.

Frisch, A. S., Feingold, G., Fairall, C. W., Uttal, T., and Snider, J. B.: On cloud radar and microwave radiometer measurements of stratus cloud liquid water profiles, Journal of Geophysical Research: Atmospheres, 103, 23 195–23 197, `http://dx.doi.org/10.1029/98JD01827`, 1998.

Frisch, S., Shupe, M., Djalalova, I., Feingold, G., and Poellot, M.: The retrieval of stratus cloud droplet effective radius with cloud radars, Journal of Atmospheric and Oceanic Technology, 19, 835–842, `http://dx.doi.org/10.1175/1520-0426(2002)019<0835:TROSCD>2.0.CO;2`, 2002.

Gaussiat, N., Hogan, R. J., and Illingworth, A. J.: Accurate liquid water path retrieval from low-cost microwave radiometers using additional information from a lidar ceilometer and operational forecast models, Journal of Atmospheric and Oceanic Technology, 24, 1562–1575, `http://dx.doi.org/10.1175/JTECH2053.1`, 2007.

George, R. C. and Wood, R.: Subseasonal variability of low cloud radiative properties over the southeast Pacific Ocean, Atmospheric Chemistry and Physics, 10, 4047–4063, `http://www.atmos-chem-phys.net/10/4047/2010/`, 2010.

Görsdorf, U., Lehmann, V., Bauer-Pfundstein, M., Peters, G., Vavriv, D., Vinogradov, V., and Volkov, V.: A 35-GHz polarimetric Doppler radar for long-term observations of cloud parameters—description of system and data processing, Journal of Atmospheric and Oceanic Technology, 32, 675–690, `http://dx.doi.org/10.1175/JTECH-D-14-00066.1`, 2015.

Grassl, H.: Possible changes of planetary albedo due to aerosol particles, Elsevier, 1979.

Gryspeerdt, E. and Stier, P.: Regime-based analysis of aerosol-cloud interactions, Geophysical Research Letters, 39, L21 802, `http://dx.doi.org/10.1029/2012GL053221`, 2012.

Hamann, U., Walther, A., Baum, B., Bennartz, R., Bugliaro, L., Derrien, M., Francis, P. N., Heidinger, A., Joro, S., Kniffka, A., Le Gléau, H., Lockhoff, M., Lutz, H.-J., Meirink, J. F., Minnis, P., Palikonda, R., Roebeling, R., Thoss, A., Platnick, S., Watts, P., and Wind, G.: Remote sensing of cloud top pressure/height from SEVIRI: analysis of ten current retrieval algorithms, Atmospheric Measurement Techniques, 7, 2839–2867, `http://www.atmos-meas-tech.net/7/2839/2014/`, 2014.

Han, Q., Rossow, W. B., and Lacis, A. A.: Near-global survey of effective droplet radii in liquid water clouds using ISCCP data, Journal of Climate, 7, 465–497, `http://dx.doi.org/10.1175/1520-0442(1994)007<0465:NGSOED>2.0.CO;2`, 1994.

Han, Q., Rossow, W. B., Chou, J., and Welch, R. M.: Global variation of column droplet concentration in low-level clouds, Geophysical Research Letters, 25, 1419–1422, `http://dx.doi.org/10.1029/98GL01095`, 1998.

Hansen, J., Ruedy, R., Sato, M., and Lo, K.: Global surface temperature change, Reviews of Geophysics, 48, `http://dx.doi.org/10.1029/2010RG000345`, rg4004, 2010.

Hansen, J. E. and Travis, L. D.: Light scattering in planetary atmospheres, Space Science Reviews, 16, 527–610, 1974.

Haywood, J. and Boucher, O.: Estimates of the direct and indirect radiative forcing due to tropospheric aerosols: A review, Reviews of Geophysics, 38, 513–543, `http://dx.doi.org/10.1029/1999RG000078`, 2000.

Heinze, R., Dipankar, A., Carbajal Henken, C., Moseley, C., Sourdeval, O., Trömel, S., Xie, X., Adamidis, P., Ament, F., Baars, H., Barthlott, C., Behrendt, A., Blahak, U., Bley, S., Brdar, S., Brueck, M., Crewell, S., Deneke, H., Di Girolamo, P., Evaristo, R., Fischer, J., Frank, C., Friederichs, P., Göcke, T., Gorges, K., Hande, L., Hanke, M., Hansen, A., Hege, H.-C., Hoose, C., Jahns, T., Kalthoff, N., Klocke, D., Kneifel, S., Knippertz, P., Kuhn, A., van Laar, T., Macke, A., Maurer, V., Mayer, B., Meyer, C. I., Muppa, S. K., Neggers, R. A. J., Orlandi, E., Pantillon, F., Pospichal, B., Röber, N., Scheck, L., Seifert, A., Seifert, P., Senf, F., Siligam, P., Simmer, C., Steinke, S., Stevens, B., Wapler, K., Weniger, M., Wulfmeyer, V., Zängl, G., Zhang, D., and Quaas, J.: Large-eddy simulations over Germany using ICON: A comprehensive evaluation, Quarterly Journal of the Royal Meteorological Society, `http://dx.doi.org/10.1002/qj.2947`, qJ-16-0198.R1, 2016.

Hewison, T.: 1D-VAR retrieval of temperature and humidity profiles from a ground-based microwave radiometer, Geoscience and Remote Sensing, IEEE Transactions on, 45, 2163–2168, 2007.

Hogan, R. J. and O'Connor, E. J.: Facilitating cloud radar and lidar algorithms: the Cloudnet Instrument Synergy/Target Categorization product, Cloudnet documentation, 2004.

Holz, R. E., Ackerman, S. A., Nagle, F. W., Frey, R., Dutcher, S., Kuehn, R. E., Vaughan, M. A., and Baum, B.: Global Moderate Resolution Imaging Spectroradiometer (MODIS) cloud detection and height evaluation using CALIOP, Journal of Geophysical

Research: Atmospheres, 113, D00A19, `http://dx.doi.org/10.1029/2008JD009837`, 2008.

Hünerbein, A., Deneke, H., Macke, A., Ebell, K., and Görsdorf, U.: Combining the perspective of satellite- and ground-based observations to analyze cloud frontal systems, Journal of Applied Meteorology and Climatology, 53, 2538–2552, `http://dx.doi.org/10.1175/JAMC-D-13-0274.1`, 2014.

Illingworth, A. J., Hogan, R. J., O'Connor, E. J., Bouniol, D., Delanoë, J., Pelon, J., Protat, A., Brooks, M. E., Gaussiat, N., Wilson, D. R., Donovan, D. P., Baltink, H. K., van Zadelhoff, G.-J., Eastment, J. D., Goddard, J. W. F., Wrench, C. L., Haeffelin, M., Krasnov, O. A., Russchenberg, H. W. J., Piriou, J.-M., Vinit, F., Seifert, A., Tompkins, A. M., and Willén, U.: Cloudnet - Continuous evaluation of cloud profiles in seven operational models using ground-based observations, Bulletin of the American Meteorological Society, 88, 883–898, `http://dx.doi.org/10.1175/BAMS-88-6-883`, 2007.

Janssen, R. H. H., Ganzeveld, L. N., Kabat, P., Kulmala, M., Nieminen, T., and Roebeling, R. A.: Estimating seasonal variations in cloud droplet number concentration over the boreal forest from satellite observations, Atmospheric Chemistry and Physics, 11, 7701–7713, `http://www.atmos-chem-phys.net/11/7701/2011/`, 2011.

Karydis, V. A., Kumar, P., Barahona, D., Sokolik, I. N., and Nenes, A.: On the effect of dust particles on global cloud condensation nuclei and cloud droplet number, Journal of Geophysical Research: Atmospheres, 116, D23 204, `http://dx.doi.org/10.1029/2011JD016283`, 2011.

Kato, S., Mace, G. G., Clothiaux, E. E., Liljegren, J. C., and Austin, R. T.: Doppler cloud radar derived drop size distributions in liquid water stratus clouds, Journal of the atmospheric sciences, 58, 2895–2911, 2001.

Katzwinkel, J., Siebert, H., and Shaw, R. A.: Observation of a self-limiting, shear-induced turbulent inversion layer above marine stratocumulus, Boundary-Layer Meteorology, 145, 131–143, `http://dx.doi.org/10.1007/s10546-011-9683-4`, 2012.

Kiehl, J. T. and Trenberth, K. E.: Earth's annual global mean energy budget, Bulletin of the American Meteorological Society, 78, 197–208, `http://dx.doi.org/10.1175/1520-0477(1997)078<0197:EAGMEB>2.0.CO;2`, 1997.

Kim, B.-G., Miller, M. A., Schwartz, S. E., Liu, Y., and Min, Q.: The role of adiabaticity in the aerosol first indirect effect, Journal of Geophysical Research: Atmospheres, 113, D05 210, `http://dx.doi.org/10.1029/2007JD008961`, 2008.

King, M., Kaufman, Y., Menzel, W., and Tanre, D.: Remote sensing of cloud, aerosol, and water vapor properties from the moderate resolution imaging spectrometer (MODIS), Geoscience and Remote Sensing, IEEE Transactions on, 30, 2–27, 1992.

King, M. D., Tsay, S.-C., Platnick, S. E., Wang, M., and Liou, K.-N.: Cloud retrieval algorithms for MODIS: Optical thickness, effective particle radius, and thermodynamic phase, MODIS Algorithm Theoretical Basis Document, 1997.

King, N. J. and Vaughan, G.: Using passive remote sensing to retrieve the vertical variation of cloud droplet size in marine stratocumulus: An assessment of information content and the potential for improved retrievals from hyperspectral measurements, Journal of Geophysical Research: Atmospheres, 117, D15 206, `http://dx.doi.org/10.1029/2012JD017896`, 2012.

King, N. J., Bower, K. N., Crosier, J., and Crawford, I.: Evaluating MODIS cloud retrievals with in situ observations from VOCALS-REx, Atmospheric Chemistry and Physics, 13, 191–209, `http://www.atmos-chem-phys.net/13/191/2013/`, 2013.

Kniffka, A., Stengel, M., Lockhoff, M., Bennartz, R., and Hollmann, R.: Characteristics of cloud liquid water path from SEVIRI onboard the Meteosat Second Generation 2 satellite for several cloud types, Atmospheric Measurement Techniques, 7, 887–905, `http://www.atmos-meas-tech.net/7/887/2014/`, 2014.

Knist, C. L.: Retrieval of liquid water cloud properties from ground-based remote sensing observations, Ph.D. thesis, TU Delft, Delft University of Technology, 2014.

Kollias, P., Clothiaux, E. E., Miller, M. A., Albrecht, B. A., Stephens, G. L., and Ackerman, T. P.: Millimeter-wavelength radars: New frontier in atmospheric cloud and precipitation research, Bulletin of the American Meteorological Society, 88, 1608–1624, `http://dx.doi.org/10.1175/BAMS-88-10-1608`, 2007.

Kollias, P., Rémillard, J., Luke, E., and Szyrmer, W.: Cloud radar Doppler spectra in drizzling stratiform clouds: 1. Forward modeling and remote sensing applications, Journal of Geophysical Research: Atmospheres, 116, D13 201, `http://dx.doi.org/10.1029/2010JD015237`, 2011.

Korolev, A. V., Isaac, G. A., Strapp, J. W., Cober, S. G., and Barker, H. W.: In situ measurements of liquid water content profiles in midlatitude stratiform clouds, Quarterly Journal of the Royal Meteorological Society, 133, 1693–1699, `http://dx.doi.org/10.1002/qj.147`, 2007.

Krzywinski, M. and Altman, N.: Points of significance: Visualizing samples with box plots, Nat Meth, 11, 119–120, `http://dx.doi.org/10.1038/nmeth.2813`, 2014.

Liao, L. and Sassen, K.: Investigation of relationships between Ka-band radar reflectivity and ice and liquid water contents, Atmospheric Research, 34, 231 – 248, `http://www.sciencedirect.com/science/article/pii/0169809594900949`, 1994.

Loeb, N. G. and Coakley, J. A.: Inference of marine stratus cloud optical depths from satellite measurements: Does 1D theory apply?, Journal of Climate, 11, 215–233, `http://dx.doi.org/10.1175/1520-0442(1998)011<0215:IOMSCO>2.0.CO;2`, 1998.

Lohmann, U. and Feichter, J.: Global indirect aerosol effects: a review, Atmospheric Chemistry and Physics, 5, 715–737, `http://hal.archives-ouvertes.fr/hal-00295633`, 2005.

Löhnert, U., Crewell, S., Simmer, C., and Macke, A.: Profiling cloud liquid water by combining active and passive microwave measurements with cloud model statistics, Journal of Atmospheric and Oceanic Technology, 18, 1354–1366, `http://dx.doi.org/10.1175/1520-0426(2001)018<1354:PCLWBC>2.0.CO;2`, 2001.

Löhnert, U., Feingold, G., Uttal, T., Frisch, A. S., and Shupe, M. D.: Analysis of two independent methods for retrieving liquid water profiles in spring and summer Arctic boundary clouds, Journal of Geophysical Research: Atmospheres, 108, 4219, `http://dx.doi.org/10.1029/2002JD002861`, 2003.

Löhnert, U., van Meijgaard, E., Baltink, H. K., Groß, S., and Boers, R.: Accuracy assessment of an integrated profiling technique for operationally deriving profiles of temperature, humidity, and cloud liquid water, Journal of Geophysical Research: Atmospheres, 112, D04 205, `http://dx.doi.org/10.1029/2006JD007379`, 2007.

Lonitz, K., Stevens, B., Nuijens, L., Sant, V., Hirsch, L., and Seifert, A.: The signature of aerosols and meteorology in long-term cloud radar observations of trade wind cumuli, Journal of the Atmospheric Sciences, 72, 4643–4659, `http://dx.doi.org/10.1175/JAS-D-14-0348.1`, 2015.

Ma, X., Yu, F., and Quaas, J.: Reassessment of satellite-based estimate of aerosol climate forcing, Journal of Geophysical Research: Atmospheres, 119, 10 394–10 409, `http://dx.doi.org/10.1002/2014JD021670`, 2014JD021670, 2014.

Mace, G. G. and Sassen, K.: A constrained algorithm for retrieval of stratocumulus cloud properties using solar radiation, microwave radiometer, and millimeter cloud radar data, Journal of Geophysical Research: Atmospheres, 105, 29 099–29 108, `http://dx.doi.org/10.1029/2000JD900403`, 2000.

Madhavan, B. L., He, Y., Wu, Y., Gross, B., Moshary, F., and Ahmed, S.: Development of a ground based remote sensing approach for direct evaluation of aerosol-cloud interaction, Atmosphere, 3, 468, `http://www.mdpi.com/2073-4433/3/4/468`, 2012.

Mann, G. W., Carslaw, K. S., Spracklen, D. V., Ridley, D. A., Manktelow, P. T., Chipperfield, M. P., Pickering, S. J., and Johnson, C. E.: Description and evaluation of GLOMAP-mode: a modal global aerosol microphysics model for the UKCA composition-climate model, Geoscientific Model Development, 3, 519–551, `http://www.geosci-model-dev.net/3/519/2010/`, 2010.

Marshak, A., Platnick, S., Várnai, T., Wen, G., and Cahalan, R. F.: Impact of three-dimensional radiative effects on satellite retrievals of cloud droplet sizes, Journal of Geophysical Research: Atmospheres, 111, D09 207, `http://dx.doi.org/10.1029/2005JD006686`, 2006.

Martin, G. M., Johnson, D. W., and Spice, A.: The measurement and parameterization of effective radius of droplets in warm stratocumulus clouds, Journal of the Atmospheric Sciences, 51, 1823–1842, `http://dx.doi.org/10.1175/1520-0469(1994)051<1823:TMAPOE>2.0.CO;2`, 1994.

Mayer, B., Schröder, M., Preusker, R., and Schüller, L.: Remote sensing of water cloud droplet size distributions using the backscatter glory: a case study, Atmospheric Chemistry and Physics, 4, 1255–1263, `http://www.atmos-chem-phys.net/4/1255/2004/`, 2004.

Mayer, B.: Radiative transfer in the cloudy atmosphere, EPJ Web of Conferences, 1, 75–99, `http://dx.doi.org/10.1140/epjconf/e2009-00912-1`, 2009.

McComiskey, A. and Feingold, G.: The scale problem in quantifying aerosol indirect effects, Atmospheric Chemistry and Physics, 12, 1031–1049, `http://www.atmos-chem-phys.net/12/1031/2012/`, 2012.

McComiskey, A., Feingold, G., Frisch, A. S., Turner, D. D., Miller, M. A., Chiu, J. C., Min, Q., and Ogren, J. A.: An assessment of aerosol-cloud interactions in marine stratus clouds based on surface remote sensing, Journal of Geophysical Research: Atmospheres, 114, D09 203, `http://dx.doi.org/10.1029/2008JD011006`, 2009.

McFarlane, S. A., Evans, K. F., and Ackerman, A. S.: A Bayesian algorithm for the retrieval of liquid water cloud properties from microwave radiometer and millimeter radar data, Journal of Geophysical Research: Atmospheres, 107, AAC 12–1–AAC 12–21, `http://dx.doi.org/10.1029/2001JD001011`, 2002.

McFarlane, S. A., Mather, J. H., Ackerman, T. P., and Liu, Z.: Effect of clouds on the calculated vertical distribution of shortwave absorption in the tropics, Journal of Geophysical Research: Atmospheres, 113, D18 203, `http://dx.doi.org/10.1029/2008JD009791`, 2008.

McFiggans, G., Artaxo, P., Baltensperger, U., Coe, H., Facchini, M. C., Feingold, G., Fuzzi, S., Gysel, M., Laaksonen, A., Lohmann, U., Mentel, T. F., Murphy, D. M., O'Dowd, C. D., Snider, J. R., and Weingartner, E.: The effect of physical and chemical aerosol properties on warm cloud droplet activation, Atmospheric Chemistry and Physics, 6, 2593–2649, `http://www.atmos-chem-phys.net/6/2593/2006/`, 2006.

Meerkötter, R. and Bugliaro, L.: Diurnal evolution of cloud base heights in convective cloud fields from MSG/SEVIRI data, Atmospheric Chemistry and Physics, 9, 1767–1778, `http://www.atmos-chem-phys.net/9/1767/2009/`, 2009.

Meerkötter, R. and Zinner, T.: Satellite remote sensing of cloud base height for convective cloud fields: A case study, Geophysical Research Letters, 34, L17 805, `http://dx.doi.org/10.1029/2007GL030347`, 2007.

Menon, S., Del Genio, A. D., Kaufman, Y., Bennartz, R., Koch, D., Loeb, N., and Orlikowski, D.: Analyzing signatures of aerosol-cloud interactions from satellite retrievals and the GISS GCM to constrain the aerosol indirect effect, Journal of Geophysical Research: Atmospheres, 113, D14S22, `http://dx.doi.org/10.1029/2007JD009442`, 2008.

Merk, D., Deneke, H., Pospichal, B., and Seifert, P.: On the reliability of geostationary satellite observations for diagnosing indirect aerosol effects, Proc. SPIE, Remote sensing of clouds and the atmosphere XX, 9640, 96 400D, `http://dx.doi.org/10.1117/12.2194897`, 2015.

Merk, D., Deneke, H., Pospichal, B., and Seifert, P.: Investigation of the adiabatic assumption for estimating cloud micro- and macrophysical properties from satellite and ground observations, Atmospheric Chemistry and Physics, 16, 933–952, `http://www.atmos-chem-phys.net/16/933/2016/`, 2016.

Miles, N. L., Verlinde, J., and Clothiaux, E. E.: Cloud droplet size distributions in low-level stratiform clouds, Journal of the Atmospheric Sciences, 57, 295–311, `http://dx.doi.org/10.1175/1520-0469(2000)057<0295:CDSDIL>2.0.CO;2`, 2000.

Miller, M. A., Jensen, M. P., and Clothiaux, E. E.: Diurnal cloud and thermodynamic variations in the stratocumulus transition regime: A case study using in situ and remote sensors, Journal of the Atmospheric Sciences, 55, 2294–2310, `http://dx.doi.org/10.1175/1520-0469(1998)055<2294:DCATVI>2.0.CO;2`, 1998.

Min, Q. and Duan, M.: Simultaneously retrieving cloud optical depth and effective radius for optically thin clouds, Journal of Geophysical Research: Atmospheres, 110, D21 201, `http://dx.doi.org/10.1029/2005JD006136`, 2005.

Min, Q., Joseph, E., Lin, Y., Min, L., Yin, B., Daum, P. H., Kleinman, L. I., Wang, J., and Lee, Y.-N.: Comparison of MODIS cloud microphysical properties with in-situ measurements over the Southeast Pacific, Atmospheric Chemistry and Physics, 12, 11 261–11 273, `http://www.atmos-chem-phys.net/12/11261/2012/`, 2012.

Morcrette, J.-J., Boucher, O., Jones, L., Salmond, D., Bechtold, P., Beljaars, A., Benedetti, A., Bonet, A., Kaiser, J. W., Razinger, M., Schulz, M., Serrar, S., Simmons, A. J., Sofiev, M., Suttie, M., Tompkins, A. M., and Untch, A.: Aerosol analysis and forecast in the European Centre for Medium-Range Weather Forecasts Integrated Forecast System: Forward modeling, Journal of Geophysical Research: Atmospheres, 114, D06 206, `http://dx.doi.org/10.1029/2008JD011235`, 2009.

Nakajima, T. and King, M. D.: Determination of the optical thickness and effective particle radius of clouds from reflected solar radiation measurements. Part I: Theory, Journal of the Atmospheric Sciences, 47, 1878–1893, `http://dx.doi.org/10.1175/1520-0469(1990)047<1878:DOTOTA>2.0.CO;2`, 1990.

Nakajima, T., Higurashi, A., Kawamoto, K., and Penner, J. E.: A possible correlation between satellite-derived cloud and aerosol microphysical parameters, Geophysical Research Letters, 28, 1171–1174, `http://dx.doi.org/10.1029/2000GL012186`, 2001.

Noble, S. R. and Hudson, J. G.: MODIS comparisons with northeastern Pacific in situ stratocumulus microphysics, Journal of Geophysical Research: Atmospheres, 120, 8332–8344, `http://dx.doi.org/10.1002/2014JD022785`, 2014JD022785, 2015.

Painemal, D. and Zuidema, P.: Microphysical variability in southeast Pacific Stratocumulus clouds: synoptic conditions and radiative response, Atmospheric Chemistry and Physics, 10, 6255–6269, `http://www.atmos-chem-phys.net/10/6255/2010/`, 2010.

Painemal, D. and Zuidema, P.: Assessment of MODIS cloud effective radius and optical thickness retrievals over the Southeast Pacific with VOCALS-REx in situ measurements, Journal of Geophysical Research: Atmospheres, 116, D24 206, `http://dx.doi.org/10.1029/2011JD016155`, 2011.

Painemal, D. and Zuidema, P.: The first aerosol indirect effect quantified through airborne remote sensing during VOCALS-REx, Atmospheric Chemistry and Physics, 13, 917–931, `http://www.atmos-chem-phys.net/13/917/2013/`, 2013.

Petty, G. W. and Huang, W.: The modified Gamma size distribution applied to inhomogeneous and nonspherical particles: Key relationships and conversions, Journal of the Atmospheric Sciences, 68, 1460–1473, `http://dx.doi.org/10.1175/2011JAS3645.1`, 2011.

Platnick, S.: Vertical photon transport in cloud remote sensing problems, Journal of Geophysical Research: Atmospheres, 105, 22 919–22 935, `http://dx.doi.org/10.1029/2000JD900333`, 2000.

Platnick, S. and Valero, F. P. J.: A validation of a satellite cloud retrieval during ASTEX, Journal of the Atmospheric Sciences, 52, 2985–3001, `http://dx.doi.org/10.1175/1520-0469(1995)052<2985:AVOASC>2.0.CO;2`, 1995.

Platnick, S., King, M. D., Ackerman, S. A., Menzel, W. P., Baum, B. A., Riédi, J. C., and Frey, R. A.: The MODIS cloud products: Algorithms and examples from Terra, Geoscience and Remote Sensing, IEEE Transactions on, 41, 459–473, 2003.

Pruppacher, H. and Klett, J.: Microphysics of clouds and precipitation, vol. 18, Springer Science & Business Media, 2010.

Quaas, J., Boucher, O., and Bréon, F.-M.: Aerosol indirect effects in POLDER satellite data and the Laboratoire de Météorologie Dynamique–Zoom (LMDZ) general circulation model, Journal of Geophysical Research: Atmospheres, 109, D08 205, `http://dx.doi.org/10.1029/2003JD004317`, 2004.

Quaas, J., Boucher, O., and Lohmann, U.: Constraining the total aerosol indirect effect in the LMDZ and ECHAM4 GCMs using MODIS satellite data, Atmospheric Chemistry and Physics, 6, 955, `http://hal.archives-ouvertes.fr/hal-00328423`, 2006.

Quaas, J., Boucher, O., Bellouin, N., and Kinne, S.: Satellite-based estimate of the direct and indirect aerosol climate forcing, Journal of Geophysical Research: Atmospheres, 113, D05 204, `http://dx.doi.org/10.1029/2007JD008962`, 2008.

Rémillard, J., Kollias, P., and Szyrmer, W.: Radar-radiometer retrievals of cloud number concentration and dispersion parameter in nondrizzling marine stratocumulus, Atmospheric Measurement Techniques, 6, 1817–1828, `http://www.atmos-meas-tech.net/6/1817/2013/`, 2013.

Reutter, P., Su, H., Trentmann, J., Simmel, M., Rose, D., Gunthe, S. S., Wernli, H., Andreae, M. O., and Pöschl, U.: Aerosol- and updraft-limited regimes of cloud droplet formation: influence of particle number, size and hygroscopicity on the activation of cloud condensation nuclei (CCN), Atmospheric Chemistry and Physics, 9, 7067–7080, `http://www.atmos-chem-phys.net/9/7067/2009/`, 2009.

Roberts, G. C. and Nenes, A.: A continuous-flow streamwise thermal-gradient CCN chamber for atmospheric measurements, Aerosol Science and Technology, 39, 206–221, `http://dx.doi.org/10.1080/027868290913988`, 2005.

Rodgers, C.: Inverse methods for atmospheric sounding, World Scientific, vol. 2 of series on atmospheric, oceanic and planetary physics edn., 2000.

Roebeling, R., Placidi, S., Donovan, D., Russchenberg, H., and Feijt, A.: Validation of liquid cloud property retrievals from SEVIRI using ground-based observations, Geophysical Research Letters, 35, L05 814, 2008a.

Roebeling, R. A., Feijt, A. J., and Stammes, P.: Cloud property retrievals for climate monitoring: Implications of differences between Spinning Enhanced Visible and Infrared Imager (SEVIRI) on METEOSAT-8 and Advanced Very High Resolution Radiometer (AVHRR) on NOAA-17, Journal of Geophysical Research: Atmospheres, 111, D20 210, `http://dx.doi.org/10.1029/2005JD006990`, 2006.

Roebeling, R. A., Deneke, H. M., and Feijt, A. J.: Validation of cloud liquid water path retrievals from SEVIRI using one year of CloudNET observations, Journal of Applied Meteorology and Climatology, 47, 206–222, `http://dx.doi.org/10.1175/2007JAMC1661.1`, 2008b.

Rosenfeld, D., Wang, H., and Rasch, P. J.: The roles of cloud drop effective radius and LWP in determining rain properties in marine stratocumulus, Geophysical Research Letters, 39, L13 801, `http://dx.doi.org/10.1029/2012GL052028`, 2012.

Sarna, K. and Russchenberg, H. W. J.: Ground-based remote sensing scheme for monitoring aerosol–cloud interactions, Atmospheric Measurement Techniques, 9, 1039–1050, `http://www.atmos-meas-tech.net/9/1039/2016/`, 2016.

Saunders, R., Matricardi, M., and Brunel, P.: An improved fast radiative transfer model for assimilation of satellite radiance observations, Quarterly Journal of the Royal Meteorological Society, 125, 1407–1425, `http://dx.doi.org/10.1002/qj.1999.49712555615`, 1999.

Schmetz, J., Pili, P., Tjemkes, S., Just, D., Kerkmann, J., Rota, S., and Ratier, A.: An introduction to Meteosat Second Generation (MSG)., Bulletin of the American Meteorological Society, 83, 2002.

Schmidt, J., Ansmann, A., Bühl, J., Baars, H., Wandinger, U., Müller, D., and Malinka, A. V.: Dual-FOV Raman and Doppler lidar studies of aerosol-cloud interactions: Simultaneous profiling of aerosols, warm-cloud properties, and vertical wind, Journal of Geophysical Research: Atmospheres, 119, 5512–5527, `http://dx.doi.org/10.1002/2013JD020424`, 2014.

Schmidt, J., Ansmann, A., Bühl, J., and Wandinger, U.: Strong aerosol–cloud interaction in altocumulus during updraft periods: lidar observations over central Europe, Atmospheric Chemistry and Physics, 15, 10 687–10 700, `http://www.atmos-chem-phys.net/15/10687/2015/`, 2015.

Schueller, L., Brenguier, J.-L., and Pawlowska, H.: Retrieval of microphysical, geometrical, and radiative properties of marine stratocumulus from remote sensing, J. Geophys. Res., 108, 8631, `http://dx.doi.org/10.1029/2002JD002680`, 2003.

Schüller, L., Bennartz, R., Fischer, J., and Brenguier, J.-L.: An algorithm for the retrieval of droplet number concentration and geometrical thickness of stratiform marine boundary layer clouds applied to MODIS radiometric observations, Journal of Applied Meteorology, 44, 28–38, `http://dx.doi.org/10.1175/JAM-2185.1`, 2005.

Schwartz, S. E., Harshvardhan, and Benkovitz, C. M.: Influence of anthropogenic aerosol on cloud optical depth and albedo shown by satellite measurements and chemical transport modeling, Proceedings of the National Academy of Sciences, 99, 1784–1789, `http://www.pnas.org/content/99/4/1784.abstract`, 2002.

Seifert, A. and Beheng, D. K.: A two-moment cloud microphysics parameterization for mixed-phase clouds. Part 1: Model description, Meteorology and Atmospheric Physics, 92, 45–66, `http://dx.doi.org/10.1007/s00703-005-0112-4`, 2005.

Sekiguchi, M., Nakajima, T., Suzuki, K., Kawamoto, K., Higurashi, A., Rosenfeld, D., Sano, I., and Mukai, S.: A study of the direct and indirect effects of aerosols using global satellite data sets of aerosol and cloud parameters, Journal of Geophysical Research: Atmospheres, 108, 4699, `http://dx.doi.org/10.1029/2002JD003359`, 2003.

Sena, E. T., McComiskey, A., and Feingold, G.: A long-term study of aerosol–cloud interactions and their radiative effect at the Southern Great Plains using ground-based measurements, Atmospheric Chemistry and Physics, 16, 11 301–11 318, `http://www.atmos-chem-phys.net/16/11301/2016/`, 2016.

Shao, H. and Liu, G.: Why is the satellite observed aerosol's indirect effect so variable?, Geophysical Research Letters, 32, L15 802, `http://dx.doi.org/10.1029/2005GL023260`, 2005.

Shao, H. and Liu, G.: Influence of mixing on evaluation of the aerosol first indirect effect, Geophysical Research Letters, 33, L14 809, `http://dx.doi.org/10.1029/2006GL026021`, 2006.

Shao, H. and Liu, G.: A critical examination of the observed first aerosol indirect effect, Journal of the Atmospheric Sciences, 66, 1018–1032, `http://dx.doi.org/10.1175/2008JAS2812.1`, 2009.

Siebert, H., Lehmann, K., Wendisch, M., Franke, H., Maser, R., Schell, D., Saw, E. W., and Shaw, R. A.: Probing finescale dynamics and microphysics of clouds with helicopter-borne measurements, Bulletin of the American Meteorological Society, 87, 1727–1738, `http://dx.doi.org/10.1175/BAMS-87-12-1727`, 2006.

Stammes, P.: Spectral radiance modelling in the UV-Visible range: IRS 2000: Current problems in atmospheric radiation, edited by: Smith, WL and Timofeyev, YM, A, Deepak Publ., Hampton (VA), 2001.

Stephens, G. L., Vane, D. G., Boain, R. J., Mace, G. G., Sassen, K., Wang, Z., Illingworth, A. J., O'Connor, E. J., Rossow, W. B., Durden, S. L., Miller, S. D., Austin, R. T., Benedetti, A., Mitrescu, C., and CloudSat Science Team, T.: The CLOUDSAT mission and the A-TRAIN, Bulletin of the American Meteorological Society, 83, 1771–1790, `http://dx.doi.org/10.1175/BAMS-83-12-1771`, 2002.

Stephens, G. L., Li, J., Wild, M., Clayson, C. A., Loeb, N., Kato, S., LÉcuyer, T., Stackhouse, P. W., Lebsock, M., and Andrews, T.: An update on Earth's energy balance in light of the latest global observations, Nature Geosci, 5, 691–696, `http://dx.doi.org/10.1038/ngeo1580`, 2012.

Stier, P.: Limitations of passive remote sensing to constrain global cloud condensation nuclei, Atmospheric Chemistry and Physics, 16, 6595–6607, `http://www.atmos-chem-phys.net/16/6595/2016/`, 2016.

Stocker, T., Qin, D., Plattner, G., Tignor, M., Allen, S., Boschung, J., Nauels, A., Xia, Y., Bex, V., and Midgley, P.: IPCC, 2013: summary for policymakers in climate change 2013: the physical science basis, contribution of working group I to the fifth assessment report of the intergovernmental panel on climate change, 2013.

Stuhlmann, R., Rodriguez, A., Tjemkes, S., Grandell, J., Arriaga, A., Bézy, J.-L., Aminou, D., and Bensi, P.: Plans for EUMETSAT's Third Generation Meteosat geostationary satellite programme, Advances in Space Research, 36, 975 – 981, `http://www.sciencedirect.com/science/article/pii/S0273117705003832`, atmospheric Remote Sensing: Earth's Surface, Troposphere, Stratosphere and Mesosphere- I, 2005.

Su, W., Loeb, N. G., Xu, K.-M., Schuster, G. L., and Eitzen, Z. A.: An estimate of aerosol indirect effect from satellite measurements with concurrent meteorological analysis, Journal of Geophysical Research: Atmospheres, 115, D18 219, `http://dx.doi.org/10.1029/2010JD013948`, 2010.

Szczodrak, M., Austin, P. H., and Krummel, P. B.: Variability of optical depth and effective radius in marine stratocumulus clouds, Journal of the Atmospheric Sciences, 58, 2912–2926, `http://dx.doi.org/10.1175/1520-0469(2001)058<2912:VOODAE>2.0.CO;2`, 2001.

Tjemkes, S. A.: On the conversion from radiances to equivalent brightness temperatures, URL: http://www.eumetsat.int/groups/ops/documents/document/pdf_msg_ seviri_rad2bright.pdf, 2005.

Tölle, M. H. and Krueger, S. K.: Effects of entrainment and mixing on droplet size distributions in warm cumulus clouds, Journal of Advances in Modeling Earth Systems, 6, 281–299, `http://dx.doi.org/10.1002/2012MS000209`, 2014.

Turner, D. D., Vogelmann, A. M., Johnson, K., Miller, M., Austin, R. T., Barnard, J. C., Flynn, C., Long, C., McFarlane, S. A., Cady-Pereira, K., Clough, S. A., Chiu, J. C., Khaiyer, M. M., Liljegren, J., Lin, B., Minnis, P., Marshak, A., Matrosov, S. Y., Min, Q., O'Hirok, W., Wang, Z., and Wiscombe, W.: Thin liquid water clouds: Their importance and our challenge, Bulletin of the American Meteorological Society, 88, 177–190, `http://dx.doi.org/10.1175/BAMS-88-2-177`, 2007.

Twomey, S.: Pollution and the planetary albedo, Atmospheric Environment (1967), 8, 1251–1256, `http://www.sciencedirect.com/science/article/pii/0004698174900043`, 1974.

Twomey, S.: The influence of pollution on the shortwave albedo of clouds, Journal of the atmospheric sciences, 34, 1149–1152, 1977.

Verheggen, B., Cozic, J., Weingartner, E., Bower, K., Mertes, S., Connolly, P., Gallagher, M., Flynn, M., Choularton, T., and Baltensperger, U.: Aerosol partitioning between the interstitial and the condensed phase in mixed-phase clouds, Journal of Geophysical Research: Atmospheres, 112, D23 202, `http://dx.doi.org/10.1029/2007JD008714`, 2007.

Warner, J.: The water content of cumuliform cloud, Tellus, 7, 449–457, `http://dx.doi.org/10.1111/j.2153-3490.1955.tb01183.x`, 1955.

Watts, P. D., Bennartz, R., and Fell, F.: Retrieval of two-layer cloud properties from multispectral observations using optimal estimation, Journal of Geophysical Research: Atmospheres, 116, D16 203, `http://dx.doi.org/10.1029/2011JD015883`, 2011.

Wetzel, M. A. and Stowe, L. L.: Satellite-observed patterns in stratus microphysics, aerosol optical thickness, and shortwave radiative forcing, Journal of Geophysical Research: Atmospheres, 104, 31 287–31 299, `http://dx.doi.org/10.1029/1999JD900922`, 1999.

Winker, D. M., Vaughan, M. A., Omar, A., Hu, Y., Powell, K. A., Liu, Z., Hunt, W. H., and Young, S. A.: Overview of the CALIPSO Mission and CALIOP Data Processing Algorithms, Journal of Atmospheric and Oceanic Technology, 26, 2310–2323, `http://dx.doi.org/10.1175/2009JTECHA1281.1`, 2009.

Wood, R.: Relationships between optical depth, liquid water path, droplet concentration, and effective radius in adiabatic layer cloud, University of Washington, 3, `http://www.atmos.washington.edu/~robwood/papers/chilean_plume/optical_depth_relations.pdf`, 2006.

Yang, Y., Marshak, A., Mao, J., Lyapustin, A., and Herman, J.: A method of retrieving cloud top height and cloud geometrical thickness with oxygen A and B bands for the Deep Space Climate Observatory (DSCOVR) mission: Radiative transfer simulations, Journal of Quantitative Spectroscopy and Radiative Transfer, 122, 141–149, `http://www.sciencedirect.com/science/article/pii/S0022407312004281`, international Symposium on atmospheric light scattering and remote sensing (ISALSaRS'11), 2013.

Zeng, S., Riedi, J., Trepte, C. R., Winker, D. M., and Hu, Y.-X.: Study of global cloud droplet number concentration with A-Train satellites, Atmospheric Chemistry and Physics, 14, 7125–7134, `http://www.atmos-chem-phys.net/14/7125/2014/`, 2014.

Zhang, S., Xue, H., and Feingold, G.: Vertical profiles of droplet effective radius in shallow convective clouds, Atmospheric Chemistry and Physics, 11, 4633–4644, `http://www.atmos-chem-phys.net/11/4633/2011/`, 2011.

Zhao, C., Xie, S., Klein, S. A., Protat, A., Shupe, M. D., McFarlane, S. A., Comstock, J. M., Delanoë, J., Deng, M., Dunn, M., Hogan, R. J., Huang, D., Jensen, M. P., Mace, G. G., McCoy, R., O'Connor, E. J., Turner, D. D., and Wang, Z.: Toward understanding of differences in current cloud retrievals of ARM ground-based measurements, Journal of Geophysical Research: Atmospheres, 117, D10 206, `http://dx.doi.org/10.1029/2011JD016792`, 2012.

Zinner, T. and Mayer, B.: Remote sensing of stratocumulus clouds: Uncertainties and biases due to inhomogeneity, J. Geophys. Res., 111, D14 209, `http://dx.doi.org/10.1029/2005JD006955`, 2006.

Zuidema, P., Westwater, E. R., Fairall, C., and Hazen, D.: Ship-based liquid water path estimates in marine stratocumulus, Journal of Geophysical Research: Atmospheres, 110, D20 206, `http://dx.doi.org/10.1029/2005JD005833`, 2005.

List of Abbreviations

2NFOV	two-channel Narrow Field-Of-View radiometer
ACI	Aerosol Cloud Interactions
ACTOS	Airborne Cloud Turbulence Observation System
ACTRIS	Aerosols, Clouds, and Trace gases Research InfraStructure Network
AI	Aerosol Index
AOD	Aerosol Optical Depth
AR5	Assessment Report 5
AVHRR	Advanced Very High Resolution Radiometer
BC	Black Carbon
CALIOP	Cloud-Aerosol-Lidar with Orthogonal Polarization
CALIPSO	Cloud-Aerosol Lidar and Infrared Pathfinder Satellite Observation
CBH	Cloud Base Height
CCN	Cloud Condensation Nuclei
COSMO-EU	Consortium for Small-scale Modeling – EUropean domain
CPP	Cloud Physical Properties
CTH	Cloud Top Height
CTP	Cloud Top Pressure
CTT	Cloud Top Temperature
DAK	Doubling Adding KNMI
DGF	DeGrees of Freedom
DSD	Droplet Size Distribution
DWD	Deutscher Wetterdienst (German weather service)
ECMWF	European Centre for Medium-Range Weather Forecasts
HATPRO	Humidity And Temperature PROfiler
HOPE	High Definition Clouds and Precipitation for advancing Climate Prediction Observational Prototype Experiment
HD(CP)^2	High Definition Cloud and Precipitation
HRV	High Resolution Visible
ICON	ICOsahedral Non-hydrostatic
IE	Indirect Effect
IPCC	Intergovernmental Panel on Climate Change
IQR	Interquartile Range
IR	InfraRed
ISCPP	International Satellite Cloud Climatology Project
KNMI	Koninklijk Nederlands Meteorologisch Instituut
LACROS	Leipzig Aerosol and Cloud Remote Observations System
LES	Large Eddy Simulation
MACC	Monitoring Atmospheric Composition and Climate
MFRSR	Multi-Filter Rotating Shadowband Radiometer
MODIS	Moderate Resolution Imaging Spectrometer
MSG	Meteosat Second Generation
MTG	Meteosat Third Generation

NWCSAF	Satellite Application Facility for Nowcasting and Very Short Range Forecasting
NWP	Numerical Weather Prediction
OE	Optimal Estimation
OM	Organic Matter
PDF	Probability Density Function
PDI	Phase-Doppler-Interferometer
PVM	Particle-Volume-Monitor
RGB	Red-Green-Blue
RMSD	Root Mean Square Difference
RSS	Rapid Scan Service
RTTOV	Radiative Transfer for the Television and Infrared Observation Satellite Operational Vertical Sounder
SEVIRI	Spinning Enhanced Visible and Infrared Imager
VIS	VISible

List of Symbols

symbol	**name**
α_{ext}	volumetric extinction coefficient $[m^{-1}]$
β	parameter of Gamma size distribution
β^*	attenuated lidar backscatter coefficient $[\mathrm{m^{-1}\,sr^{-1}}]$
β^*_a	integrated attenuated lidar backscatter coefficient $[\mathrm{sr^{-1}}]$
$\eta(r)$	Gamma size distribution
Γ_{ad}	adiabatic rate of increase of q_L $[\mathrm{g\,m^{-4}}]$
Λ	parameter of Gamma size distribution
λ	wavelength [m]
μ	cosine of angle of incident radiation [-]
ν	effective variance of Gamma size distribution
ρ_w	density of liquid water $[\mathrm{g\,m^{-3}}]$
σ_D	spectral width of Doppler spectrum $[\mathrm{m\,s^{-1}}]$
σ_x	width parameter of lognormal droplet size distribution
τ	optical depth [-]
θ_s	solar zenith angle [°]
$\zeta(r)$	Lognormal size distribution
ω_0	single scattering albedo [-]
$\mathbf{B}$	a-priori error covariance matrix
$\mathbf{K}$	Jacobian matrix of the forward model
$\mathbf{R}$	observation error covariance matrix
$\mathbf{S}$	a-posteriori covariance matrix
$\mathbf{X}$	averaging kernel
$\vec{x}$	state vector
$\delta\vec{x_a}$	state innovation vector
$\delta\vec{y}$	observation innovation vector
$\vec{x_a}$	optimal state vector
$\vec{x_p}$	a priori state vector
$\vec{y}$	observation vector
A	parameter of Gamma size distribution
A_{ad}	adiabatic rate of increase of liquid water content mixing ratio $[\mathrm{m^{-1}}]$
ACI_N	aerosol-cloud interaction metric for N_d
ACI_r	aerosol-cloud interaction metric for r_e
ACI_τ	aerosol-cloud interaction metric for τ
$B(T)$	Planck function $[\mathrm{W\,m^{-2}\,sr^{-1}}]$
c_p	heat capacity of liquid water $[\mathrm{J\,K^{-1}}]$
CCN_m	mean cloud condensation nuclei between surface and cloud top pressure level $[\mathrm{cm^{-3}}]$
CCN_{CTP}	cloud condensation nuclei at cloud top pressure level $[\mathrm{cm^{-3}}]$
$d^2\Omega$	infititesimal solid angle [sr]
e_s	saturation vapour pressure [Pa]
f_ν	spectral response function

f_{ad}	subadiabatic factor [-]
H	cloud geometrical depth [m]
K	forward model
k	wavenumber [m]
k_2	function of width parameter of DSD
k_6	function of width parameter of DSD
L	radiance [$\mathrm{W\,m^{-2}\,sr^{-1}}$]
L_v	latent heat [$\mathrm{J\,kg^{-1}}$]
M_n	n-th moment of size distribution
$n(r)$	size distribution
N_d	cloud droplet number concentration [$\mathrm{cm^{-3}}$]
P	phase function [sr]
p	pressure [hPa]
P	probability density function
q	liquid water content mixing ratio [-]
q_L	liquid water content [$\mathrm{g\,m^{-3}}$]
Q_L	liquid water path [$\mathrm{g\,m^{-2}}$]
q_s	saturation mixing ratio [-]
Q_V	integrated water vapour content [$\mathrm{g\,m^{-2}}$]
Q_{ext}	extinction efficiency [-]
r	radius [m]
r_a	area equivalent radius [m]
r_e	effective radius [m]
r_M	mean radius [m]
r_v	volume equivalent radius [m]
T	temperature [K]
t	time [s]
T_B	brightness temperature [K]
T_{inv}	inversion strength [K]
V	volume [m^{-3}]
v_D	Doppler velocity [$\mathrm{m\,s^{-1}}$]
x	size parameter [-]
x_ϵ	a priori uncertainty vector
y_ϵ	oberservation uncertainty vector
z	height [m]
Z	radar reflectivity [dBZ]

List of Figures

List of Tables

Acknowledgements

I would like to take the opportunity to thank a number of people that made this dissertation possible in the first place.

Foremost, I would like to express my sincere gratitude to my supervisors, Hartwig Deneke, Bernhard Pospichal and Patric Seifert, for their outstanding support and the fruitful discussions during all the phases of this thesis. Especially the amount and diversity of ideas have been always a great motivation for exploring new aspects of the scientific problems.

I would also like to thank the former and current members of the satellite working group at TROPOS for the very enjoyable working environment, the always helpful discussions, and last but not least a lot of fun events outside the office. I want to mention some persons explicitely: Anja Hühnerbein, who helped me a lot understanding the Optimal Estimation problem; my former office mate Timo Hanschmann, for all his help when I was new in Leipzig; Sebastian Bley, who was most of the time the first one I approached with any question; Fabian Senf, who seems to always have the important questions on your results you haven't really thought about yet.

I am very glad Karoline Block gave me the opportunity to work with her new dataset of CCN concentrations derived from the MACC-II reanalysis, which she developed at LIM during her PhD work.

Furthermore I would like to thank all the people in the Leipzig Graduate School of Clouds, Aerosols and Radiation, especially Vasilis Barlakas, Henner Bieligk, Özge Can, Sabrina Horn and Ferdinand Stolz, who made the last years an outstanding time. And of course I also enjoyed the time spent with the other PhD students at TROPOS very much.

Many people helped improving this thesis, by e.g. proofreading or commenting on individual chapters. I am very grateful for this support.

Last but not least, I am very thankful to my family for their encouragement, and continuous support throughout all the years.

Curriculum Vitae

Name	Daniel Merk
Date of birth	13 May 1987
Place of birth	Memmingen, Germany
Citizenship	German
Current address	Wichernstr. 18 04318 Leipzig, Germany Email: danielmerk@freenet.de

Education

06/2012 – present	**Ph.D. student** Leibniz Institute for Tropospheric Research, Leipzig Graduate school on Clouds, Aerosols and Radiation
10/2009 – 03/2012	**Master's in Meteorology** LMU Munich A two-year degree Graduation: March 2012 Average grade: 1.7
10/2006 – 09/2009	**Bachelor's in Physics plus Meteorology** LMU Munich A three-year degree Graduation: September 2009 Average grade: 2.25
06/2006	Abitur Average grade: 1.7

Work experience

06/2012 – 03/2017	Scientific employee at the Leibniz Institute for Tropospheric Research, Leipzig
12/2011 – 03/2012	Assistant at the meteorological institute at LMU, Munich
12/2010 – 03/2011	Assistant at the meteorological institute at LMU, Munich